

# NOTE TO USERS

This reproduction is the best copy available.

**UMI**<sup>®</sup>



# A Study of Jet Exhaust-Wing Interaction

Joshua P. Sementi

A dissertation submitted in partial fulfillment  
of the requirements for the degree of

Doctor of Philosophy

University of Washington

2005

Program Authorized to Offer Degree: Aeronautics and Astronautics

UMI Number: 3198852

### INFORMATION TO USERS

The quality of this reproduction is dependent upon the quality of the copy submitted. Broken or indistinct print, colored or poor quality illustrations and photographs, print bleed-through, substandard margins, and improper alignment can adversely affect reproduction.

In the unlikely event that the author did not send a complete manuscript and there are missing pages, these will be noted. Also, if unauthorized copyright material had to be removed, a note will indicate the deletion.

**UMI**<sup>®</sup>

---

UMI Microform 3198852

Copyright 2006 by ProQuest Information and Learning Company.

All rights reserved. This microform edition is protected against unauthorized copying under Title 17, United States Code.

ProQuest Information and Learning Company  
300 North Zeeb Road  
P.O. Box 1346  
Ann Arbor, MI 48106-1346

University of Washington  
Graduate School

This is to certify that I have examined this copy of a doctoral dissertation by

Joshua P. Sementi

and have found that it is complete and satisfactory in all respects,  
and that any and all revisions required by the final  
examining committee have been made.

Chair of the Supervisory Committee:

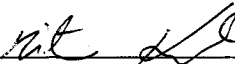


Dr. David A. Russell

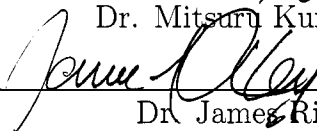
Reading Committee:



Dr. David A. Russell



Dr. Mitsuru Kurosaka

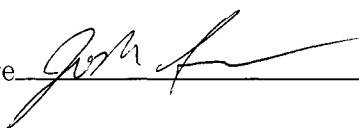


Dr. James Riley

Date:

12/14/05

In presenting this dissertation in partial fulfillment of the requirements for the doctoral degree at the University of Washington, I agree that the Library shall make its copies freely available for inspection. I further agree that extensive copying of this dissertation is allowable only for scholarly purposes, consistent with "fair use" as prescribed in the U.S. Copyright Law. Requests for copying or reproduction of this dissertation may be referred to Proquest Information and Learning, 300 North Zeeb Road, Ann Arbor, MI 48106-1346, 1-800-521-0600, to whom the author has granted "the right to reproduce and sell (a) copies of the manuscript in microform and/or (b) printed copies of the manuscript made from microform."

Signature 

Date 12/14/05

University of Washington

Abstract

## A Study of Jet Exhaust-Wing Interaction

Joshua P. Sementi

Chair of the Supervisory Committee:  
Professor Emeritus Dr. David A. Russell  
Aeronautics and Astronautics

Non-steady loading of surfaces embedded in a two-dimensional shear-layer is studied as a first step in understanding and predicting the forces generated in aircraft exhaust-jet and wing interactions. It is hypothesized that, for small separation distances between the jet and wing, coherent structures within the jet will cause non-steady lift forces. The coherent jet structures are approximated by those in a two dimensional shear-layer. A modified wind-tunnel has been used to produce a such a layer. A wing was inserted into this layer and the root mean square and power spectral density lift of the wing measured. In addition, a Vortex-Method based numerical model of the shear-layer and wing was used to provide predictions of the non-steady lift forces generated by the coherent structures. The experimental response of the wing at zero angle of attack was found to be self-similar and well behaved, with root mean square (rms) lift variations equivalent to a wing angle-of-attack, of  $2.3^\circ$ . The numerical calculations are found to be in qualitative agreement with the experimental data. While the model predicts the location and distribution of lift variation frequencies, it over-estimates the magnitude of the interaction by up to a factor of 4.

## TABLE OF CONTENTS

List of Figures . . . . .	iv
List of Tables . . . . .	x
Definition of Variables . . . . .	xi
Chapter 1: Introduction . . . . .	1
Chapter 2: Background Considerations and Literature Review . . . . .	5
2.1 Coaxial Jet Behavior . . . . .	5
2.2 Shear-Layer Fundamentals . . . . .	9
2.2.1 Coherent Structure Characteristics . . . . .	10
2.2.2 Non-steady Shear-Layer Properties . . . . .	16
2.2.3 Forced Shear-Layers . . . . .	17
2.3 Numerical Blade Vortex Interactions . . . . .	21
Chapter 3: Experimental Investigation and Results . . . . .	27
3.1 Facilities and Shear-Layer Design and Characteristics . . . . .	28
3.1.1 Shear-Layer Design . . . . .	28
3.1.2 Velocity Measurement Instrumentation . . . . .	31
3.1.3 Mean Shear-Layer Characteristics . . . . .	34
3.1.4 Spectral Shear-Layer Properties . . . . .	39
3.1.5 Forcing Source Analysis . . . . .	45
3.2 Wing and Support Structure Design and Characteristics . . . . .	46
3.2.1 Dynamic Behavior of Wing and Support Structure . . . . .	48
3.2.2 Lift Measurement . . . . .	50
3.3 Experimental Data . . . . .	52
3.3.1 Experimental Conditions . . . . .	52
3.3.2 Non-dimensionalization of Lift Data . . . . .	52

3.3.3	Effects of $U_1$ on Wing Lift Spectra . . . . .	53
3.3.4	Effects of $x$ on Lift Spectra . . . . .	58
3.3.5	$L'_{rms}$ Cross-Layer Profiles . . . . .	62
3.3.6	Vortex Passage Frequency . . . . .	67
Chapter 4:	Numerical Modeling . . . . .	68
4.1	Vortex Method Development . . . . .	69
4.1.1	Shear-Layer Vortices . . . . .	70
4.1.2	Model Boundary Treatments . . . . .	72
4.1.3	Wing and Wake Modeling . . . . .	74
4.1.4	Time Integration and Viscosity Treatment . . . . .	75
4.2	Mathematical Formulation . . . . .	77
4.2.1	Local Velocity Determination . . . . .	78
4.2.2	Wing and Wake Vortex Strength Determination . . . . .	83
4.2.3	Wing Lift Determination . . . . .	85
4.3	Model Verification . . . . .	88
4.3.1	Model Shear-Layer Testing . . . . .	89
4.3.2	Wing Model Testing . . . . .	92
4.3.3	Accuracy Considerations . . . . .	93
4.4	Numerical Model Results . . . . .	98
4.4.1	Effect of $U_1$ on $L'$ PSD Profiles . . . . .	98
4.4.2	Numerical Downstream Position Lift Spectra Data . . . . .	100
4.4.3	Numerical $L'_{rms}$ Cross-Layer Profiles . . . . .	105
4.4.4	Peak Location Analysis . . . . .	110
4.4.5	Chord Effects . . . . .	111
4.4.6	Angle of Attack Effects on Coherent Structure Development . . . . .	112
Chapter 5:	Discussion . . . . .	116
5.1	Experimental Results Summary . . . . .	116
5.1.1	Forced Shear-Layer Behavior . . . . .	117
5.2	Numerical Results Summary . . . . .	118
5.3	Comparison of Numerical and Experimental Data . . . . .	119
5.4	Recommendations for Additional Work . . . . .	122

Chapter 6: Conclusions . . . . .	125
Bibliography . . . . .	129
Appendix A: . . . . .	134
A.1 Fixed Position, Variable Velocities . . . . .	134
A.2 Fixed Height, Fixed Velocity, Variable Downstream Distance . . . . .	142
A.3 Fixed Velocity Profile . . . . .	150
Appendix B: . . . . .	153
B.1 Fixed Position Numerical Data . . . . .	153
B.2 Variable Downstream Position Numerical Data . . . . .	160
B.3 Numerical $L'_{rms}$ Cross Layer Profiles . . . . .	168
Appendix C: Calibration Data . . . . .	171
Appendix D: Experimental Data Collection Programs . . . . .	174
Appendix E: Numerical Model Computer Code . . . . .	182
E.1 Cutoff Function . . . . .	182
E.2 Random Walk . . . . .	183
E.3 Vortex Induced Velocity . . . . .	183
E.4 Shear Layer Induced Velocity . . . . .	184
E.5 Main Program Sample . . . . .	186

## LIST OF FIGURES

Figure Number	Page
1.1 Relative wing and nacelle position . . . . .	2
1.2 2-D flow cross section . . . . .	3
1.3 Flow configuration under investigation . . . . .	3
2.1 Coaxial jet velocity profiles . . . . .	7
2.2 Coaxial jet mixing regions . . . . .	8
2.3 Flow visualization of a pairing event . . . . .	11
2.4 Re number effects on a shear-layer . . . . .	14
2.5 Free shear-layer frequency spectra characteristics . . . . .	18
2.6 $u'$ frequency spectra for a $30Hz$ forced layer . . . . .	20
2.7 $u'$ frequency spectra for a $50Hz$ forced layer . . . . .	20
2.8 Tip vortex trails and rotor blade position interaction . . . . .	22
3.1 Wind-tunnel schematic . . . . .	29
3.2 Shear-layer generation schematic . . . . .	31
3.3 Hot film calibration data ( $Z_s = 0.0155$ , $Z_o = -2.35$ ) . . . . .	34
3.4 Shear-layer generation setup . . . . .	35
3.5 Shear-layer growth and virtual origin . . . . .	36
3.6 Velocity vs $\eta$ . . . . .	37
3.7 Initial boundary layer profile, $U_1 = 48m/s$ , $x = 2cm$ . . . . .	38
3.8 $u'_{rms}/U_1$ magnitude variation with $U_1$ . . . . .	39
3.9 PSD of $u'$ for varying velocity . . . . .	40
3.10 PSD of $u'$ for $U_1 = 9$ and $11m/s$ . . . . .	41
3.11 PSD of $u'$ for $x = 1.19m$ . . . . .	42
3.12 PSD of $u'$ for $x = 1.96m$ . . . . .	43
3.13 Peak velocity variation frequency . . . . .	44
3.14 Low-speed smoke visualization . . . . .	44
3.15 Optics table and risers . . . . .	47

3.16	.076m chord wing on support frame . . . . .	47
3.17	Balsa wood wing . . . . .	48
3.18	.076m chord wing natural frequency . . . . .	49
3.19	Raw $L'_{rms}$ PSD, $x = 1.19m$ , $\eta = -0.015$ . . . . .	54
3.20	Normalized experimental $L'_{rms}$ PSD, $x = 1.19m$ , $\eta = 0.02$ . . . . .	55
3.21	Normalized experimental $L'_{rms}$ PSD, $x = 1.19m$ , $\eta = -0.015$ . . . . .	56
3.22	Normalized experimental $L'_{rms}$ PSD, $x = 1.45m$ , $\eta = 0.02$ . . . . .	57
3.23	Normalized experimental $L'_{rms}$ PSD, $x = 1.70m$ , $\eta = 0.05$ . . . . .	58
3.24	Normalized experimental $L'_{rms}$ PSD, $x = 1.96m$ , $\eta = -0.09$ . . . . .	59
3.25	Normalized experimental $L'_{rms}$ PSD, $\eta = -0.015$ , $U_1 \approx 3m/s$ . . . . .	60
3.26	Normalized experimental $L'_{rms}$ PSD, $\eta = 0.02$ , $U_1 \approx 5m/s$ . . . . .	60
3.27	Normalized experimental $L'_{rms}$ PSD, $\eta = -0.015$ , $U_1 \approx 7m/s$ . . . . .	61
3.28	Normalized experimental $L'_{rms}$ PSD, $\eta = 0.02$ , $U_1 \approx 9m/s$ . . . . .	62
3.29	Normalized experimental $L'_{rms}$ PSD, $\eta = 0.05$ , $U_1 \approx 11m/s$ . . . . .	63
3.30	$L'_{rms}$ raw profiles . . . . .	64
3.31	Normalized experimental $L'_{rms}$ profile, $x = 1.19m$ . . . . .	65
3.32	Normalized experimental $L'_{rms}$ profile, $x = 1.70m$ . . . . .	65
3.33	Normalized experimental $L'_{rms}$ profile, $U_1 \approx 5m/s$ . . . . .	66
3.34	Normalized experimental $L'_{rms}$ profile, $U_1 \approx 7m/s$ . . . . .	66
3.35	Experimental lift peak location vs normalized $U_1$ , $U_1 \leq 7m/s$ . . . . .	67
4.1	Numerical flow field . . . . .	70
4.2	Finalized numerical flow field . . . . .	77
4.3	Shear-layer mean velocity profile test case . . . . .	89
4.4	Shear-layer $u'_{rms}/U_1$ profile test case . . . . .	90
4.5	Shear-layer $v'_{rms}/U_1$ profile test case . . . . .	90
4.6	Shear-layer $-u'v'_{rms}/(U_1^2)$ profile test case . . . . .	91
4.7	Wing flow-field streamlines . . . . .	94
4.8	Impulsive start test . . . . .	95
4.9	$L'_{rms}$ numerical effects, variable time step . . . . .	96
4.10	$L'_{rms}$ numerical effects, variable speed and time step . . . . .	96
4.11	Effect of increased averaging time on L' PSD . . . . .	97
4.12	Raw numerical $L'_{rms}$ PSD, $x = 1.19m$ , $\eta = 0.03$ . . . . .	99

4.13	Normalized numerical $L'_{rms}$ PSD, $x = 1.19m$ , $\eta = -0.03$ . . . . .	100
4.14	Normalized numerical $L'_{rms}$ PSD, $x = 1.45m$ , $\eta = 0.03$ . . . . .	101
4.15	Normalized numerical $L'_{rms}$ PSD, $x = 1.70m$ , $\eta = 0.07$ . . . . .	101
4.16	<i>Normalized numerical</i> $L'_{rms}$ PSD, $x = 1.96m$ , $\eta = 0.03$ . . . . .	102
4.17	Normalized numerical $L'_{rms}$ PSD, $\eta = 0.07$ , $U_1 = 7m/s$ . . . . .	103
4.18	Normalized numerical $L'_{rms}$ PSD, $\eta = 0.03$ , $U_1 = 9m/s$ . . . . .	103
4.19	Normalized numerical $L'_{rms}$ PSD, $\eta = -0.03$ , $U_1 = 5m/s$ . . . . .	104
4.20	Normalized numerical $L'_{rms}$ PSD, $\eta = -0.07$ , $U_1 = 9m/s$ . . . . .	104
4.21	Heavily averaged $L'_{rms}$ PSD, $U_1 = 5m/s$ , $x = 1.45m$ . . . . .	106
4.22	Raw numerical $L'_{rms}$ $\eta$ profiles . . . . .	107
4.23	Normalized numerical $L'_{rms}$ profile, $x = 1.19m$ . . . . .	108
4.24	Normalized numerical $L'_{rms}$ Profile, $x = 1.70m$ . . . . .	108
4.25	Normalized numerical $L'_{rms}$ profile, $U_1 = 3m/s$ . . . . .	109
4.26	Normalized numerical $L'_{rms}$ profile, $U_1 = 7m/s$ . . . . .	109
4.27	Fine $\eta$ resolution numerical $L'_{rms}$ profile . . . . .	110
4.28	Numerical peak frequency vs normalized $U_1$ . . . . .	111
4.29	Numerical extrapolations to variable chord . . . . .	112
4.30	$\alpha = 0^\circ$ vortex evolution . . . . .	114
4.31	$\alpha = 10^\circ$ vortex evolution . . . . .	115
5.1	Comparison of numerical and experimental normalized $L'$ PSD profiles	120
5.2	Comparison of numerical and experimental $L_{rms}$ profiles, for $x=1.96m$	121
A.1	Experimental Lift PSD $\eta = 0.05$ , $x=1.19m$ . . . . .	134
A.2	Experimental Lift PSD $\eta = -0.05$ , $x=1.19m$ . . . . .	135
A.3	Experimental Lift PSD $\eta = -0.09$ , $x=1.19m$ . . . . .	135
A.4	Experimental $L'_{rms}$ PSD, $x=1.45$ m, $\eta=0.05$ . . . . .	136
A.5	Experimental $L'_{rms}$ PSD, $x=1.70$ m, $\eta=0.02$ . . . . .	136
A.6	Experimental Lift PSD $\eta = -0.015$ , $x=1.45m$ . . . . .	137
A.7	Experimental Lift PSD $\eta = -0.05$ , $x=1.45m$ . . . . .	137
A.8	Experimental Lift PSD $\eta = -0.09$ , $x=1.45m$ . . . . .	138
A.9	Experimental Lift PSD $\eta = -0.015$ , $x=1.70m$ . . . . .	138
A.10	Experimental Lift PSD $\eta = -0.05$ , $x=1.70m$ . . . . .	139
A.11	Experimental Lift PSD $\eta = -0.09$ , $x=1.70m$ . . . . .	139

A.12	Experimental Lift PSD $\eta = 0.05$ , $x=1.96\text{m}$ . . . . .	140
A.13	Experimental $L'_{rms}$ PSD, $x=1.96$ m, $\eta=0.02$ . . . . .	140
A.14	Experimental Lift PSD $\eta = -0.015$ , $x=1.96\text{m}$ . . . . .	141
A.15	Experimental Lift PSD $\eta = -0.05$ , $x=1.96\text{m}$ . . . . .	141
A.16	Experimental Lift PSD $\eta = 0.05$ , $U1=3$ . . . . .	142
A.17	Experimental $L'_{rms}$ PSD, $\eta=0.02$ , $U1=3$ m/s . . . . .	143
A.18	Experimental Lift PSD $\eta = -0.05$ , $U1=3$ . . . . .	143
A.19	Experimental Lift PSD $\eta = 0.05$ , $U1=5$ . . . . .	144
A.20	Experimental $L'_{rms}$ PSD, $\eta=-0.015$ , $U1=5$ m/s . . . . .	144
A.21	Experimental Lift PSD $\eta = -0.05$ , $U1=5$ . . . . .	145
A.22	Experimental Lift PSD $\eta = 0.05$ , $U1=7$ . . . . .	145
A.23	Experimental Lift PSD $\eta = 0.02$ , $U1=7$ . . . . .	146
A.24	Experimental $L'_{rms}$ PSD, $\eta=-0.05$ , $U1=7$ m/s . . . . .	146
A.25	Experimental Lift PSD $\eta = 0.05$ , $U1=9$ . . . . .	147
A.26	Experimental Lift PSD $\eta = -0.015$ , $U1=9$ . . . . .	147
A.27	Experimental $L'_{rms}$ PSD, $\eta=-0.05$ , $U1=9$ m/s . . . . .	148
A.28	Experimental Lift PSD $\eta = 0.02$ , $U1=11$ . . . . .	148
A.29	Experimental $L'_{rms}$ PSD, $\eta=-0.015$ , $U1=11$ m/s . . . . .	149
A.30	Experimental Lift PSD $\eta = -0.05$ , $U1=11$ . . . . .	149
A.31	Experimental $L'_{rms}$ Profile, $U1=3$ m/s . . . . .	150
A.32	Experimental $L'_{rms}$ Profile, $U1=9$ m/s . . . . .	151
A.33	Experimental $L'_{rms}$ Profile, $U1=11$ m/s . . . . .	151
A.34	Experimental $L'_{rms}$ Profile, $x=1.45$ m . . . . .	152
A.35	Experimental $L'_{rms}$ Profile, $x=1.96$ m . . . . .	152
B.1	Numerical $L'_{rms}$ PSD, $x=1.19\text{m}$ , $\eta=0.07$ . . . . .	153
B.2	Numerical $L'_{rms}$ PSD, $x=1.19$ m, $\eta=0.03$ . . . . .	154
B.3	Numerical $L'_{rms}$ PSD, $x=1.19$ m, $\eta=-0.07$ . . . . .	154
B.4	Numerical $L'_{rms}$ PSD, $x=1.45$ m, $\eta=0.07$ . . . . .	155
B.5	Numerical $L'_{rms}$ PSD, $x=1.45\text{m}$ , $\eta=-0.03$ . . . . .	155
B.6	Numerical $L'_{rms}$ PSD, $x=1.45$ m, $\eta=-0.07$ . . . . .	156
B.7	Numerical $L'_{rms}$ PSD, $x=1.70\text{m}$ , $\eta=0.03$ . . . . .	156
B.8	Numerical $L'_{rms}$ PSD, $x=1.70$ m, $\eta=-0.03$ . . . . .	157

B.9	Numerical $L'_{rms}$ PSD, $x=1.70$ m, $\eta=-0.07$ . . . . .	157
B.10	Numerical $L'_{rms}$ PSD, $x=1.96$ m, $\eta=0.07$ . . . . .	158
B.11	Numerical $L'_{rms}$ PSD, $x=1.96$ m, $\eta=-0.03$ . . . . .	158
B.12	Numerical $L'_{rms}$ PSD, $x=1.96$ m, $\eta=-0.07$ . . . . .	159
B.13	Numerical $L'_{rms}$ PSD, $\eta=0.07$ , $U1=5$ m/s . . . . .	160
B.14	Numerical $L'_{rms}$ PSD, $\eta=0.07$ , $U1=3$ . . . . .	160
B.15	Numerical $L'_{rms}$ PSD, $\eta=0.07$ , $U1=9$ m/s . . . . .	161
B.16	Numerical $L'_{rms}$ PSD, $\eta=0.07$ , $U1=11$ m/s . . . . .	161
B.17	Numerical $L'_{rms}$ PSD, $\eta=0.03$ , $U1=3$ m/s . . . . .	162
B.18	Numerical $L'_{rms}$ PSD, $\eta=0.03$ , $U1=5$ m/s . . . . .	162
B.19	Numerical $L'_{rms}$ PSD, $\eta=0.03$ , $U1=7$ m/s . . . . .	163
B.20	Numerical $L'_{rms}$ PSD, $\eta=0.03$ , $U1=11$ m/s . . . . .	163
B.21	Numerical $L'_{rms}$ PSD, $\eta=-0.03$ , $U1=3$ m/s . . . . .	164
B.22	Numerical $L'_{rms}$ PSD, $\eta=-0.03$ , $U1=7$ m/s . . . . .	164
B.23	Numerical $L'_{rms}$ PSD, $\eta=-0.03$ , $U1=9$ m/s . . . . .	165
B.24	Numerical $L'_{rms}$ PSD, $\eta=-0.03$ , $U1=11$ m/s . . . . .	165
B.25	Numerical $L'_{rms}$ PSD, $\eta=-0.07$ , $U1=3$ m/s . . . . .	166
B.26	Numerical $L'_{rms}$ PSD, $\eta=-0.07$ , $U1=5$ m/s . . . . .	166
B.27	Numerical $L'_{rms}$ PSD, $\eta=-0.07$ , $U1=7$ m/s . . . . .	167
B.28	Numerical $L'_{rms}$ PSD, $\eta=-0.07$ , $U1=11$ m/s . . . . .	167
B.29	Numerical $L'_{rms}$ Profile, $U1=5$ m/s . . . . .	168
B.30	Numerical $L'_{rms}$ Profile, $U1=9$ m/s . . . . .	168
B.31	Numerical $L'_{rms}$ Profile, $U1=11$ m/s . . . . .	169
B.32	Numerical $L'_{rms}$ Profile, $x=1.45$ m . . . . .	169
B.33	Numerical $L'_{rms}$ Profile, $x=1.96$ m . . . . .	170
C.1	Pressure Transducer Calibration Plot . . . . .	172
D.1	Main data collection program front panel . . . . .	175
D.2	Main data collection program front panel: Additional plots for trouble shooting . . . . .	176
D.3	Full block diagram . . . . .	177
D.4	Block diagram closeup: Page 1 . . . . .	178
D.5	Block diagram closeup: Page 2 . . . . .	179

D.6 Labview block and formula descriptions: Page 1 . . . . .	180
D.7 Labview block and formula descriptions: Page 2 . . . . .	181

## LIST OF TABLES

Table Number	Page
2.1 Experimental Values of $C$ . . . . .	16
3.1 Layer Initial Momentum Thickness Estimates ( $\Theta_e$ ) . . . . .	38
3.2 Load Cell Specifications, MDB-5 . . . . .	51
4.1 Shear-layer test case statistical quantities (data taken from Inoue . . . . .	92
C.1 Pressure Transducer Calibration Data . . . . .	171
C.2 Hot Film Anemometer Calibration Data Set: Probe 1 . . . . .	173

## DEFINITION OF VARIABLES

$\alpha$  : angle of attack of the wing.

$\beta_1$  : the upstream extent of the vorticity sheet modeling the splitter plate.

$\beta_2$  : the downstream cutoff distance past which computer model vortices are deleted.

$\beta_3$  : the downstream extent of the vorticity sheets used to model the vorticity distribution downstream of  $\beta_1$ .

$\chi$  : distance along the splitter plate, downstream of the flow conditioning screens

$\delta$  : arbitrary thickness of the shear-layer.

$\delta_\omega$  : shear-layer vorticity thickness.

$\Delta P$  : pressure difference across the splitter plate.

$\Delta t$  : time step taken by the computer model in seconds.

$\Delta St$  : Strouhal half-power band-width.

$\Delta U$  : velocity difference between the high and low speed shear-layer streams.

$\Delta x$  : a transform variable used in calculating the velocity induced by a downstream vortex sheet,  $\Delta X = x_k - \beta_2$ .

$\Delta Y$  : a transform variable used in calculating the velocity induced by a downstream vortex sheet,  $\Delta Y = y_k - Y_l$ .

$\gamma$  : circulation per unit length of a vortex sheet.

$\gamma_l$  : circulation per unit length of downstream vortex sheet  $l$ .

$\gamma_u$  : vorticity per unit length of the vortex sheet modeling the shear-layer splitter plate.

$\Gamma$  : the net circulation of a wing.

$\Gamma_b$  : circulation strength of the bound wing vortex  $b$ .

$\Gamma_s$  : circulation strength of the shear-layer vortices within the model.

$\Gamma_v$  : circulation strength of the general vortex  $v$ .

$\Gamma_w$  : circulation strength of the wake vortex  $w$ .

$\vec{\Gamma}$  : the unknown vortex strengths from the wing boundary layer application. The vector is composed of the bound wing vortex circulations and the newly formed wake vortex circulation.

$\eta$  : dimensionless vertical position relative to shear-layer origin,  $y/x-x_0$ .

$\lambda$  : a shear-layer constant defined as  $\lambda \equiv (U_1 - U_2)/(U_1 + U_2)$ .

$\kappa$  : non-dimensional strength of individual vortex particles within a model.

$\Phi$  : the velocity potential function used in the development of the lift determination formula.

$\Phi_l$  : the inclination angle of downstream vortex sheet  $l$  to the  $x$  axis.

$\rho$  : density of air.

$\rho_1$  : density of the high speed shear-layer stream.

$\rho_2$  : density of the low speed shear-layer stream.

$\sigma$  : vortex core diameter used in the computer model.

$\tau$  : dimensionless time unit used for impulsive start testing.

$\theta_e$  : initial shear-layer momentum thickness.

$a$  : hot-film probe overheat ratio.

$A$  : planform wing area.

$A_{high}(\chi)$  : the cross-sectional area of the high-speed stream a distance  $\chi$  downstream of the beginning of the splitter plate.

$A_{high-test}$  : the cross-sectional area of the high-speed stream at the test-section entrance.

$A_{low}(\chi)$  : the cross-sectional area of the low-speed stream a distance  $\chi$  downstream of the beginning of the splitter plate.

$A_{low-test}$  : the cross-sectional area of the low-speed stream at the test-section entrance.

$A_{tunnel}$  : wind-tunnel subsection cross-sectional area.

$A_0$  : amplitude of an initial model perturbation.

$b$  : the index indicating a specific bound wing vortex.

$\vec{B}$  : the vector of values forming the known, time varying portion of the system of equations developed from application of the wing boundary conditions, of the form  $E \times \vec{\Gamma} = \vec{B}$

$c$  : wing chord length.

$C$  : constant associated with the spacing of large scale structures within the shear-layer.

$C_l$  : coefficient of lift.

$C_d$  : coefficient of drag.

$C_m$  : coefficient of moment.

$D$  : the total vorticity containing domain in the computer model.

$D_i$  : inner jet core diameter.

$D_1$  : computer model region upstream of the origin.

$D_2$  : computer model region downstream of the cutoff point,  $\beta_2$ .

$D_3$  : the computer model region enclosing the shear-layer vortices between the origin and  $\beta_2$ .

$D_4$  : the computer model region enclosing the wake, upstream of  $\beta_2$ .

$D_5$  : the computer model region enclosing the wing.

$E$  : the matrix of wing influence coefficients developed from application of the wing boundary conditions, of the form  $E \times \vec{\Gamma} = \vec{B}$

$f$  : wing lift forcing frequency.

$f_m$  : the most likely passage frequency for coherent structures in the shear-layer.

$f_n$  : the frequency of initial vortex rollup in a shear-layer.

$h$  : distance downstream of the origin that vortex particles are injected into the free flow field.

$H$  : one half of the tunnel bell mouth width.

$\vec{i}$  : vector direction corresponding with the  $x$  direction.

$\vec{j}$  : vector direction corresponding with the  $y$  direction.

$k$  : a non-dimensionalized vortex strength.

$K$  : constant associated with shear-layer growth.

$K_2$  : constant associated with  $f_m$  for the experimental setup.

$l$  : the index indicating a specific downstream vorticity sheet.

$L$  : lift of the wing.

$L'$  : the time varying component of the wings lift.

$N$  : total number of freely convecting vortices in the flow.

$N_b$  : number of discretized wing panels and bound vortices.

$N_D$  : number of doublet panels used to enforce the now flow boundary condition upstream of the shear layer origin.

$N_s$  : number of shear-layer vortices in the flow.

$N_w$  : number of wake vortices in the flow.

$\vec{n}$  : vector direction that is normal to the surface of the wing.

$O$  : row index of the matrix  $E$ .

$p$  : pressure at a general point.

$p_p$  : perturbation pressure at a general point.

$p_0$  : total, or reservoir pressure.

$q$  : dynamic pressure.

$q_{high}$  : dynamic pressure of the high-speed shear-layer stream

$q_{low}$  : dynamic pressure of the high-speed shear-layer stream

$\bar{q}$  : the average dynamic pressure of the shear-layer,  $\bar{q} = 0.5 \times \rho \times ((U_1 + U_2)/2)^2$ .

$r$  : the velocity ratio of the shear-layer,  $r = U_2/U_1$ .

$R$  : vortex radius.

$R_{ambient}$  : hot-film probe resistance at the ambient temperature.

$R_{hot}$  : hot-film probe resistance at the operational temperature of  $250^{\circ}C$ .

$R_{0^{\circ}C}$  : hot-film probe resistance at  $0^{\circ}C$ .

$Re$  : Reynolds number,  $Re \equiv L \times \nu / U$  where  $L$  is a length scale,  $U$  a velocity, and  $\nu$  the dynamic viscosity of the fluid in question. Dimensionless number describing the relative importance of viscosity and momentum.

$s$  : the index indicating a specific shear-layer vortex.

$s_{\rho}$  : density ratio,  $\rho_2 / \rho_1$ .

$S$  : vortex spacing.

$Sp$  : wing span.

$St$  : Strouhal number, a dimensionless frequency defined as  $St = f \times L / U$ , where  $f$  is a frequency,  $L$  some length scale and  $U$  a velocity.

$t$  : the amount of time the computer model has been running for in seconds.

$u$  : mean velocity at a fixed general position in the downstream direction.

$U$  : the average convection speed of large scale structures, equal to the mean of the limiting shear-layer velocities.

$U_{calib}$  : the velocity measured during hot film calibration.

$U_{\infty}$  : vortex convection velocity in BVI research.

$\vec{U}$  : the total velocity at a fixed general position  $\vec{U} = u' + u$ .

$\bar{U}$  : the average shear-layer velocity,  $U_1+U_2/2$ .

$U_1$  : the speed of the high speed stream in the shear-layer.

$U_2$  : the speed of the low speed stream in the shear-layer.

$U_i$  : inner flow velocity in a coaxial jet.

$U_o$  : outer flow velocity in a coaxial jet.

$u'$  : time varying velocity component in the downstream direction.

$v$  : mean velocity at a fixed general position in the cross-layer direction.

$v'$  : time varying velocity component in the transverse direction.

$v_l$  : vertical component of the velocity induced by downstream vortex sheet  $l$ .

$V_{out}$  : hot-film manometer output voltage.

$\vec{V}$  : the velocity induced by the general vortex  $v$ .

$\vec{V}_c$  : the velocity induced regions  $D_1, D_2, D_3$ , and the wake vortices  $w = 1 \rightarrow (N_w - 1)$  in region  $D_4$ . This is used as part of the boundary condition application on the wing control points.

$\vec{V}_k$  : the net velocity induced regions  $D_1 \rightarrow D_5$  at point  $k$ .

$\vec{V}_{kl}$  : velocity induced by downstream vortex sheet  $l$  on point  $k$ , defined as  $\vec{V}_{kl} = u_l \vec{i} + v_l \vec{j}$ .

$V_{k1}$  : the velocity induced my computer model region  $D_1$ .

$V_{k2}$  : the velocity induced my computer model region  $D_2$ .

$V_{k3}$  : the velocity induced my computer model region  $D_3$ .

$V_{k4}$  : the velocity induced my computer model region  $D_4$ .

$V_{k5}$  : the velocity induced my computer model region  $D_5$ .

$w$  : the index indicating a specific wake vortex.

$w'$  : time varying velocity component in the spanwise direction.

$W$  : columnar index of the matrix  $E$ .

$W_0$  : wavelength of an initial perturbation.

$x$  : the distance downstream of the shear-layer origin.

$x_0$  : the position of the virtual origin of the shear-layer relative to the physical origin.

$x_b$  : the downstream position of wing vortex  $b$ .

item[ $x_k$  :] the downstream distance from the origin of vortex  $k$ .

$x_l$  : horizontal component of the velocity induced by downstream vortex sheet  $l$ .

$x_{le}$  : downstream position of the wings leading edge.

$x_{N_w}$  : downstream position of the newly formed wake vortex  $N_w$ .

$x_{pi}$  : the length of a jets inner potential core.

$x_{po}$  : the length of a coaxial jets outer potential core.

$x_v$  : the downstream position of general vortex  $v$ .

$x_w$  : the downstream position of wake vortex  $w$ .

$\vec{x}_k$  : the vector position of point  $k$ .

$\vec{x}_v$  : the position of the general vortex  $v$ .

$y$  : vertical distance between the wing leading edge and the shear-layer origin.

$y_b$  : vertical height of wing vortex  $b$ .

$y_k$  : the vertical position of vortex  $k$ .

$y_l$  : vertical height of the leading edge of vortex sheet  $l$ .

$y_v$  : vertical height of general vortex  $v$ .

$y_w$  : vertical height of wake vortex  $w$ .

$Z_o$  : hot-film calibration curve zero-offset.

$Z_s$  : hot-film calibration curve slope.

## ACKNOWLEDGMENTS

The author wishes to offer his sincere thanks to Dr. David Russell for his guidance, Robert Gordon for his assistance and insight into experiment fabrication, to Dennis Peterson for his patience and knowledge in machining and fabrication, Wanda Fredrick for her assistance in keeping me fed, and of course to my wife Shelly for keeping me sane. Without you all this wouldn't have been possible.

## Chapter 1

# INTRODUCTION

In modern commercial airplane designs the engine nacelle is typically located below and forward of the wing, Figure 1.1. During the development of the Boeing 777 a problem with non-steady loading of the wing and flap system occurred, likely due to the complex flow surrounding the engines. This loading may lead to significant vibrations and increased fatigue rates. Previously the phenomenon has received little attention and no complete conceptual explanation is available.

The flow field behind the engine is complex: a high-speed heated exhaust jet, surrounded by cool but accelerated bypass air, further enveloped by the free stream. This flow is also modified by the wing and flap configuration. While portions of the flow are steady, the boundaries between the free stream, bypass stream, and exhaust stream will develop important turbulent features. The boundaries between these streams form a series of concentric, roughly axi-symmetric shear-layers. As the flow evolves the vorticity present in these shear-layers will coalesce into coherent structures with significant size and life spans. Due to this phenomena, even under steady flight, the flow within the axi-symmetric shear-layers is composed of neither steady flow nor isotropic turbulence, and will exhibit strong velocity variations associated with these coherent structures.

The first step to better understanding this interaction is to investigate a simplified model that captures the primary interactions between the shear-layers and wing-flap system. The first such simplification is to consider a two-dimensional case. Figure 1.2, shows a two-dimensional cross section of the wing, engine, and flow field, taken



Figure 1.1: Relative wing and nacelle position

through the center of the engine. This two-dimensional cross-section captures many key features: the wing and flap, the free, bypass, and exhaust streams, and the evolution of the interfaces between the streams.

As this flow field is still complex and does not lend itself to intuitive modeling and experimentation, further simplification is desirable. The current investigation will focus on a single two-dimensional incompressible shear-layer interacting with an inserted wing as shown in Figure 1.3. This case retains the critical components of the flow: the non-steady evolution of the shear-layer nearest to the wing between the free and bypass streams, and the behavior of the wing and its wake.

While the loss of the three-dimensional (3-D) structure of the physical system will affect the nature and evolution of the coherent structures, it will not affect their presence. Coherent regions of vorticity have been observed in jets with Reynolds numbers,  $Re$ , up to  $2 \times 10^8$ [1], and in shear-layers up to at least  $8.5 \times 10^5$ [2], well above the Reynolds numbers under consideration.  $Re$  is defined as  $Re \equiv L\nu/U$  where

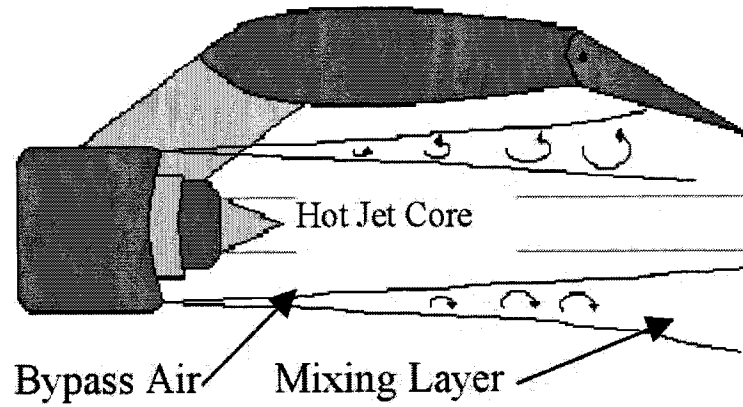


Figure 1.2: 2-D flow cross section

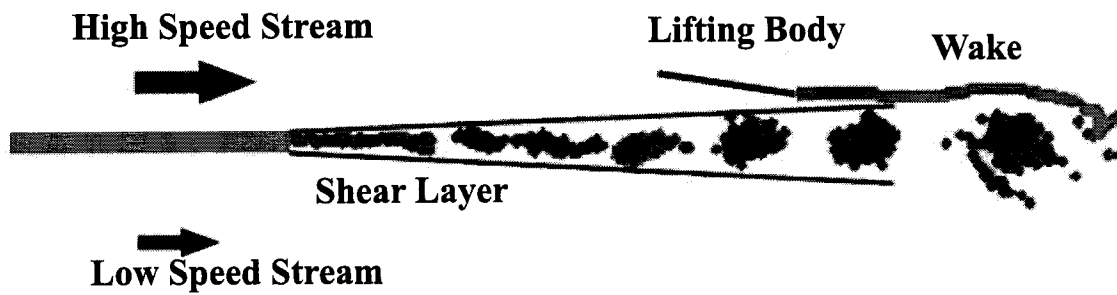


Figure 1.3: Flow configuration under investigation

$L$  is an appropriate length scale,  $\nu$  is the kinematic viscosity of the fluid, and  $U$  an appropriate velocity. These structures have been observed for large density ratios[3] and compressible flow as well[4].

The two-dimensional (2-D) shear-layer model proposed here is a logical beginning to understanding the jet-wing interaction, allowing investigation of the simplified exhaust-jet/wing interaction through experimentation and numerical modeling. Experimentation is used to identify any persistent non-steady lift variations of a wing exposed to the shear-layer, and to characterize the magnitude and frequencies at which they occur. A Vortex-Dynamics numerical model is developed and verified against experimental data. This allows a more controlled analysis of the flow and extrapolation to a larger variety of geometries than available experimentally.

The following work is broken down into five sections: background considerations and literature review, experimental investigation and results, numerical modeling and results, comparison of experimental and numerical data, recommendations for additional work, and conclusions.

## Chapter 2

# BACKGROUND CONSIDERATIONS AND LITERATURE REVIEW

A first step in investigating the effects of jet-exhaust on a wing is to consider available research which might be relevant. Three areas strongly relate to the un-simplified flow field: the behavior of coaxial jets, the evolution and dynamics of free and forced shear-layers, and the blade-vortex interaction, BVI, developed in rotorcraft research. Understanding the behavior of co-axial jets reinforces the decision to proceed with a 2-D simplification. Free and forced shear-layer research provides an understanding of the evolution of the shear-layer and the velocity and vorticity variations in the flow. Finally BVI research serves to provide a basis for understanding how the wing reacts to the coherent structures within the shear-layer, and how numerical modeling might be accomplished.

### **2.1 Coaxial Jet Behavior**

While the structure of the current physical problem is somewhat different than classical coaxial jet structure (Figure 2.1)[5], many of the qualitative results and behaviors are applicable. The primary difference is that in the classical case (Champagne and Wygnanski[6], Ko and Au[7], Tang and Ko[8] and others) the central jet is at a lower velocity than the surrounding flow, while for the current case the central jet is at a higher velocity.

In the classical case there is a competition between wake-like effects at the edges of the central flow, and jet-like effects at the edges of the outer flow. The flow-field is dominated by two, opposite-sign, vorticity sheets generated at the inner and outer

interfaces. For the problem at hand, the central flow is at a higher velocity than the surrounding flow, with the same vorticity sign in the inner and outer layers. However, both cases will be dominated by the interactions of vorticity containing structures present in the flow. Vortical structures have been observed and modeled, and their interactions found to control the evolution of free and forced jets and shear-layers over a broad range of  $Re$ , density ratios, and forcing conditions[1][5][9]. This change in vorticity sign should strongly affect the dynamics of the flow, and will likely lead to self-similar jet behavior earlier due to the absence of wake effects.

It has been demonstrated and verified that there is a high degree of interaction between the vortex structures of the inner and outer shear-layers[5][10], and that the inner and outer jets cannot be assumed to be developing independently. In general the flow field for a coaxial jet can be broken down into three regions: the initial merging zone, where potential cores exist for both the inner and outer jets and develop nearly independently, the intermediate merging zone where the vorticity sheets begin converging, and the fully merged zone where the flow becomes progressively more like a self-similar jet whose characteristics are determined only by the net momentum excess and local conditions Figure 2.2[10][11]. Overall the characteristics of these regions are controlled by the “sign, strength, mutual position and consequent dynamics of the vortical structures that are present in the shear-layers developing between the two jets and between the outer jet and the ambient fluid.”[12].

Each zone is of a different downstream extent, which is connected to the velocity ratio between the streams, and to the diameter of the streams. For an area ratio between the streams of  $A_i/A_o = 2.79$ , where  $A_i$  is the inner cross sectional area, and  $A_o$  the outer area, Au and Ko found, and Buresti et al. verified, a relationship of  $x_{pi}/D_i \approx 9.9U_i/U_o$  for the length of the inner potential core[10], for the range  $0.15 \leq U_i/U_o \leq 0.8$ , where  $x_{pi}$  is the length of the inner potential core,  $D_i$  the inner diameter,  $U_i$  the inner velocity, and  $U_o$  the outer velocity. During the same experiment it was determined that for these conditions the outer potential core extends a distance

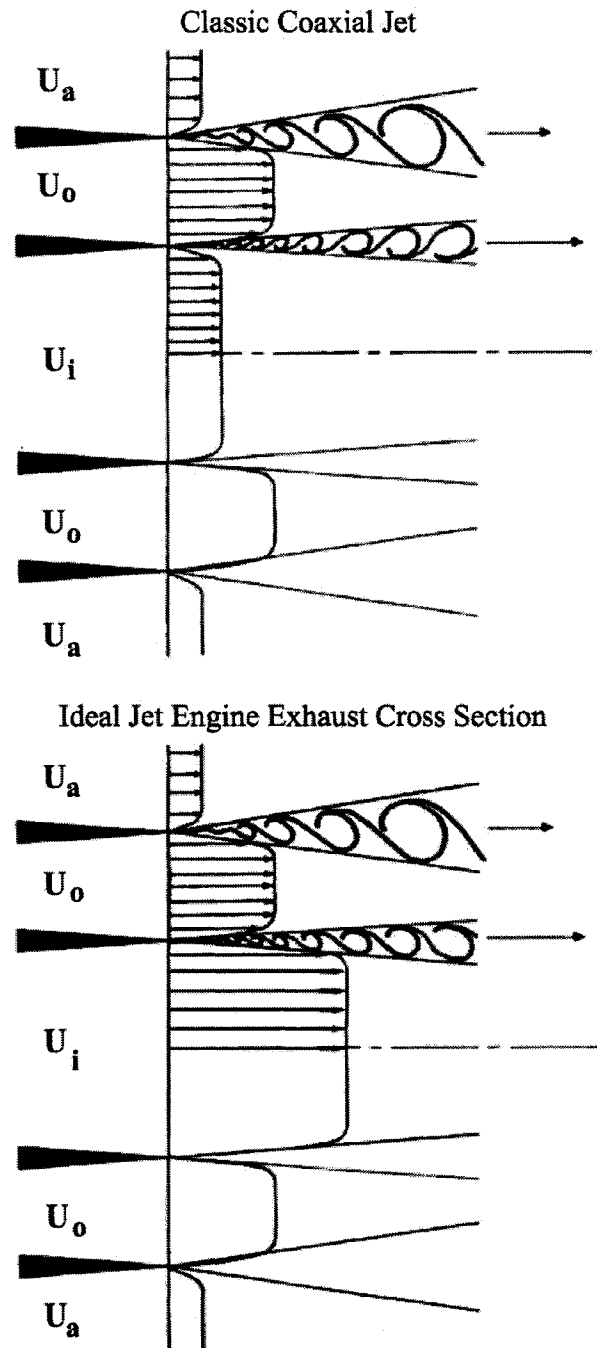


Figure 2.1: Coaxial jet velocity profiles, canonical, and jet-exhaust cross section, developed from Dahm, Friedler, and Tryggvason[5]

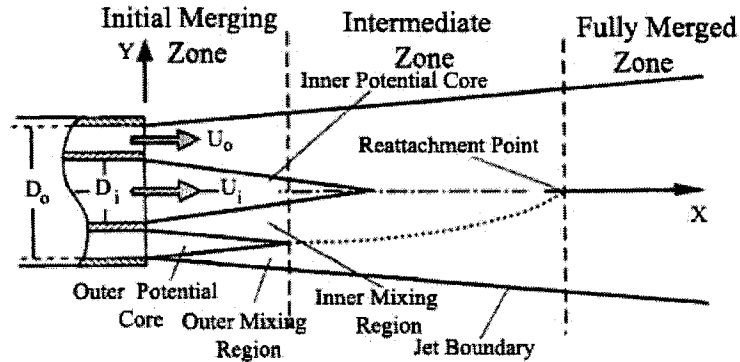


Figure 2.2: Coaxial jet mixing regions[10]

of  $x_{po}/D_i \approx 3.4$ , roughly half the length of the inner potential core. Based on these findings it is reasonable to assume that for most cases the inner and outer potential cores will persist downstream for at least one if not more inner diameters.

In modern hi-bypass engines area ratios are in the vicinity of 2, while velocity ratios are commonly 0.2 or lower. In the case of a jet engine where the flow is compressible and exhibiting large density ratios these potential cores will likely persist for longer downstream distances, as compressibility effects inhibit shear-layer growth[4]. While density ratios greater than one,  $s_\rho \equiv \rho_2/\rho_1 > 1$ , where  $\rho_1$  is the density of the high-speed stream and  $\rho_2$  the density of the low-speed stream, have been shown to slightly increase the spreading rate of shear-layers, the decrease in growth rate due to increasing Mach number is a much stronger effect[4]. In the case of supersonic flow this thinning of the mixing layer between streams is greatly amplified, with reports of up to a factor of 5 decrease in growth rates over an incompressible flow with the same values of  $r$  and  $s_\rho$ [4], where  $r$  is the velocity ratio  $r \equiv U_2/U_1$ . In all cases the subscript “1” corresponds to the high-speed stream, and the subscript “2” corresponds to the low-speed stream. Within the region where the inner and outer potential cores remain, there is little interaction between the vortex structures within

the various mixing layers. Once the intermediate region is reached the flow becomes more complex as the concentric layers interact more fully and the evolution of the layer is closely tied to the relative strengths of the vortex sheets. The fully mixed region is not currently of interest as it will likely occur well downstream of the wing.

Vortical structures of either a shear-layer-like or modified single-jet-like character should be present in the physical flow under consideration. While many features of shear-layers and jets differ, the presence of vortex rings in axi-symmetric jets is well established[9]. For hi-bypass ratio engines the leading edge of the wing flaps are often located at a distance of  $4D_i$  downstream of the engine exit, or 2.5 to 3 times  $D_o$ , which is in the region where the inner and outer potential cores will likely be present. The investigation of the effect of a 2-D shear-layer on a wing, should provide a good starting point to investigate this complex flow, as both shear-layers and jets are dominated by vortical structures whose vorticity is perpendicular to the mean flow and since the wings and flaps are located in the region where the jet exhausts potential cores should still be present minimizing the interaction between the vorticity sheets.

## **2.2 Shear-Layer Fundamentals**

When a sharp 2-D velocity discontinuity between two parallel streams evolves freely, it forms a mixing or shear-layer. This flow has been the subject of ongoing research because of its importance in a wide variety of flows, from axi-symmetric jets to flame sheets. In addition it can be set up and controlled in a laboratory, making it useful for investigating vortex dynamics and validating computational models.

As the flow evolves the velocity discontinuity is smoothed out in a layer that widens with downstream distance. The dynamics are controlled by the vorticity sheet formed by the velocity gradient between the streams. The primary growth mechanism derives from the inherent instability of a single sign vortex sheet or of a train of like-sign vortices. The mean velocity gradient generating vorticity within the layer is 2-D. Once

a sufficiently high  $Re$  has been reached, as in the experimental case, the layer becomes fully turbulent, and through stretching and localized turbulence a portion of the vorticity within the layer aligns itself with the streamwise and cross-layer directions, which 2-D models can't capture. The effect of this vorticity redistribution is quite apparent when the experimental maximum rms values of  $u'_{rms}/U_1$ ,  $v'_{rms}/U_1$ , and  $w'_{rms}/U_1$  are considered. The maximum values of  $u'_{rms}/U_1$ ,  $v'_{rms}/U_1$ , and  $w'_{rms}/U_1$  typically vary from each other by less than a factor of 2.

Layer self-similarity comes from the small number of fundamental parameters associated with the layer. The canonical 2-D shear-layer has only three independent properties: the velocity of the high-speed stream  $U_1$ , the velocity ratio  $r$ , and the distance downstream of the shear-layer origin  $x$ . Once the shear-layer has evolved far enough to forget it's initial conditions, and attains self-similarity, the mean statistical properties,  $u'_{rms}/U_1$ ,  $v'_{rms}/U_1$  etc., are distributed according to these fundamental variables. Here  $u'$  is the varying component of the downstream velocity and  $v'$  the varying component of the cross-layer velocity, while  $\vec{U}$  at a fixed point is decomposed as  $\vec{U} = (u' + u)\vec{i} + (v' + v)\vec{j}$ . In general this takes between 500 and 1000 initial momentum thicknesses,  $\Theta_e$ , to attain[13].

### 2.2.1 Coherent Structure Characteristics

Beginning with the work of Brown and Roshko[3], it became clear that shear-layers and other shear flows contain not only fine-scale turbulence, as had been historically accepted, but also large-scale coherent vortical structures that evolve and grow in a deterministic and inviscid manner, as they convect downstream. Figure 2.3[3] shows the presence of these structures in a shear-layer formed between helium and nitrogen. Flows of this nature can be treated through methods focused on capturing the behavior of these structures without resorting to statistical treatment.

Shear-layers take on three distinct regions downstream of their origin: an initial laminar region where the layer grows exponentially, ending in roll-up of the first

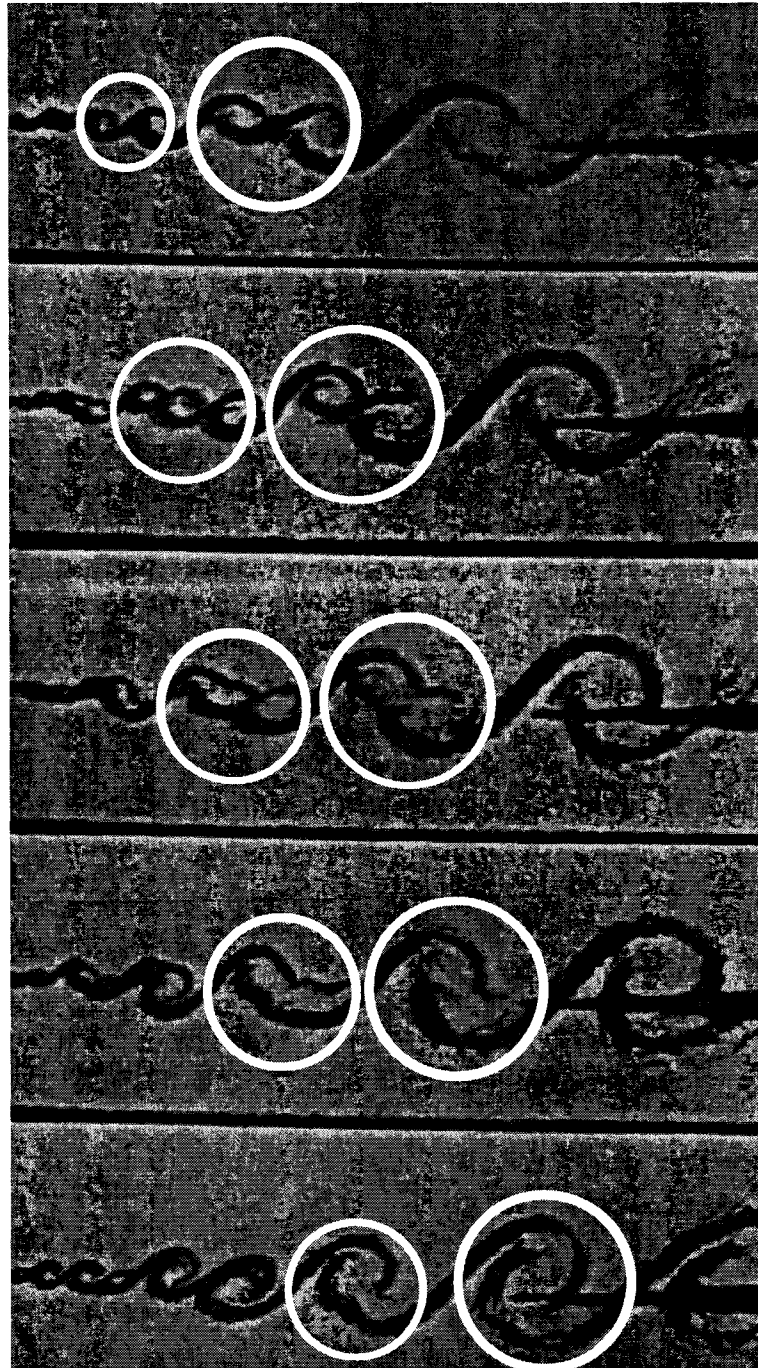


Figure 2.3: Flow visualization of a pairing event[3]. A sequential series of movie frames showing shear-layer evolution with time.

coherent structure, a period of delayed growth between roll-up of the first distinct vortical structure and the first instance of pairing, and a self-similar region extending far downstream where growth occurs primarily through vortex pairing. The distance necessary to attain full self-similarity is dependent upon the initial conditions of the layer, usually quantified by  $\Theta_e$ . The frequency of the first structure that appears with initial roll-up can be estimated from linear stability theory for a hyperbolic tangent mean velocity profile, which closely approximates the profile produced by shear-layers. For this profile the dimensionless frequency of initial roll-up is the Strouhal Number,  $St_{roll-up} = f_n \Theta_e / \bar{U} \approx 0.032$ , where  $\bar{U} = (U_1 + U_2)/2$  and  $f_n$  is the initial roll-up frequency.

Based on flow visualization, it is clear that coherent structure pairing, where two neighboring vortices counter-rotate and merge into a single larger and stronger vortex with vorticity equal to the sum of the vorticity of the component vortices, is the dominant layer growth mechanism in the self-similar region. An example of pairing can be seen by tracking the progress of the two sets of highlighted vortices in Figure 2.3[3]. Additional research has pointed toward a second important growth mechanism[14][2][15], the entrainment of irrotational fluid which leads to growth of the structures between pairing events. Tripling, where three vortices counter rotate and merge; and tearing, where a coherent structure is pulled apart and absorbed by its neighboring vortices, have also been observed playing a minor role.

Since pairing is a discrete process the instantaneous statistical properties of the layer,  $u'_{rms}/U_1$ ,  $v'_{rms}/U_1$ ,  $-u'v'_{rms}/U_1^2$  etc., are not self-similar but controlled by the local position and size of these structures. The size, spacing, and net vorticity of these structures form a distribution about a self-similar mean value due to the pseudo-random nature of pairing. This process leads to self-similar values for the time-averaged shear-layer properties. It is this self-similar region, where the behavior of the vortices is predictable, that is of interest for the current work.

It has also been shown that for free shear-layers the size and dynamics of these

structures are  $Re$  number invariant. Figure 2.4[3], shows no discernible modification of the largest structures for a factor of 4 change in  $Re$ , though there is a significant increase in the amount of fine-scale turbulence. According to Komolgorov's energy spectrum work, the separation between the largest and smallest turbulent length scales varies as  $Re$ . Since the turbulent region is fixed by the growth rate of the layer, the size of the largest scales is also fixed, and approximately equal to the visual width of the layer. Increasing the  $Re$  serves to increase the separation between the largest and smallest scales by imposing progressively finer scale turbulence on top of largest coherent structures.

Secondary vortices in the stream-wise direction were identified by Breidenthal[16]. These structures do not significantly affect the evolution of the primary 2-D vortices. The initiation and formation of these streamwise structures are  $Re$  dependant and, once formed, the stream wise structures maintain their character and spacing through several pairings of the primary-vortices[17]. As such they do not behave in a self-similar manner. Bernal and Roshko determined that shear-layers containing a wake component may be more susceptible to these 3-D disturbances[17]. While these structures are worth noting, their influence on the development of the quasi-2-D primary structures is small. The stream-wise vortices should lead to spanwise variations in wing loading. However this effect should be averaged out over the span of the wing. The net lift variations should then be primarily due to the quasi-2-D spanwise structures.

For the current research the most critical layer properties for determining the effects of the shear-layer on the wing are the spacing of the largest coherent structures and their net vorticity, which is directly dependant on  $U_1$ . Since these structures contain most of the turbulent kinetic energy in the flow, cause the largest velocity fluctuations in the flow, and control the dynamics of the layer, they should determine the magnitude of the lift variations and the frequency at which these variations occur.

The net circulation of the largest structures depends directly on their size and the

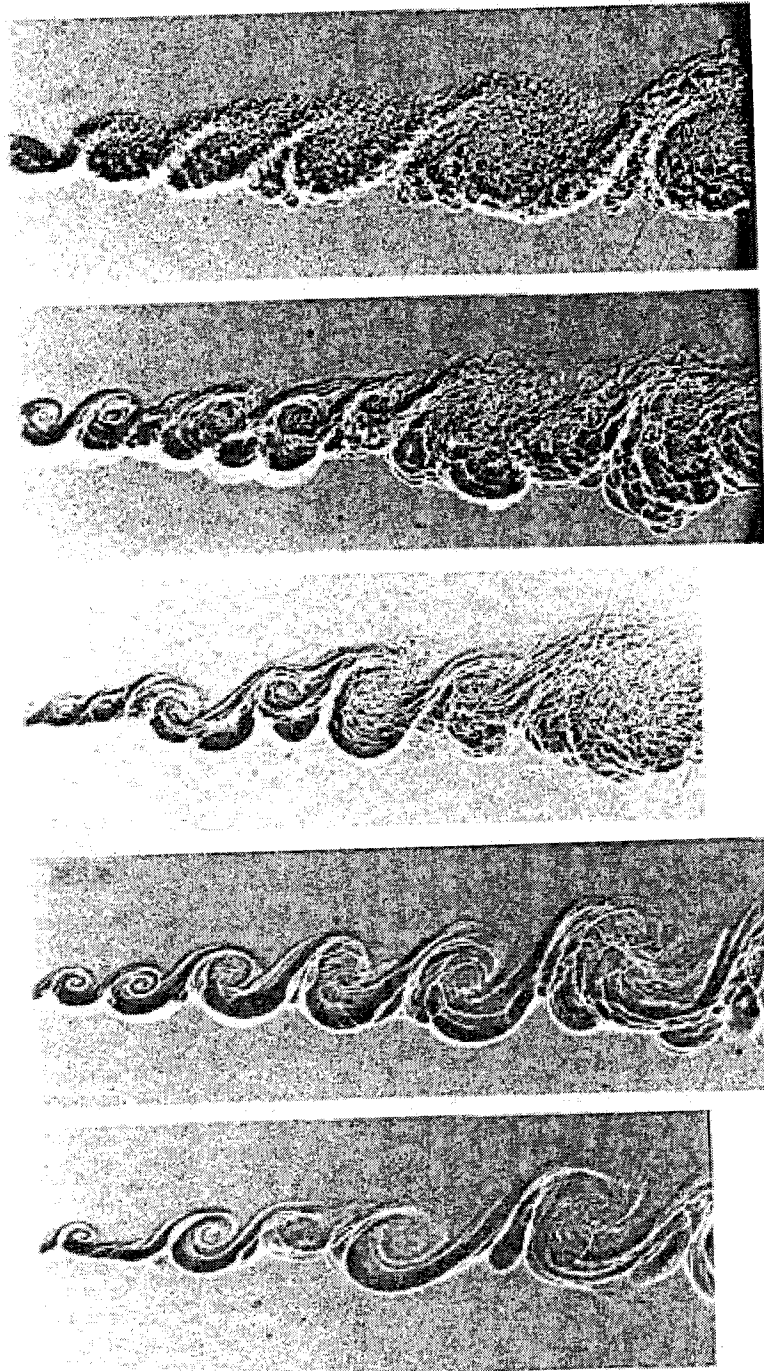


Figure 2.4: Re number effects on a shear-layer formed between helium and nitrogen.  $\rho_2 U_2^2 = \rho_1 U_1^2$ , Re number varies from  $(1.2 \rightarrow 0.3) \times 10^5$ [3] from the top to the bottom.

velocity difference across the layer, which depend on  $U_1$ ,  $r$  and  $x$ . The spacing of the dominant coherent structures is self-similar and must be related to the local layer width by a constant. Further, the width of the layer at a given downstream position is equal to a constant dependant on  $r$  multiplied by the distance downstream of the layer's virtual origin. A virtual origin is utilized to help account for the un-self-similar growth rates upstream of the self-similar region. Definitions of the layer width are arbitrary but this research will utilize the vorticity thickness,  $\delta_\omega$ , defined as

$$\delta_\omega \equiv \frac{\Delta U}{\left(\frac{\partial U}{\partial y}\right)_{max}} = K \frac{(x - x_0)}{\lambda}. \quad (2.1)$$

where  $K$  is an experimentally determined constant,  $x - x_0$  is the distance between the point of interest and the virtual origin, and  $\left(\frac{\partial U}{\partial y}\right)_{max}$  is the maximum slope of the cross stream velocity profile, while  $1/\lambda \equiv \frac{U_1 + U_2}{U_1 - U_2}$ . The constant  $\lambda$  results from the layer growth rate which depends on the velocity difference between the layers  $U_1 - U_2$ , and the average convection speed  $(U_1 + U_2)/2$ . This model assumes linear growth from an infinitely thin vorticity sheet at  $x_0$  where  $\delta_\omega = 0$ , known as the Abramovich-Sabin relation.

Since the mean layer properties are self-similar, they only vary from each other by a scaling constant. As such the average spacing of the coherent structures can be expressed as the layer thickness multiplied by an experimentally determined constant  $C$ [3]. When  $\lambda$  is expressed in terms of  $r$ ,  $1/\lambda = (1+r)/(1-r)$ , and the average vortex spacing can be expressed as

$$S = C\delta_\omega = CK(x - x_0)/\lambda = \frac{CK(x - x_0)(1 - r)}{(1 + r)}. \quad (2.2)$$

Dividing the  $S$  by the mean vortex convection rate,  $\bar{U}$ , results in the average structure passage frequency,  $f_m$ ,

$$f_m = S/\bar{U} = \frac{U_1(1+r)^2}{2CK(x - x_0)(1 - r)} = \frac{U_1(1+r)^2}{2K_2(x - x_0)(1 - r)}, \quad (2.3)$$

Table 2.1: Experimental Values of  $C$ [3]

Reference	Data Conditions	C
Brown and Roshko	$s_\rho = 7$	2.9
	$s_\rho = 1$	3.5
Winant and Browand	$s_\rho = 1$	3.3
Spencer and Jones	experimental $\delta_\omega$	3.3
	theoretical $\delta_\omega$ calculated by Brown and Roshko	2.8
Jones et. al	experimental $\delta_\omega$	5.1
	theoretical $\delta_\omega$ calculated by Brown and Roshko	3.8

where  $K_2 \equiv KC$ . Brown and Roshko[3] report a range of values for  $C$  that they calculated based on reported data from several researchers, Table 2.1.

After considering the work of various researchers, Brown and Roshko settled on a value of  $C = 3$  and  $K = 0.18$ . Based on reported values for  $C$  and  $K$  through a variety of density ratios,  $K_2$  ranges from  $K_{2max} = 0.69$  to  $K_{2min} = 0.45$ , with the most likely value being  $K_2 = 0.54$ . Several other values of  $K_2$  can be determined from additional researchers[18][19], all of which fall within the expected range. Based on this constant, an approximate Strouhal number associated with coherent structure passage normalized by the mean convection velocity, and downstream distance is  $St = f_m(x - x_0)/U_1 = 3.3$ .

### 2.2.2 Non-steady Shear-Layer Properties

The discussion thus far has focused on the self-similar behavior of the layer and its mean statistical properties. With respect to the problem at hand, the magnitudes and dominant wing-forcing frequencies are important, but the nature of the forcing

will also play into the wing response to the layer. Broad-band forcing at a low magnitude and narrow-band forcing at a higher magnitude may result in equivalent statistical properties but different consequences for the wing. Experiments with free shear-layers have shown that velocity variations occur over a spectrum of frequencies in a broad, smooth peak. With increasing downstream distance the energy contained in these frequencies is concentrated into progressively longer wavelengths and lower frequencies. This can be seen in Figure 2.5, taken from Hussain and Zaman[20]. The ordinate on the  $u'$  frequency spectrum is an arbitrary magnitude linear scale chosen to highlight the peak frequency, while the abscissa is a linear frequency scale. The location of the peak frequency has been shown for clarity. The curves were collected at  $u/U_1 = 0.99$ , corresponding to the upper edge of the layer. While the magnitudes of the plots were chosen to highlight the frequency peaks, the behavior of the location and width of the spectral humps is quite clear. With increasing downstream distance the fluctuations in  $u'$  become concentrated into a narrower and lower frequency band. Once a downstream distance of roughly  $300\Theta_e$  has been surpassed, the variation in peak frequency with downstream distance becomes self-similar.

Based on the PSD curves provided at various transverse locations from Hussain and Zaman[20] it is clear that the footprint of the coherent structures is most clearly visible in the velocity variations at the edge of the mixing layer on the high-speed side. In the core of the layer the presence of the coherent structures is obscured by the high frequencies associated with the shorter wavelength turbulence found in the core, Figures 2.3 and 2.4. While the hump in the spectral peak is again visible on the low-speed side of the layer, it is not as distinct.

### *2.2.3 Forced Shear-Layers*

Forced shear-layers are a subset of shear-layers where the flow is perturbed at a fixed frequency upstream of the origin. The perturbations may be axial or transverse and are achieved through a variety of means from acoustic forcing[21][22] to restrictions

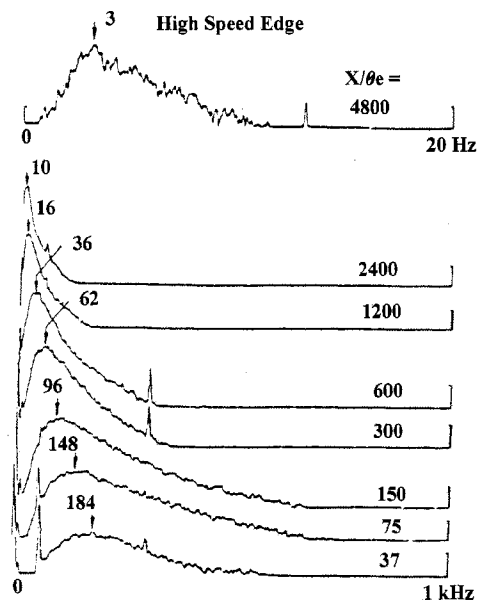


Figure 2.5: Free shear-layer frequency spectra characteristics at  $u/U_1 = 0.99$  [20]

of the incoming flow[23][24]. Large scale effects on the layer are independent of the forcing mechanism. Forcing shifts the development of the layer from three distinct phases to four: roll-up, accelerated growth, impaired growth, and natural growth where the layer becomes self-similar. The initial roll-up frequency, occurs at the closest harmonic of the forcing frequency to the natural roll-up frequency of an equivalent unforced layer. The transition to forced behavior is independent of forcing amplitude above a forcing value of 1% of  $U_1$ , or slightly higher if high amplitude white background noise is present[25].

During the period of accelerated growth, either through a sequence of single or multiple pairings, a vortex of passage frequency equal to the forcing frequency is formed more rapidly than in a free layer. The mechanism for the formation of this resonant eddy, which is in tune with the forcing frequency, is dependant upon the magnitude of the forcing. Following the formation of the resonant eddies, pairing and layer growth is suppressed. During this phase the layer displays a stable periodic train

of like-sign vortices with equal spacing. Layer growth during this period is extremely slow, and due only to entrainment of irrotational fluid and diffusion. The length of this period is dependant upon the forcing amplitude. Following this stage the centers of resonant eddies become displaced from the stable configuration and normal pairing and growth resumes.

The effects of forcing can be clearly observed in most measurable characteristics of the layer during the accelerated and suppressed growth stages. In general it is found that forcing only has an effect on coherent structures with a passage frequency equal to or higher than the forcing frequency. When eddies of a lower passage frequency are formed, by either natural pairing, or when the forcing frequency is above the initial roll-up frequency, the layer acts as if unforced.

Spectra of  $u'$  exhibit a marked difference from the character of a free shear-layer. Instead of smooth peaks displaying self-similar peak locations, the forced shear-layer displays a broad lower magnitude peak punctuated by sharp peaks at the forcing frequency and its harmonics. Figures 2.6 and 2.7, from Oster and Wygnanski[26] display the behavior of  $u'$  with variable downstream distance, at the upper and lower layer edges respectively. The data in Figure 2.6 is taken at the upper edge of a layer forced at  $30Hz$ . While the  $30Hz$  peak is the dominant feature, an additional peak at  $60Hz$  is also apparent. In addition the plots suggest a sub-harmonic at  $15Hz$ . All three peaks are insensitive to downstream distance within the layer, so long as the velocity fluctuation frequencies are above the individual peak. At  $x = 1200mm$  the probe is far enough downstream that there are no longer significant velocity fluctuations at  $60Hz$  and the effect of the forcing at that frequency falls off, though the  $15$  and  $30Hz$  peaks remain. The primary result of the forcing is that the fluctuations at the forcing frequency are generally insensitive to downstream distance, and velocity variations. Figure 2.7 displays similar characteristics, though the data was collected at the low velocity edge of the layer, with a forcing frequency of  $50Hz$ . Here the two distinct sharp peaks are at  $50Hz$  with a  $100Hz$  harmonic.

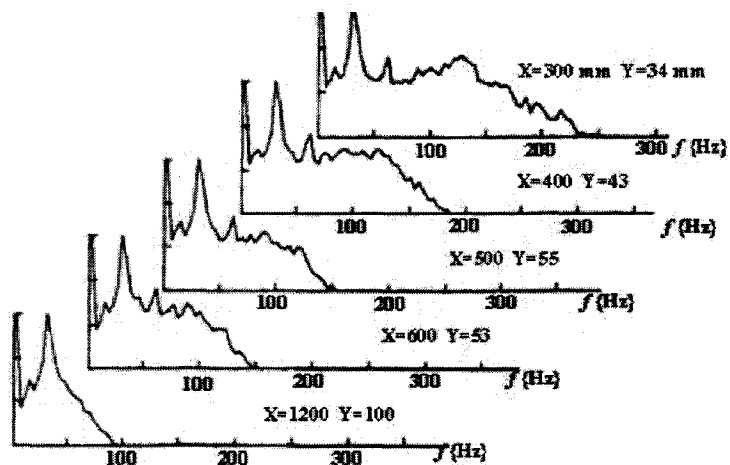


Figure 2.6:  $u'$  frequency spectra for a  $30\text{Hz}$  force layer. Data taken at the layers upper boundary[26]

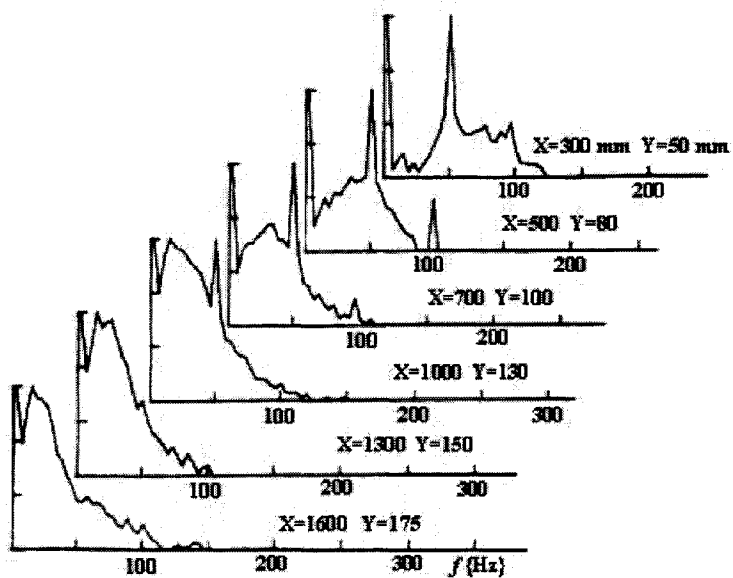


Figure 2.7:  $u'$  frequency spectra for a  $50\text{Hz}$  forced layer. Data taken at layers lower boundary[26]

While the distribution of turbulent kinetic energy changes significantly due to forcing, it is generally true that “the total turbulent intensity integrated across the shear-layer does not change appreciably under the influence of forcing: it is simply redistributed...”[26][27]. In the canonical case of 2-D forcing in the transverse or flow directions, this results in amplified 2-D organization leading to larger values of  $u'_{rms}$  and  $v'_{rms}$ , and a lower value of  $w'_{rms}$ .

### **2.3 Numerical Blade Vortex Interactions**

The current research goes beyond the basic shear-layers just discussed to consider the interaction with a wing which is somewhat related to the BVI phenomena that occurs in helicopters. As the helicopter blades rotate they shed a continuous tip-vortex in a spiral pattern which can intersect the blades in a nearly parallel fashion[28][29], Region 1, see Figure 2.8 developed from Tangler[28]. In most cases the blades and tip-vortices are nearly perpendicular to each other, Region 2, and their interaction does not lead to strong vibration. However the parallel reaction in Region 1 results in a series of like-sign vortices convecting past the blade and strong lift fluctuations. From a blade-fixed perspective it appears as a stable chain of vortices convecting past. Unlike the coherent structures within a shear-layer these vortices occur at roughly fixed intervals and there is little interaction between them.

This train of vortices causes significant pressure variations along the rotor surface leading to oscillations in rotor lift, high levels of noise, and rotor vibration. Qualitatively the situation is similar to coherent shear-layer structures causing lift oscillations on a wing, and several aspects of BVI research are applicable to the shear-layer/wing problem. In both cases loading will occur at a forcing frequency that goes as the vortex convection velocity. Further, numerical methods used to treat the BVI problem provide insight into difficulties likely to be experienced while developing a numerical shear-layer/wing model. Numerical modeling of the BVI has been extensively investigated by Poling, Dadone, and Telionis[29], Panaras[30], Qian and Veza[31]

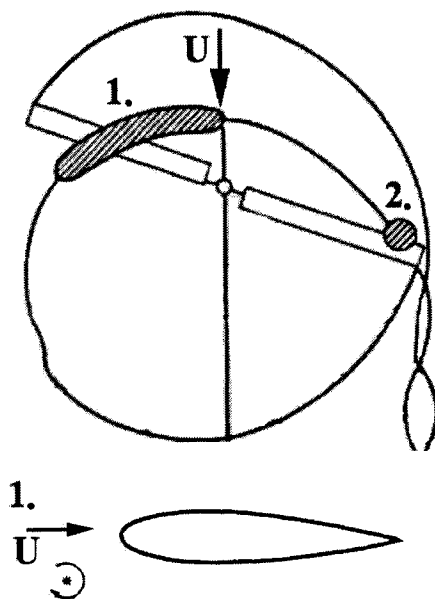


Figure 2.8: Tip vortex trails and rotor blade position interaction[28]

and others. The numerical schemes used by Panaras, Qian and Vezza, and Poling, Dadone, and Telionis present somewhat unique techniques that shows promise for the current research.

Poling, Dadone, and Telionis used a point vortex representation of the impinging vortices in their work. It was assumed that the vortices were well-formed and convect toward the airfoil from far upstream. An inviscid incompressible model for the interaction of a 2-D airfoil with discrete evenly-spaced impinging vortices was developed. A non-steady Kutta condition was applied, and vorticity continually shed from the trailing edge of the airfoil to satisfy Kelvin's Circulation Theorem, which states that the net vorticity within the flow must be conserved. In order to investigate lift histories, the pressure distribution was directly integrated to determine the non-steady lift. The traditional lift formula of  $L = \rho U_\infty \Gamma$  does not apply to unsteady attached or separated flow. In this relation  $L$  is wing lift,  $U_\infty$  the free stream velocity,  $\rho$  the density of air, and  $\Gamma$  the wings net circulation. They determined that if the impinging

vortex passes a distance of one chord length or greater above or below the airfoil then the point vortex model is sufficient. However, if the vortex passes closer than one chord a more accurate scheme is needed.

When compared to experimental results their model accurately predicted the timing of lift peaks, however it failed to accurately predict their magnitude. They felt that this could be due to two phenomena that were not sufficiently modeled by point vortices: the effect of the vortex being cut by the blade leading to two reduced strength vortices traversing the upper and lower surfaces of the wing, and the possibility that the vortex induces local separation bubbles which drift downstream along the wing surface. When the effect of a single vortex passage was compared to experimental results, it was found that the numerical model over-predicted the maximum positive value of the coefficient of lift  $C_l \equiv L/qA$  by up to factor of 2, but performed somewhat better on the peak negative  $C_l$  value. Further, they found that utilizing discrete vortices provides accurate timing of the interaction, and with a vortex-path/airfoil separation distance of 0.05 chords or larger, predicts lift variation magnitudes with a reasonable degree of accuracy.

Panaras[30] took into account the finite size of real vortices instead of representing them solely as point vortices. Three cases were investigated: a system of point vortices, a distributed layer of vorticity which was allowed to roll-up into discrete structures, and a series of circular amalgamations of discrete vortices. The system of point vortices was used as a control case. The majority of the investigation assumed a non-dimensional vortex strength of  $\kappa = \Gamma_v/(\alpha U_\infty) = 0.3$ , where  $\alpha$  is defined as the wings angle of attack, and  $\Gamma_v$  the circulation of the impinging vortex. Separation distances between the vortical structure and the airfoil of  $0.3c$ ,  $0.06c$ , and  $0c$  were utilized.

Multiple methods were used to generate the initial distribution of vorticity, the simplest being a discrete series of vortices evenly spaced along a sine wave. Their position history is calculated by applying the Biot-Savart law and integrating forward

in time. The sine wave is slowly deformed from a well-ordered distribution into a series of distinct vortices. Panaras found that better results were obtained if a finite thickness was given to the sine wave distribution by utilizing multiple rows of point vortices spread along the sine wave. The final method was intended to study the interaction of an airfoil with well-formed circular vortices, represented by clouds of point vortices. The vortices were assumed to have been formed far upstream and to have attained a steady state distribution before reaching the airfoil.

These methods were used to calculate wing pressure profiles for the passage of several vortical structures, and to determine the induced lift variations. Panaras utilized only the steady Kutta condition which does not satisfy Kelvin's Circulation Theorem. This leads to changes in circulation about the wing not being offset by vorticity continually shed from the airfoil trailing edge. However, Panaras[30] felt, "that the small value of the strength of the vortices used in the present work and the fact that their vorticity is distributed rather than concentrated results in non-significant (wake) vorticity shedding."

It was found that for large separations between the airfoil and vortical structure path there was no effective difference between the cases. Furthermore the finite size of the vortex core does not play a significant role, which is in agreement with the work of Poling, Dadone, and Telionis. However, for close spacing the finite area structure becomes important. The initial vortical structure deforms considerably and the amplitude of the pressure pulses is lower than for a single point vortex. When the vortical structure is allowed to impinge on the leading edge of the airfoil, it is severely deformed or cut into two vortices. For this case the finite area vortex system generates a pressure coefficient amplitude that is one-third the strength of the point vortex model, though the timing of pressure and lift fluctuations is unaffected by the separation distance between the vortex path and airfoil.

Qian and Veza[31] performed a similar investigation to Panaras simulating a parallel blade-vortex interaction with a distributed vortex method. However, where

Panaras considered the passage of multiple vortices, Qian and Vezza focused on more accurately modeling the effect of a single impinging vortex. The primary advance was to model the vorticity distribution and vorticity shedding process present in the wing's entire boundary layer. The evolution of the vorticity field was accomplished through application of the Biot-Savart law in conjunction with a random-walk diffusion model, the Scully vortex-core model, and a second order Adams-Bashforth integration scheme. The incoming vortex's core was discretized into a series of particles, each with equal strength, overlapping cores, and equal area. Instead of utilizing a typical panel method and Kutta condition for the wing, the surface of the wing was discretized into panels, each with a control volume above the wing representing the boundary layer. Each control volume was then seeded with nascent vortex particles. The no-penetration boundary condition is applied at the nodes between panels, and the resulting linear series of equations is solved for the circulation strength at each node. This vorticity distribution is then used to determine the strength of the nascent-vortices, which are convected forward in time along with all of the vortices in the flow. If, at the end of the convection step, the nascent vortices have moved outside of the control volume borders they are assumed to have been shed into the wake, and become independent vortex particles. If they remain within the control volume they are absorbed as residual vorticity within the boundary layer.

For this model, comparisons were made both to other numerical models and to experimental measurements. Very good agreement was found with other BVI models and reasonable agreement with experiments. It accurately captured the formation of leading edge suction as the impinging vortex approaches the wing and the rapid collapse of the  $C_l$  peak as the vortex passes the wing. For the case where the vortex impinges on the leading edge and is split into two parts convecting along the upper and lower surfaces of the wing there is a slight discrepancy between this model and previous ones. Qian and Vezza's model predicts a small local separation bubble on the aft portion of both the upper and lower surfaces, which standard panel methods

are incapable of predicting.

When compared to appropriate experimental data Qian and Vezza found good agreement. For  $C_L$  the magnitude of the peak was predicted to within 30% for the vortex impinging directly on the leading edge and out to a passing distance of  $0.2c$ . There is a slight time shift present in the location of the peaks, with the numerical peak occurring slightly before the vortex reaches the leading edge and the experimental peak occurring when the vortex center is either at, or slightly past the leading edge. Drag and moment coefficients ( $C_d$  and  $C_m$ ) were also measured and calculated, both agreeing reasonably well. The only major discrepancy with experiments occurs when the impinging vortex nears the trailing edge of the airfoil. For this position a significant peak in  $C_m$  was measured in experiments but not present in the numerical results.

Qian and Vezza's model accurately predicts the behavior of the wing in response to an impinging vortex, accurately capturing  $C_l$ ,  $C_d$ , and to a lesser degree  $C_m$ . A slight discrepancy in the timing is present but Qian and Vezza attribute this to the substantial amounts of wander in the vertical and horizontal location of the interaction vortices that are reported in experimental data.

## Chapter 3

### EXPERIMENTAL INVESTIGATION AND RESULTS

In order to understand the shear-layer/wing interaction, the expected behaviors discussed in Chapter 2 must be compared to the physical behavior of the system and quantified. While available BVI and shear-layer data is extensive, extrapolations from this data can not take into account the interaction of the growing layer and the wing. Qualitatively it is expected that lift variations will occur at frequencies surrounding  $f_m$ . When viewed in the frequency domain, the PSD of the lift history should show a broad peak around  $f_m$ , similar to the  $u'/U_1$  PSD plots of Hussain and Zaman, Figure 2.5.

In order to investigate this flow, a unique system has been designed to produce a shear-layer with a negligible static pressure gradient across the flow at the origin. Due to size limitations, it is not feasible to completely remove the effect of the tunnel-wall boundary-layers on the flow, however in light of the work of Ghoniem and Ng[25] the presence of the boundary-layers should not effect the dynamics of the coherent structures. The system generates a quasi 2-D shear-layer, with three dimensionality due only to the formation of classical 3-D shear-layer structure[16], and the wall boundary layers. An instrumented wing is then placed in the flow well downstream of the shear-layer origin on an adjustable height, rigid support structure.

This chapter will discuss the design and development of the shear-layer and wing support structure, the instrumentation utilized in measuring shear-layer characteristics and the wing response, preliminary layer and wing testing, and the experimentally measured wing response to the shear-layer.

### 3.1 Facilities and Shear-Layer Design and Characteristics

The University of Washington, Aeronautics and Astronautics, 3'x3' test-section wind-tunnel was chosen for development of the shear-layer. The tunnel is open return, and capable of operating at dynamic pressures up to 1.5 KPa. With the shear-layer inserted into the tunnel, operation speeds are limited to  $U_1 \leq 25m/s$  or  $0.4KPa$  due to structural concerns on the flow restricting screens. This tunnel was designed and manufactured by Engineering Laboratories Design Inc. At full speed the mean flow varies by less than 1%, facing the entrance from lower left hand corner to the upper right hand corner, and the  $u'_{rms}$  level is 0.1% of the free stream velocity. Turbulence levels are slightly higher at low speeds, with RMS variations between 0.2% and 0.4% of the free stream for the experimental velocities investigated.

Figure 3.1 shows a schematic of the tunnel. Here the abscissa is measured from the beginning of the contraction, while the ordinate is the vertical distance from the tunnel centerline. The tunnel is symmetric about the mid-line plane, and the plane normal to it. Upstream of the origin is a series of flow conditioning screens, a section of honeycomb, and an orifice plate, all designed to produce a uniform flow. The initial width is approximately 2.8x2.8 m, narrowing through a bell shaped contraction to a 0.91x0.91 m test section (3x3 ft). The test section is 2 m long, though only 1.5 m is accessible for testing. Following the test section a 2 m diffuser leads to a short flow conditioning section composed of fine mesh screens to prevent swirl induced by the fan motor from reaching the test section. Following the fan motor an additional diffuser smooths the transition into the room. The tunnel sits on the floor of a narrow high-bay room with other asymmetries such as stairs and equipment along the walls.

#### 3.1.1 Shear-Layer Design

Shear-layers are usually studied in facilities that bring two fluid streams, drawn from separate reservoirs, together at the sharpened trailing end of a splitter plate. However,

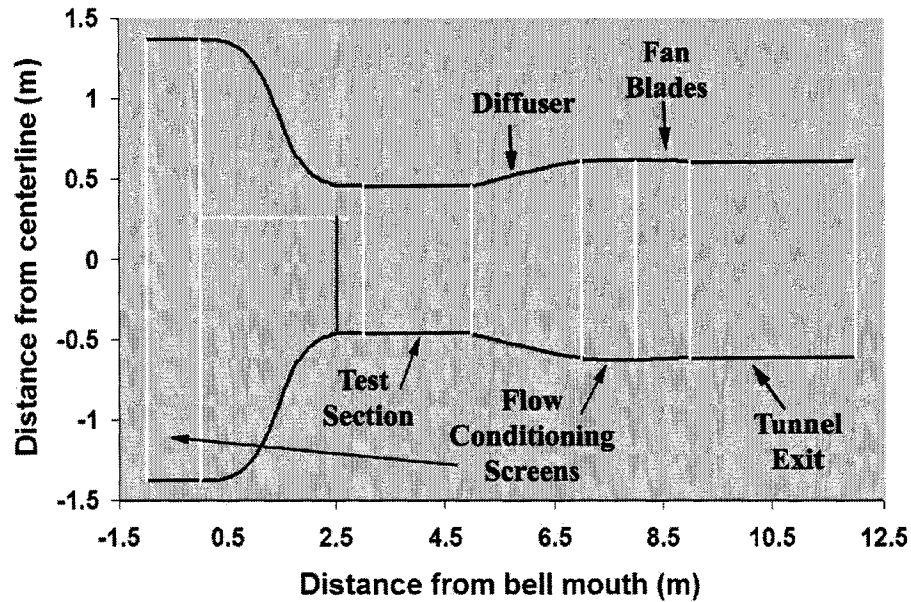


Figure 3.1: Wind-tunnel schematic

this was not currently feasible and it was decided to modify the available 3'x3' Tunnel for the present study. Initial experiments aimed at producing a  $U_2 = 0$  shear-layer were only marginally successful. Instead a novel technique was employed in a fashion similar to that used by Yang and Karlsson[21].

A splitter-plate, suspended in the bell-mouth of the tunnel from the upstream flow conditioning screens to the start of the test section, separates the incoming flow into two streams of equal total pressure. By offsetting the splitter plate from the tunnel midline, the two streams undergo different contraction ratios generating different velocities and subsequently different static pressures. While the velocity difference is needed, the static pressure gradient across the layer is undesirable and could cause layer deflection. Inserting a series of fine mesh screens supported by honeycomb into the low-speed stream serves to drop the static pressure in that stream.

The dimensions that affect the free stream velocity at a given point are the cross-sectional areas of the two streams at the entrance, test section, and at a general

position  $\chi$ , downstream of the splitter plate origin, shown in Figure 3.2. These variables control the velocity of the two streams and subsequently the pressure difference across the splitter. Upstream of the screens the pressure difference across the plate is given by the expression,

$$\Delta P(x) = q_{high} \left( \frac{A_{high-test}}{A_{high}(\chi)} \right)^2 - q_{low} \left( \frac{A_{low-test}}{A_{low}(\chi)} \right)^2, \quad (3.1)$$

where  $q_{high}$  and  $q_{low}$  are the dynamic pressures of the high and low-speed streams,  $A_{high-test}$  and  $A_{low-test}$  the test section entrance areas of the high and low-speed streams and  $A_{high}(\chi)$  and  $A_{low}(\chi)$  the areas of the high and low-speed streams a distance  $\chi$  downstream from the flow conditioning screens. Finite element modeling of the deflection of the splitter for various materials under its own weight and these pressure loading conditions led to choosing smoothly surfaced 3/4in plywood for construction of the splitter plate. Downstream of the screens the static pressure difference is given by

$$\Delta P(\chi) = \left[ \left( \frac{A_{high-test} + A_{low-test}}{A_{low}(\chi)} \right) - 1 \right] q_{high} + \left[ 1 - \left( \frac{A_{high-test} + A_{low-test}}{A_{low}(\chi)} \right) \right] q_{low}. \quad (3.2)$$

To avoid shear-layer deflection  $\Delta P$  should be equal to zero. Setting  $\Delta P = 0$ , Equation 3.2 can be manipulated to relate the splitter plate offset from the centerline,  $\Delta Y$ , to the velocity ratio  $r$ , and one half of the height of the tunnel bell mouth entrance,  $H$ , resulting in

$$\Delta Y = \left( \frac{H}{3} \right) \left( \frac{r+1}{r-1} \pm \left[ \left( \frac{r+1}{r-1} \right)^2 + 3 \right] \right). \quad (3.3)$$

For the 3x3 wind-tunnel,  $H = 1.45m$ , and a desired value of  $r = 0.5$ , Equation 3.3 yields an offset of  $0.2m$  from the centerline. Utilizing these results, the center of the splitter plate is positioned at  $0.66m$  above the floor of the test section and  $0.25m$  below the ceiling. The larger low-speed stream is passed through two 20 mesh (wires/inch)

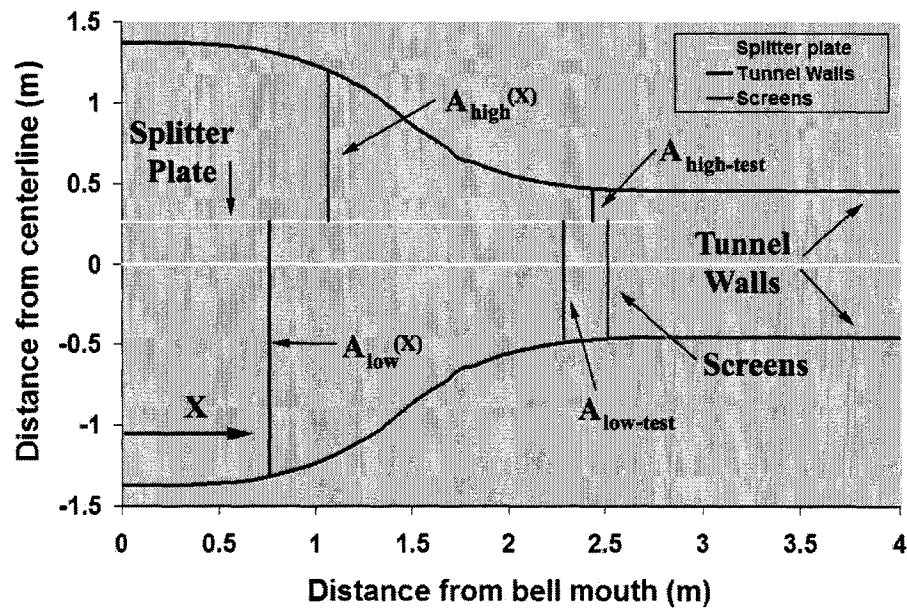


Figure 3.2: Shear-layer generation schematic

screens. A grid, composed of 1 inch wide aluminum strips on 1 inch centers, is used to support the screens.

In order to bring the two flows together smoothly the last 45cm of the splitter plate is composed of an aluminum plate. This plate has been milled to allow the frame that supports the screens to be inset such that the flow passing through the screens directly below the splitter is undisturbed by the presence of the frame. The trailing edge of the aluminum plate has been milled to a  $10^\circ$  wedge to smoothly join the two streams.

### 3.1.2 Velocity Measurement Instrumentation

The first key measurement needed to characterize the shear-layer is  $U_1$ . This stream remains at the same total pressure from the end of the flow conditioning system to the test section entrance. By assuming that the tunnel velocity prior to the contraction is small, it is possible to approximate  $q$  by measuring the static pressure difference

across the contraction. For this measurement a Datametrics 13.3 KPa Barocel Pressure Sensor, Type 590D differential pressure transducer is utilized. The transducer has a maximum differential of 13.3 KPa, and is accurate to 0.05% of the reading with a repeatability of 0.01% and an 8 msec response time. It outputs a voltage directly proportional to the pressure difference in KPa. This transducer was calibrated against a water filled manometer, over a range of pressures from 0.9 to 7.5 KPa. The manometer and pressure transducer were connected in parallel to a pump, and the second ports left exposed to atmospheric pressure. The vacuum pump was then activated to produce a pressure differential and the transducer and manometer measurements compared. The manometer and transducer measurements were found to agree within 1%, verifying the current calibration (data located in Appendix C).

In addition to measurements of  $U_1$ , measurements of  $u$  are needed to characterize the shear-layer. For these measurements a TSI-1020 hot-film has been used in conjunction with a DISA 56C01 Constant Temperature Anemometry Unit (CTA) and a DISA 5617 CTA Bridge. This combination has a frequency response in excess of 1 KHz, higher than the maximum velocity fluctuation frequency due to coherent structure passage. Equation 2.3 predicts the maximum frequency of interest to be approximately 75 Hz, for the experimental range of  $x = 1 \rightarrow 2m$  and  $U_1 = 3 \rightarrow 11m/s$ . Velocities were obtained by raising the output voltage to the fifth, dividing by the overheat ratio, and using a linear calibration curve

$$\frac{V_{out}^5}{a} Z_s + Z_o = U_{calib} \quad (3.4)$$

where  $V_{out}$  is the probe voltage,  $U_{calib}$  the calibration velocity,  $Z_s$  the best fit line slope,  $Z_o$  the zero offset, and  $a$  the overheat ratio. The overheat ratio is defined as the difference between the hot film's resistance at the operating temperature of 250°C and the film resistance that would be present at the ambient temperature, divided by the film resistance at the ambient temperature.

$$a \equiv \frac{R_{hot} - R_{ambient}}{R_{ambient}}. \quad (3.5)$$

In this formula  $R_{hot}$  is the probe's hot resistance, and  $R_{ambient}$  the resistance at ambient conditions. For the probe utilized  $R_{hot} = 9.22\Omega$  at  $250^\circ C$ , while  $R_{ambient}$  is determined during each experimental run. Both  $R_{hot}$  and  $R_{ambient}$  are calculated from the probes resistance at  $0^\circ C$ ,  $R_{0^\circ C} = 5.79\Omega$ , and the rate of change of hot film resistance with temperature is  $1.37\Omega/100^\circ C$ , both provided by the manufacturer. The overheat ratio is then calculated at each time step based on the ambient temperature. As the tunnel is an open return, and the building has minimal heating/cooling capacity, experimental temperature is difficult to control. During a single run, variations in temperature up to  $4^\circ C$  have been measured during a 2 hr run. While King's Law and the overheat ratio corrected version of King's Law were both considered, the current calibration was found to have better accuracy over the wide range of temperatures experienced during a single experimental data collection run.

For calibration, the probe was placed in the center of the wind-tunnel, with no shear-layer present. The hot film bridge was then balanced as per manufacturer recommendations. The tunnel velocity was swept through the experimental range from  $q = 0 \rightarrow 0.26$  KPa. At each step  $q$ , ambient temperature as determined from an Omega Model 115KC Thermocouple Thermometer, and  $V_{out}$  were recorded through a LABVIEW VI. Based on the calibration data, Figure 3.3 (numerical values are located in Appendix C), the constants were determined to be  $Z_s = 0.0155$ , and  $Z_o = -2.35$ . At most this calibration curve differs from the measured  $u$  by less 5%, with a linear fit measure  $R^2 = 0.99$ . This data was taken at two separate times with temperature varying from  $18.4^\circ C$  to  $24.5^\circ C$ . For calibration, the probe was placed in the center of the wind-tunnel, with no shear-layer present. The hot film bridge was then balanced as per manufacturer recommendations. The tunnel velocity was swept through the experimental range from  $q = 0 \rightarrow 0.26$  KPa. At each step  $q$ , ambient temperature as determined from an Omega Model 115KC Thermocouple Thermometer, and  $V_{out}$

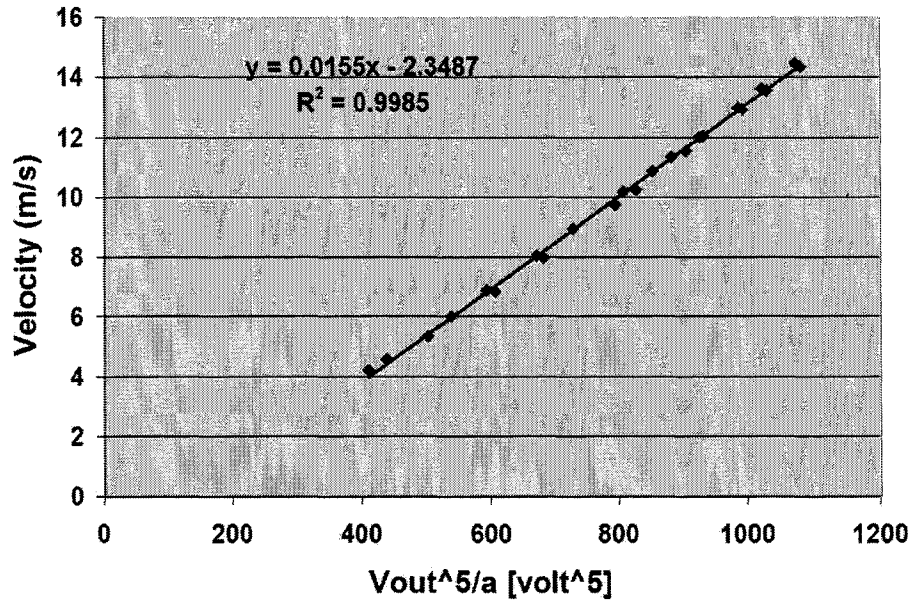


Figure 3.3: Hot film calibration data ( $Z_s = 0.0155$ ,  $Z_o = -2.35$ )

were recorded through a LABVIEW VI. Based on the calibration data, Figure 3.3 (numerical values are located in Appendix C), the constants were determined to be  $Z_s = 0.0155$ , and  $Z_o = -2.35$ . At most this calibration curve differs from the measured  $u$  by less 5%, with a linear fit measure  $R^2 = 0.99$ . This data was taken at two separate times with temperature varying from  $18.4^\circ C$  to  $24.5^\circ C$ .

### 3.1.3 Mean Shear-Layer Characteristics

For an offset from the centerline of 0.2m, the contraction ratio of the smaller stream rises to 15.5 and the contraction ratio of the larger stream falls to 7.9. Assuming the incoming flow velocities for both streams are equal, this should result in an  $r = 0.51$  shear-layer, though practically the shear-layer generated has  $r = 0.43$ . This slight discrepancy is likely due to two sources, a small uncertainty in the analysis of the pressure drop caused by the screens, and the possibility that the velocity at the high

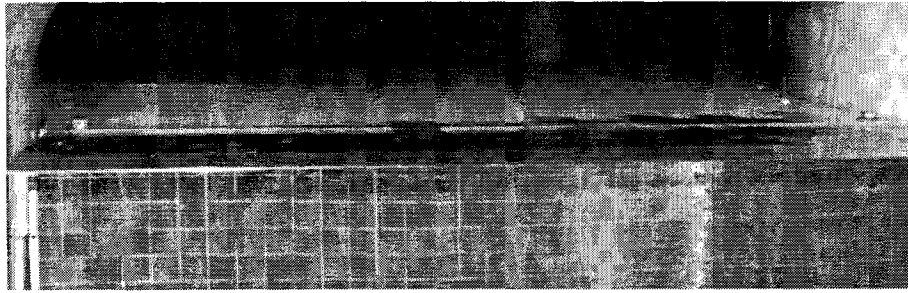


Figure 3.4: Shear-layer generation setup

and low speed streams origin is not identical. This shift is likely the cause of the slight deflection of the layer center towards the low speed side that has been observed in the mean velocity profiles. Figure 3.4 is a view of the splitter plate, screen and high speed stream taken from downstream.

The shear-layer was characterized by measuring mean velocity profiles, calculating the spreading rate, the initial momentum thickness,  $f_m$  and the associated constants  $C$  and  $K$ , as well as by flow visualization. The hot-film probe was used to measure velocity profiles at four downstream positions. At each position a vertical traverse measured velocity every 0.2 cm. The maximum slope of the velocity profile was calculated with a multi-point centered difference scheme to smooth out any localized error due to insufficient averaging time.  $\delta_\omega$ , was calculated from Equation 2.1, and plotted versus  $x$ , as seen in Figure 3.5. A virtual origin of  $x_0 = 0.026m$  upstream of the origin was determined from the best-fit straight line. The data displayed on Figure 3.5 supports the conclusion that the layer has attained self-similarity.

The linear fit of the data in Figure 3.5 results in a growth rate of  $\partial\delta_\omega/\partial x = 0.066$ . Using this and the estimate provided by the Abramovich-Sabin relation in Equation 2.2, the growth constant is  $K_{exp} = 0.17$ . This falls within the range of values reported by Brown and Roshko, Table 2.1.

For a self-similar flow the mean velocity profiles should collapse to a single curve

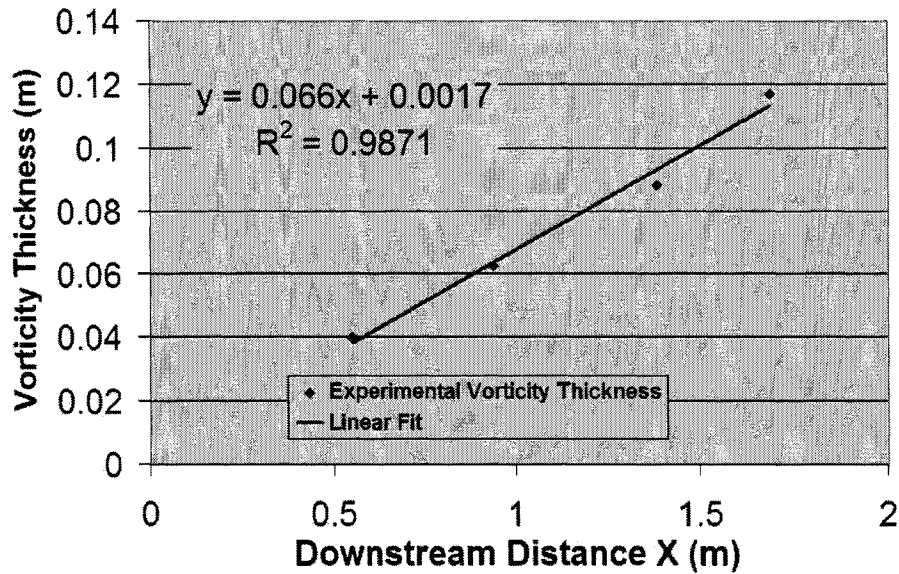


Figure 3.5: Shear-layer growth and virtual origin

when plotted on the dimensionless ordinate  $\eta = y/(x - x_0)$ , where  $\eta$  is the vertical distance normalized by the distance downstream of the virtual origin. Figure 3.6 shows that curves collapse, indicating that the velocity profiles are self-similar when a virtual origin of 0.026 m upstream of the splitter plate end is used. A point of interest is that the layer is growing somewhat preferentially into the low-speed stream, with the center of the layer occurring at approximately  $\eta = -0.015$ . This value will be used subsequently as the layer center.

An additional mean velocity profile was taken 2cm downstream of the splitter end for  $U_1 = 48\text{m/s}$ , Figure 3.7. From this an initial momentum thickness of  $\Theta_e = 0.8\text{mm}$  was calculated from the definition[26]

$$\Theta_e = \int_{-\infty}^{\infty} \frac{u - U_2}{U_1 - U_2} \left(1 - \frac{u - U_2}{U_1 - U_2}\right) dy. \quad (3.6)$$

An identical value was calculated through the discrete application of Thwaites method on both the upper and lower surfaces of the splitter plate. This value and the calculated values for other  $U_1$  are shown in Table 3.1. Based on the largest estimate of

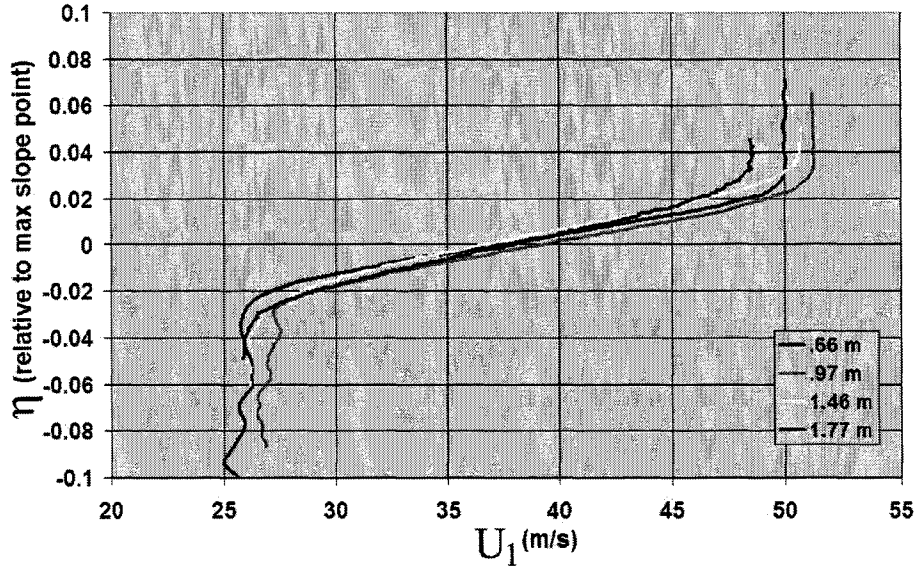


Figure 3.6: Velocity vs  $\eta$

$\Theta_e$  at the lowest experimental velocity the closest experimental wing position will be a distance of  $370\Theta_e$  downstream, and the final position is  $760\Theta_e$  downstream. While these distance do not meet Bradshaw's[13] conservative estimate of up to  $1000\Theta_e$  needed to attain self-similarity, they are well downstream of the initial roll-up location, and likely near the beginning of the self-similar region of the layer based on the collapse of the mean velocity profiles, the growth of  $\delta_\omega$ , and the virtual origin.

In addition to mean information, velocity spectra were taken for several velocities. Analysis of velocity spectra, without the shear-layer present, revealed no dominant fluctuation frequencies in the clean flow. Shear-layer velocity spectra were taken at the upper edge to show the effect of coherent structures. However, data collected at  $x = 1.19m$  displayed unexpected results. Figure 3.8 shows the magnitude of  $u'_{rms}/U_1$  versus  $U_1$ . From self-similarity considerations the magnitude of  $u'_{rms}/U_1$  should be constant at fixed  $\eta$  regardless of changes in  $x$  or  $U_1$ . However, Figure 3.8 displays a marked drop between  $U_1 = 5$  and  $9m/s$ .

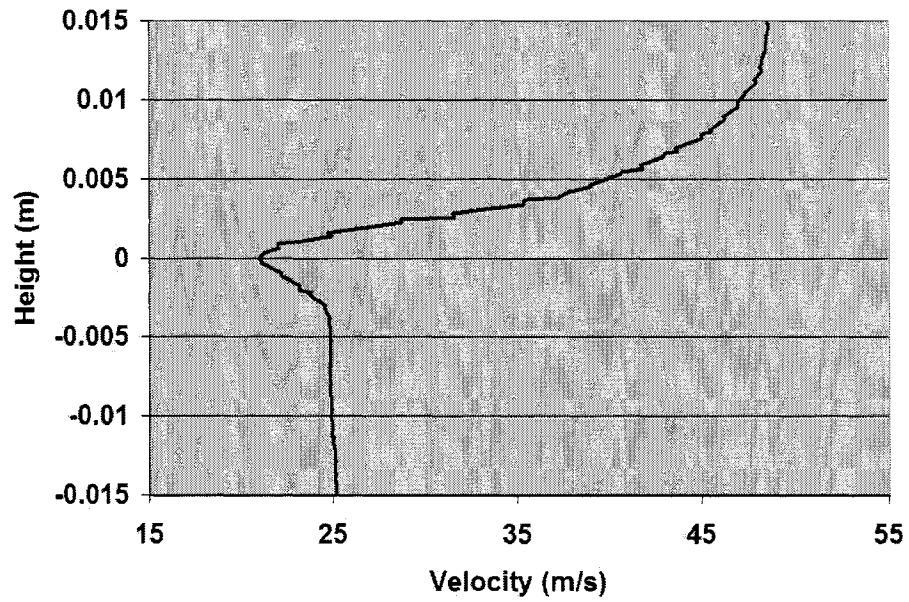


Figure 3.7: Initial boundary layer profile,  $U_1 = 48\text{m/s}$ ,  $x = 2\text{cm}$

Table 3.1: Layer Initial Momentum Thickness Estimates ( $\Theta_e$ )

$U_1$	Theoretical Value (mm)	Experimental Value (mm)
48	0.8	0.8
11	1.7	
9	1.9	
7	2.1	
5	2.5	
3	3.2	

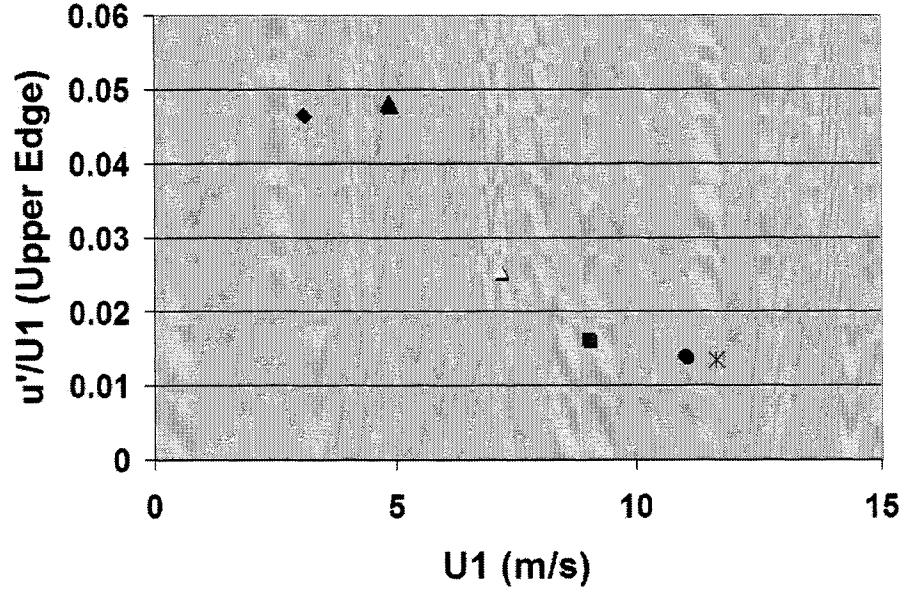


Figure 3.8:  $u'_{rms}/U_1$  magnitude variation with  $U_1$

### 3.1.4 Spectral Shear-Layer Properties

PSD plots of  $u'$  display additional unexpected results as apparent in Figure 3.9. Figure 3.9 shows the PSD of  $u'$  [ $(m/s)^2/Hz$ ] versus frequency [ $Hz$ ], and has not been non-dimensionalized, to make several profile characteristics clear. There is a direct relationship between the rms value of  $u'$  and the PSD of  $u'$  given by

$$\int_0^{\infty} PSD(u'/U_1)df = u'_{rms}/U_1, \quad (3.7)$$

at constant,  $U_1$ . From self-similarity the rms value of  $u'$  should be constant a fixed value of  $\eta$  and as such the behavior of the PSD of  $u'$  in response to changes in  $U_1$  and  $x$  can be predicted. With increasing  $U_1$  the range of excited frequencies in the PSD of  $u'$  should also increase, and the peak magnitude should decrease as the peak widens. However, it is clear from Figure 3.8 that the rms value  $u'_{rms}/U_1$  falls off with increasing  $U_1$ , inconsistent with free shear-layer behavior. In addition the  $u'$  PSD profiles taken at  $U_1 = 9.0$ , and  $11.0m/s$  display unexpected characteristics. The profiles at  $U_1 = 3.1$ ,

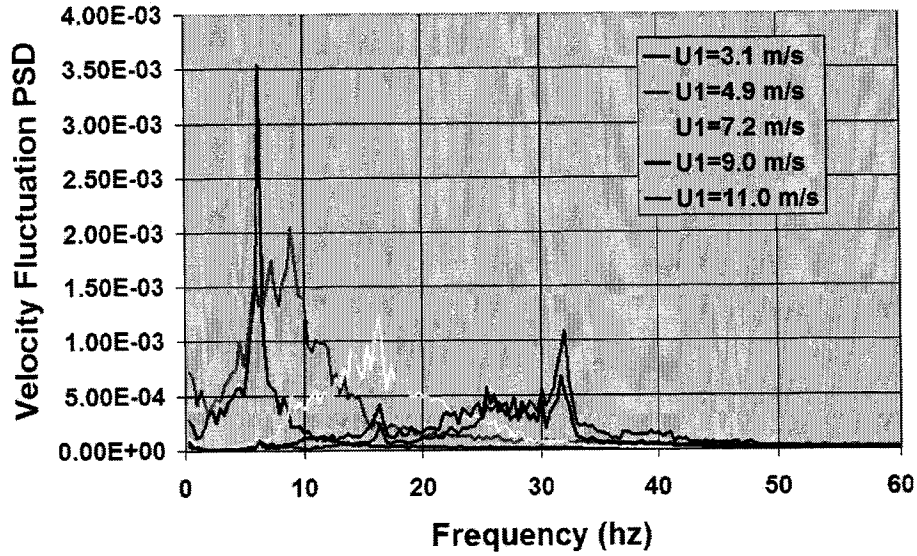


Figure 3.9: PSD of  $u'$  for varying velocity

4.9, and  $7.2\text{m/s}$  show relatively broad peaks, with steadily increasing magnitude up to a maximum value, and occasional sharp sub peaks which are likely remnants of insufficient averaging time. However, the  $U_1 = 9.0$  and  $11.0\text{m/s}$  cases display broad peaks where the PSD of  $u'$  is above background noise level, and punctuated by sharp peaks at 16 and  $32\text{Hz}$ . The peak at  $16\text{Hz}$  is also present in the profile taken at  $U_1 = 7.2\text{m/s}$ , though it appears to coincide with  $f_m$ , which is not the case for the higher velocities. Further the peaks at 16 and  $32\text{Hz}$  are insensitive to changes in  $U_1$ , which should not be the case for a freely evolving shear-layer. Figure 3.10 re-scales Figure 3.9, and removes the  $U_1 = 3.1, 4.9,$  and  $7.2\text{m/s}$  cases to more clearly show the characteristics of the high-speed plots. Similarity between Figure 3.10 and Figures 2.6 and 2.7 suggests that the layer is developing in a forced manner.

While turbulence suppression due to forcing has been observed in some cases [32] this is not likely the current case. The Strouhal number based on  $\Theta_e$  for  $32\text{Hz}$  is below the critical value  $St = 0.017$  determined by Zaman and Hussain for turbulence

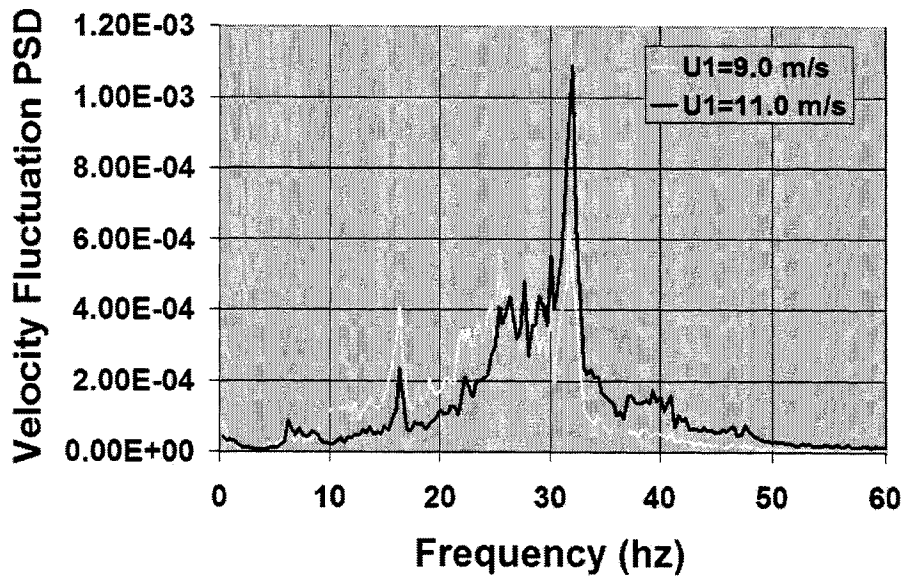


Figure 3.10: PSD of  $u'$  for  $U_1 = 9$  and  $11\text{m/s}$

suppression[32]. In contrast, classical shear-layer forcing typically accentuates the two-dimensionality of the layer leading to a slight decrease in  $u'_{rms}$ , an increase in the maximum value of  $v'_{rms}$  by up to a factor of 2, and a decrease in the maximum value of  $w'_{rms}$  by up to a factor of 2.

The overall behavior of the PSD peak locations and the velocity insensitivity of the sharp peaks at  $32\text{Hz}$  and  $16\text{Hz}$  leads to the conclusion that the layer is being forced at  $32\text{Hz}$ . As expected from the results of Zaman and Hussain[32], Fiedler and Mensing[22], and others, once  $f_m$  falls below the forcing frequency, either due to lower layer velocities or increased downstream distance, the layer returns to self-similar behavior. This accounts for the validity of the PSD profiles at  $U_1 = 3.1$  and  $4.9\text{m/s}$ . As the dynamics of the layer downstream of the forced region quickly return to free shear-layer characteristics with the possibility of a somewhat shifted value of  $x_0$ , the distribution of energy and the subsequent magnitudes of  $u'_{rms}$ ,  $v'_{rms}$ , and  $w'_{rms}$  should return to their unforced distribution.

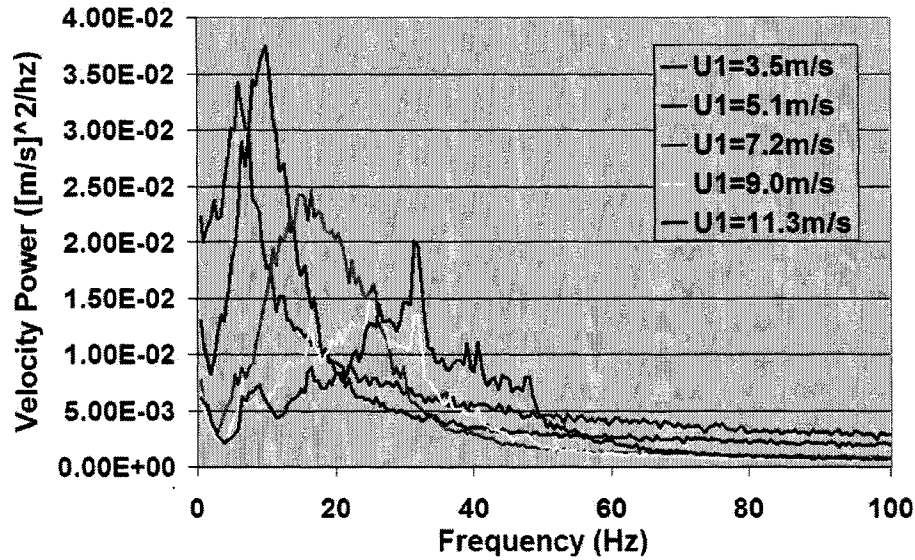


Figure 3.11: PSD of  $u'$  for  $x = 1.19m$

Additional velocity data was collected at the upper edge of the layer for  $U_1 \approx 3, 5, 7, 9,$  and  $11m/s$  and for  $x = 1.19, 1.45, 1.70,$  and  $1.96m$  to further investigate the behavior of the shear-layer. Figures 3.11 and 3.12 display the data for  $x = 1.19$  and  $1.96m$  respectively. Both the  $32$  and  $16Hz$  forcing peaks are present, though for  $x = 1.96m$  the magnitude of the  $32 Hz$  peak is somewhat reduced as the frequency of the velocity fluctuations slowly shifts below  $32Hz$  due to increased downstream distance. In addition the lower speed plots behave as expected, with broad relatively smooth peaks displaying no insensitivity to  $U_1$ .

Further analysis of the velocity spectra for fixed  $\eta$  and  $U_1$ , with variable  $x$  found the layer to be well behaved with no variation in magnitude due to position for the low-speed cases, and a persistent decrease in normalized magnitudes for the high-speed cases. The curves for  $U_1 \geq 9m/s$  are somewhat difficult to analyze for a distinct value of  $f_m$ , so only the data for  $U_1 \leq 7m/s$  was considered when determining the value of  $C$ . Figure 3.13 shows the relationship between  $f_m$  and the normalized velocity

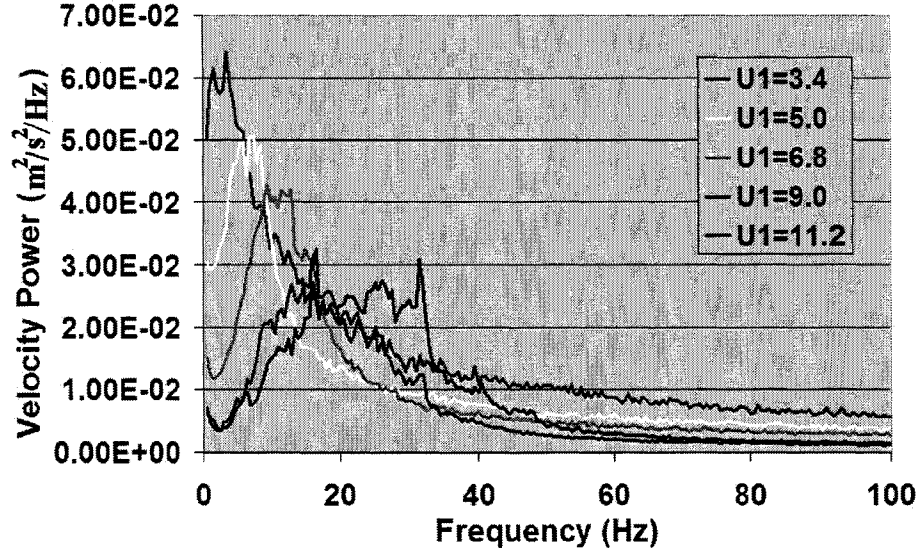


Figure 3.12: PSD of  $u'$  for  $x = 1.96m$

$U_1/x - x_0$ . Performing a linear fit, while forcing the curve to pass through the origin gives a slope of 3.2, with an  $R^2$  fit of 0.87.

Equation 2.3 can now be used along with  $K$  to estimate the coherent structure spacing constant  $C$ .

$$C_{exp} = \frac{f_m}{\frac{\bar{U}}{x-x_0}} \left( \frac{1+r}{1-r} \right) \left( \frac{1}{K} \right). \quad (3.8)$$

For the current layer  $C_{exp} = 4.7$ . While this is on the high end of the values reported by Brown and Roshko it is within reason and corresponds to a value of  $K_2 = 0.78$ .

As a final verification tool visualization was carried out by injecting smoke into the flow near the trailing edge of the splitter plate. Though not as clear as the images of Brown and Roshko[3], it is apparent from Figure 3.14 that vortex roll-up is occurring and that coherent structures are visually present in the layer at low speeds.

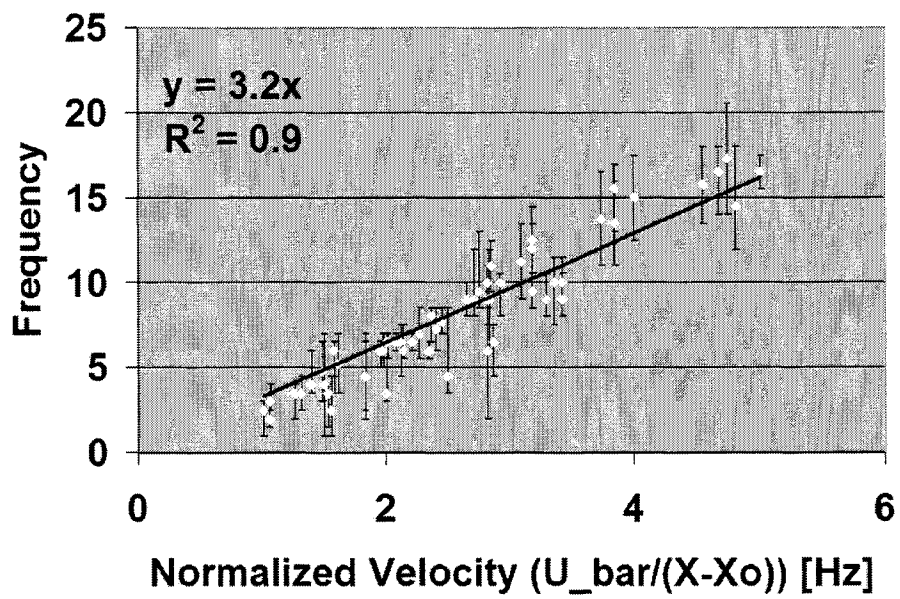


Figure 3.13: Peak velocity variation frequency

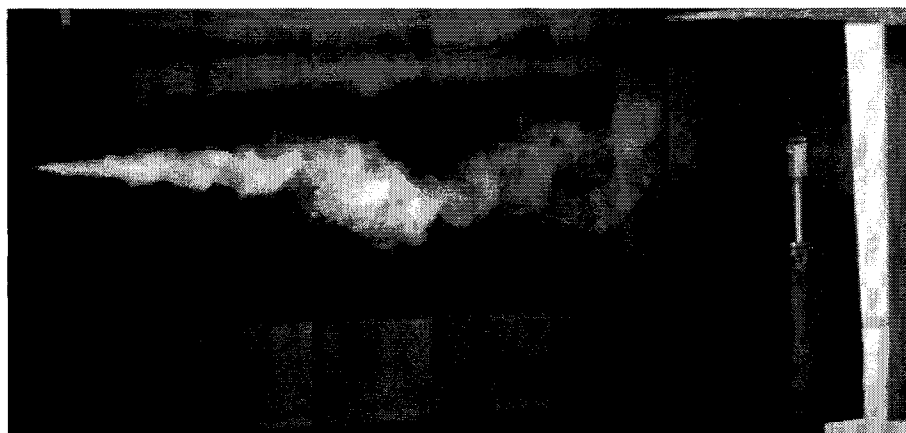


Figure 3.14: Low-speed smoke visualization

### 3.1.5 Forcing Source Analysis

Searching for the source of the forcing revealed that the wind-tunnel fan motor rotates at  $1800RPM$ , or  $30Hz$ . Vibrations at or slightly above this frequency were found in structures ranging from the motor supports to the wall of the test section and the bell mouth of the tunnel. Further, the magnitude of this vibration appears to be load dependant, with increased tunnel velocity corresponding to higher magnitude vibration. While not evident in past research using the facility, the high sensitivity of shear-layers to low-amplitude forcing, combined with the fact that  $f_m$  at the higher  $U_1$  overlaps the forcing frequency, has amplified the effect. Based on this, extra care must be taken in the study when considering the response of the wing to the layer.

A number of potential mechanisms for transmitting vibration to the flow have been identified: vibration of the splitter plate, screens, and bell mouth, direct flow fluctuations from the tunnel motor, and low-amplitude pulsation of the flow within the building itself. A combination of several steps may be needed to eliminate vibration within the layer and within the facility: the replacement of rigid connections between the tunnel sections to prevent direct transmission of vibration, a settling chamber and series of flow conditioners placed between the test section and the fan motor, the addition of flow conditioners downstream of the fan motor to eliminate the possibility of pressure fluctuations within the room itself, and acoustic isolation of the fan motor to prevent the excitation of other structures within the room.

Fortunately free shear-layer dynamics are Reynolds Number independent and thus a wide range of velocities is not necessarily required for understanding. As the current research is focused on the response of a wing to forcing by a free shear-layer, and not the dynamics of forced shear-layers, the primary analysis of experimental results will be limited to data taken at the lower velocities. The full complement of experimental data will be presented and discussed though the magnitudes measured for the higher velocities are likely inaccurate, and not generally representative of the interaction of

a wing and free shear-layer.

### **3.2 Wing and Support Structure Design and Characteristics**

Once the layer was established and its properties evaluated, a lifting wing was designed and inserted into the flow. The wing was initially sting-mounted to a force balance, however the requirement of high sensitivity led to excessive flexibility and low-frequency natural vibrations. A more rigid system was needed than a sting could provide.

In addition to natural vibration, problems occurred due to vibration induced by the wind-tunnel fan-motor discussed in section 3.2.1. Vibration was not present at low  $U_1$ , but a significant peak fixed at  $32Hz$  appeared for higher  $U_1$  both with and without the shear-layer present. In order to avoid contamination of the lift signal by this vibration, the wing support structure needed to be isolated from the tunnel. The floor of the building is composed of multiple, independently poured concrete slabs which were found to be vibration free and the wing was mounted to these slabs.

The final support structure for the wing is composed of an optics table mounted on a series of concrete risers to minimize the length of the wing support struts. These blocks rest directly on the concrete floor, Figure 3.15. The high mass of this arrangement serves to minimize vibrations, as well as provide a rigid platform to support the wing. Two support struts are bolted to the optics table and extend into the tunnel test section. These supports are formed from 0.76 m long, 7.8 cm chord pieces of aero-strut, which were then welded onto 0.6 cm thick angle iron with 3.8 cm wide flanges. The aero-tube is then braced by welding struts from the trailing edge of the aero-tube to the angle iron. In addition three cross braces, two angled and one straight, laterally stiffen the struts, Figure 3.16.

The final wing has  $c = 0.076m$  and  $Sp = 0.46m$  for an aspect ratio of 6. After investigating various shapes and materials including a .32cm thick aluminum plate, and .6cm hollow plate, it was finally decided to use a 1cm thick balsa wood plate.



Figure 3.15: Optics table and risers

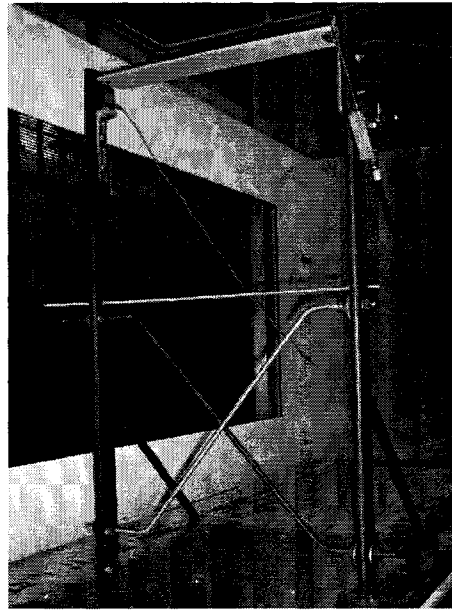


Figure 3.16: .076m chord wing on support frame

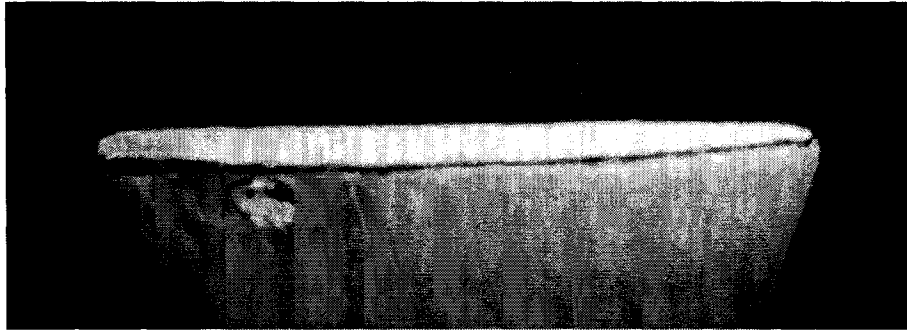


Figure 3.17: Balsa wood wing

Vibration testing revealed that the aluminum wings had undesirably low natural frequencies, in the same range as the coherent structure passage frequencies. The balsa wood proved much stiffer, having a natural frequency of  $94Hz$ . The leading edge was blunted, and the trailing edge tapered to form an approximately symmetrical airfoil, Figure 3.17.

The load cell is rigidly mounted on a bracket bolted to one of the aero-tubes to align the sensor vertically. The wing is then rigidly fixed to the top of the sensor on one end, and to a second bracket mounted on the opposing strut.

### *3.2.1 Dynamic Behavior of Wing and Support Structure*

The wing assembly was tested to find its natural frequencies, and to determine whether vibration of the support structure would contaminate the lift signal. Deflecting and releasing the center of the wing determined the primary natural frequency to be  $94Hz$ . This natural frequency was subsequently observed during testing as a low magnitude, persistent, broad peak at  $94Hz$  whose location is insensitive to changes in  $U_1$ , though with higher amplitudes at higher  $U_1$ , Figure 3.18.

The vibrational characteristics of the support structure were studied using an accelerometer placed at the upper end of the aero-tube. The frame was then deflected,

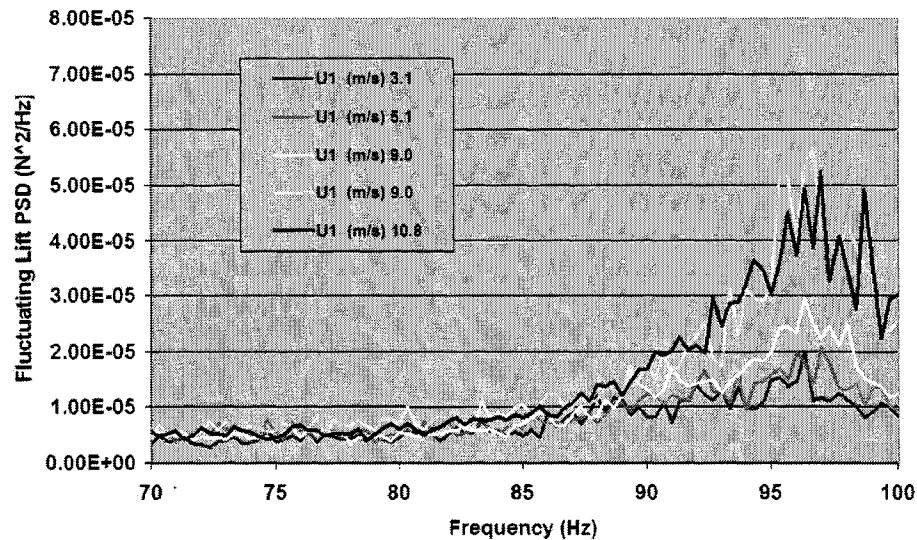


Figure 3.18: .076m chord wing natural frequency

and allowed to vibrate freely. Various modes were investigated by changing the orientation of the accelerometer. In addition, the frame was excited by impacts on the trailing support strut, and the optics table. The stream-wise natural frequency of the struts was found to be  $90\text{Hz}$ . However, the spanwise direction displayed frequencies of  $13.5$ ,  $58.5$ , and  $99\text{Hz}$  when allowed to vibrate freely. When the wing was placed on the struts, and the spanwise vibrational modes investigated, it was not found to induce fluctuations in the lift signal due to the orientation of the sensor. Finally the accelerometer was rigidly fixed to the optics table, to verify that the  $30\text{Hz}$  vibration induced by the fan motor was not present in the support structure when the wing and aero-struts were not exposed to the effects of the shear-layer. Based on these findings any fluctuations in the wing lift will be due to the interaction between the wing and layer.

### 3.2.2 *Lift Measurement*

After considering available sensors and lift measurement schemes, a Transducer Techniques MDB-5 lb load cell was chosen. The manufacturer reported characteristics of the load cell are given in Table 3.2. A calibration was performed by statically loading the cell up to 80% of its maximum load. Calibration results agreed with the manufacturer specifications to within a few percent. With a ringing frequency of  $765Hz$  the response rate is high enough to accurately capture lift variations due to coherent structure passage. While there may be some roll off of the signal at frequencies approaching the  $765Hz$  it is expected that the frequencies of interest will be below  $100Hz$  for which there should be negligible roll off. A variable voltage power supply, set to provide a fixed excitation voltage of  $9.8V$  was used to power the load cell. While the lift forces being measured are at the lower end of the range, the sensor is able to produce repeatable and dependable measurements of the wing's time varying lift.

Table 3.2: Load Cell Specifications, MDB-5

Specification	Value
Model:	MDB-5
Capacity:	5 lbs
Natural Ringing Frequency:	765 HZ
Deflection at Full Load:	.004 in
Nominal Excitation Voltage:	$V_{exc} = 10VDC$
Output per unit load	$(2/5)mV/V_{exc}$
Rated Output (R.O.):	2 mV/V nominal
Nonlinearity:	0.05% of R.O.
Hysteresis:	0.05% of R.O.
Non-repeatability:	0.05% of R.O.

### 3.3 Experimental Data

Once the design of the layer generation, wing support, and measurement systems was complete, wing and shear-layer interaction data was collected. The primary data forms are PSD profiles of  $L'$  and  $L'_{rms}$  at numerous locations throughout the accessible portion of the shear-layer. These spectral and  $\eta$  profiles were analyzed to investigate the effects of changes in  $U_1$ ,  $x$ , and  $\eta$ . To streamline the discussion of experimental results only a small representative sample of the data will be presented here, 4 to 5 plots per variable for  $L'$  PSD profiles, and fewer for  $L'_{rms}$  comparisons. The remaining data is located in Appendix A, though will be discussed here.

#### 3.3.1 Experimental Conditions

Lift data sets were taken at 5 downstream distances:  $x = 1.19, 1.45, 1.70,$  and  $1.95m$ , covering the range of accessible stream-wise tunnel positions. At each station 5 values of  $\eta$  were investigated: above the layer, at the layer upper edge, within the layer core, at the layers lower edge, and below the layer,  $\eta = 0.05, 0.02, -0.015, -0.05,$  and  $-0.9$  respectively. The locations are asymmetric to account for the deflection of the layer towards the low-speed side and to insure that the wing is not in the boundary layer on the high-speed tunnel wall.  $U_1$  was varied from 3 to 11m/s in 2m/s increments. Each velocity value was approximate due to limitations on the adjustability of the  $U_1$  at low speeds. All data has been collected with  $\alpha = 0$  to minimize the number of variables being investigated.

#### 3.3.2 Non-dimensionalization of Lift Data

If the response of the wing is self-similar, the various profiles should collapse when properly normalized. The most likely normalization for the  $L'$  PSD abscissa is the factor  $\bar{U}/(x - x_0)$ . Dividing by this produces a Strouhal scale with  $St = \frac{f(x-x_0)}{\bar{U}}$ , where  $f$  varies along the axis. The non-dimensionalization of the PSD ordinate is

somewhat more complex. The integral of the lift of the wing should vary with  $\bar{q}A$ , where  $\bar{q}$  is the dynamic pressure associated with  $\bar{U}$  and  $A = cSp$ , the planform wing area. Coupled with the scaling of the abscissa by  $\bar{U}/(x - x_0)$ , the PSD  $L'$  at a fixed Strouhal number should vary as some combination of the fundamental variables  $U_1$ ,  $r$ ,  $\rho$ ,  $c$ , and  $Sp$ . However as  $c$ ,  $Sp$ , and  $\rho$  have not varied during testing, they should have no effect on the results. As the units of the PSD of the Lift signal are  $N^2/Hz = (kgm/s^2)^2/(1/s) = kg^2m^2s^{-3}$  the normalization factor must have the same units. Based on the units of the available fundamental variables the most likely normalization factor is  $U_1^3\rho^2A^2(x - x_0)$ . Several other possibilities exist, potentially incorporating  $Sp^3$  or  $c^3$  while not including  $(x - x_0)$ . However it is expected that  $L'_{rms}$  will remain constant, and as discussed in Section 3.1.3, this will necessitate that the magnitude of the PSD vary with  $x$ , as the peak width varies with  $x$ .

One unavoidable result of this normalization is a shift in the number of points that effectively model the spectral peak. For the low velocity cases the major peaks are confined to a much smaller frequency range than for the higher velocity cases. When coupled with a fixed frequency resolution, this causes a higher Strouhal resolution for higher velocities.

$L'_{rms}$  data is also normalized though a different set of factors is needed. Like the mean velocity profiles, the spread of  $L'_{rms}$  should collapse on an  $\eta$  abscissa. The ordinate needs to be normalized by a factor with units of  $kgm/s^2$ . The most obvious choice is to use  $\bar{q}A$ . After extensive testing, both the  $L'$  PSD and  $L'_{rms}$  factors normalize the appropriate profiles well.

### 3.3.3 Effects of $U_1$ on Wing Lift Spectra

After a wing position was fixed within the tunnel, the tunnel was brought up to the desired  $U_1$  and the data collected. At the end of data collection  $U_1$  was either raised to the next value or the tunnel shut down and  $U_1$  allowed to return to zero, as currently the tunnel is only capable of being brought up to a fixed velocity from a lower value.

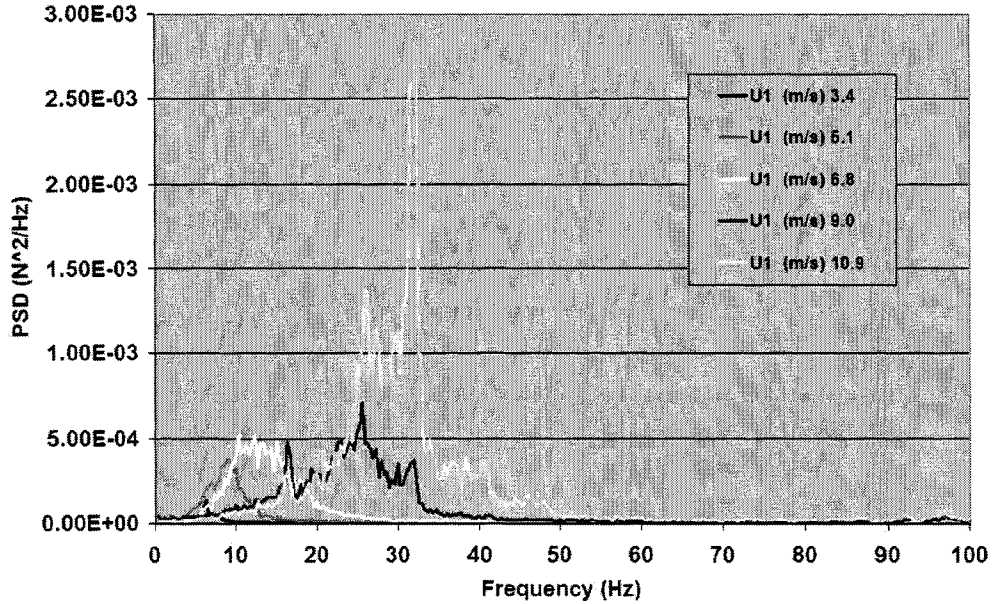


Figure 3.19: Raw  $L'_{rms}$  PSD,  $x = 1.19m$ ,  $\eta = -0.015$

Data sets at fixed  $x$  and  $\eta$  were collected over a period of one to two hours.

The first data points were collected at a  $x = 1.19m$ . The data taken at  $\eta = -0.015$  shows a representative sample of the raw  $L'$  PSD profiles, with units of  $Hz$  on the abscissa, and  $N^2/Hz$  on the ordinate, Figure 3.19. Several trends are apparent in the data. With increasing  $U_1$  the width of the curves progressively increases, as does maximum profile magnitude. In addition both the profiles taken at  $U_1 = 9$  and  $11m/s$  display sharp peaks at 16, 25, and 32 Hz. While the presence of sharp peaks is not unexpected, that both profiles display sharp peaks at several of the same frequencies is inconsistent with free shear-layer behavior. However it is difficult discern which of these trends are due to self-similar processes and which are due to more complex interactions.

Using the normalization factors discussed should cause any self-similar trends to become apparent. The normalized  $L'$  PSD profiles at  $\eta = 0.02$  and  $-0.015$  are the clearest samples for  $x = 1.19m$  and are shown in Figures 3.20 and 3.21 respec-

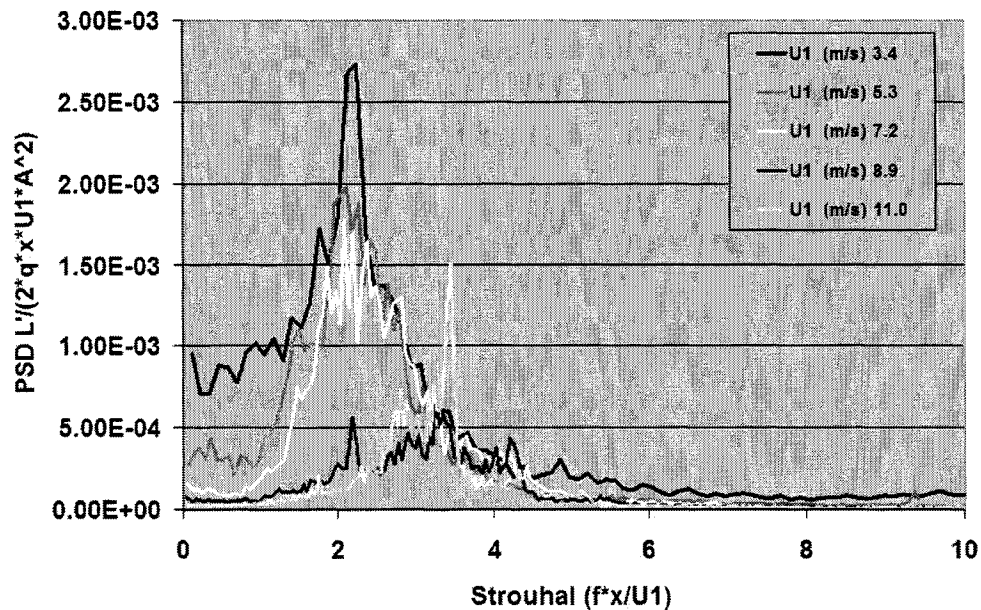


Figure 3.20: Normalized experimental  $L'_{rms}$  PSD,  $x = 1.19m$ ,  $\eta = 0.02$

tively. The additional profiles display many of the same traits, though the data is less clear due to the reduced clarity of the effects marking the presence of coherent structures[20].

As can be seen from both Figures 3.20 and 3.21 the normalized PSD data taken at  $U_1 \approx 3, 5$ , and  $7m/s$  all agree reasonably well. In the first plot the profiles at 5 and  $7m/s$  show maximum magnitudes that vary by approximately 10%. The  $3m/s$  case has a somewhat higher magnitude while both the 9 and  $11m/s$  cases have significantly lower average magnitudes. The only exception is the maximum magnitude of the single sharp peak in the  $11m/s$  case, which is comparable in magnitude to the 5 and  $7m/s$  cases. In Figure 3.21 the 3 and  $5m/s$  profiles agree well while the  $7m/s$  case has a slightly lower magnitude. In the same manner as the velocity data the profiles for the 9 and  $11m/s$  cases display reduced magnitudes and a different shape. Instead of a relatively smooth peak, often with a sharper section at its center, the 9 and  $11m/s$

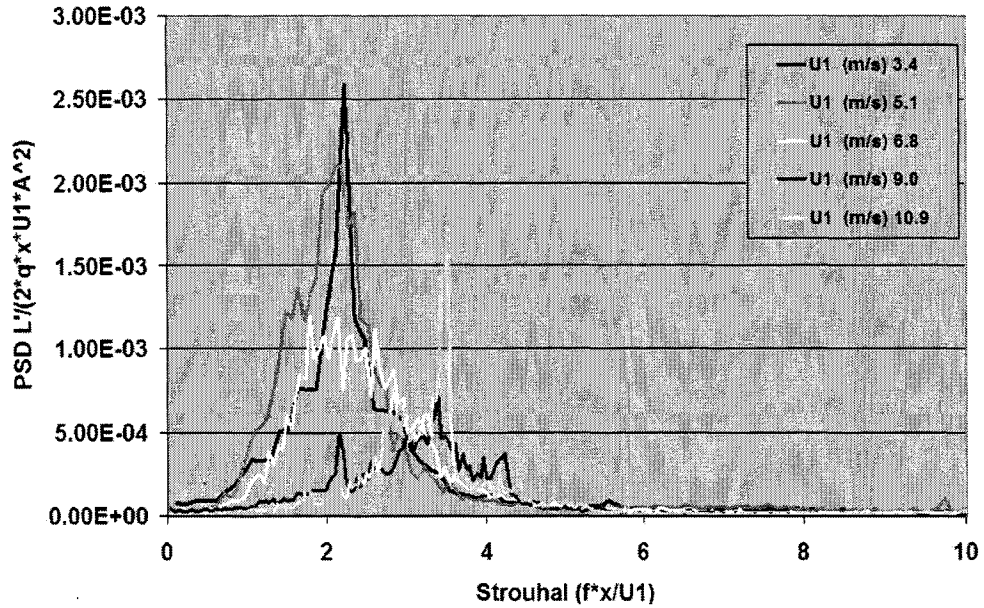


Figure 3.21: Normalized experimental  $L'_{rms}$  PSD,  $x = 1.19m$ ,  $\eta = -0.015$

cases display multiple sharp peaks.

An additional characteristic of the wings response is the width of the forcing peak. The frequency interval between the half-power points on the spectrum peak, defined as the Strouhal half-power band-width,  $\Delta St$ [33], is used to characterize this. For both cases the broad peaks found in the  $U_1 \approx 3, 5$ , and  $7m/s$  cases have  $\Delta St \approx 1.5$ , with the peaks centered at a  $St \approx 2$ . For the higher speed cases  $\Delta St \approx 2$ , with scattered sharp peaks present at  $St \approx 2, 2.75, 3.5$ . When the profiles are considered on a normalized ordinate but a dimensional abscissa with units of  $Hz$ , it is apparent that fixed, velocity insensitive peaks are present at  $16$ , and  $32Hz$ , with a lesser peak sometimes appearing at  $25Hz$ . The additional data taken at the remaining values of  $\eta$  display much of the same behavior.

Figure 3.22 displays data taken at  $x = 1.45m$  and  $\eta = 0.02$ . Once again the magnitude of the  $3$  and  $5 m/s$  data sets agree quite well, with the  $7 m/s$  data displaying

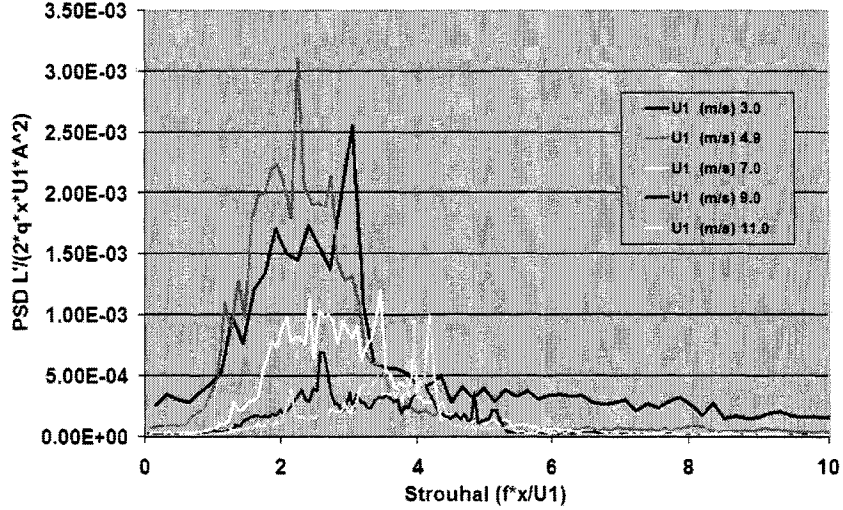


Figure 3.22: Normalized experimental  $L'_{rms}$  PSD,  $x = 1.45m$ ,  $\eta = 0.02$

a magnitude that is approximately a factor of 2 lower, and the 9 and 11m/s data displaying significantly reduced magnitudes.  $\Delta St$  of the  $U_1 \approx 3, 5,$  and  $7m/s$  cases remains at 1.5, with peaks centered at  $St \approx 2$ . Again the  $U_1 \approx 9$  and  $11m/s$  cases show  $\Delta St \approx 2$ , with sharp peaks present at  $St \approx 2.5,$  and  $4.25$ . While a sharp, uncentered peak is present in the  $U_1 \approx 3m/s$  case at  $St = 3$ , this peak is only present in the  $\eta = 0.05,$  and  $0.02$  cases. The additional  $x = 1.45m$  data sets display similar trends, with no additional features of note.

Figure 3.23 shows the data taken at  $x = 1.70m$  and  $\eta = 0.05$ . As in the previous profiles the 3 and 5m/s cases agree in magnitude closely, while the magnitude of the 7m/s case is somewhat reduced and the 9 and 11m/s cases are significantly reduced. For the 5m/s case  $\Delta St \approx 1.5$ , with the peak centered at  $St \approx 2$ . The 7m/s case has  $\Delta St \approx 1.5$  with a somewhat increased peak frequency of  $St \approx 3$ . The 9 and 11m/s cases display broader peaks with  $\Delta St \approx 2$ , and sharp peaks at  $St \approx 2.5$  and 3. The remaining data in Appendix A shows no additional trends or behaviors of note.

Figure 3.24 displays the data for  $x = 1.96m$  and  $\eta = -0.09$ . For the  $U_1 \approx 3,$  and

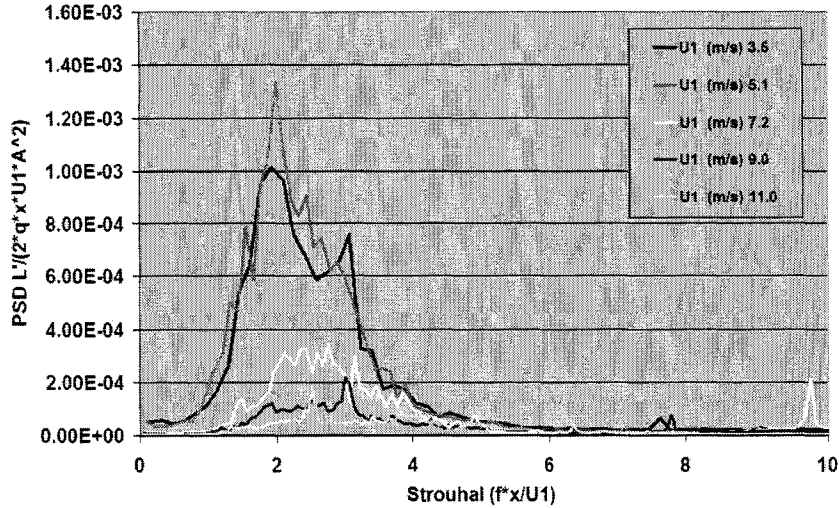


Figure 3.23: Normalized experimental  $L'_{rms}$  PSD,  $x = 1.70m$ ,  $\eta = 0.05$

$5m/s$  data sets  $\Delta St \approx 1.5$ , with the peaks at  $St \approx 2$ , agreeing well with the preceding data. Following the trends previously discussed, the  $U_1 \approx 7m/s$  case displays a reduced magnitude, while the higher speed profile magnitudes are significantly reduced. Once again the 9 and  $11m/s$  data sets have a somewhat larger  $\Delta St$ , and again display sharp, instead of broad, peaks at  $St \approx 3$ , and 3.5. The additional data presented in Appendix A shows the same trends though not always as clearly.

The normalized, variable velocity data shows a significant shift in the wings behavior for  $U_1 \geq 5m/s$ , though there appears to be good agreement between the  $U_1 \approx 3$ , and  $5m/s$  cases at each position. The trends closely mimic those discussed for the  $u'$  PSD profiles in Section 3.1.3, and likely the wing is responding in a direct manner to shear-layer forcing for  $U_1 > 5m/s$ .

#### 3.3.4 Effects of $x$ on Lift Spectra

Data profiles for varying  $x$  at fixed values of  $\eta$  and  $U_1$ , were evaluated for changes in layer growth due to the presence of the wing. The shear-layer was found, in Section

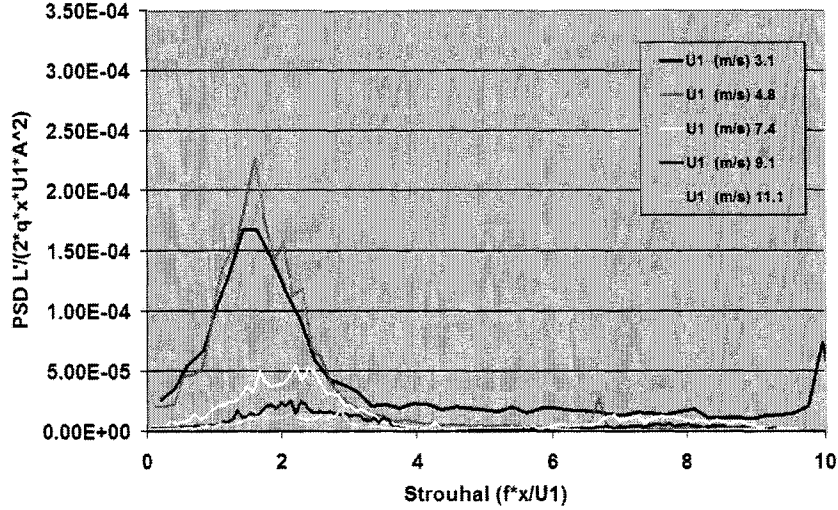


Figure 3.24: Normalized experimental  $L'_{rms}$  PSD,  $x = 1.96m$ ,  $\eta = -0.09$

3.1.3, to grow from a minimum width of  $\delta_\omega = 0.08m$  at  $x = 1.19m$  to a maximum value of  $\delta_\omega = 0.131m$  at  $x = 1.96m$ . When the thickness of the layer is compared to the chord of the wing, the ratio of  $\delta_\omega/c$  increases from  $1.1 \rightarrow 1.7$ , a factor of 1.6.

Figure 3.25 shows the data taken at  $U_1 \approx 3m/s$  for  $\eta = -0.015$ . While there is some variability in the magnitudes as well as the presence of occasional sharp peaks, it is clear that the current normalization factors account for variations in the PSD profiles with downstream position for  $U_1 \approx 3m/s$ . The remaining data in Appendix A displays the same trends.

Figure 3.26 shows that the downstream profiles for  $U_1 \approx 5m/s$  and  $\eta = 0.02$ , collapse onto each other and generally agree with the  $U_1 \approx 3m/s$  case. Data taken at the remaining values of  $\eta$  further support the trends. A departure from this is noted on the  $x = 1.19m$  profile which appears to be shifted to a slightly lower Strouhal band than the rest.

Data taken at  $U_1 \approx 7m/s$  for  $\eta = -0.015$  is displayed in Figure 3.27. Again the profiles collapse on each other when plotted on normalized axes. However the broad

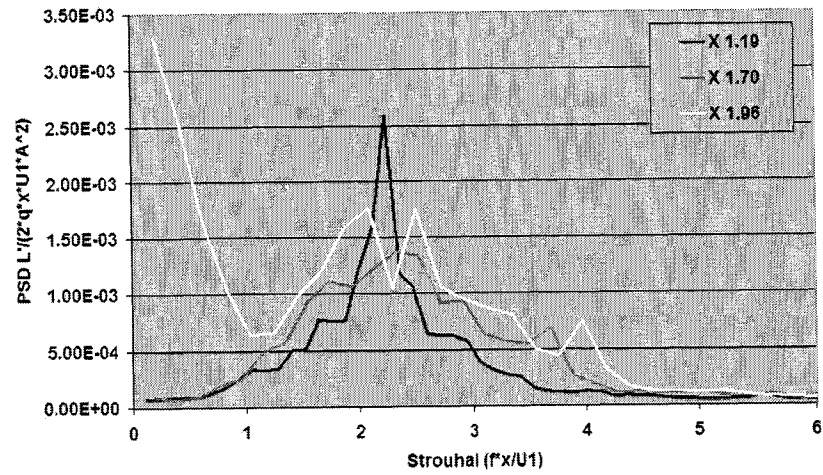


Figure 3.25: Normalized experimental  $L'_{rms}$  PSD,  $\eta = -0.015$ ,  $U_1 \approx 3m/s$

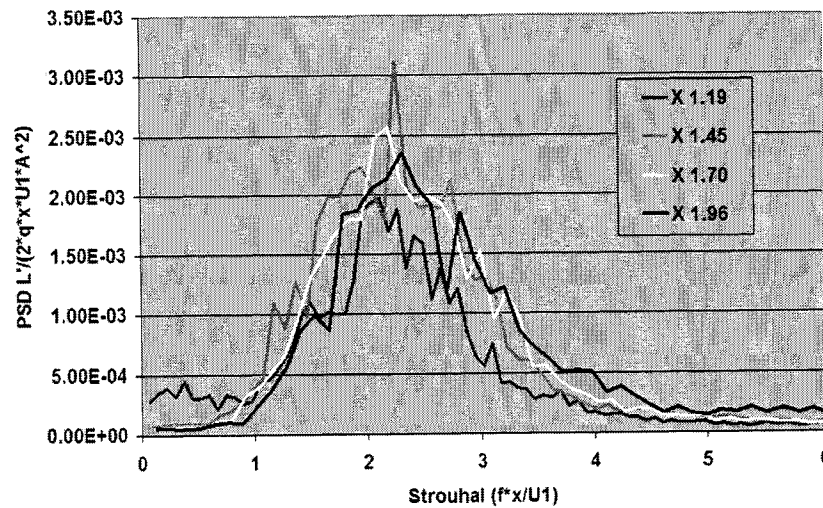


Figure 3.26: Normalized experimental  $L'_{rms}$  PSD,  $\eta = 0.02$ ,  $U_1 \approx 5m/s$

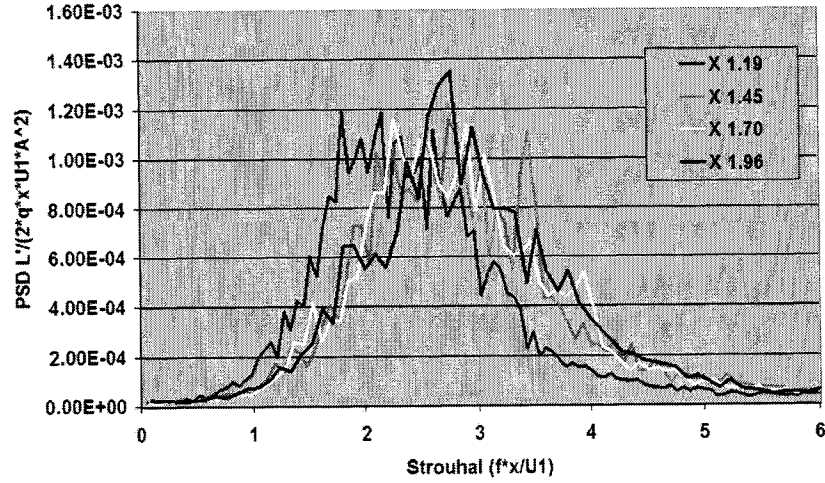


Figure 3.27: Normalized experimental  $L'_{rms}$  PSD,  $\eta = -0.015$ ,  $U_1 \approx 7m/s$

peaks appear to be centered at  $St \approx 2.5$ . Beyond the decreased magnitude and the slight shift to higher frequencies, the qualitative behavior of these PSD profiles are quite similar to those taken at lower  $U_1$ . The remaining data at  $U_1 \approx 7$  displays the same trends.

The data taken at the higher values of  $U_1$  is more poorly behaved than the data taken at lower  $U_1$ . In addition to peaks at frequency locations that are velocity insensitive, the magnitudes of the PSD profiles are reduced. Figure 3.28 shows the data for  $U_1 \approx 9m/s$ . Qualitatively there is some similarity between this data, and that at lower  $U_1$ . The magnitudes normalize well with downstream distance as does  $\Delta St$ . However, when the  $9m/s$  data is viewed on a dimensional abscissa it is apparent that there is a sharp peak at  $16Hz$  regardless of  $x$ . This peak appears at  $St = 2$  for  $x = 1.19m$ ,  $St = 2.7$  for  $x = 1.45m$ ,  $St = 3.0$  for  $x = 1.70m$ , and  $St = 3.5$  for  $x = 1.96m$ . None of the lower velocity data sets display this behavior, and it is inconsistent with free shear-layer behavior, though in agreement with forced shear-layer behavior.

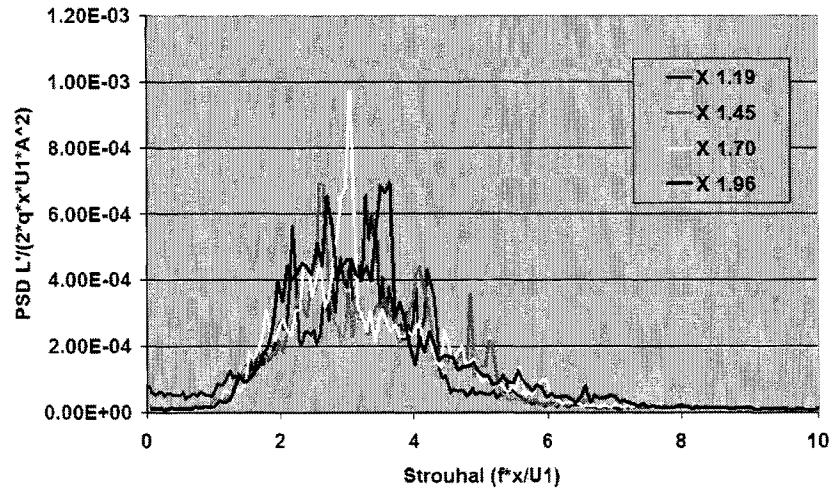


Figure 3.28: Normalized experimental  $L'_{rms}$  PSD,  $\eta = 0.02$ ,  $U_1 \approx 9m/s$

Figure 3.29 shows the data for  $U_1 \approx 11m/s$ , taken at  $\eta = 0.05$ . It is apparent that this data is even more poorly behaved than  $U_1 \approx 9m/s$  data. Sharp peaks are abundant, with none of the broad relatively smooth characteristics of the lower speed data. Further there is no consistent peak location, though  $\Delta St$  is relatively stable between 2 and 2.5. When the data is plotted on a dimensional abscissa it is apparent that, in a similar fashion to the data at  $9m/s$ , the current data displays sharp peaks insensitive to downstream positions. Peaks of varying magnitude are present at 16, 26, 30, and  $32Hz$  in each of the profiles. At  $x = 1.19$  and  $1.45m$ , the higher frequency peaks, 26, 30, and  $32Hz$ , are heavily excited, while the  $16Hz$  peak is more prominent at  $x = 1.70$  and  $1.96m$ . This presence of sharp peaks, insensitive to  $x$  is expected at this velocity, based on the previously noted wing and velocity behaviors.

### 3.3.5 $L'_{rms}$ Cross-Layer Profiles

Directly integrating the dimensional PSD profiles of  $L'$  gives  $L'_{rms}$ . Analysis of  $L'_{rms}$  vs  $y$  profiles shows that there are significant variations in behavior of  $L'_{rms}$  with

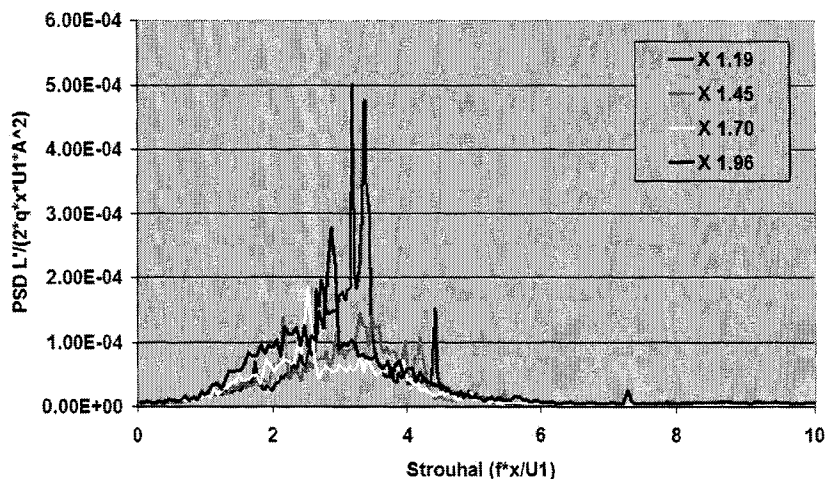
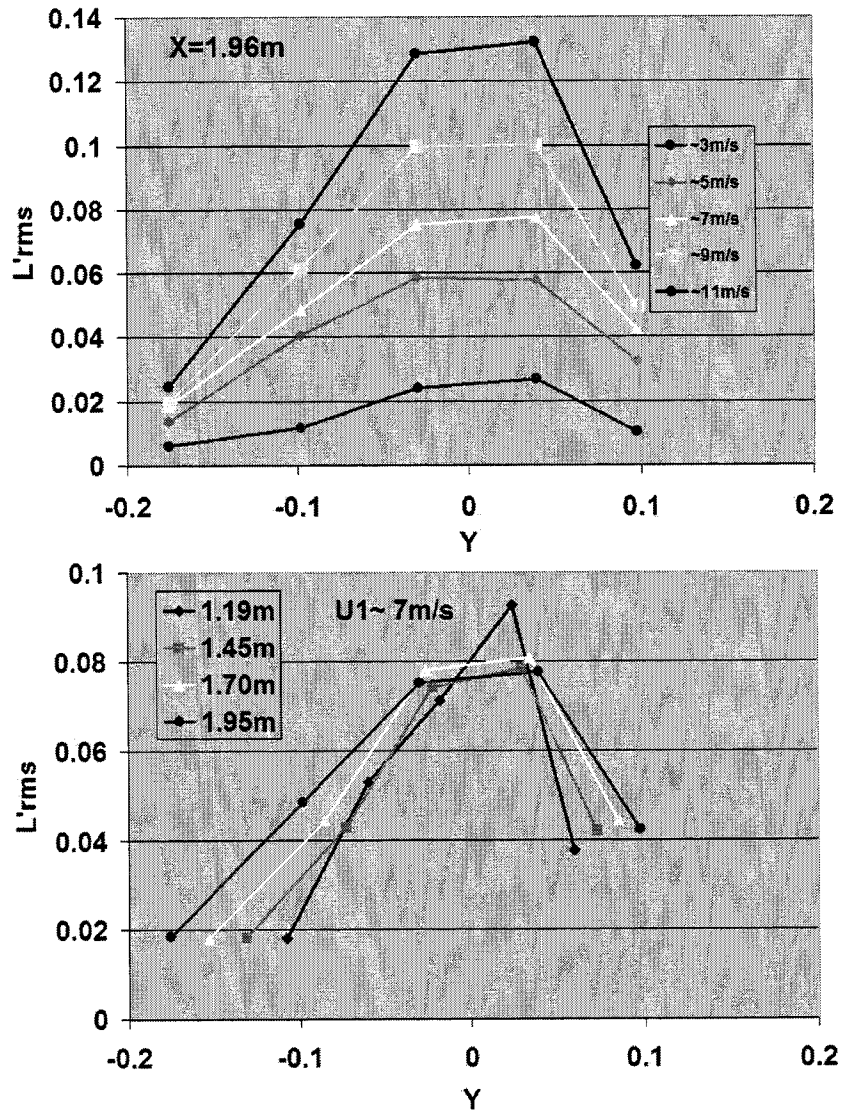


Figure 3.29: Normalized experimental  $L'_{rms}$  PSD,  $\eta = 0.05$ ,  $U_1 \approx 11m/s$

changes in  $U_1$  and  $x$ , Figure 3.30. The first of the plots shows that in general there is a significant increase in the magnitude of  $L'_{rms}$  with increasing velocity, while the second shows the spreading the profiles with increasing  $x$ . As the dimensional profiles do not collapse a normalization that accounts for changes in  $x$  and  $U_1$  is used.

This data has been calculated for each  $\eta$  and  $x$  position and presented in several forms. The first comparison investigates the effect of  $U_1$  on  $L'_{rms}$ , plotted on Figures 3.31 and 3.32, taken at  $x = 1.19$  and  $1.70m$ . Here the ordinate is  $L'_{rms}/\bar{q}A$  with  $\eta$  as the abscissa. The  $U_1 \approx 3$  and  $5m/s$  profiles are nearly identical for the two figures showing self-similarity. These figures also show that while the higher  $U_1$  profiles have generally the same shape, their magnitude is significantly reduced as expected from the normalized  $L'$  PSD profiles. Figures 3.33 and 3.34 show  $L'_{rms}(\eta)$  profiles at various  $x$  for  $U_1 \approx 5$  and  $7m/s$  respectively, and reinforce the finding that the non-steady lift profiles are self-similar. The data taken at  $U_1 \approx 3, 9$ , and  $11m/s$  displays the same behavior.

Figure 3.30:  $L'_{rms}$  raw profiles

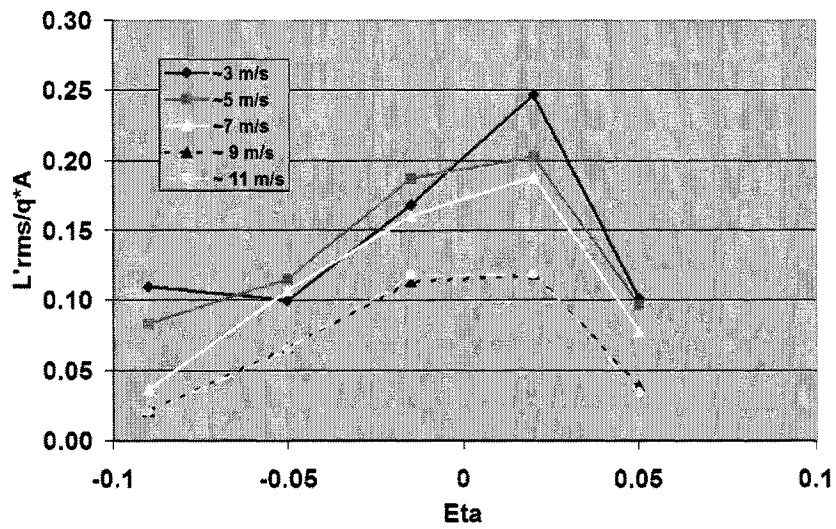


Figure 3.31: Normalized experimental  $L'_{rms}$  profile,  $x = 1.19m$

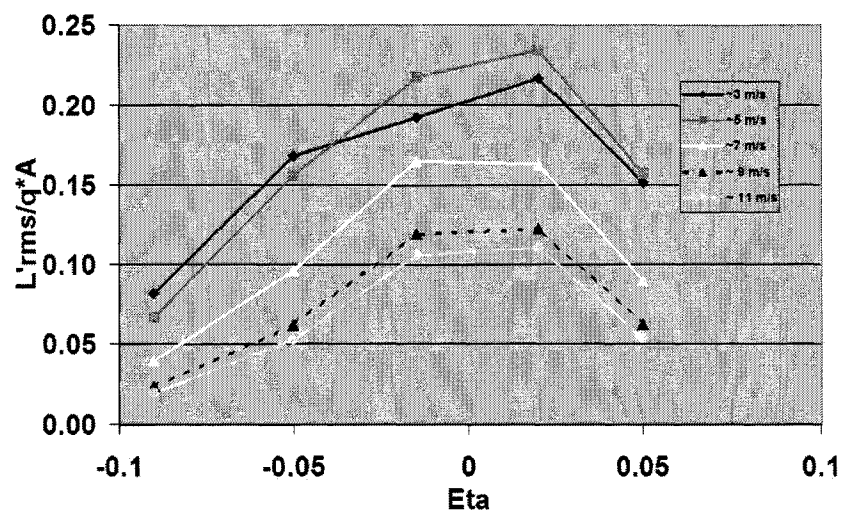


Figure 3.32: Normalized experimental  $L'_{rms}$  profile,  $x = 1.70m$

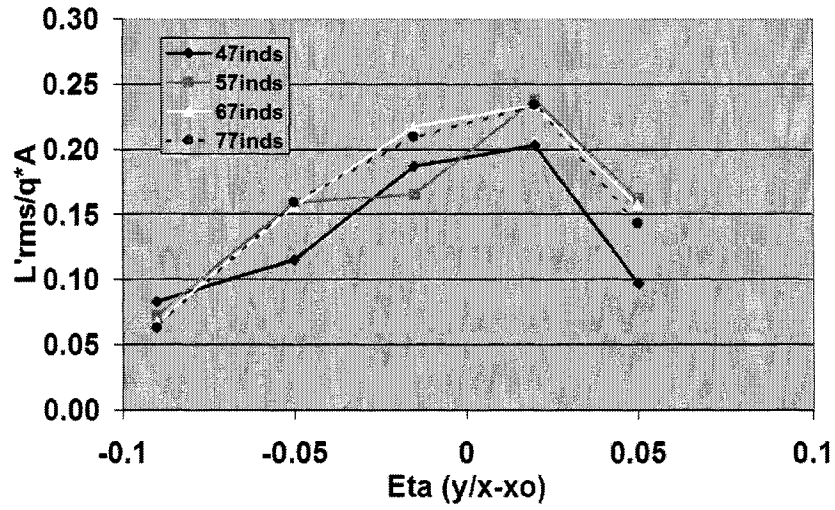


Figure 3.33: Normalized experimental  $L'_{rms}$  profile,  $U_1 \approx 5m/s$

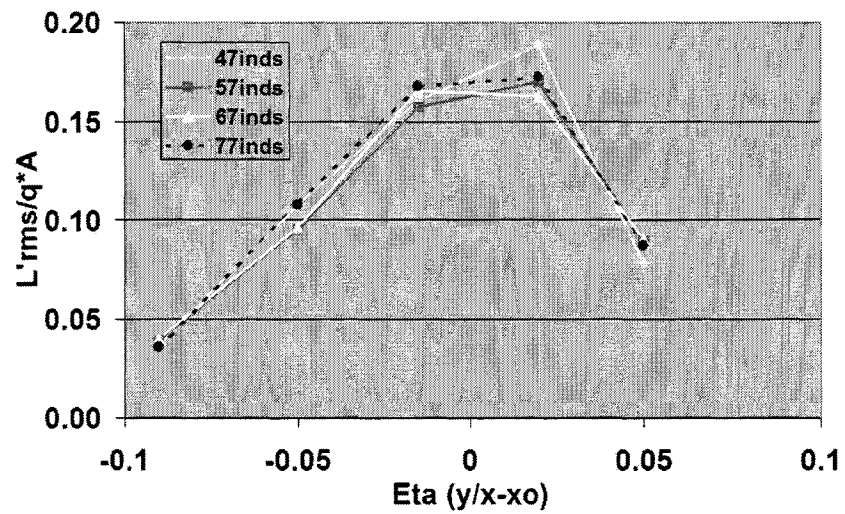


Figure 3.34: Normalized experimental  $L'_{rms}$  profile,  $U_1 \approx 7m/s$

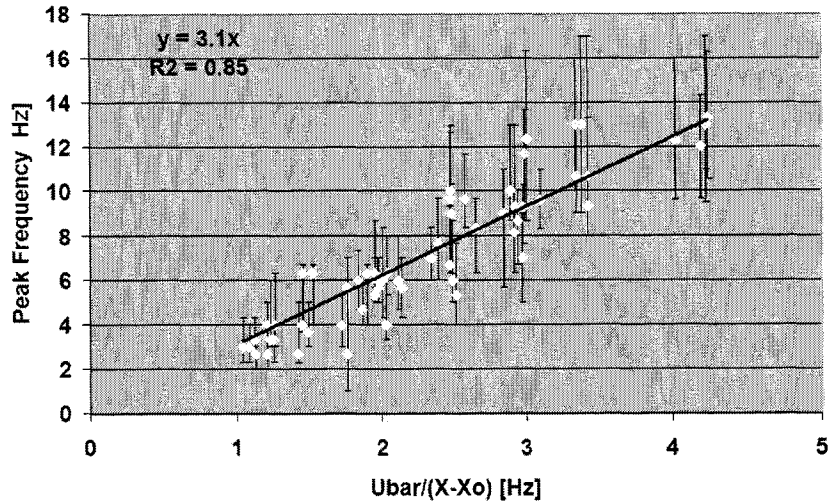


Figure 3.35: Experimental lift peak location vs normalized  $U_1$ ,  $U_1 \leq 7m/s$

### 3.3.6 Vortex Passage Frequency

The frequency constant  $K_2$  can be determined from the relationship between  $f_m$ ,  $U_1$ , and  $x - x_0$ . When there is a clear peak it is shown as a point, along with the upper and lower error bounds on the peak location. In some cases no distinct peak is present, and the peak location is estimated by averaging the upper and lower half-power points. Figure 3.35 presents the Peak Frequency vs. Velocity, normalized by downstream distance. From this data  $K_{2-lift} = 0.8$ , 5% above the value determined from  $u'$  PSD information in, Section 3.1.3.

## Chapter 4

# NUMERICAL MODELING

The flow under investigation is numerically modeled to further investigate the flow field, create a visualization tool, provide a verification method for the experimental setup, and as a method to extrapolate beyond the experimental conditions. As the flow has a single region of concentrated vorticity evolving under its own influence and interacting with a single streamlined body it is suited to Vortex Method modeling, rather than standard Reynolds Averaged Navier-Stokes solvers, Large Eddy Simulations, or Direct Numerical Simulations. The latter would require dense gridding of the entire shear-layer, wing, and wake regions, possible simulation of the wind-tunnel boundary layers, and potentially longer computational periods. Further complexity and computing power would also be needed to accurately model the time varying interactions under consideration, as well as compiling time averaged data. In contrast, through the use of a grid-free Lagrangian Vortex Method, a minimal number of computational elements are required in the form of point vortices. Upstream and downstream conditions can be treated in a theoretical sense without requiring additional calculations such as image vortices, and the wall boundary layers can be effectively ignored.

Vortex methods have been under development since their initial use by von Karman and Rubach in 1912. Various sorts have been applied to internal flows, external flows, 2-D and 3-D flows, and flows evolving in both time and space. Vortex methods have been shown to converge to the Inviscid Euler equations[34], and when the Random Walk technique proposed by Chorin is applied to model viscosity, to converge to the Navier Stokes equations[35]. They have been successfully applied to

spatially evolving 2-D shear-layers by Ashurst[36], Inoue[18], Inoue and Leonard[37], Basu et. al.[38], and to 3-D layers by Ashurst and Meiburg[39] and others. In general these researchers have found reasonable agreement with experimental data for average spreading rates, mean profiles of downstream velocity, the rms fluctuating velocities  $u'_{rms}$ ,  $v'_{rms}$ , and  $w'_{rms}$ , Reynolds stresses, and in some cases higher order moments as well[38]. In addition good qualitative agreement has been found with the evolution of coherent structures and the dynamics of shear-layer growth including pairing, tearing, and tripling, and the formation of 3-D braid structures. Finally the frequency distribution of velocity fluctuations observed in forced shear-layers, as well as the qualitative evolution of forced shear-layers has been modeled by Ghoniem and Ng[25] and others. Vortex methods have also been successfully applied to the BVI problem by several researchers including Qian and Vezza[31], Panaras[30], and Poling, Dadone, and Telionis[29], with good agreement with experiments noted for the timing of lift variations in the rotor and in some cases for the magnitude of those variations as well. This type of modeling has also been successfully applied to more general fluid-structure interactions by Blevins[40] and others, again finding reasonable agreement with theory and experiments.

#### **4.1 Vortex Method Development**

The flow field under consideration can be broken up into three distinct regions that will need to be modeled for accurate formulation of the shear-layer/wing interaction problem: the flow upstream of the splitter plate termination, the evolving region of the shear-layer, wing, and wake, and the flow downstream of the region of interest, Figure 4.1. A successful model will need to account for: the velocity discontinuity upstream of the modeled region, the creation of vorticity at the shear-layer origin, the initial vorticity distribution in the modeled region, the presence of the wind-tunnel walls, the vorticity distribution downstream of the model, viscous effects, time integration, the presence of the wing and the creation of vorticity in its wake.

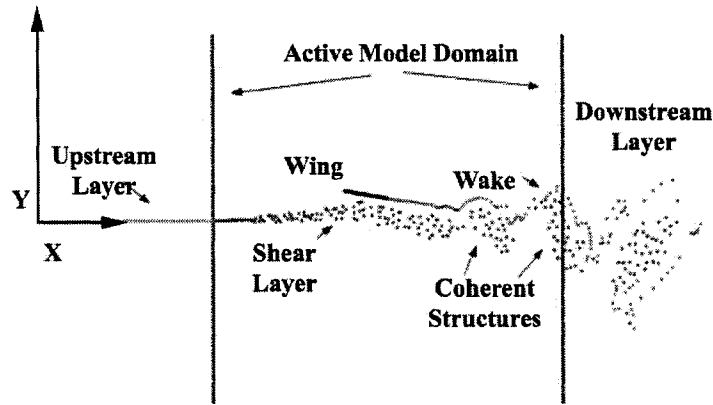


Figure 4.1: Numerical flow field

#### 4.1.1 Shear-Layer Vortices

Vorticity creation at the origin has been previously investigated in three different fashions. Ashurst[39], Inoue[18][41], and Inoue and Leonard[37] have all injected individual vortex particles of fixed core size either at the origin or a short distance downstream of the origin. These particles are then allowed to freely convect into the shear-layer. Ghoniem and Ng[25] utilized  $N_0$  particles per time step placed in a linear distribution between the origin and  $x = \bar{U}\Delta t$  where  $\Delta t$  is the size of the numerical time step in seconds. While this is more accurate than representing the shed vorticity as a single particle at each time step, it increases the number of vortices by a factor of  $N_0$ , and the number of calculations per time step by  $N_0^2$ . It's overall effect is an accuracy increase similar to decreasing the size of the time step to  $\Delta t/N_0$ . Basu et. al.[38] investigated the effect of utilizing vortex sheets instead of particles. Instead of a single particle being shed into the flow field an additional vortex sheet element is created between the origin and  $x = \bar{U}\Delta t$ , with a new node created at the downstream edge of the sheet element. As all the vorticity injection methods are quite similar, the current model adopts the simpler technique of Ashurst and Inoue, wherein a single vortex particle is injected at  $x = \bar{U}\Delta t/2$  on the  $x$  axis at each time step.

Several techniques have been utilized to treat the vorticity distribution within the flow during model startup. For the calculations of Inoue[18][41] and Inoue and Leonard[37], at  $t = 0$ , no vortices were present downstream of the origin, and the flow was allowed to evolve only from the vortices injected at the origin during each time step. While this technique accurately describes the start up process, a large number of time steps are needed to reach a quasi-steady-state, as vorticity is not initially present in the entire flow field, and must be convected in from the origin. Initially a large starting vortex is formed from the vortex elements shed at the beginning of the computation. This starting vortex does not grow evenly along the stream-wise axis due to the asymmetric effect of the vorticity sheet upstream of the layer. It must first convect out of the computational domain, and the flow allowed to relax to its quasi-steady-state configuration. This requires longer computational runs as statistical data on the fully developed shear-layer can only be collected after the startup period. Basu et. al.[38] initially utilized a vortex sheet along the  $x$  axis. This vortex sheet is discretized into flat sections between nodes, with a perturbation of the form

$$y = A_0 \sin\left(\frac{2\pi x}{W_0}\right), \quad (4.1)$$

where  $A_0$  and  $W_0$  are the amplitude and wavelength of the perturbation. The process of the layer rolling up into coherent structures is accelerated by providing an initial perturbation to the vorticity sheet. In addition, the settling time necessary for the flow to relax into quasi steady state is reduced as the effects of the asymmetric starting vortex growth are not present. Following the work of Basu et. al., the current model will discretize the vorticity within the computational domain into a series of vortex particles placed along a perturbed waveform of the type created by Equation 4.1, to minimize startup time.

#### 4.1.2 Model Boundary Treatments

Simplifications are sought to minimize the number of computations and iterations necessary to achieve a fully developed flow. The first is an accurate way to model the fluid upstream of the splitter termination that preserves the velocity discontinuity between the two streams and its effect on the modeled region. Typically a vorticity sheet of strength per unit length  $\gamma = \Delta U/2$  is utilized to generate the velocity jump between the streams. Ashurst[39] modeled the vorticity sheet through a series of discrete vortices with finite core size,  $\sigma$ , below which the induced velocity becomes constant and with each particle having a fixed circulation strength  $\kappa = \Delta U H = \Delta U \bar{U} \Delta t$ . While Ashurst did not specify the number of vortices upstream of the shear-layer origin that were utilized, Inoue[18][41] utilized a similar treatment with 400 vortices for both 2-D and 3-D calculations. While this model preserves the strength of the vorticity sheet necessary to create the appropriate velocity jump, it only does so in the mean as there will be local velocity jumps in the vicinity of the point vortices. Further, it increases the number of calculations necessary at each time step by approximately  $400N$  where  $N$  is the number of freely convecting vortices in the flow field.

An alternate treatment was developed by Basu et. al.[38] who modeled the upstream region as a vorticity sheet of constant strength per unit length of  $2\gamma$ , with a superimposed doublet sheet to ensure zero normal velocity on the surface. As velocity fluctuations normal to the splitter are strongest near the origin, the doublet sheet does not extend upstream to  $-\infty$  but only a fixed distance. This sheet is discretized into  $N_D$  elements whose strength is solved for at each time step to satisfy the boundary condition at the midpoint of each element, subject to the velocity induced by the current flow field. While this formulation is more accurate, it increases the number of calculations necessary at each iteration by  $N_D^2 + N_D N$ .

Ghoniem and Ng, in their investigation of forced shear-layers chose to model the

splitter plate through conformal mapping and boundary layers. While again, this is more accurate than the model utilized by Ashurst and Inoue, it requires additional vortices be used to model the boundary layers, resulting in an increased computational load.

After considering these references a vortex sheet model was chosen in the manner of Basu et. al, however the vortex sheet is modeled analytically instead of discretely. This minimizes computational loads while preserving the mean effect of the velocity discontinuity. The doublet sheet is neglected due to its minimal effect on the evolution of the layer in the self-similar downstream region.

The effect of walls on the evolution of the numerical shear-layer has been investigated by Inoue and Leonard[37], Inoue[41], and Ghoniem and Ng[25]. Inoue and Leonard found better agreement with experimental data when walls were considered in their flow calculations. However, the more recent work of Ghoniem and Ng determined that wall boundary layers do not have a significant effect on the evolution of coherent structures until the structures impinge on the boundary layer. Modeling of the wall layers will be neglected in the present study as intersection between the shear and wall boundary layers occurs downstream of the test section.

The final model boundary is at the downstream edge of the computational region. While the most consistent models track all of the vortex particles for the entire computational time, this becomes computationally intensive as the number of calculations per time step goes as  $N^2$ , while the number of vortices increases by one with each additional time step. Four treatments have been considered to increase code efficiency: tracking all vortices in the flow-field for the entire computational run[39][18], applying a cutoff well downstream of the computational zone of interest and deleting vortices as they cross this boundary[37][41][25], deleting the vortices after passing the downstream boundary but replacing their mean effect with a series of vortex sheets extending downstream[38], and amalgamating the vortices into increasingly large concentrations of vorticity after they have passed the downstream

boundary[31].

The first option was ruled out due to the computational time required. While the second option is this most computationally efficient, it leads to an offset in the position of the numerical layer relative to the experimental layer due to the asymmetric effect of modeling the upstream vorticity sheet but not the downstream sheet. The remaining options are qualitatively similar. Both maintain the vorticity distribution downstream of the primary computational domain, and thus the mean velocity profiles. The amalgamation scheme also preserves the non-steady dynamics of the large scale structures as they convect out of the computational domain, however it is not as computationally efficient as replacing the downstream region with a series of analytically evaluated vortex sheets. Preservation of the mean effects of the region outside of the computational domain is deemed sufficient for the current model. The effect of the layer downstream of the domain will be modeled with a vorticity distribution that retains the self-similar velocity profiles as well as the net vorticity per unit length of the layer, while neglecting the non-steady effects in a manner similar to Basu et. al[38].

#### *4.1.3 Wing and Wake Modeling*

Modeling of bodies in the flow field has been investigated primarily with regard to the BVI problem, as well as more general cases by Blevins[40]. The primary techniques are transforms, surface distributions of singularities, and panel methods. Transforms are typically utilized to achieve a zero normal velocity along the body surface, while a vorticity boundary layer is created along the surface to achieve zero tangential velocity. This technique has been employed by numerous researchers including Panaras[30] and Poling et. al[29]. The boundary layer vortices are convected along the body and released into the flow, typically at the point of boundary layer separation, or the airfoil trailing edge. Alternatively, vortex panel methods are simpler, capable of representing arbitrary shapes, and require no change in the computational algorithm.

The surface of the body is discretized into a series of panels, each represented by a concentrated or distributed singularity. The strength of the singularity is determined at each time step by satisfying the boundary conditions at one location per panel. Typically concentrated vortices, or vortex panels are utilized[40],[31] though doublet panels were utilized to partially represent a splitter plate by Basu et. al[38]. For the numerical model at hand a flat plate is modeled through a vortex panel method of the type discussed by Katz and Plotkin[42]. Each panel is represented by a single point vortex, treated with the core model, located at the 1/4 panel-chord point. The non-porous boundary condition is then solved for at the 3/4 panel-chord point.

#### *4.1.4 Time Integration and Viscosity Treatment*

The choice of a time integration scheme is less clear as several have been found effective. Inoue[18][41], Inoue and Leonard[37], Basu et. al[38], and Ashurst[36] opted to use the computationally efficient first-order, forward-Euler scheme. While this scheme is inherently less accurate than higher resolution schemes Inoue[18] reported that this inaccuracy induces a numerical viscosity. This numerical viscosity has similar properties to “turbulent viscosity”, and thus the model effectively simulates high Reynolds number flows. However, Ghoniem and Ng[25] felt that a higher-order integration scheme was necessary. Qian and Vezza[31] opted for a second order Adams-Bashforth time integration scheme for their BVI research. Preliminary numerical research revealed that the first-order forward Euler scheme is insufficient for the BVI problem as the numerical errors result in radial expansion of the impinging vortices. However as shear-layers grow with downstream distance this is not critical inaccuracy, and a first order forward Euler scheme will be used.

The dynamics of the large coherent structures is effectively inviscid, however viscous effects are still present in the smaller scales and contribute to initial roll-up and layer growth. Viscous treatments typically take on two forms, treatment of the finite size vortex core and treatment of viscous diffusion. Point vortices are inaccurate due

to the singularity in induced velocity at their core. To negate this singularity a core function needs to be applied, whereby within the core radius  $\sigma$ , the induced velocity remains finite. Several velocity distributions have been considered: Chorin[35] chose a constant value equal to the induced velocity at the outer edge of the vortex core. A second technique is to use a Rankine core where the induced tangential velocity varies directly with distance from the center[25]. Various other researchers have used Gaussian cores, the Scully model[31], and cores that evolve in time or “age”[43] increasing in radius over time to model viscous diffusion. There appears to be little difference between these models, though vortex aging better simulates viscous core diffusion. The Rankine core is often utilized to represent finite core vortices[44], and will be utilized in the current model. Viscous diffusion is often modeled through perturbation of vortex core positions in the manner suggested by Chorin[35]. Chorin’s “Random Walk” technique perturbs the core position by a random direction and magnitude with zero mean, and a Gaussian distribution[31][39][25][40]. This has been found effective in its standard form and will be utilized in the current model.

Figure 4.2 shows many aspects of the final numerical model. The upstream vorticity distribution is modeled as an analytical sheet, while the downstream region is modeled by a collection of inclined vorticity sheets, with a Gaussian distribution of circulation per unit length tailored so that the flow upstream and downstream of the boundary exhibit the same mean velocity profiles. Further, boundary layers on the wing surfaces are neglected, and vorticity will only be injected into the flow at the trailing edge. At each time step a wake vortex located a distance  $\bar{U}\Delta t/2$  downstream of the trailing edge is inserted. The strength of this vortex is calculated at the same time as the strength of the vortices bound to the wing, and determined by application of Kelvin’s circulation theorem[44] to the wing and wake.

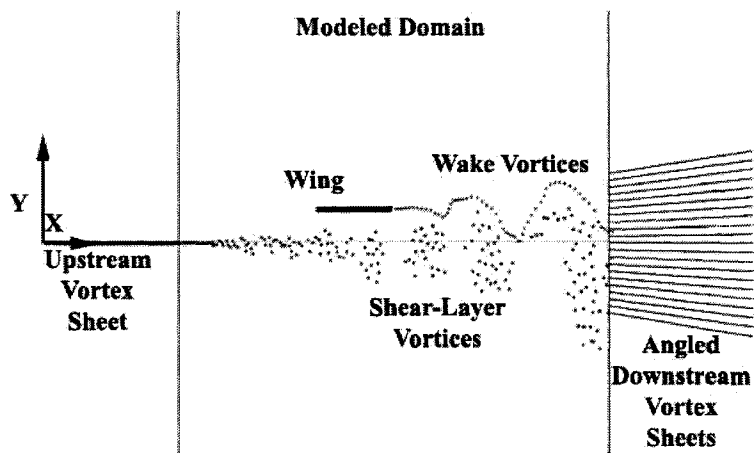


Figure 4.2: Finalized numerical flow field

## 4.2 Mathematical Formulation

With the theoretical aspects of the computational model determined the formulation of the specific mathematical relationships and numerical schemes can be undertaken. The progress of the numerical model through each time step can be broken into four steps: initiation, wing and wake vortex strength determination, vortex convection, and lift determination.

The initiation and convection steps require minimal discussion. At the beginning of each step a new wake vortex of unknown strength is injected a distance of  $h = \bar{U} \Delta t / 2$  downstream of the wings trailing edge, and a new shear-layer vortex is injected a distance of  $h$  downstream of the shear-layer origin. The strength of the shear-layer vortex is fixed, by the rate of vorticity flow from the upstream sheet into the model,  $\Gamma_s = \Delta U \bar{U} \Delta t$ . As the forward Euler scheme has been chosen for time integration, the convection step is straight forward. Once the local velocity at the core of each of the vortex particles has been determined, the velocity is multiplied by,  $\Delta t$ , and the vector result added the current position of the vortex,

$$\vec{x}_k^{Q+1} = \vec{x}_k^Q + \vec{U}_k^Q \Delta t, \quad (4.2)$$

where the superscript  $Q$  denotes the current time step,  $Q + 1$  the next time step,  $\vec{x}_k$  is the position of vortex  $k$ , and  $U_k$  the velocity of vortex  $k$ . During this step, Chorin's Random Walk is also applied, and small random direction and magnitude perturbation is added to the updated vortex position.

#### 4.2.1 Local Velocity Determination

Both the convection and wing/wake vortex strength determination steps share the need to determine the local velocity at a general point. The 2-D version of the Biot-Savart law, Equation 4.2 relates the velocity at any point in the flow,  $\vec{x}_k$ , to the vorticity at a second point in the flow  $\vec{x}$ . By integrating over the entire vorticity containing domain  $D$ , the velocity at  $\vec{x}_k$  can be determined[44].

$$\vec{u}(\vec{x}_k) = \frac{1}{2\pi} \int_D \frac{\omega(\vec{x})(\vec{x} - \vec{x}_k)}{|\vec{x} - \vec{x}_k|^3} dA, \quad (4.3)$$

where  $\omega(\vec{x})$  is the vorticity at the point  $\vec{x}$ , and  $\vec{u}(\vec{x}_k) = u\vec{i} + v\vec{j}$  is the velocity at the point  $\vec{x}_k$ . The determination of the velocity at each point is best accomplished by dividing up the domain to take advantage of the analytical nature of several of the sub-domains, and the constant strength shear-layer vortices

$$\vec{V}_k(\vec{x}) = \vec{V}_{k1} + \vec{V}_{k2} + \vec{V}_{k3} + \vec{V}_{k4} + \vec{V}_{k5} = \frac{1}{4\pi} \int_{D_1+D_2+D_3+D_4+D_5} \frac{\omega(\vec{x})(\vec{x} - \vec{x}_k)}{|\vec{x} - \vec{x}_k|^3} dA. \quad (4.4)$$

$D_1$  represents the area surrounding the splitter plate upstream of the origin,  $D_2$  the area downstream of the computational domain,  $D_3$  the freely evolving vortices in the shear-layer,  $D_4$  the freely evolving vortices in the shed wake, and  $D_5$  the vortex-panels representing the wing. The integrated effect of these domains is represented by the individual velocity components  $\vec{V}_{k1}$  through  $\vec{V}_{k5}$ . While  $D_1$  and  $D_2$  can all

be evaluated analytically,  $D_3$ ,  $D_4$ , and  $D_5$  must all be evaluated discretely as the vorticity is concentrated into discrete vortex particles.

Writing Equation 4.2 over  $D_1$  with circulation per unit length of the vorticity sheet  $\gamma_u = \Delta U$ , from  $x = -\beta_1 \rightarrow 0$  along the  $y$  axis gives

$$\vec{V}_{k1}(\vec{x}) = \frac{\gamma_{D_1}}{2\pi} \int_{-\beta_1}^0 \frac{(\vec{x} - \vec{x}_k)}{|\vec{x} - \vec{x}_k|^3} ds. \quad (4.5)$$

This expression can be integrated[42] with  $\vec{V}_{k1} = (u_k \vec{i} + v_k \vec{j})_1$  to yield an analytical expression for the velocity at a point induced by the splitter plate

$$\vec{V}_{k1} = \frac{\gamma_u}{2\pi} \left( \left[ \tan^{-1} \frac{y_k}{x_k} - \tan^{-1} \frac{y_k}{x_k - \beta_1} \right] \vec{i} + \frac{1}{2} \ln \left[ \frac{x_k^2 + y_k^2}{(x_k - \beta_1)^2 + y_k^2} \right] \vec{j} \right). \quad (4.6)$$

Performing a similar series of operations on the vortex sheets in  $D_2$  results in the more complex formulation for the downstream region. Defining a new coordinate system relative to the individual downstream vortex sheet under consideration, sheet  $l$ , with the leading edge at  $\vec{x}_l = x_l \vec{i}_l + y_l \vec{j}_l$  where

$$\begin{aligned} x_l &= \Delta X \cos \Phi_l + \Delta Y \sin \Phi_l \\ y_l &= -\Delta X \sin \Phi_l + \Delta Y \cos \Phi_l, \end{aligned} \quad (4.7)$$

where  $\Delta X = x_k - \beta_2$  and  $\Delta Y = y_k - Y_l$ .  $\beta_2$  is defined as the downstream distance at which the vorticity sheet is initiated, and  $y_l$  is the height of the leading edge of vortex sheet  $l$ .  $\beta_2$  is a constant for all of the downstream vortex sheets.  $Y_l$  is dependant on the angle of inclination of the vortex sheet  $\Phi_l$  and the distance between  $\beta_2$  and the downstream vortex sheet emanation point. Based on this formulation, the velocity induced in the shear-layer origin-centered reference frame can be most compactly expressed as

$$\vec{V}_{kl} = u_l \vec{i} + v_l \vec{j}, \quad (4.8)$$

where  $\vec{V}_{kl}$  is the velocity induced by vortex sheet  $l$ . The velocity induced by all of the downstream vortex sheets is

$$\vec{V}_{k2} = \sum_1^l \vec{V}_{kl}. \quad (4.9)$$

Where

$$u_l = \left(\frac{\gamma_l}{2\pi}\right) \left[ \tan^{-1}\left(\frac{x_l}{y_l}\right) - \tan^{-1}\left(\frac{y_l}{x_l - \left(\frac{\beta_3 - \beta_2}{\cos \Phi_l}\right)}\right) \cos \Phi_l - \frac{1}{2} \ln \frac{(x_l - \left(\frac{\beta_3 - \beta_2}{\cos \Phi_l}\right))^2 + y_l^2}{x_l^2 + y_l^2} \sin \Phi_l \right], \quad (4.10)$$

$$v_l = \left(\frac{\gamma_l}{2\pi}\right) \left[ \tan^{-1}\left(\frac{x_l}{y_l}\right) - \tan^{-1}\left(\frac{y_l}{x_l - \left(\frac{\beta_3 - \beta_2}{\cos \Phi_l}\right)}\right) \sin \Phi_l + \frac{1}{2} \ln \frac{(x_l - \left(\frac{\beta_3 - \beta_2}{\cos \Phi_l}\right))^2 + y_l^2}{x_l^2 + y_l^2} \cos \Phi_l \right]. \quad (4.11)$$

where  $\beta_3$  is the downstream extent of the vortex sheets, and  $\gamma_l$ , the circulation strength per unit length of sheet  $l$ . This gives,

$$\begin{aligned} \vec{V}_{k2} &= \sum_1^l \left[ u_l \vec{i} + v_l \vec{j} \right] = \\ &\sum_1^l \left[ \left( \left(\frac{\gamma_l}{2\pi}\right) \left[ \tan^{-1}\left(\frac{x_l}{y_l}\right) - \tan^{-1}\left(\frac{y_l}{x_l - \left(\frac{\beta_3 - \beta_2}{\cos \Phi_l}\right)}\right) \cos \Phi_l - \frac{1}{2} \ln \frac{(x_l - \left(\frac{\beta_3 - \beta_2}{\cos \Phi_l}\right))^2 + y_l^2}{x_l^2 + y_l^2} \sin \Phi_l \right] \right) \vec{i} + \right. \\ &\left. \left( \left(\frac{\gamma_l}{2\pi}\right) \left[ \tan^{-1}\left(\frac{x_l}{y_l}\right) - \tan^{-1}\left(\frac{y_l}{x_l - \left(\frac{\beta_3 - \beta_2}{\cos \Phi_l}\right)}\right) \sin \Phi_l + \frac{1}{2} \ln \frac{(x_l - \left(\frac{\beta_3 - \beta_2}{\cos \Phi_l}\right))^2 + y_l^2}{x_l^2 + y_l^2} \cos \Phi_l \right] \right) \vec{j} \right]. \end{aligned} \quad (4.12)$$

Extending the vortex sheets downstream to  $\infty$  was considered but the integrals become unbounded.

For the discrete portions of the model Equation 4.2 must be altered from an analytical expression to its discrete counterpart. For a 2-D point vortex

$$\vec{V} = \frac{\Gamma_v}{2\pi} \left[ \frac{-(y - y_v)\vec{i} + (x - x_v)\vec{j}}{(x - x_v)^2 + (y - y_v)^2} \right], \quad (4.13)$$

where the vortex is located at  $\vec{x}_v = x_v\vec{i} + y_v\vec{j}$ , with vortex strength  $\Gamma_v$ , inducing velocity  $\vec{V}$ . For the sub-domain  $D_3$  the vortices are numbered from  $m = 1 \rightarrow N_s$ , where  $N_s$  is the number of shear-layer vortices in the computational domain. Writing equation 4.12 for all of the vortices in  $D_3$  results in

$$\vec{V}_{k3} = \left(\frac{\Gamma_s}{2\pi}\right) \sum_{m=1}^{N_s} \left[ \frac{-(y_v - y_k)\vec{i} + (x_v - x_k)\vec{j}}{(x_v - x_k)^2 + (y_v - y_k)^2} \right]. \quad (4.14)$$

The vortices contained in  $D_4$  are numbered from  $w = 1 \rightarrow N_w$ , where  $w=1$  represents the wake vortex shed at time  $t = \Delta t$  and  $N_w$  is the number of the newly formed wake vortex. In a manner similar to that employed in  $D_3$ , any vortices leaving the computational domain are deleted, while a new vortex is inserted at  $x_{N_w} = x_{le} + C + h$  where  $x_{le}$  is the downstream position of the wings leading edge. The strength of the vortex shed will be discussed in Section 4.2.2. The circulation of each wake vortex  $\Gamma_w$  is constant once created, but varies between vortices. Integration of the Biot-Savart law over  $D_4$  results in

$$\vec{V}_{k4} = \sum_{w=1}^{N_w} \left(\frac{\Gamma_w}{2\pi}\right) \left[ \frac{-(y_w - y_k)\vec{i} + (x_w - x_k)\vec{j}}{(x_w - x_k)^2 + (y_w - y_k)^2} \right], \quad (4.15)$$

where the position of the wake vortex is given by  $x_w\vec{i} + y_w\vec{j}$ .

The strength of the vortices bound to the wing,  $\Gamma_b$ , vary from time step to time step in order to satisfy the zero normal velocity condition at the control points. The expression for the contribution of this sub domain to the velocity at  $\vec{x}_k$  can be expressed as

$$\vec{V}_{k5} = \sum_{b=1}^{N_b} \left( \frac{\Gamma_b}{2\pi} \right) \left[ \frac{-(y_b - y_k)\vec{i} + (x_b - x_k)\vec{j}}{(x_b - x_k)^2 + (y_b - y_k)^2} \right], \quad (4.16)$$

where  $N_b$  is the number of wing panels, and bound vortices.

Combining the expressions for the velocity induced at a point  $\vec{x}_k$  by the various domains with the flow field, Equations 4.3, 4.6, 4.13, 4.14 and 4.15, results in the net induced velocity at  $\vec{x}_k$ . Adding the effect of the mean flow on the system,  $\vec{U} = \frac{U_1 + U_2}{2} \vec{i}$  produces the relationship for the net induced velocity at a general point within the flow-field, Equation 4.16.

$$\begin{aligned} \vec{V}_k = & \frac{\gamma_u}{2\pi} \left( \left[ \tan^{-1} \frac{y_k}{x_k} - \tan^{-1} \frac{y_k}{x_k - \beta_1} \right] \vec{i} + \frac{1}{2} \ln \left[ \frac{x_k^2 + y_k^2}{(x_k - \beta_1)^2 + y_k^2} \right] \vec{j} \right) + \\ & \sum_{l=1}^l \left[ \left( \left( \frac{\gamma_l}{2\pi} \right) \left[ \tan^{-1} \left( \frac{x_l}{y_l} \right) - \tan^{-1} \left( \frac{y_l}{x_l - \left( \frac{\beta_3 - \beta_2}{\cos \Phi_l} \right)} \right) \cos \Phi_l - \frac{1}{2} \ln \frac{(x_l - \left( \frac{\beta_3 - \beta_2}{\cos \Phi_l} \right))^2 + y_l^2}{x_l^2 + y_l^2} \sin \Phi_l \right] \right) \vec{i} + \right. \\ & \left. \left( \left( \frac{\gamma_l}{2\pi} \right) \left[ \tan^{-1} \left( \frac{x_l}{y_l} \right) - \tan^{-1} \left( \frac{y_l}{x_l - \left( \frac{\beta_3 - \beta_2}{\cos \Phi_l} \right)} \right) \sin \Phi_l + \frac{1}{2} \ln \frac{(x_l - \left( \frac{\beta_3 - \beta_2}{\cos \Phi_l} \right))^2 + y_l^2}{x_l^2 + y_l^2} \cos \Phi_l \right] \right) \vec{j} \right] + \\ & \left( \frac{\Gamma_s}{2\pi} \right) \sum_{m=1}^{N_s} \left[ \frac{-(y_v - y_k)\vec{i} + (x_v - x_k)\vec{j}}{(x_v - x_k)^2 + (y_v - y_k)^2} \right] + \\ & \sum_{w=1}^{N_w} \left( \frac{\Gamma_w}{2\pi} \right) \left[ \frac{-(y_w - y_k)\vec{i} + (x_w - x_k)\vec{j}}{(x_w - x_k)^2 + (y_w - y_k)^2} \right] + \\ & \sum_{b=1}^{N_b} \left( \frac{\Gamma_b}{2\pi} \right) \left[ \frac{-(y_b - y_k)\vec{i} + (x_b - x_k)\vec{j}}{(x_b - x_k)^2 + (y_b - y_k)^2} \right] + \\ & \frac{U_1 + U_2}{2} \vec{i} \end{aligned} \quad (4.17)$$

This full expression is evaluated to determine the velocity induced on each of the vortex particles prior to the convection step within the model. In addition a modified version which does not include the effect of the wing or the newly formed wake vortex is applied during determination of the wing and newly formed wake vortex strengths,

$$\begin{aligned}
\vec{V}_c = & \frac{\gamma_u}{2\pi} \left( \left[ \tan^{-1} \frac{y_k}{x_k} - \tan^{-1} \frac{y_k}{x_k - \beta_1} \right] \vec{i} + \frac{1}{2} \ln \left[ \frac{x_k^2 + y_k^2}{(x_k - \beta_1)^2 + y_k^2} \right] \vec{j} \right) + \\
\sum_1^l & \left[ \left( \left( \frac{\gamma_l}{2\pi} \right) \left[ \tan^{-1} \left( \frac{x_l}{y_l} \right) - \tan^{-1} \left( \frac{y_l}{x_l - \left( \frac{\beta_3 - \beta_2}{\cos \Phi_l} \right)} \right) \cos \Phi_l - \frac{1}{2} \ln \frac{(x_l - \left( \frac{\beta_3 - \beta_2}{\cos \Phi_l} \right))^2 + y_l^2}{x_l^2 + y_l^2} \sin \Phi_l \right] \right) \vec{i} + \right. \\
& \left. \left( \left( \frac{\gamma_l}{2\pi} \right) \left[ \tan^{-1} \left( \frac{x_l}{y_l} \right) - \tan^{-1} \left( \frac{y_l}{x_l - \left( \frac{\beta_3 - \beta_2}{\cos \Phi_l} \right)} \right) \sin \Phi_l + \frac{1}{2} \ln \frac{(x_l - \left( \frac{\beta_3 - \beta_2}{\cos \Phi_l} \right))^2 + y_l^2}{x_l^2 + y_l^2} \cos \Phi_l \right] \right) \vec{j} \right] + \\
& \left( \frac{\Gamma_s}{2\pi} \right) \sum_{m=1}^{N_s} \left[ \frac{-(y_v - y_k) \vec{i} + (x_v - x_k) \vec{j}}{(x_v - x_k)^2 + (y_v - y_k)^2} \right] + \\
& \sum_{w=1}^{N_w - 1} \left( \frac{\Gamma_w}{2\pi} \right) \left[ \frac{-(y_w - y_k) \vec{i} + (x_w - x_k) \vec{j}}{(x_w - x_k)^2 + (y_w - y_k)^2} \right] + \\
& \frac{U_1 + U_2}{2} \vec{i}
\end{aligned} \tag{4.18}$$

#### 4.2.2 Wing and Wake Vortex Strength Determination

In order to determine the strength of the wing, and newly formed wake, vortices a zero-normal-flow boundary condition is applied at the wing control points, at the 3/4 panel-length position. Analytically this is expressed as  $\vec{V}_c \cdot \vec{n} = 0$  where  $\vec{V}_c$  is the velocity induced at the control point  $c$  and  $\vec{n}$  is the vector normal to the surface of the wing. The condition results in the set of equations

$$\sum_{b=1}^{N_b} \left( \frac{\Gamma_b}{2\pi} \right) \left[ \frac{-(y_b - y_k) \vec{i} + (x_b - x_k) \vec{j}}{(x_b - x_k)^2 + (y_b - y_k)^2} \right] + \sum_{w=N_w}^{N_w} \left( \frac{\Gamma_w}{2\pi} \right) \left[ \frac{-(y_w - y_k) \vec{i} + (x_w - x_k) \vec{j}}{(x_w - x_k)^2 + (y_w - y_k)^2} \right] \cdot \vec{n} = -\vec{V}_c \cdot \vec{n}, \tag{4.19}$$

where the circulation strengths  $\Gamma_b$  and  $\Gamma_{N_w}$  are unknown, and  $x_k$  and  $y_k$  are the  $x$  and  $y$  position of the wing control points. Equation 4.19 forms a set of  $N_b + 1$  unknowns and  $N_b$  independent equations. The final equation needed to solve for the unknowns is Kelvin's Circulation theorem. This requires that the sum of the vorticity present in the flow be constant at all time. The amount of circulation present in the shear-layer, including the upstream and downstream regions is assumed constant. As such the

amount of circulation present in the wing at any time must equal that previously shed into the wake. This forms a linear system of the type  $E\vec{\Gamma} = \vec{B}$ , with the unknown vector  $\vec{\Gamma}$  given by

$$\vec{\Gamma} = \begin{pmatrix} \Gamma_1 \\ \Gamma_2 \\ \cdot \\ \Gamma_b \\ \cdot \\ \Gamma_{N_b-1} \\ \Gamma_{N_b} \\ \Gamma_{N_w} \end{pmatrix}$$

where  $\Gamma_1 \rightarrow \Gamma_{N_b}$  are strengths of the vortices bound to the wing panels  $\Gamma_b$ , and  $\Gamma_{N_w}$  is the strength of the wake vortex formed during the current time step. The vector  $\vec{B}$  is determined at each time step, with  $B_1 \rightarrow B_{N_b}$  determined from the application of  $-\vec{V}_c \cdot \vec{n}$  and  $B_{N_b+1} = -\sum_{w=1}^{N_w} \Gamma_w$ . The matrix  $E$  is composed of the interaction coefficients between the bound wing and new wake vortices and the wing control points, and Kelvin's Circulation theorem. The first  $N_b$  rows are the influence coefficients of the wing panel vortices and the newest wake vortex on the panel control points, while row  $N_b+1$  is formed from the application of Kelvins circulation theorem.

$$E = \begin{pmatrix} E_{1,1} & E_{1,2} & E_{1,3} & \cdot & \cdot & \cdot & E_{1,W_{N_w}} \\ E_{2,1} & E_{2,2} & \cdot & \cdot & \cdot & \cdot & E_{2,W_{N_w}} \\ E_{3,1} & \cdot & \cdot & \cdot & \cdot & \cdot & E_{3,W_{N_w}} \\ \cdot & \cdot & \cdot & \cdot & \cdot & E_{N_b-2,N_b} & E_{N_b-2,W_{N_w}} \\ \cdot & \cdot & \cdot & \cdot & E_{N_b-1,N_b-1} & E_{N_b-1,N_b} & E_{N_b-1,W_{N_w}} \\ \cdot & \cdot & \cdot & E_{N_b,N_b-2} & E_{N_b,N_b-1} & E_{N_b,N_b} & E_{N_b,W_{N_w}} \\ 1 & 1 & \cdot & \cdot & \cdot & 1 & 1 \end{pmatrix}$$

where the components of  $E$  are determined such that  $E_{O,P}$  is the influence of bound vortex  $P$  with unknown strength  $\Gamma_P$  on control point  $O$ . The index  $W_{N_w}$  represents the newly released wake vortex of still unknown strength such that  $E_{O,W_{N_b}}$  represents the effect of the wake vortex on control point  $O$ . Considering the 2-D wing geometry

$$E_{O,P} = \frac{\text{sign}(x_p - x_o)}{2\pi\sqrt{(x_o - x_p)^2 + (y_o - y_p)^2}}. \quad (4.20)$$

As the positions of the bound and newly formed wake vortices are constant for a given wing geometry, the matrix  $E$  is constant. Once  $\vec{B}$  is calculated the unknown  $\vec{\Gamma}$  can be found through any of the available linear system solvers. Once the strength of the bound wing vortices and new wake vortex have been determined, the model moves forward to the convection step.

#### 4.2.3 Wing Lift Determination

Following determination of the wing and wake strengths, the velocity of each vortex particle is determined from Equation 4.17 and the particles are convected forward in time. After this the parameters which track the wing and layer response are calculated and recorded. These parameters include the circulation and lift of the wing, and the instantaneous velocity at various points. The net circulation of the wing is determined through direct summation of the individual bound vortices. The instantaneous velocity at the various probe points is calculated in the same manner as the velocity at each of the vortex particle locations. Key statistics such as the varying component of the lift,  $L'$ , the spreading rate of the layer  $\partial\delta_\omega/\partial x$ , and the layer statistical properties the rms values of  $u'_{rms}/U_1$ ,  $v'_{rms}/U_1$ , and  $-u'v'_{rms}/U_1^2$  are calculated directly during post run processing from time histories of the velocity for various points within the flow.

While calculating the net wing circulation, and velocity statistics is straight for-

ward, determination of the wing lift from the circulation is somewhat more complex. For clarity the derivation is expanded upon from the brief discussion provided in Katz and Plotkin[42]. Beginning with the Euler equation while assuming the effect of gravity is negligible,

$$\frac{\partial \vec{U}}{\partial t} + \vec{U} \cdot \nabla \vec{U} + \frac{\nabla p}{\rho} = 0. \quad (4.21)$$

where  $p$  is the pressure at a point. Utilizing the vector identity  $\zeta \cdot \nabla \zeta = \nabla \frac{\zeta^2}{2} - \zeta \otimes (\nabla \otimes \zeta)$  and applying it to the velocity field, while noting that  $\vec{\omega} \equiv \nabla \otimes \vec{U}$ , we are left with  $\vec{U} \cdot \nabla \vec{U} = \nabla \frac{\vec{U}^2}{2} - \vec{U} \otimes (\nabla \otimes \vec{U}) = \nabla \frac{\vec{U}^2}{2} - \vec{U} \otimes \vec{\omega}$ . If we further assume that the fluid outside of the individual vortex particles is irrotational then in general  $\vec{\omega} = 0$  which leaves  $\vec{U} \cdot \nabla \vec{U} = \nabla \frac{\vec{U}^2}{2}$ . Substituting this expression into preceding expression yields

$$\frac{\partial \vec{U}}{\partial t} + \frac{\nabla p}{\rho} + \nabla \frac{\vec{U}^2}{2} = 0. \quad (4.22)$$

Further, as the operators  $\frac{\partial}{\partial t}$  and  $\nabla$  are independent of each other, and the fluid along a streamline is irrotational, then  $\vec{U}$  can be replaced with  $\nabla \Phi$  in Equation 4.21 giving

$$\frac{\partial \vec{U}}{\partial t} + \frac{\nabla p}{\rho} + \nabla \frac{\vec{U}^2}{2} = \nabla \left( \frac{\partial \Phi}{\partial t} \right) + \frac{\nabla p}{\rho} + \nabla \frac{(\nabla \Phi)^2}{2} = \nabla \left[ \frac{\partial \Phi}{\partial t} + \frac{p}{\rho} + \frac{(\nabla \Phi)^2}{2} \right] = 0. \quad (4.23)$$

For this relationship to remain true  $\frac{\partial \Phi}{\partial t} + \frac{p}{\rho} + \frac{(\nabla \Phi)^2}{2}$  must be at most a function of time only. If we write this expression between two points, a reservoir point where  $p = p_0$  and  $\vec{U} = 0$ , and a general point it leaves

$$\frac{\partial \Phi}{\partial t} + \frac{p}{\rho} + \frac{(\nabla \Phi)^2}{2} = \frac{p_0}{\rho}, \quad (4.24)$$

reorganizing slightly results in

$$\frac{p_0 - p}{\rho} = \frac{1}{2} (\nabla \Phi)^2 + \frac{\partial \Phi}{\partial t}. \quad (4.25)$$

This is the non-steady formulation of the Bernoulli equation assuming inviscid, incompressible, irrotational flow, in the Eulerian reference frame. However a Lagrangian reference will make calculation of the wing lift somewhat more direct. Shifting from the Eulerian to Lagrangian frame affects the time derivative of the velocity frame, with

$$\left[\frac{\partial\phi}{\partial t}\right]_{Eulerian} \rightarrow \left[\frac{\partial\phi}{\partial t}_{Eulerian} - \vec{U} \cdot \nabla\phi\right]_{Lagrangian} \quad (4.26)$$

and

$$\frac{p_0 - p}{\rho} = \frac{1}{2}(\nabla\Phi)^2 + \frac{\partial\Phi}{\partial t} + \vec{U} \cdot \nabla\Phi. \quad (4.27)$$

If the small disturbance assumption, that any velocity disturbance caused by the presences of the wing is small compared to the magnitude of the free stream velocity, is applied then  $\vec{U} \gg \nabla\Phi$ . Based on this, then it also holds that  $\vec{U} \cdot \nabla\Phi \gg \frac{\nabla\Phi^2}{2}$ , and

$$\frac{p_0 - p}{\rho} \approx \frac{\partial\phi}{\partial t} + \vec{U} \cdot \nabla\Phi, \quad (4.28)$$

with the perturbation pressure given by

$$p_p \approx p_0 - \rho\left(U \cdot \nabla\Phi + \frac{\partial\phi}{\partial t}\right). \quad (4.29)$$

Defining  $\Delta p$  as the pressure on the top surface of the wing subtracted from the pressure on the bottom surface

$$\Delta p \approx p_B - p_T \approx \left(p_0 - \rho\left(U \cdot \nabla\Phi_B + \frac{\partial\phi_B}{\partial t}\right)\right) - \left(p_0 - \rho\left(U \cdot \nabla\Phi_T + \frac{\partial\phi_T}{\partial t}\right)\right). \quad (4.30)$$

As the wing is represented by a discretized vortex sheet, the velocity difference across the wing equals  $\gamma$ . An alternate formulation is that the velocity on the upper surface equals the local velocity plus  $\nabla\Phi_T = \frac{\gamma}{2}\vec{i}$  while the velocity on the lower surface is

the local velocity plus  $\nabla\Phi_B = -\frac{\gamma}{2}\vec{i}$ . Further  $\nabla(-\Phi) = -\nabla\Phi$  and  $-\nabla\Phi_T = \nabla\Phi_B$ . Using these relationships and substituting them into the previous equation results in

$$\Delta p \approx 2\rho(\vec{U} \cdot \nabla\Phi + \frac{\partial\Phi}{\partial t}). \quad (4.31)$$

As the wing is assumed to be infinitely thin,  $\nabla\Phi$  depends only on the  $x$  coordinate along the surface of the wing. With  $\nabla\Phi = \frac{\gamma}{2}$  to assure the appropriate velocity jump, then

$$\Phi = \int_0^c \frac{d\Phi}{dx} dx = \int_0^c \nabla\Phi dx = \int_0^x \frac{\gamma}{2} dx. \quad (4.32)$$

This leaves the expression for  $\Delta p$

$$\Delta p = \rho(\vec{U} \cdot \gamma + \frac{\partial}{\partial t} \int_0^c \gamma(x) dx). \quad (4.33)$$

Finally, integrating from  $x = 0 \rightarrow c$ , to determine the net pressure difference results in the lift per unit span

$$L/Sp = \rho \left( \int_0^c [U\gamma(x) + \frac{\partial}{\partial t} (\int_0^c \gamma(x) dx)] dX \right), \quad (4.34)$$

with  $\Gamma = \int_0^c \gamma(x) dx$ , this expression can be reduced to it's final form

$$L/Sp = \rho U \Gamma + \rho c \frac{\partial \Gamma}{\partial t}. \quad (4.35)$$

The instantaneous wing lift depends on not only  $\Gamma$ , but on  $\partial\Gamma/\partial t$  as well. During steady conditions this reduces to the classic form  $L/Sp = \rho U \Gamma$ . When this is applied in the current numerical model,  $U$  is assumed equal to  $\vec{U}$ ,  $\Gamma = \sum \Gamma_b$ .

### 4.3 Model Verification

To test model accuracy the shear-layer portion was independently run and profiles of  $u/U_1$ ,  $u'_{rms}/U_1$ ,  $v'_{rms}/U_1$ ,  $-u'v'_{rms}/U_1^2$ , as well as  $\partial\delta_\omega/\partial x$ . The wing and wake model

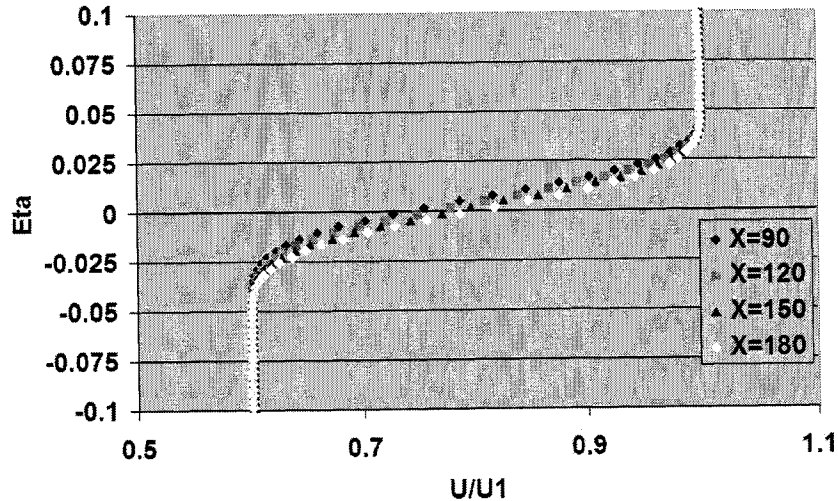


Figure 4.3: Shear-layer mean velocity profile test case

was also tested independently from an impulsive start, and steady state and transient lift profiles compared with theoretical results. A test comparison against available BVI data was not possible due to the use of the forward Euler time integration scheme. Changes in the accuracy of the model due to purely numerical effects were also investigated to allow the separation of physical trends from numerical ones.

#### 4.3.1 Model Shear-Layer Testing

The first test of the shear-layer model was to collect data at several downstream positions for  $U_1 = 5\text{m/s}$  and  $r = 0.5$ , chosen by Inoue[18]. Figures 4.3 to 4.6 show  $\eta$  profiles of  $\bar{U}/U_1$ ,  $u'_{rms}/U_1$ ,  $v'_{rms}/U_1$ ,  $-u'v'_{rms}/U_1^2$ , and  $\delta_\omega/x$  calculated for various downstream positions. All four plots demonstrate that self-similarity has been achieved by the layer for these conditions.

Table 4.1 lists the calculated values of  $\delta_\omega/x$ , along with the maximum values of the  $u'_{rms}/U_1$ ,  $v'_{rms}/U_1$ , and  $-u'v'_{rms}/U_1^2$   $\eta$  profiles, as well as the values reported in Inoue[18], for various shear-layer researchers with the same values of  $\lambda$  and  $r$ . The

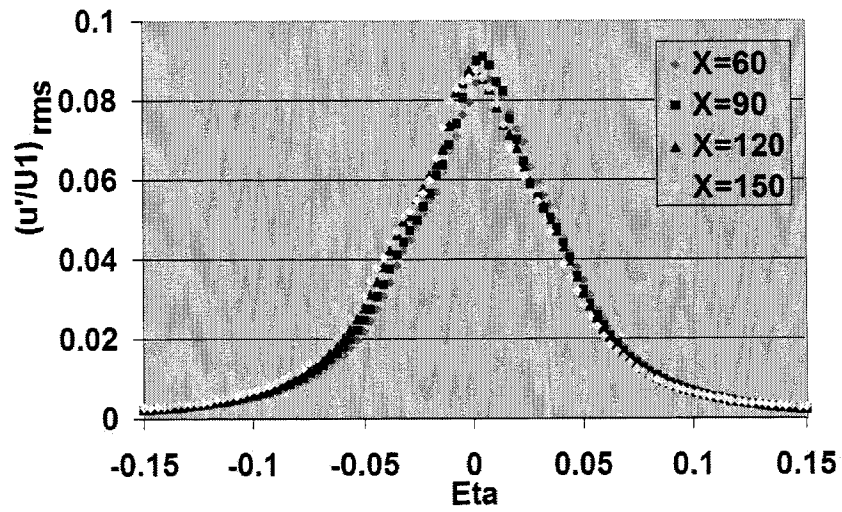


Figure 4.4: Shear-layer  $u'_{rms}/U_1$  profile test case

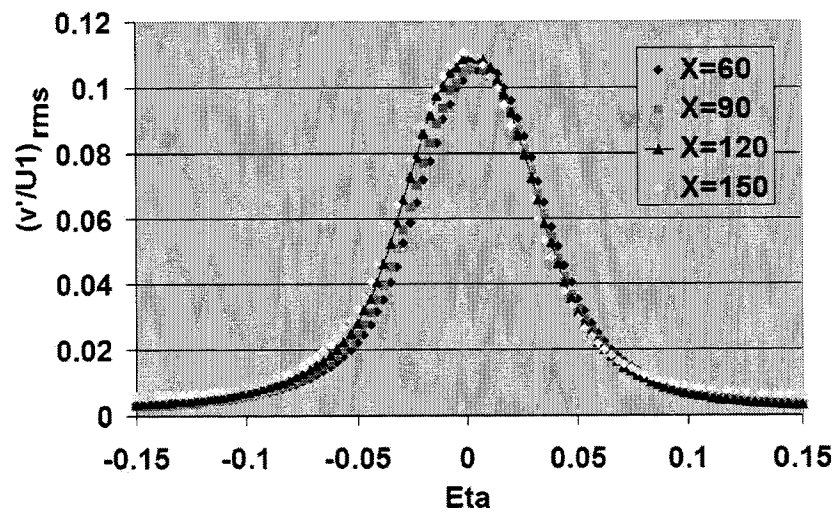


Figure 4.5: Shear-layer  $v'_{rms}/U_1$  profile test case



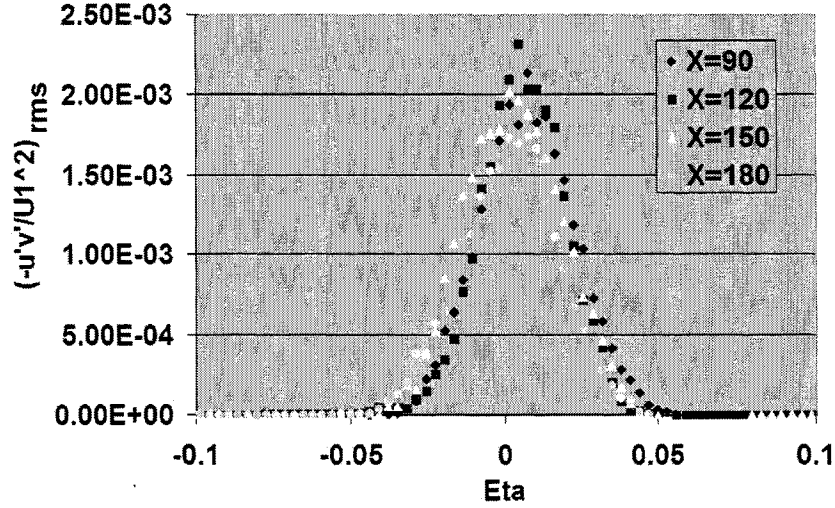


Figure 4.6: Shear-layer  $-u'v'_{rms}/(U_1^2)$  profile test case

current model displays reasonable agreement with experimental data. The spreading rate is approximately 25% low,  $u'_{rms}/U_1$  and  $v'_{rms}/U_1$  are 30% and 80% high respectively, while  $-u'v'_{rms}/U_1^2$  is 15% high. The over-estimate of  $u'_{rms}/U_1$  and  $v'_{rms}/U_1$  is likely due to the 2-D nature of the computer model being unable to accurately capture the 3-D nature of the flow. While the largest coherent structures are quasi-2-D, the vorticity in a shear-layer is distributed between all three orientations, leading to values of  $u'_{rms}/U_1$ ,  $v'_{rms}/U_1$ ,  $w'_{rms}/U_1$  that vary from each other by less than a factor of 2. As the numerical model freezes the vorticity in a single orientation it overstates the two dimensionality of the layer, resulting in values of  $u'_{rms}/U_1$  and  $v'_{rms}/U_1$  that are too high. When compared with Inoue's numerical data, good agreement is found in  $u'_{rms}/U_1$  and  $v'_{rms}/U_1$ , though the current model finds better agreement with experiments in  $-u'v'_{rms}/U_1^2$ . The only discrepancy of note is the low spreading rate of the current numerical layer. Inoue's model over-estimates the spreading rate by 28%. This shift is likely due to the difference in core function choice.

Table 4.1: Shear-layer test case statistical quantities (data taken from Inoue[18])

Researcher	r	$\lambda$	$\delta_\omega/x$	$\frac{u'_{rms}}{U_1} ax$	$\frac{v'_{rms}}{U_1} ax$	$\frac{-u'v'_{rms}}{U_1^2} ax$
Oster and Wygnanski	0.6	0.25	0.045	0.072	0.061	$0.21x10^{-2}$
Yule	0.6	0.25	0.054	0.069	0.064	$0.21x10^{-2}$
Spencer	0.6	0.25	?	0.068	0.056	$0.18x10^{-2}$
Average Value			0.05	0.07	0.06	$0.2x10^{-2}$
Current Model	0.6	0.25	0.038	0.091	0.11	$0.23x10^{-2}$
Percent Error			-24%	+30%	+80%	+15%
Inoue	0.6	0.25	0.064	0.126	0.100	$0.43x10^{-2}$
Percent Error			+28%	+80%	+67%	+115%

#### 4.3.2 Wing Model Testing

The first wing test was to determine how accurately the numerical scheme predicted steady state lift. Inviscid general theory estimates the coefficient of lift, to be

$$C_L \approx 2\pi\alpha, \quad (4.36)$$

for small  $\alpha$ . While

$$L \equiv C_L q A. \quad (4.37)$$

Numerical calculations for a free stream velocity of  $5m/s$ ,  $c = 1m$ ,  $N_b = 50$ , and  $\alpha = 0^\circ \rightarrow 10^\circ$ , found excellent agreement with less than a 0.5% difference for all  $\alpha$ .

The second test was to inject tracer particles on both sides of the stagnation streamline and allow them to convect downstream past the wing. The local velocities of the tracer particles were calculated under the influence of the wing and free stream only. Figure 4.7 displays the path taken by the tracers over the entire wing, and over the leading edge of the wing showing the streamlines behaving as expected. The

streamlines were calculated with 50 wing panels, at  $\alpha = 10^\circ$ . As the wing circulation strength and the free stream velocity are directly related, the free stream velocity is irrelevant.

The final test performed on the wing was to calculate the lift history of the wing from an impulsive start. At  $t = 0$ , the free stream velocity was increased from 0 to  $5m/s$ , and the instantaneous lift, and circulation were determined and plotted for a period of 5 dimensionless time units,  $\tau = t(5m/s)/c$ , Figure 4.8. This tested both the accuracy of the non-steady lift calculation scheme, and development of the wake, as the two are closely tied. The results of the  $N_b = 50$  wing were compared to those of a single panel wing from Katz and Plotkin[42]. When compared to the results reported in Katz and Plotkin it is clear that the accuracy of the multi-panel wing lies between that of a single panel wing and theory. While the wings net circulation is determined quite accurately the lift determination scheme over-estimates the theoretical lift of the wing. During shear-layer wing interaction testing the circulation will be changing quite rapidly. The current lift determination scheme should accurately capture the frequency behavior of the wing, though will likely over-estimate both  $L'$  PSD and  $L'_{rms}$ .

### 4.3.3 Accuracy Considerations

Increasing  $U_1$  with a fixed  $\Delta t$  results in fewer vortex particles modeling the fluid domain. This leads to a decrease in accuracy in a similar fashion to increasing the time step for a fixed  $U_1$ . Both cases result in fewer vortices and larger distances traveled by individual particles during each time step. Figure 4.9 displays the effect of changing the time step alone for  $U_1$  varying from 2.5 to  $20m/s$  and  $c = 0.05$  to  $0.4m$ , such that  $U_1\Delta t/c = 0.4$ . From this data it is apparent that decreases in the size of the time step result in increases in the magnitude of  $L'_{rms}$  due to purely numerical considerations. Figure 4.10 shows the result of changing  $\Delta t$  in conjunction with  $U_1$  with  $c = 0.05m$  so that  $U_1\Delta t/c = 0.4$ . This results in a constant number of vortex

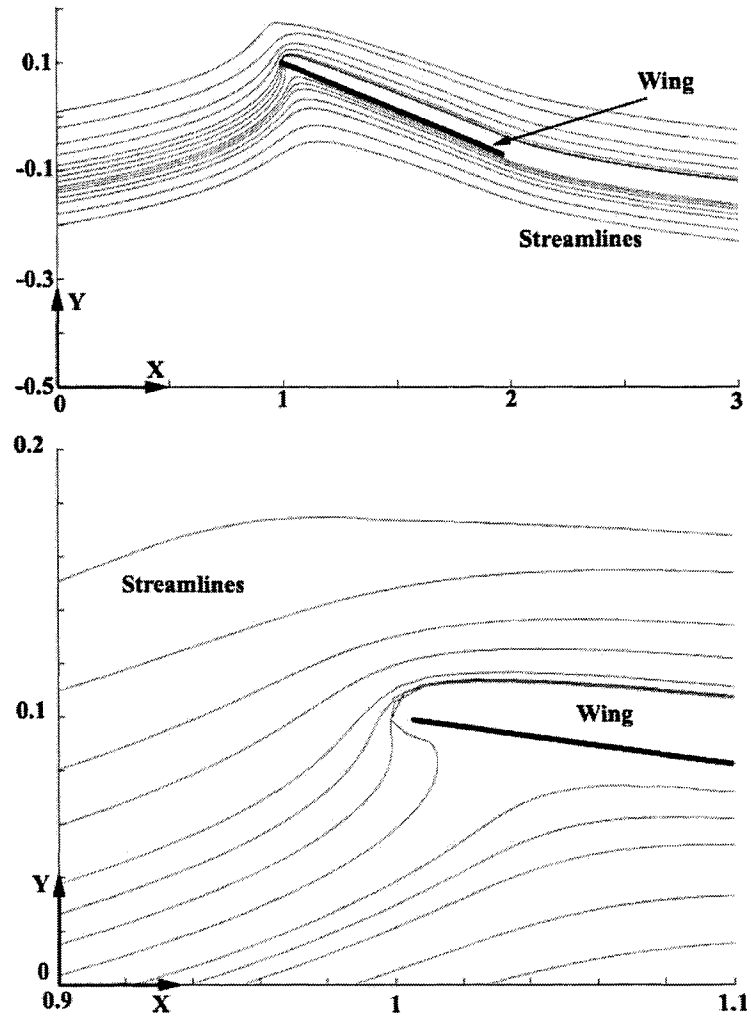


Figure 4.7: Wing flow-field streamlines

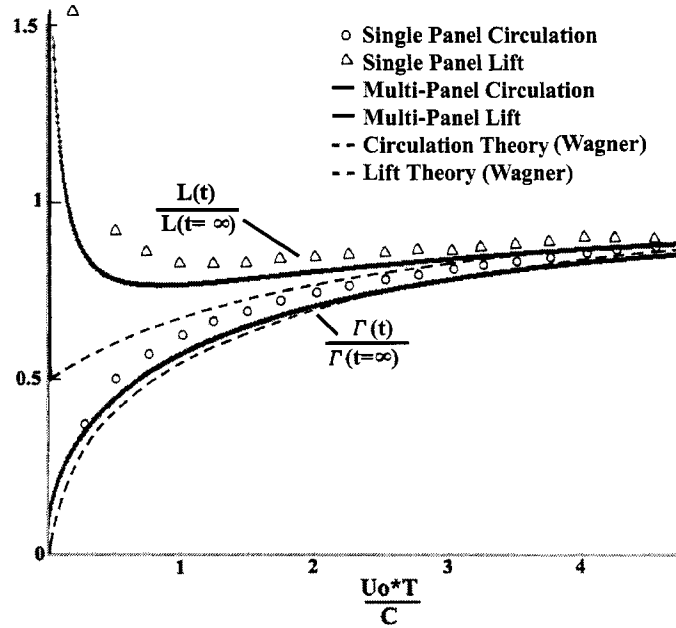


Figure 4.8: Impulsive start test

particles in the flow field. These profiles collapse to a single curve. Further Figures 4.9 and 4.10 show that increasing  $U_1$  with fixed  $\Delta t$  leads to decreases in the magnitude of  $L'_{rms}$  that are not attributable to changes in the flow but due to the number of particles. For the current work  $\Delta t = 0.002s$ . This has been found to give a good balance between accuracy of the model and reasonable run times.

Changes in  $\Delta t$  affect the accuracy of the model and the magnitudes of  $L'_{rms}$  and  $L'$  PSD. However, the smoothness of the PSD profiles are a function of the number of  $L'$  values in a sample, and in the number of samples averaged. For the current work a sample size of 1028  $L'$  values, has been chosen as a default, and when combined with  $\Delta t = 0.002s$  this produces a frequency resolution of approximately  $0.5Hz$ . Figure 4.11 shows the effect of increasing the number of PSD samples that are averaged for each  $L'$  PSD profile by a factor of 10. Both the ordinate and abscissa have been normalized in the same fashion as the experimental data. From this plot it is clear

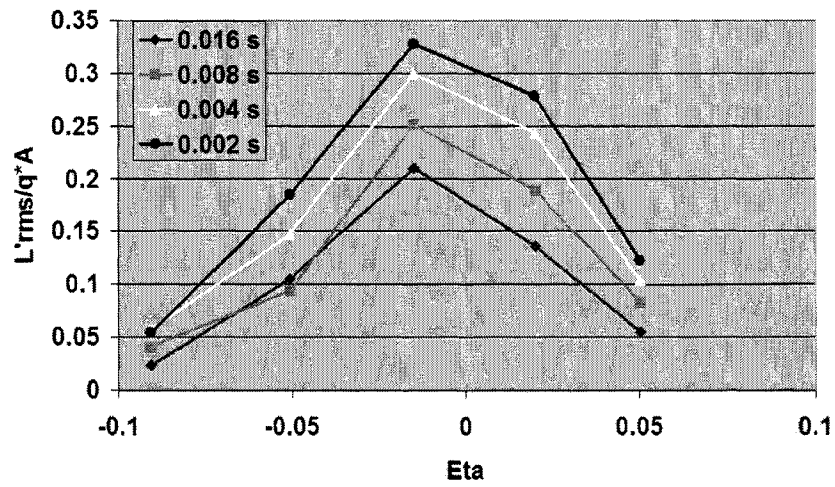


Figure 4.9:  $L'_{rms}$  numerical effects, variable time step

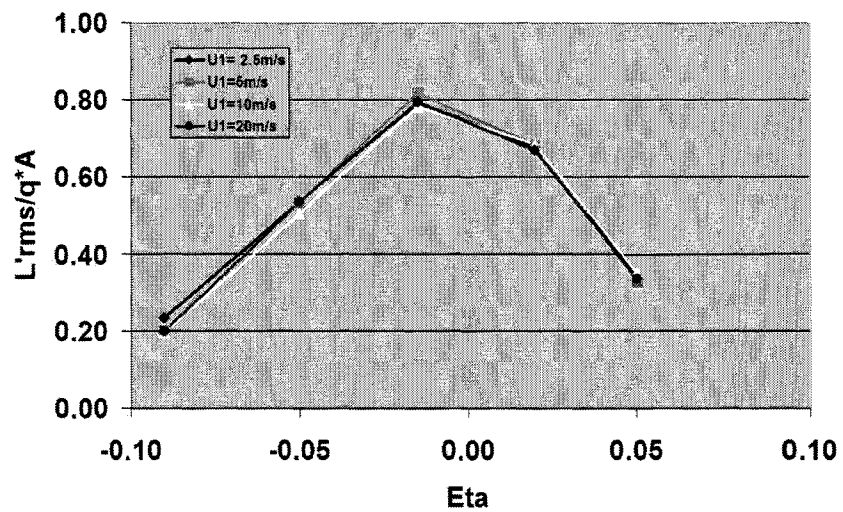


Figure 4.10:  $L'_{rms}$  numerical effects, variable speed and time step

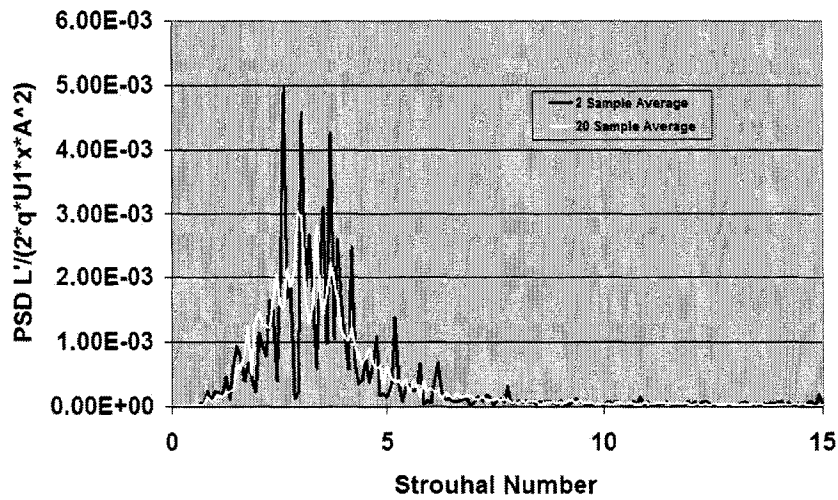


Figure 4.11: Effect of increased averaging time on  $L'$  PSD

that the widths of the profiles are unaffected, but the increased number of averages results in a smoother more consistent curve. For the current work a total of 10 samples will be averaged for each of the PSD profiles. While this does not produce a uniformly smooth curve the results are sufficiently accurate to compare their behavior with the experimental data, and evaluate the effects due to changes in  $x$ ,  $\eta$ , and  $U_1$ . Further a small data set will be produced at higher averaging and resolution with which to compare experimental data.

#### 4.4 Numerical Model Results

The majority of the numerical data was collected over a grid of wing positions that approximates the experimental positions with  $x = 1.19, 1.45, 1.70,$  and  $1.96m$  and  $\eta = 0.07, 0.03, -0.03,$  and  $-0.07,$  for  $U_1 = 3, 5, 7, 9,$  and  $11m/s$ . The downstream distance was shifted slightly to account for the experimental value of  $x_0 = -0.026m$ . In order to find a balance between long run times and reasonable accuracy levels the following model values were used:  $\Delta t = 0.002s$ , 1028 points per PSD sample, 10 samples averaged for each  $L'$  PSD profile,  $\beta_1 = -1000m,$   $\beta_2 = 5m,$   $\beta_3 = 1000m$ . The arbitrary initial vortex particle distribution constants are  $A_0 = 0.01m,$  and  $W_0 = 0.1m$ . The wing was modeled with  $N_b = 50$ . Finally the downstream region is modeled with 21 vortex sheets, with an outer sheet spreading angle of  $10^\circ$ , and a Gaussian distribution of circulation per unit length chosen to match the velocity profiles at the downstream edge of the modeled region.

Within this section a sample of the numerical data will be presented for later comparison with the experimental data. The remaining data will be presented in Appendix B. Additional data for several extrapolations will also be presented and discussed here. Both a complete discussion and summary of the numerical data, as well as a direct comparison with the experimental data will be reserved for Chapter 5.

##### 4.4.1 Effect of $U_1$ on $L'$ PSD Profiles

As with the experimental data, numerical data was collected as averaged PSD profiles of  $L'$  at fixed locations, and will be presented in the order collected. Figure 4.12 shows a sample of the raw numerical data taken at  $x = 1.19m$  and  $\eta = 0.03$ . The profiles are quite ragged due to the limited number of samples averaged, though they still display reasonable behavior with smooth shouldered curves leading to a single, broad spectral peak. However, without normalization neither the width of the curves nor

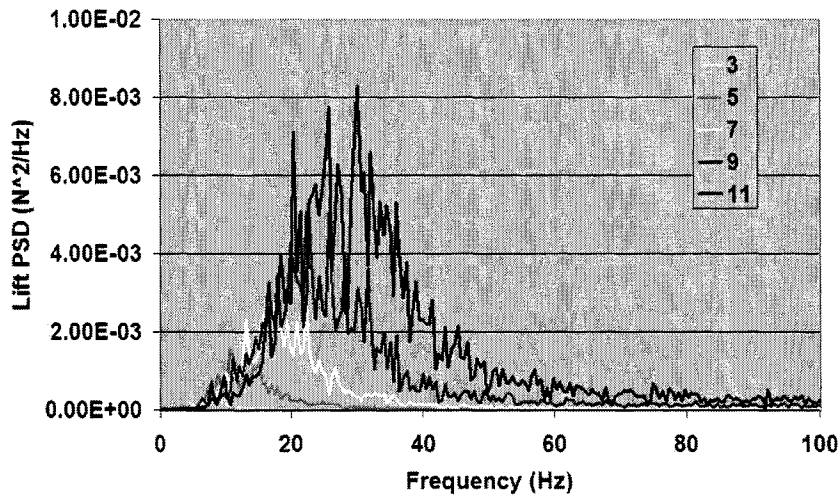


Figure 4.12: Raw numerical  $L'_{rms}$  PSD,  $x = 1.19m$ ,  $\eta = 0.03$

the magnitude of the peaks agree well.

To better analyze the behavior of the curves the numerical data has been normalized in the same fashion as the experimental data, with  $U_1^3 \rho^2 A^2 (x - x_0)$  for the PSD of  $L'$  and  $U_1 / (x - x_0)$  for the frequency, resulting in a Strouhal number scale. Profiles of  $L'_{rms}$  are normalized by  $\bar{q}A$  and plotted against  $\eta$ . Figure 4.13 displays a sample from  $x = 1.19m$ , taken at  $\eta = -0.03$ . When normalized the  $x = 1.19m$  PSD profiles are consistent in curve shape and extent though the magnitudes differ somewhat due to effects of the fixed time step and variable velocity. Analysis of the PSD on dimensional axes reveals none of the sharp, fixed frequency peaks apparent in the experimental cases for  $U_1 \geq 5m/s$ . For  $x = 1.19m$   $\Delta St \approx 2$  while the peaks are centered at  $St \approx 3$ . The additional data in Appendix B, displays the same trends.

Figure 4.14 provides a sample of the data taken at  $x = 1.45m$  and  $\eta = 0.03$ . The data displays good agreement between the velocity curves, with  $\Delta St \approx 2$ . Further there is good agreement between the normalized magnitudes for the profiles. When dimensional axes were considered no further trends became apparent. Data from the

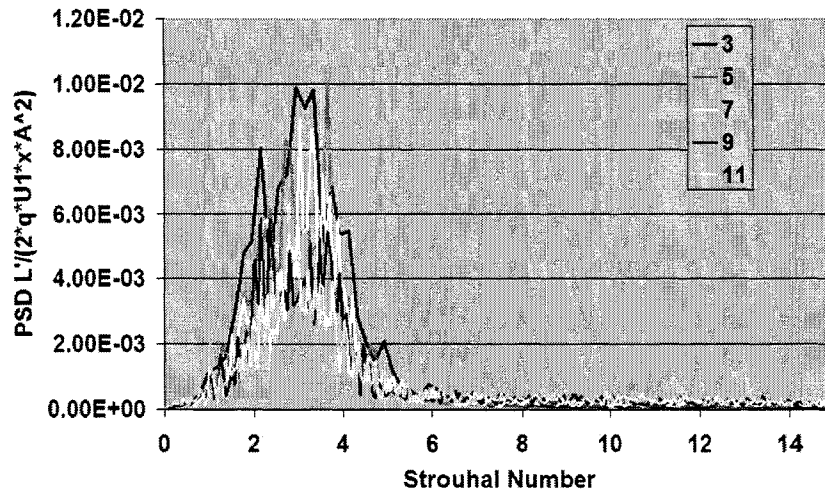


Figure 4.13: Normalized numerical  $L'_{rms}$  PSD,  $x = 1.19m$ ,  $\eta = -0.03$

remaining  $\eta$  values reinforces these results.

For the downstream distance of  $x = 1.70m$  data is presented at  $\eta = 0.07$ , Figure 4.15. This data agrees well with the preceding data. The profiles for each of the tested velocities display lift variations with  $\Delta St \approx 2$ . The normalized magnitudes of the tested velocities agree well. The remaining data does not display any additional trends or discrepancies. Figure 4.16 displays the data taken at height  $x = 1.96m$  and  $\eta = 0.03$ , and shows nearly identical characteristics to the preceding cases.

#### 4.4.2 Numerical Downstream Position Lift Spectra Data

Once the variation in lift characteristics for a fixed position and variable velocity was considered the evolution of the layer with downstream distance was evaluated. The following plots display data collected from each of the downstream distances,  $x = 1.19, 1.45, 1.70$ , and  $1.96m$ . Figure 4.17 presents the data for  $\eta = 0.07$  and  $U_1 = 3m/s$ . Once again  $\Delta St$  is in the range expected and the PSD profile peaks are centered at approximately  $St = 2.5$ . Further the magnitudes of each of the tested

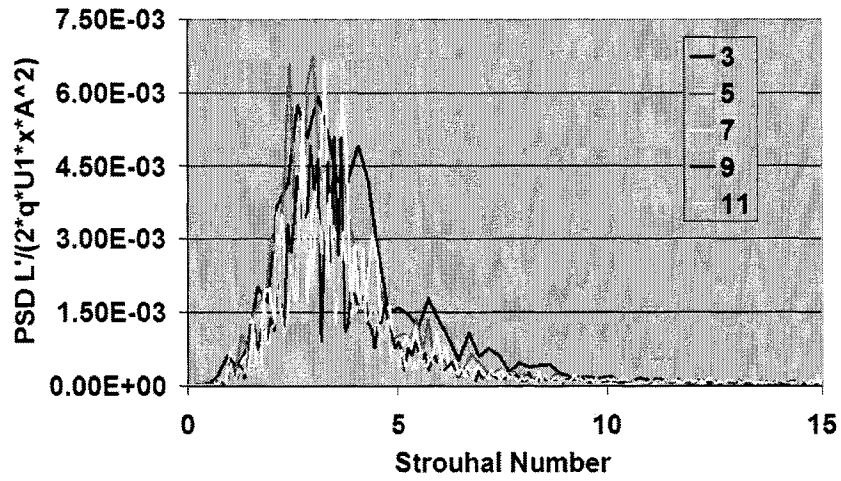


Figure 4.14: Normalized numerical  $L'_{rms}$  PSD,  $x = 1.45m$ ,  $\eta = 0.03$

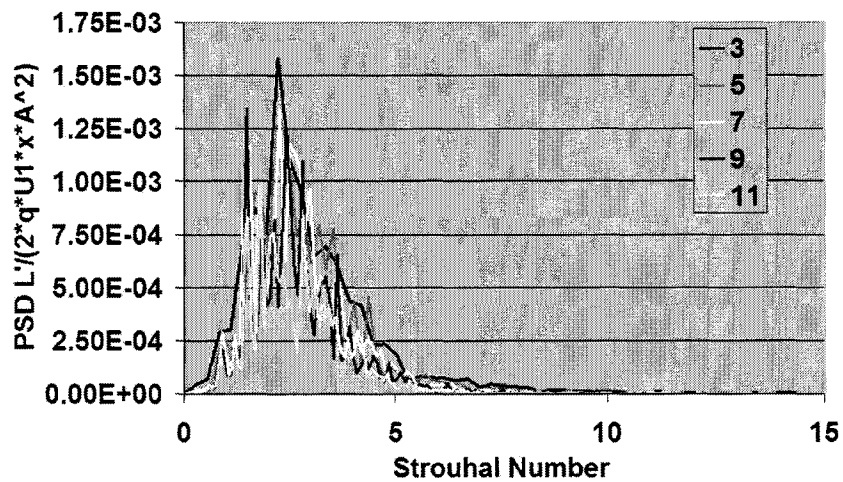


Figure 4.15: Normalized numerical  $L'_{rms}$  PSD,  $x = 1.70m$ ,  $\eta = 0.07$

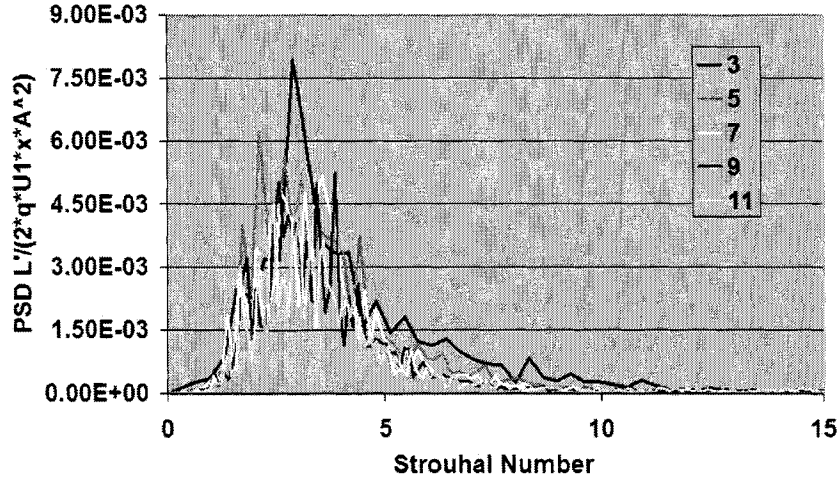


Figure 4.16: *Normalized numerical  $L'_{rms}$  PSD,  $x = 1.96m$ ,  $\eta = 0.03$*

downstream positions agree surprisingly well, with maximum values varying by less than 20%.

Comparisons focusing on variation in the behavior of the PSD profiles with downstream distance have been formulated for all of the available data, however the behavior of the various plots is quite similar, following the same trends as fixed position and variable velocity. As such the majority of the data is reserved for Appendix B, and only a single plot from each of the available heights is provided here. Figure 4.18 provides the data sample from the height of  $\eta = 0.03$ , for a velocity of  $U_1 = 9m/s$ . Once again the characteristics of this data set closely mirror those of the  $\eta = 0.07$  data. The PSD peak has  $\Delta St \approx 2$  and is centered at  $St \approx 3$ . Figures 4.19 and 4.20 display a sample of the data taken at  $\eta = -0.03$  and  $-0.07$  for velocities of  $U_1 = 5$  and  $9m/s$  respectively. For both cases there is excellent agreement in the extent of the  $L'$  PSD peak with  $\Delta St \approx 2$ , as well as in the maximum magnitudes of the peaks which agree to within approximately 20%. For Figure 4.19 the peak is centered at  $St \approx 3$ , and for 4.20 the peak is centered at approximately  $St = 2.5$ .

From this set of plots it is clear that both the magnitude and frequency normaliza-

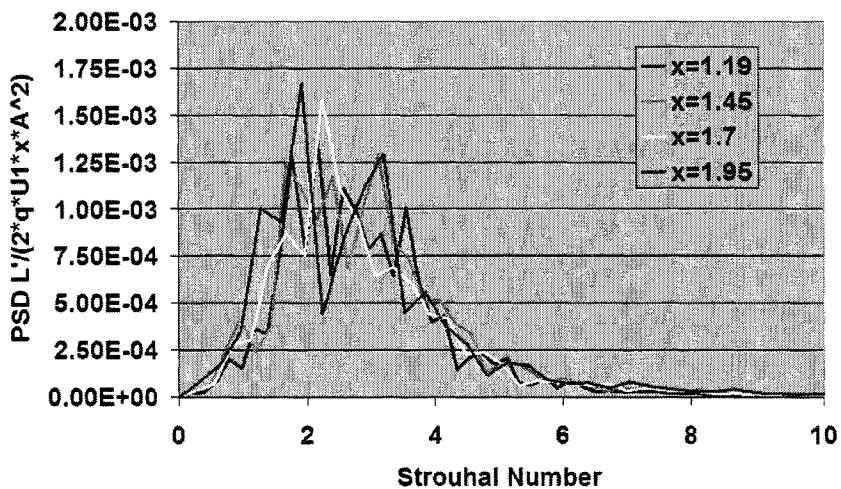


Figure 4.17: Normalized numerical  $L'_{rms}$  PSD,  $\eta = 0.07$ ,  $U_1 = 7m/s$

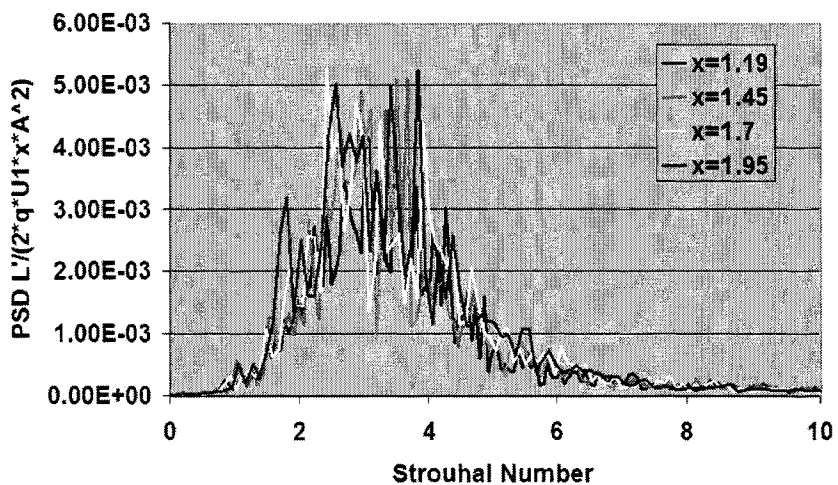


Figure 4.18: Normalized numerical  $L'_{rms}$  PSD,  $\eta = 0.03$ ,  $U_1 = 9m/s$

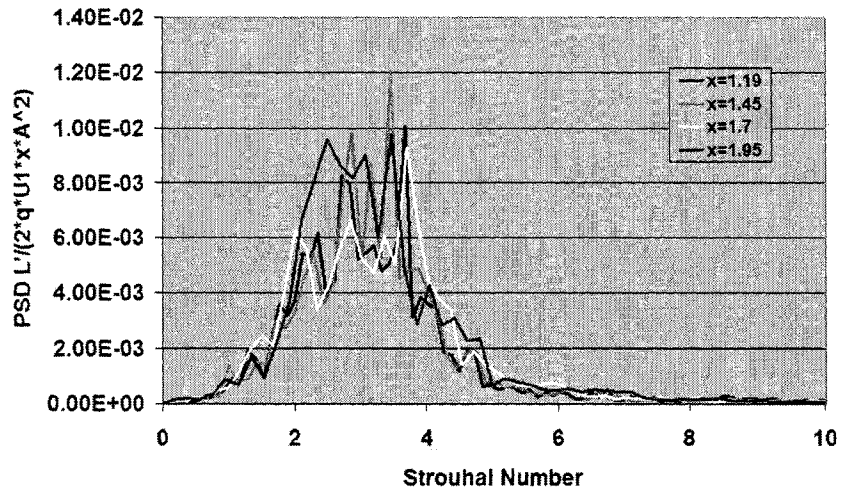


Figure 4.19: Normalized numerical  $L'_{rms}$  PSD,  $\eta = -0.03$ ,  $U_1 = 5m/s$

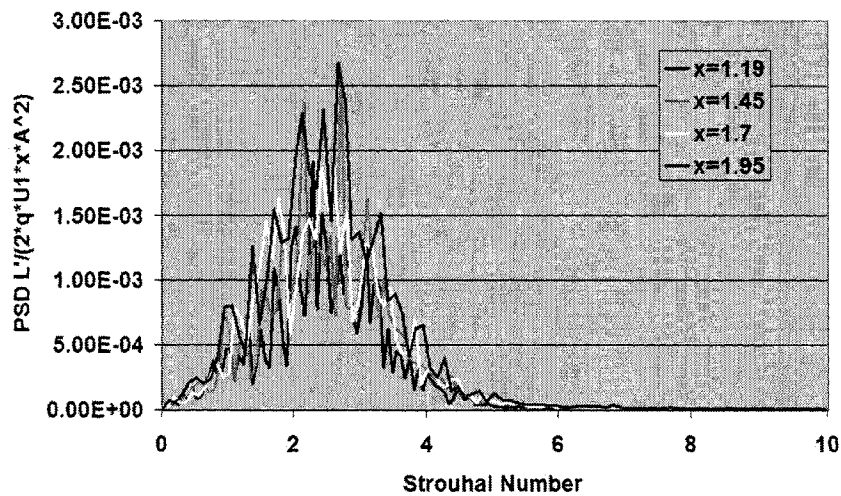


Figure 4.20: Normalized numerical  $L'_{rms}$  PSD,  $\eta = -0.07$ ,  $U_1 = 9m/s$

tion factors being utilized accurately capture the variation of the wings lift behavior in the frequency domain. It is expected that given a sufficiently long averaging time the data will properly collapse to a single curve, lending weight to the belief that the response of the wing to the shear-layer is self-similar, for  $\alpha = 0$  and so long as the chord length of the wing is on the same order as the thickness of the layer. This behavior can be further evaluated by analyzing the mean values and profiles of  $L'_{rms}$  for each of the considered positions.

The rough character of the profiles makes determination of maximum  $L'$  PSD magnitude, and average  $\Delta St$  somewhat difficult. Figure 4.21 shows the results from a more heavily averaged set of PSD profiles taken at  $x = 1.45m$ ,  $U_1 = 5m/s$ , and  $\eta = 0.02$ ,  $-0.015$ , and  $-0.05$  respectively. From these profiles the maximum value of  $L'$  PSD occurs at  $\eta$  just below zero and is  $\frac{L'PSD}{U_1^3 \rho^2 A^2 (x-x_0)} = 1.17 \times 10^{-2}$ , and  $\Delta St = 2$ , with the peak centered at  $St = 3.2$ . In addition it appears that the profiles both above and below the center of the layer have a slightly smaller  $\Delta St$ , and may have slightly lower Strouhal peak values.

#### 4.4.3 Numerical $L'_{rms}$ Cross-Layer Profiles

Figure 4.22 shows a brief sample of the dimensional  $L'_{rms}$  data. For both plots the ordinate is the magnitude of  $L'_{rms}$ , and the abscissa the vertical position of the wing in meters. The first profile set shows variation of  $L'_{rms}$  with velocity for a fixed position,  $x = 1.19m$ . The overall magnitude of  $L'_{rms}$  increases significantly with increasing velocity, though the general shape displayed does not change. The second plot shows that with increasing  $x$  the profiles become wider. It is clear that a normalization is needed for both the ordinate and the abscissa.

Figures 4.23 and 4.24 show the results for variable velocity, for the cross-layer profiles taken at  $x = 1.19$  and  $1.70m$  respectively. For these plots the ordinate is normalized by  $\bar{q}A$  and plotted against the abscissa  $\eta$ . While the curve shapes agree well, there appears to be a consistent variation in the magnitudes with increasing

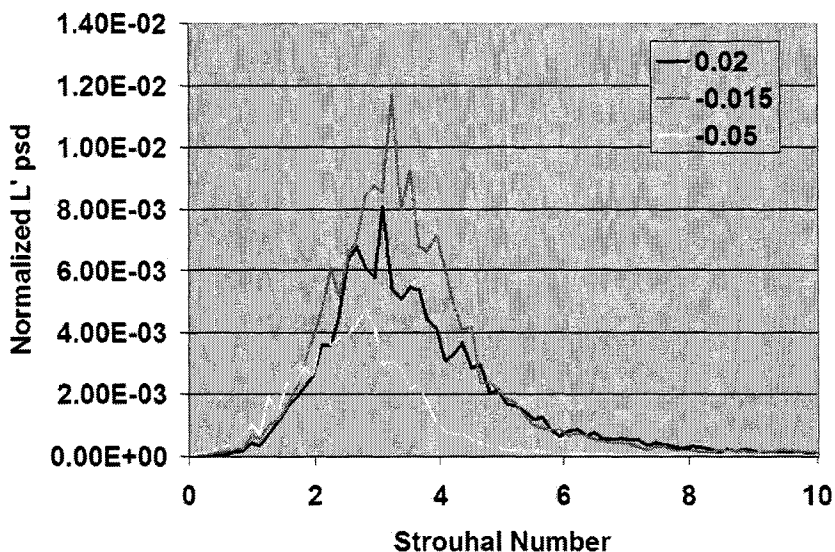


Figure 4.21: Heavily averaged  $L'_{rms}$  PSD,  $U_1 = 5m/s$ ,  $x = 1.45m$

velocity due to the accuracy changes discussed in section 4.3.3. Between the  $U_1 = 3$  and  $11m/s$  cases for  $x = 1.19m$  the maximum magnitude decreases by 25%. For the  $x = 1.70m$  case an overall decrease in magnitude of approximately 15% is experienced. The additional profiles at  $x = 1.45$  and  $1.96m$  are located in Appendix B, and display the same trends.

Additional comparisons of the variation in  $L'_{rms}$  with  $x$  have been made and agree well, Figures 4.25 and 4.26. These plots show that the wing and layer are responding to changes in  $x$  as expected, and as accounted for by the normalizing factors. All of the profiles collapse to a single curve when normalized, displaying equal magnitudes and closely agreeing curve shapes.

A final  $L'_{rms}$  profile was taken at a much higher  $\eta$  resolution, though for shorter run times at each point. As the profiles are self-similar, and the effects of changes  $U_1$  and  $x$  are well accounted for by the normalization, only a single profile is needed to fully characterize  $L'_{rms}$  vs  $\eta$ . Figure 4.27 shows the distribution of  $L'_{rms}$  vs  $\eta$  for  $x = 1.45m$ , and  $U_1 = 5m/s$ . The profile closely resembles the general character of

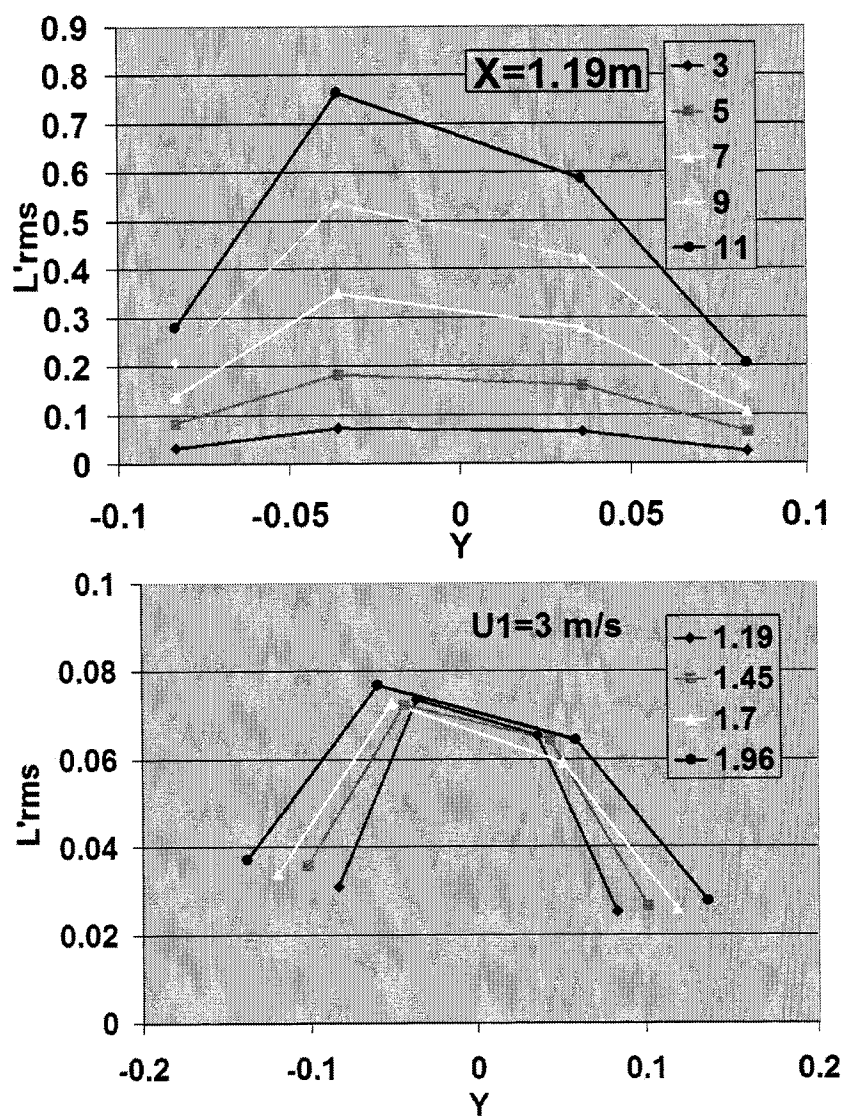


Figure 4.22: Raw numerical  $L'_{rms}$   $\eta$  profiles

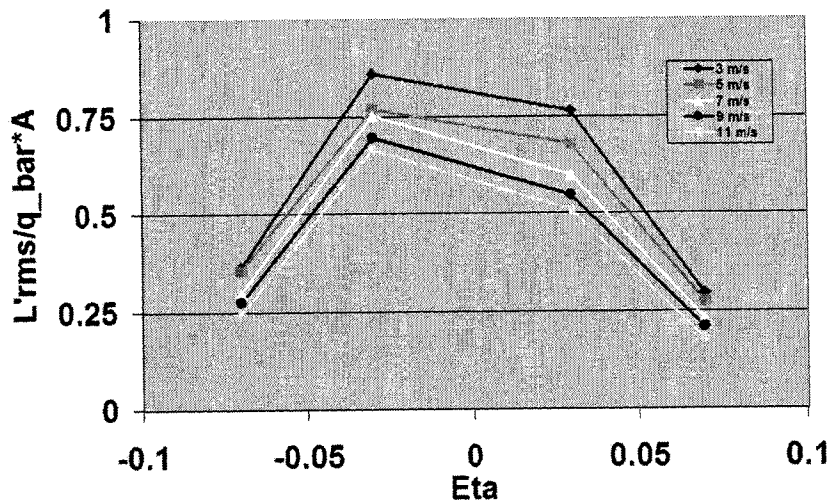


Figure 4.23: Normalized numerical  $L'_{rms}$  profile,  $x = 1.19m$

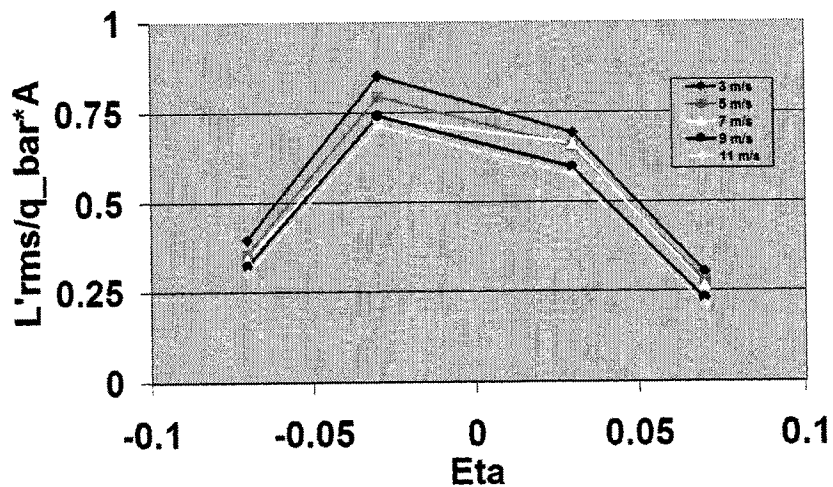


Figure 4.24: Normalized numerical  $L'_{rms}$  Profile,  $x \approx 1.70m$

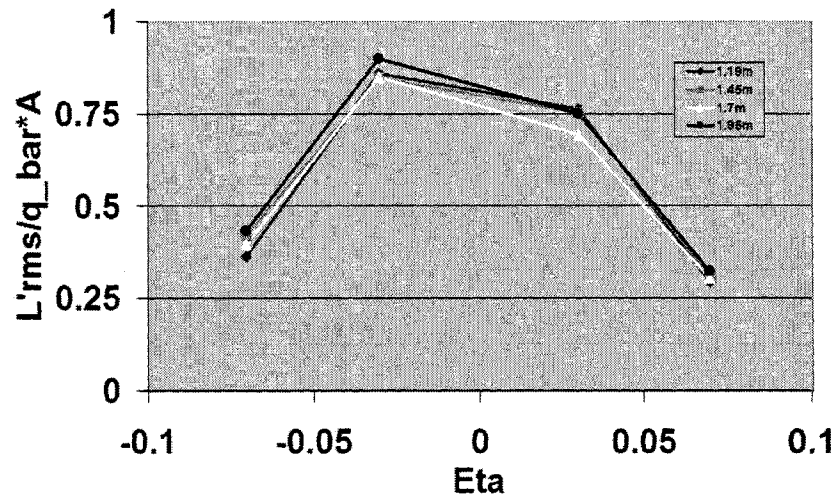


Figure 4.25: Normalized numerical  $L'_{rms}$  profile,  $U_1 = 3\text{ m/s}$

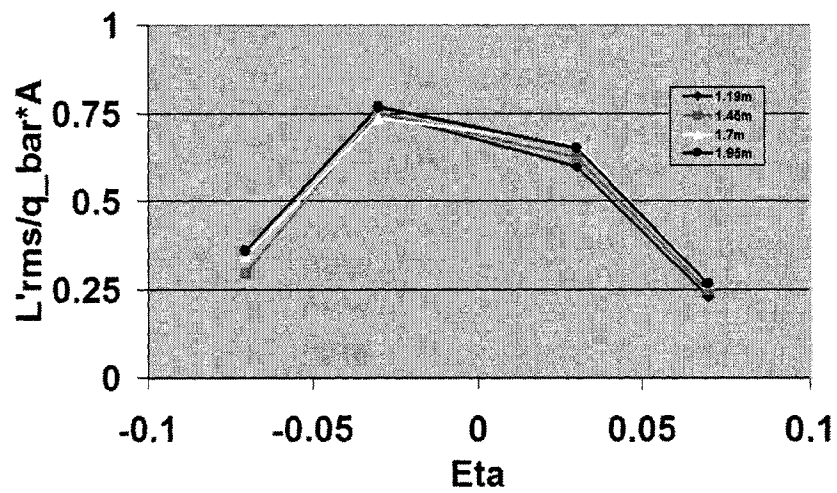


Figure 4.26: Normalized numerical  $L'_{rms}$  profile,  $U_1 = 7\text{ m/s}$

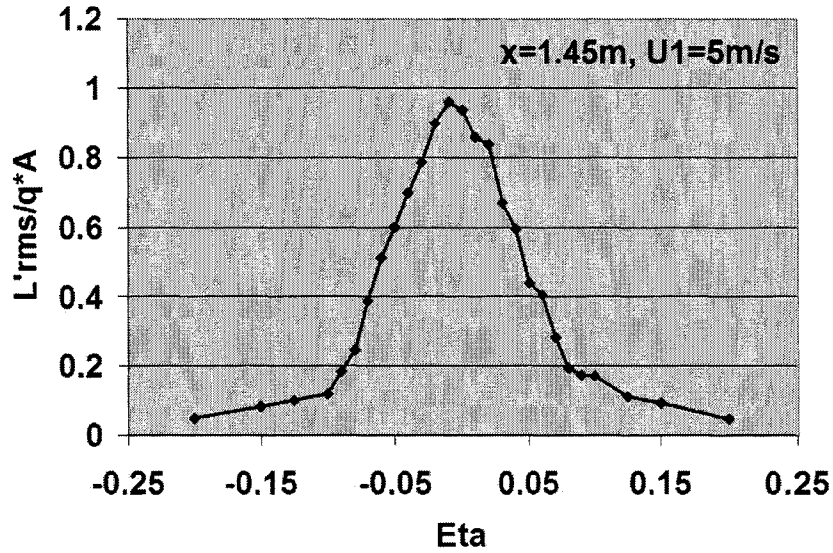


Figure 4.27: Fine  $\eta$  resolution numerical  $L'_{rms}$  profile

the other shear-layer statistics,  $u'_{rms}/U_1$ ,  $v'_{rms}/U_1$  etc. The profile peaks at  $\eta$  slightly below 0, with smooth transitions to the far-field values. In close agreement with the preceding profiles the maximum value of  $L'_{rms}/\bar{q}A$  is approximately 0.9.

#### 4.4.4 Peak Location Analysis

Based on the individual  $L'_{rms}$  PSD profiles the value of the constant  $K_2$  can be determined in the same manner as utilized for the experimental case. As the high-speed velocity profiles are much better behaved in the numerical model than the experimental model it is not necessary to consider only the low-speed data. However, as many of the profiles are still quite rough without a single central peak, determination of many of the peak centers was accomplished by averaging the half-power points of the peak. Figure 4.28 shows the relationship between the location of the frequency peak, and the downstream position normalized velocity,  $\bar{U}/x - x_0$ . Based on the slope of the best fit line the frequency constant was found to be  $K_{2-model} = 0.64$ .

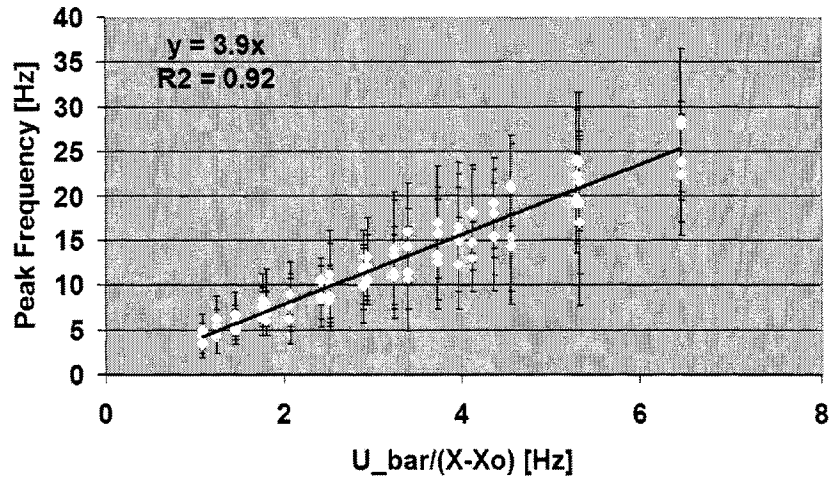


Figure 4.28: Numerical peak frequency vs normalized  $U_1$

#### 4.4.5 Chord Effects

An additional variable to be considered by the model is the relative effect of chord length on  $L'_{rms}$ . Small changes in chord length should be properly normalized by  $\bar{q}A$ . However, with large changes in chord length there is the possibility that changes in the dynamics of the shear-layer/wing interaction could significantly alter the character of the results. The relationship between the wing and shear-layer can likely be divided into three broad categories with transition regions likely existing between them:  $\delta_\omega/c \gg 1$ ,  $\delta_\omega/c \approx 1$ , and  $\delta_\omega/c \ll 1$ . The experimental and numerical data considered thus far characterizes only the case  $\delta_\omega/c \approx 1$ . Intuitively the case  $\delta_\omega/c \ll 1$  should be dominated by the shear-layer flow, with the wing merely responding to the flow and not significantly modifying it. As such it is expected that  $L'_{rms}/\bar{q}A$  will be self-similar for this regime and its behavior will closely mimic that of the layers statistical properties,  $u'_{rms}/U_1$ ,  $v'_{rms}/U_1$  etc. Figure 4.29 evaluates  $\delta_\omega/c \approx 0.3 \rightarrow 2.6$ . Over this range the behavior remains self-similar, and the magnitudes collapse when normalized by  $\bar{q}A$ . Additional runs were performed for  $U_1 = 5m/s$ ,  $\eta = 0.03$ ,  $\alpha = 0$

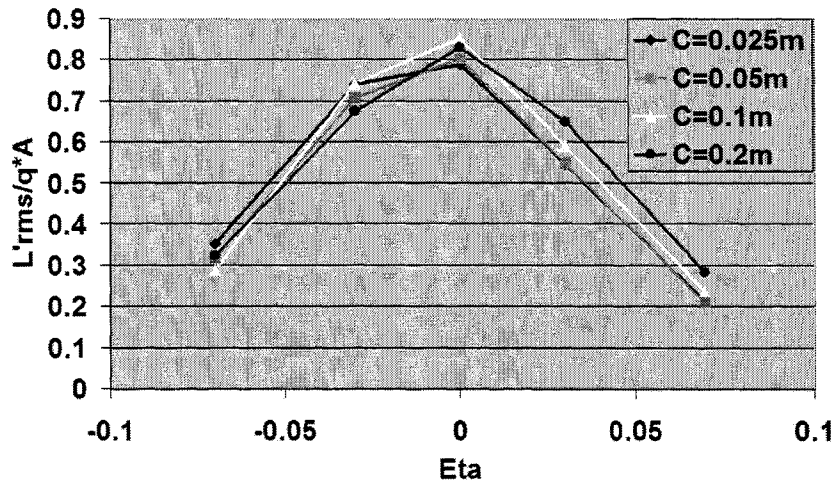


Figure 4.29: Numerical extrapolations to variable chord

and a range of chord lengths from  $c = 0.01 \rightarrow 1$ . As with the previous cases the results collapsed when normalized to a value of  $L'_{rms}/\bar{q}A = 0.69$ .

#### 4.4.6 Angle of Attack Effects on Coherent Structure Development

After the behavior of the layer and the wings response were determined to be independent of  $c$  at  $\alpha = 0^\circ$ , a final brief investigation was performed into the effects of  $\alpha$  on the evolution of the layer. Figure 4.30 shows several frames showing the relative positions and interactions of the wing, wake, and layer. The abscissa for this plot is  $x$  in meters, and the ordinate is  $y$  in m. In order to focus on the layer upstream and downstream of the wing, different scales have been chosen for the axes with  $x = 0 \rightarrow 2$  and  $y = -0.1 \rightarrow 0.1$ . The difference in scales distorts the appearance of the structures, which when plotted on equal scales appear roughly circular. For this case a larger chord length wing, with  $c = 0.25$  has been chosen to amplify the wings effect on the layer. The wing was located at  $\eta = 0.04$  and  $x = 1.19m$ . From this it is clear that with the wing above the layer and  $\alpha = 0^\circ$ , the wing and wake interact in a relatively passive manner. The coherent structures within the layer convect evenly by the wing

and appear relatively undisturbed. The wake is shed smoothly from the trailing edge, and eventually rolls into the layer. Within this series of frames the structures labeled as 1 and 2 undergo a pairing event, while structures 3, 4, and 5 all convect smoothly past the wing.

Figure 4.31 shows the behavior of the layer in response to an  $\alpha = 10^\circ$  wing. The remaining conditions are the same as the previous figure. In this series of frames the effect of the wing has changed significantly. Instead of passively interacting with the layer the wing draws the layer up to the leading edge and forces it down past the trailing edge. The mean shape of the layer closely mimics the shape of streamlines passing a wing for  $\alpha > 0^\circ$ . In addition to this mean effect the individual coherent structures are strongly affected. As the structures reach the leading edge of the wing they are often split into two components, with one convecting along the upper surface and one along the lower surface. At the trailing edge the two parts of the structure are re-combined but are spread out over a downstream length that is longer than the width of an undisturbed structure. This interaction is very similar to the BVI interaction where the bound vortex impinges on the wings leading edge. The deformation of these structures serves to decrease their coherence and disrupts the pairing process, upstream and downstream of the wing. In addition to strongly affecting the development of the layer, the interaction is likely sensitive to the vertical position of the wing for  $\alpha \neq 0^\circ$ , and deserves additional attention.

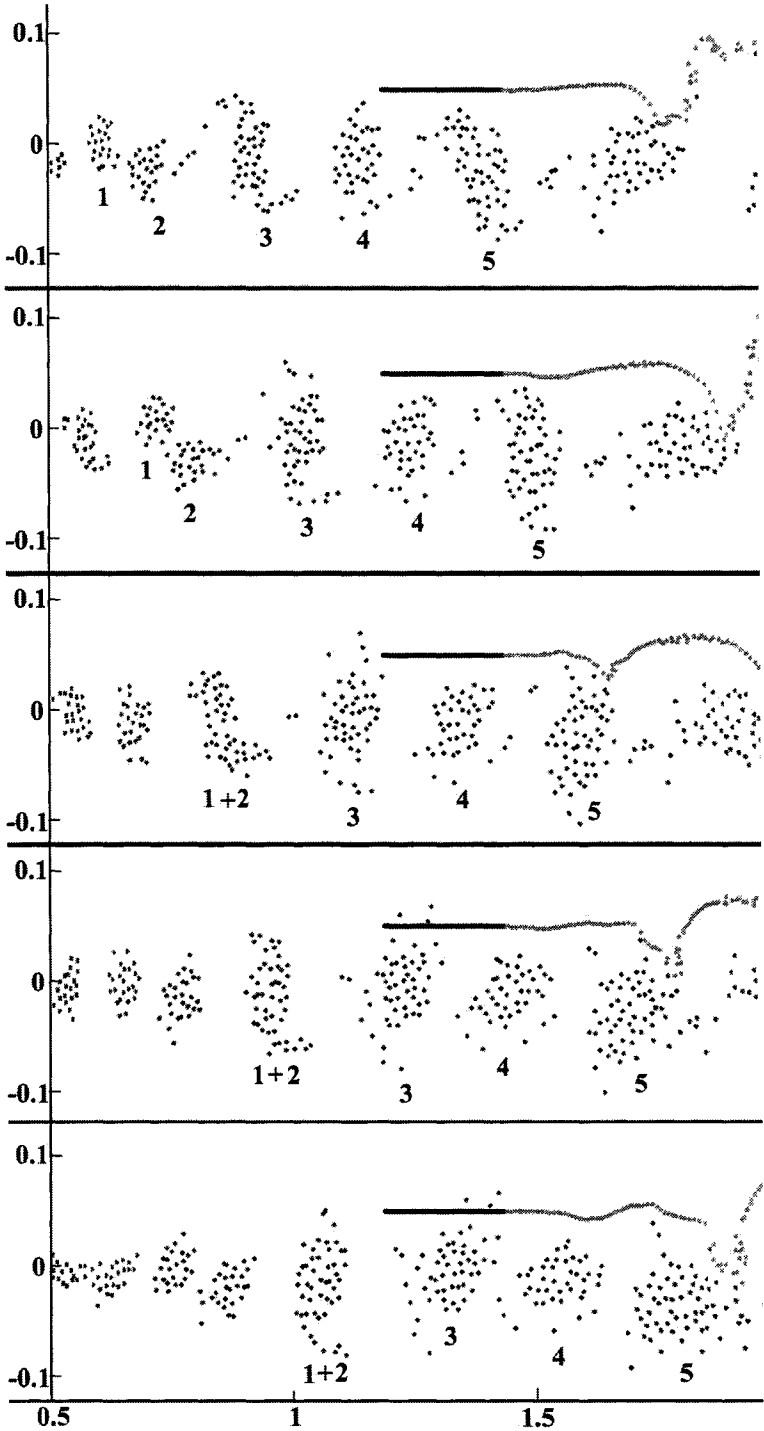


Figure 4.30:  $\alpha = 0^\circ$  vortex evolution

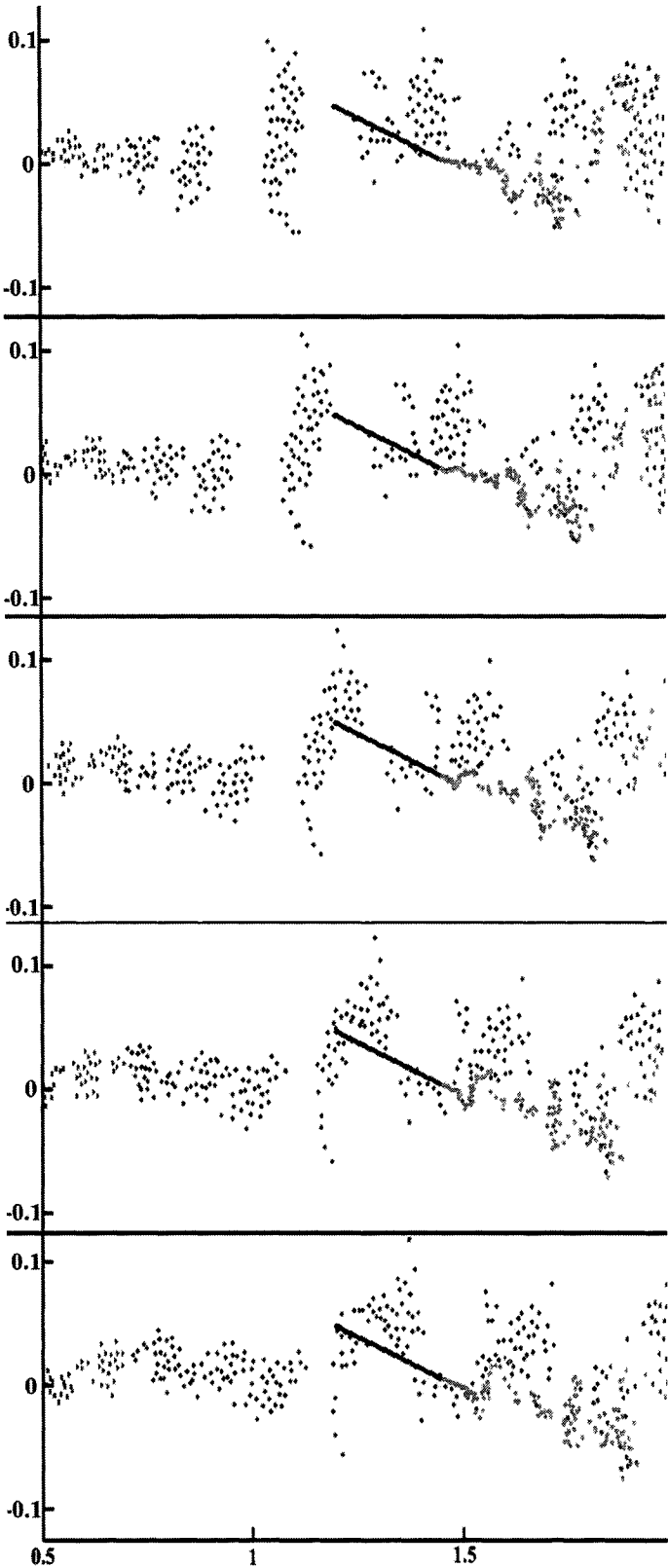


Figure 4.31:  $\alpha = 10^\circ$  vortex evolution

## Chapter 5

### DISCUSSION

#### 5.1 *Experimental Results Summary*

After consideration of the qualitative response of the experimental  $L'$  PSD and  $L'_{rms}$  profiles to changes in  $U_1$ ,  $x$ , and  $\eta$  several trends become apparent: excellent magnitude agreement for changes in  $x$ , appropriate change in magnitude with  $\eta$ , and a transition from free to forced shear-layer behavior for  $U_1 > 5m/s$ . After considering the unforced data, the  $L'$  PSD and  $L'_{rms}$  profiles collapse to a common set of normalized curves when changes in  $x$  and  $U_1$  are considered. For the  $L'_{rms}$  profiles  $y$  is normalized by  $x - x_0$ , and the magnitude of  $L'_{rms}$  is normalized by  $\bar{q}A$ . The frequency axis of  $L'$  PSD profiles are normalized by  $U_1/(x - x_0)$  while the ordinate is normalized by  $U_1^3 \rho A^2 (x - x_0)$ . While the current profiles remain rough this is an artifact of limited available averaging time. With longer averaging times the profiles should collapse more completely. Based on these profiles the wing's response is self-similar in the same fashion as the statistical properties,  $u'_{rms}$ ,  $v'_{rms}$ , etc.

Above  $U_1 = 7m/s$  sharp peaks appear in the PSD profiles at fixed frequencies whose locations are insensitive to further increases in  $U_1$  or  $x$ . Based on these, and similar behaviors of  $u'$  PSD profiles, the layer is acting in a forced manner instead of a free manor for  $U_1 > 5m/s$ . For  $U_1 \leq 5m/s$  the behavior is consistent with a free shear-layer. While some of the behavior of the higher speed data remain self-similar, i.e. the proper collapse of the  $L'_{rms}$  with  $x$ , the magnitudes of the  $L'$  PSD and  $L'_{rms}$  profiles are significantly below those for  $U_1 \leq 5m/s$ , and must be considered suspect. Without further research into the exact nature of the forcing mechanism, and modification of the numerical model to account for it, any discussion of the high-speed

data is speculative, and only the low-speed data will be considered and compared with numerical data.

Based on the PSD profiles the wing responds directly to the passage of coherent structures and does not significantly change the dynamics of the layer for  $\alpha = 0^\circ$  and  $\delta_\omega/c \approx 1$ . While the structures in the vicinity of the wing are likely deformed, the frequency at which they convect past the wing appears to be largely unaffected. When the location of the frequency profile peaks is considered they are clustered around  $St \approx 2$ , which is 40% below the expected value based on the theory of  $St = 3.3$ , or 30% below the valued based on the experimentally determined layer velocity characteristics of  $St = 2.8$ . The average value of  $\Delta St = 1.5$

Summarizing the quantitative data the maximum experimental value of  $L'_{rms}/\bar{q}A$  is 0.26, the average Strouhal half-power band-width is  $\Delta St = 1.5$ , and the maximum value of  $\frac{L'PSD}{U_1^3 \rho^2 A^2 (x-x_0)}$  is  $3.1 \times 10^{-3}$ . The values for these statistics vary with  $x$  by less than 10% for  $L'_{rms}$ , and less than 15% variation from the mean value for  $\Delta St$ . When the location of the peaks is analyzed the frequency constant is determined to be  $K_{2-lift} = 0.8$ .

### 5.1.1 Forced Shear-Layer Behavior

The discrepancy between the low and high-speed data is one of the more prominent and troubling features of the experimental results. This was not expected as the dynamics of free shear-layers are  $Re$  invariant. While there is the possibility that the presence of the wing with it's additional length scale has modified the flow, the observed behavior is inconsistent with this possibility as the effect is not present at all  $U_1$ .

Based on the data taken for  $U_1 \geq 7m/s$ , the wing appears to be responding to a forced instead of free shear-layer. This behavior closely mirrors that observed in  $u'$  investigations during shear-layer characterization, Section 3.1.3. Plots of the statistical wing data for  $U_1 \leq 5m/s$ , with varying downstream distance display strong

self-similarity: normalized  $L'$  PSD and  $L'_{rms}$  profiles collapse well and  $\Delta St$  is approximately constant. While the high-speed values of  $L'_{rms}$  also display the appropriate variation with  $x$  and  $\eta$ , the  $L'$  PSD profiles display large peaks at fixed frequencies and poor  $\Delta St$  agreement, while the  $L'_{rms}$  profiles display reduced magnitudes that are low by a factor of 2 or greater.

This mixture of self-similar, and un-self-similar behavior indicate that the layer is being forced for  $U_1 > 5m/s$ , at  $32Hz$  with a  $16Hz$  sub-harmonic. At the lower velocity conditions either the frequency of coherent structure passage has fallen below that of the forcing frequency or the forcing due to the motor is inconsistent and appears only when a threshold level of motor load is exceeded. In either case the layer behaves as unforced for these conditions. Within a canonical forced shear-layer, 2-D forcing amplifies the two-dimensionality of the layer, leading to increased values of  $u'_{rms}/U_1$  and  $v'_{rms}/U_1$  and would likely cause higher values of  $L'_{rms}$ . Based on the  $u'_{rms}/U_1$  data the level of turbulence within the layer has decreased in an atypical fashion.

Because the layer is forced, and not acting in either a free or canonical forced fashion it's high-speed behavior is difficult to predict, and the high-speed data must be considered suspect. While some of the high-speed data reinforce the trends present at lower speeds, the character of the  $L'$  PSD profiles, and magnitudes of  $L'_{rms}$  are not representative. However, the  $U_1 \approx 3$  and  $5m/s$ , data appears to be un-corrupted: the  $L'$  PSD profiles are broad and relatively smooth with peaks whose magnitudes, locations, and widths collapse well when normalized, and the  $L'_{rms}$  profiles are likewise well behaved. To determine the specific mechanisms causing the turbulence level reduction is beyond the scope of the current research. As the low-speed data is well behaved it will be taken as generally representative.

## **5.2 Numerical Results Summary**

The numerical results have been recorded in the same fashion as the experimental data, though at fewer  $\eta$  values. The most noticeable new trend is the level of agree-

ment between the low and high-speed data. In addition to self-similarity for  $U_1$  the numerical data is self-similar in  $x$ , and shows the expected dependence on  $\eta$ . There is a slight decrease in overall magnitude for  $L'_{rms}$  and  $L'$  PSD profiles, with increasing  $U_1$ , due to the accuracy considerations discussed in Section 4.3.3, and not physical phenomena.

From the numerical data the maximum value of  $L'_{rms}/\bar{q}A$  is 0.9, while the remaining values vary by less than 5% from the mean value. The average  $\Delta St$  for the numerical profiles is 1.9 with less than 15% variability among the data. For the profiles of  $\frac{L' PSD}{U_1^3 \rho^2 A^2 (x-x_0)}$  the maximum value taken from the heavily averaged runs presented in Figure 4.21 is  $1.2 \times 10^{-2}$ , with less than 30% variability in the data from the mean value. Based on the locations of the peaks  $K_{2- numerical}$  for the model is 0.64, corresponding to an average Strouhal location of 2.7, which is 19% below the theoretically expected value, 4% below the expected value based on the velocity characteristics of the layer, and 20% below the experimental value.

### 5.3 Comparison of Numerical and Experimental Data

There is excellent qualitative agreement between the low-speed experimental data and the numerical data. Figure 5.1 shows a comparison of the normalized numerical and experimental  $L'$  PSD profiles taken for  $U_1 \approx 5m/s$  for  $\eta = 0.03$  and  $\eta = 0.02$  respectively. Both profiles display broad, relatively smooth peaks without the fixed frequency peaks found in the high-speed experimental data. Further the Strouhal extents of the profiles are similar, with the experimental profile being slightly narrower. Figure 5.2 displays the normalized  $L'_{rms}$  profiles for  $U_1 \approx 5m/s$  and  $x = 1.96m$ . Qualitatively the plots are quite similar. The curves properly collapse when normalized, with both plots showing maximum values that occur at  $\eta$  slightly below 0. The remaining profiles all compare favorably.

The Strouhal locations and half power bandwidths also compare favorably, agreeing to within 30%. This shift is likely associated with the numerical model underes-

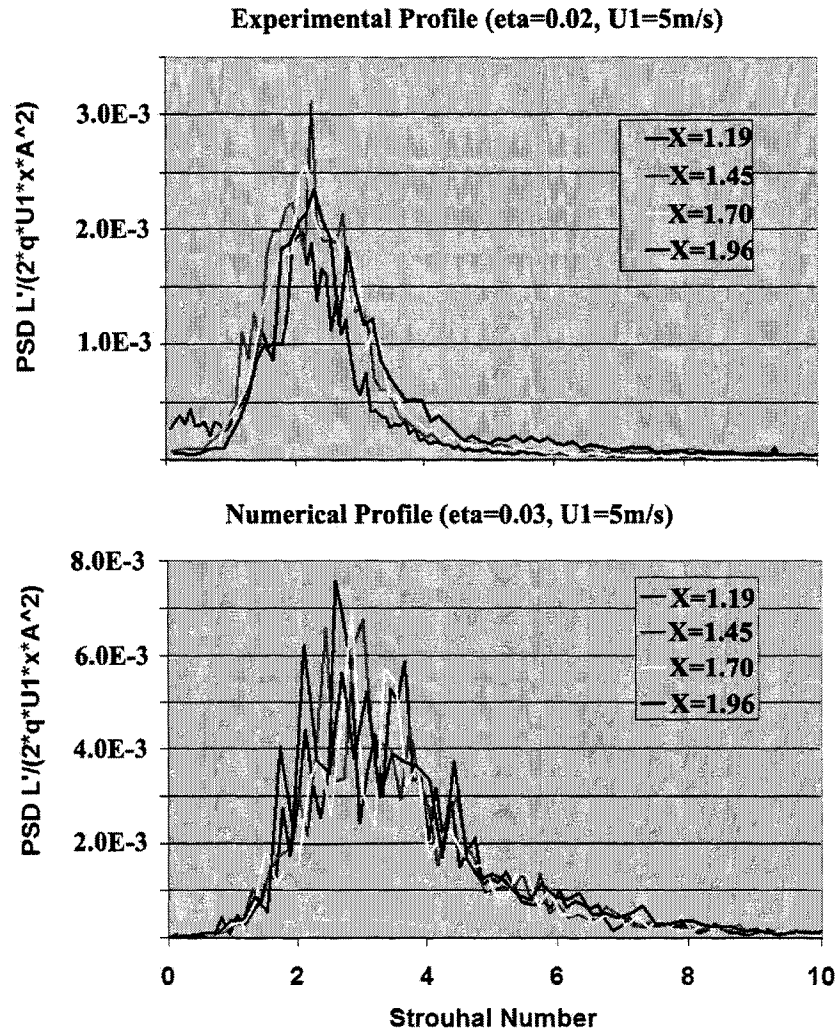


Figure 5.1: Comparison of numerical and experimental normalized  $L'$  PSD profiles ( $U_1 = 5\text{m/s}$ ,  $\eta = 0.02, 0.03$  respectively)

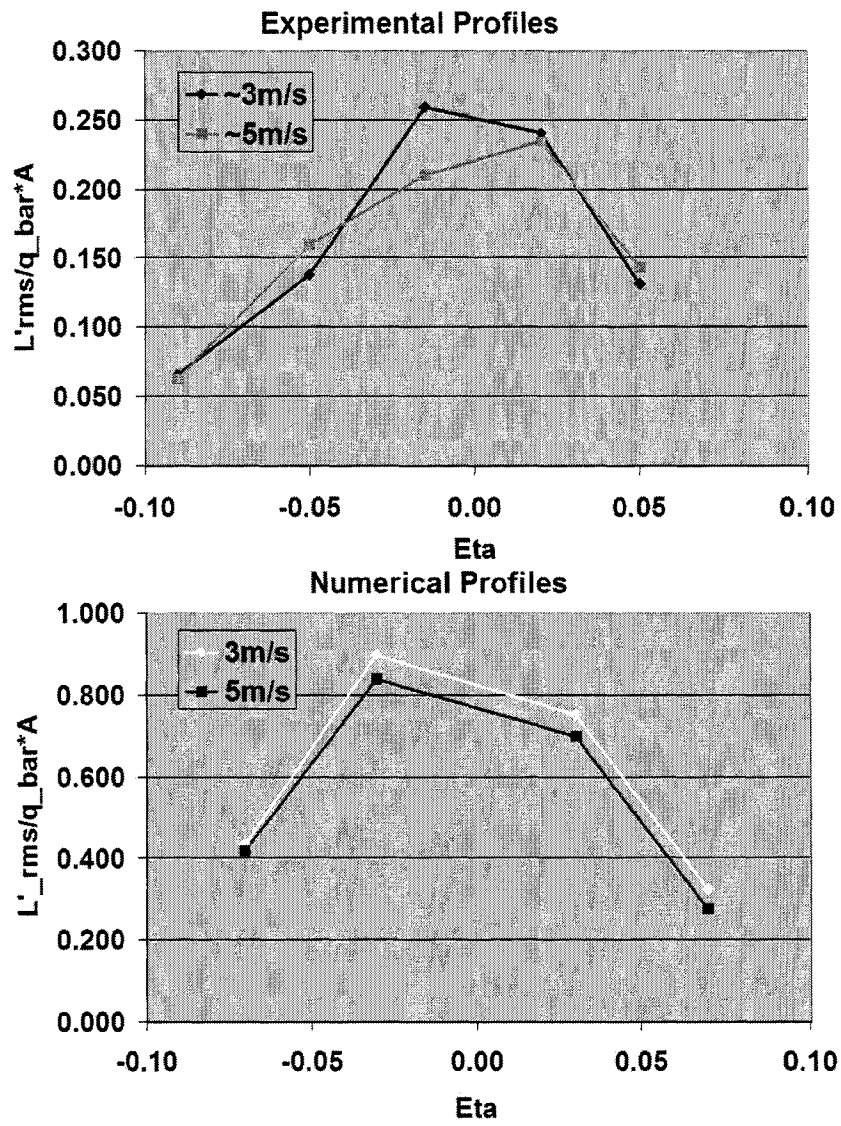


Figure 5.2: Comparison of numerical and experimental  $L_{rms}$  profiles, for  $x=1.96m$

timating the width of the layer, Table 4.2, leading to slightly higher numerical values of  $f_m$  and increased  $\Delta St$ .

The only major discrepancy between the experimental and numerical data is their magnitudes. There is a factor of 3.5 difference between the numerical and experimental values of  $L'_{rms}/\bar{q}A$ . For the peak values of  $\frac{L'PSD}{U_1^3\rho^2A^2(x-x_0)}$  there is a factor of 4 difference between the numerical and experimental cases. Two issues lead to this over-estimate of the magnitude of  $L'$  by the numerical model. The first is the convergence of the numerical model to a unrealizable purely 2-D case. This leads to an over-estimate of the layer two-dimensionality, and values of  $u'_{rms}/U_1$  and  $v'_{rms}/U_1$  that are up to a factor of 2 high, and should lead to values of  $L'$  that are too high as well. The second issue is the over-estimate of the variation in lift due to the  $\frac{\partial\Gamma}{\partial t}$  term present in Equation 4.17, and displayed in Figure 4.8. As the wing is exposed to constantly changing conditions this non-steady term is likely the major cause of lift over-estimation in both the PSD and RMS behavior of the wings. While the factor of 3.5 discrepancy is larger than desired it is in line with the errors in  $C_L$  measured by Poling, Dadone, and Telionis[29] in their BVI work. Likely by shifting the wing model from a coarse panel method to the boundary volume model of Qian and Vezza[31] would significantly improve the level of agreement between the present numerical model and experiments.

#### **5.4 Recommendations for Additional Work**

There is the potential for additional work on both the experimental and numerical aspects of the current research, which could serve to more finely characterize the shear-layer wing interaction and/or bring the current simplified model more in line with the flow system which prompted this research. Given the experimental and numerical capabilities developed for this research the next logical step is to more finely characterize the interaction. This can be accomplished through significantly longer averaging times to produce smoother PSD profiles, better estimates of  $\Delta St$ , and more

accurate peak magnitudes. The available data could also be expanded upon by considering additional  $\eta$  values within the layer to produce finer  $L'_{rms}$  profiles. In addition to more completely characterizing the current flow configuration there is room for more accurate numerical representation of the shear-layer and wing. Two promising improvements are to use overlapping particles to simulate the vorticity shed into the shear-layer at each time step in the fashion of Ghoniem and Ng[25], and to model the wing boundary layer vorticity distribution and lift determination in the manner of Qian and Vezza[31]. The use of a more accurate wing and lift determination scheme should significantly improve experimental and numerical magnitude agreement.

While these extensions would better characterize the shear-layer/wing interaction they are unlikely to elucidate new behaviors or trends. Utilizing the available setup a wider range of  $\delta_\omega/c$  and additional values of  $\alpha$  could be investigated. Likely, no additional trends will be displayed for smaller chords than those investigated thus far, but  $\delta_\omega/c \gg 1$  could change the dynamics of the relationship between the wing and layer, especially with  $\alpha \neq 0$ . Further,  $\alpha \neq 0$  more closely simulates the flow configuration when the wing flaps are extended in high lift configuration. When larger values of  $\alpha$  are considered the mean effect of the wing induces a strain field on the vortex cores that appears to strongly affect the development of the coherent structures, though the effect has not yet been quantified.

In addition to work with the current experiment and numerical code, there is room for 2-D extrapolations designed to bring the flow more in line with the driving physical system. Several 2-D configurations whose interaction with a wing bear consideration are: the near field of a wide-bore jet, two stacked shear-layers with like sign vorticity, and the interaction of a co-flowing jet and wing, Figure 2.1. While realizing these flows will necessitate developing a new experiment, they can be readily realized with the numerical model. Each flow can be created by adding additional shear-layers of appropriate vorticity sign, position, and strength, to the current model. While developing the code will be relatively easy, significantly longer computational times

will be necessary due to the increased number of vortex particles in the flow.

Two final directions for additional work are to shift the flow being considered from 2-D to 3-D, and from incompressible to compressible. To shift from 2-D to 3-D will represent a major step towards bringing the considered flow in line with the physical system. Development of a 3-D experiment and equivalent numerical model should follow the same process as the development of progressively more accurate 2-D representation: beginning with a single axi-symmetric shear-layer and wing, fully characterizing this, and then progressing towards an axi-symmetric co-flowing jet. For the numerical model this will require development of a 3-D vortex code of the type used by Srigrarom[45], Inoue[41], and Ashurst and Meiburg[36]. Shifting the flow to compressible will likely change the magnitudes of the responses though much of the character should remain, as coherent structures have also been observed in compressible layers, though their development and interaction are more poorly understood[4].

## Chapter 6

# CONCLUSIONS

The physical system motivating this research is complex: heated high-speed compressible engine exhaust, surrounded by cool but accelerated bypass air, further enveloped by the free stream, interacting with, and modifying the lift on the wing behind the engine. This work focuses on developing an understanding of this interaction through a simplified system designed to capture the key components. One critical feature of shear-flows is the development of coherent structures with significant circulations and lifespans that act in a deterministic manner[2][1]. These structures are present as vortex-rings in jets and as quasi-2-D spanwise vortices in 2-D mixing-layers. A simplified 2-D shear-layer is studied to highlight the effect of these coherent structures on a wing. This captures the non-steady nature of the physical flow, while being experimentally and numerically tractable.

The problem has not been studied before though the literature contains extensive experimental and theoretical work on shear-layers, and the helicopter blade-vortex interaction has some relevance. For the present research a 2-D shear-layer was set up in a 0.91m x 0.91m test section wind-tunnel by using a splitter plate and series of pressure dropping screens to separate the flow into two streams which are rejoined at the test section entrance. The shear-layer has  $r = 0.43$ , and is capable of continuous operation up to a maximum speed of  $U_1 = 25m/s$ , though the layer was found to become forced above  $U_1 = 5m/s$ . The behavior of layer was quantified through measurements of the  $\Theta_e$ ,  $\partial\delta_w/\partial x$ , and similarity of  $\bar{U}$  profiles. The experimental growth constant is within 10% of the theoretical value[3], with a linear fit constant of  $R^2 = 0.99$ . Further, the  $\bar{U}$  profiles collapse to within a 10% or better normalized

velocity range at any given height.

A balsa wood wing with a natural frequency of  $94\text{Hz}$  was inserted in the layer using a support structure that is isolated from the tunnel itself.  $L'$  PSD, and  $L'_{rms}$  profiles were taken at  $x = 1.19, 1.45, 1.70,$  and  $1.95\text{m}$ , corresponding to normalized distances of between 480 and 760  $\Theta_e$ . At each downstream distance positions of  $\eta = 0.05, 0.02, -0.015, -0.05,$  and  $-0.09$  were investigated. Experimental data was collected and analyzed for  $U_1 \approx 3,$  and  $5\text{m/s}$ . Higher values of  $U_1 \approx 7, 9$  and  $11\text{m/s}$  were considered, but the layer was found to be forced for  $U_1 > 5\text{m/s}$ . For simplicity all data is taken at  $\alpha = 0^\circ$ . The peak non-steady lift frequency was found to occur at  $St \approx 2$ , with a half-power band-width of  $\Delta St \approx 1.5$ . Non-dimensionalized, the maximum value of  $\frac{L' PSD}{U_1^3 \rho^2 A^2 (x-x_0)}$  was found to be  $3.11 \times 10^{-3}$ , while the maximum value of  $L'_{rms}/\bar{q}A$  was 0.26. Shifting the maximum value of  $L'_{rms}/\bar{q}A$  to a somewhat more intuitively meaningful scale; this lift variation corresponds to oscillations in the wing angle of attack with an rms value of  $2.3^\circ$ .

A numerical model has been created to help interpret the experiments, and allow extrapolation to a wider range of geometries and flow conditions. The model is based on the Vortex-Method technique of discretizing the vorticity containing portion of the flow into vortex-particles. The evolution of the layer is captured by allowing these particles to freely convect at the local velocity. Numerical runs at  $r = 0.6$  and  $\lambda = 0.25$  benchmark the model against published experimental and numerical data[18]. This test showed that the numerical layer is self-similar, and in reasonable agreement with the experiments of Yule, Spencer, and Oster and Wygnanski, as reported by Inoue[18]. The statistical values  $u'_{rms}/U_1$  and  $v'_{rms}/U_1$  were found to be 30% and 80% above the mean experimental value. When the current model is compared to the results of Inoue's[18] numerical model,  $u'_{rms}/U_1$  is low by 28% and  $v'_{rms}/U_1$  is high by 10%. The discrepancy between numerical and experimental data for this case is primarily due to 3-D vorticity distribution in experiments. The current value of  $-u'v'_{rms}/U_1^2$  is in good agreement at 15% above the experimental value though 43% below Inoue's numerical

result. The current models growth rate  $\partial\delta_\omega/\partial x$  is 40% below Inoue's numerical model, though only 24% below experimental values reported by Inoue. This low spreading rate is likely due to minor differences in Vortex Method application such as the choice of core functions, and the treatment of the flow upstream and downstream of the modeled domain.

A vortex panel scheme is used to model the wing, and the unsteady behavior tested by comparing the wings lift and circulation histories for an impulsive start with theory[42]. The paneled wing captures the wings circulation to within 10% for most of the test though over-estimates the effect of rapid fluctuations on the wing's lift. When the model is run for the experimental condition the  $L'$  PSD and  $L'_{RMS}$  profiles are self-similar and collapse to common curves when non-dimensionalized. The dominant wing forcing frequency was found to be  $St = 2.7$ , with  $\Delta St \approx 1.9$ . The maximum magnitude of  $\frac{L' PSD}{U_1^3 \rho^2 A^2 (x-x_0)} = 1.8 \times 10^{-2}$  and the maximum value of is  $L'_{rms}/\bar{q}A = 0.9$ .

There is good qualitative agreement between the experiment and numerical models, with both displaying smooth spectral and rms profiles that collapse to common curves when non-dimensionalized. The Strouhal peak locations and half-power Strouhal band-widths agree to within 35%. When considering peak magnitudes the numerical model over-estimates the maximum value of  $L'$  PSD by a factor of 4, and  $L'_{rms}$  by a factor of 3.5. This discrepancy is primarily due to limitations of the lift determination scheme and the wing model, though the discrepancy between the 3-D experiment and 2-D model also contributes.

Two extrapolations were performed with the numerical model: varying  $\delta_\omega/c$  from  $0.3 \rightarrow 2.6$ , and shifting  $\alpha$  from  $0^\circ$  to  $10^\circ$ . Varying  $\delta_\omega/c$  through this range for  $\alpha = 0$  had no effect on the response of the wing. Changes in  $\alpha$  caused a significant qualitative effect on the shear-layer/wing interaction. For  $\alpha = 10^\circ$  the strain field induced by the wing's mean circulation draws the layer up, causing the coherent structures to impinge and split on the leading edge of the wing. The split structures were eventually shed

from the trailing edge but do not re-form into distinct structures until convecting a distance approximately equal to the visual thickness of the layer. These preliminary results indicate that even more complex interactions may occur for  $\alpha > 0$  and may justify additional study.

Observation of the evolution of the vortex particle distribution within the numerical model coupled with the behavior of the  $L'$  PSD and  $L'_{rms}$  profiles indicate that for  $\alpha = 0^\circ$  and  $\delta_w/c \approx 1$  the wing responds passively to the layer and does not significantly modify it. However, as expected the coherent structures present in the shear-layer directly cause a non-steady wing lift. The current research indicates that coherent vortical structures are capable of significantly effecting the non-steady lift of a wing, and causing the flap vibrations observed during development of the Boeing 777.

## BIBLIOGRAPHY

- [1] Mungal, M. and Hollingsworth, D., "Organized motion in a very high Reynolds number jet," *Physics of Fluids A*, Vol. 10, October 1989.
- [2] Roshko, A., "Structure of Turbulent Shear Flows: A New Look," *AIAA Journal*, Vol. 14, No. 10, October 1976.
- [3] Brown, G. L. and Roshko, A., "On Density Effects and Large Structures in Turbulent Mixing Layers," *Journal of Fluid Mechanics*, Vol. 64, 1974, pp. 775–816.
- [4] Dimotakis, P., "Turbulent Free Shear Layer Mixing and Combustion," *High Speed Flight Propulsion Systems, Volume 137, Prog. Astronautics and Aeronautics*, AIAA, 1991.
- [5] Dahm, W., Friedler, C., and Tryggvason, G., "Vortex structure and dynamics in the near field of a coaxial jet," *Journal of Fluid Mechanics*, Vol. 241, 1992, pp. 371–402.
- [6] Champagne, F. and Wygnanski, I., "An experimental investigation of coaxial jets," *International Journal of Heat and Mass Transfer*, Vol. 14, 1971, pp. 1445–1461.
- [7] Ko, N. and Au, H., "Coaxial jets of different mean velocity ratios." *Journal of Sound and Vibration*, Vol. 100, 1985, pp. 203–219.
- [8] Tank, S. and Ko, N., "Coherent structure interaction in an unexcited coaxial jet," *Experiments in Fluids*, Vol. 17, 1994, pp. 147–157.
- [9] Martin, J. and Meiburg, E., "Numerical investigation of three-dimensionally evolving jets subject to axisymmetric and azimuthal perturbations," *Journal of Fluid Mechanics*, Vol. 230, 1991, pp. 271–318.
- [10] Buresti, G., Talamelli, A., and Petagna, P., "Experimental Characterization of the Velocity Field of a Coaxial Jet Configuration," *Experimental Thermal and Fluid Science*, Vol. 19, 1994, pp. 135–147.

- [11] Nickels, T. and Perry, A., "An experimental and theoretical study of the turbulent coflowing jet." *Journal of Fluid Mechanics*, Vol. 309, 1996, pp. 157–182.
- [12] Buresti, G., Petagna, P., and Talamelli, A., "Experimental investigation on the turbulent near-field of coaxial jets," *Experimental Thermal and Fluid Science*, Vol. 17, 1998, pp. 18–26.
- [13] Bradshaw, P., "The Effects of Initial Conditions on the Development of a Free Shear Layer," *Journal of Fluid Mechanics*, Vol. 26, 1966.
- [14] Hernan, M. A. and Jimenez, J., "Computer analysis of high-speed film of the plane turbulent mixing layer," *Journal of Fluid Mechanics*, Vol. 119, 1982.
- [15] Bernal, L. and Roshko, A., "Streamwise Vortex Structure in Plane Mixing Layers," *Journal of Fluid Mechanics*, Vol. 170, September 1986, pp. 499–525.
- [16] Breidenthal, R., "Structure in Turbulent Mixing Layers and Wakes Using a Chemical Reaction," *Journal of Fluid Mechanics*, Vol. 109, 1981, pp. 1–24.
- [17] Bernal, L., Breidenthal, R., Brown, G., Konrad, J., and Roshko, A., "On the Development of Three-Dimensional Small Scales in Turbulent Mixing Layers," *2nd Symposium on Turbulent Shear Flows*, 1980.
- [18] Inoue, O., "A Numerical Simulation of Turbulent Mixing Layer by Discrete Vortex Method," *AIAA Paper*, AIAA-84-0434, 1984.
- [19] Sementi, J. P., "Jet Exhaust and Wing Flap Interactions," *AIAA Paper*, AIAA-2002-0017, 2002.
- [20] Hussain, A. K. M. F. and Zaman, K., "An experimental study of organized motions in the turbulent plane mixing layer," *Journal of Fluid Mechanics*, Vol. 159, 1985, pp. 85–104.
- [21] Yang, Z. and Karlsson, S. K., "Evolution of coherent structures in a plane shear layer," *Phys. of Fluids*, Vol. 3, No. 9, 1991, pp. 2207–2219.
- [22] Fiedler, H. and Mensing, P., "The Forced mixing layer between parallel streams," *Journal of Fluid Mechanics*, Vol. 123, 1982, pp. 91–130.
- [23] Ho, C. M. and Huang, L., "Subharmonics and vortex merging in mixing layers," *Journal of Fluid Mechanics*, Vol. 119, No. 443-473, 1982.

- [24] Roberts, F. A. and Roshko, A., "Effects of periodic forcing on mixing in turbulent shear layers and wakes," *AIAA Paper*, AIAA-85-570, 1985.
- [25] Ghoniem, A. F. and NG, K. K., "Numerical study of the dynamics of a forced shear layer," *Physics of Fluids*, Vol. 30, No. 3, March 1987.
- [26] Oster, D. and Wygnanski, I., "The forced mixing layer between parallel streams," *Journal of Fluid Mechanics*, Vol. 123, 1982, pp. 91–130.
- [27] Wygnanski, I., Oster, D., and Fielder, H., "A Forced, Plane, Turbulent Mixing-Layer: A Challenge for the Predictor," *Turbulent shear flows II : selected papers from the Second International Symposium on Turbulent Shear Flows*, Springer-Verlag, 1979, p. New York.
- [28] Tangler, J., "Schlieren and Noise Studies of Rotors in Forward Flight," *33rd Annual National Forum of the American Helicopter Society*, Paper 77, 1977, pp. Washington, DC.
- [29] Poling, D. R., Dadone, L., and Telionis, D. P., "Blade-Vortex Interaction," *AIAA Journal*, Vol. 27, No. 6, June 1989.
- [30] Panaras, A., "Numerical Modeling of the Vortex/Airfoil Interaction," *AIAA Journal*, Vol. 25, 1987, pp. 5–11.
- [31] Qian, L. and Vezza, M., "Simulation of parallel blade-vortex interaction using a discrete vortex method," *The Aeronautical Journal*, November 1999, pp. 537–543.
- [32] Zaman, K. and Hussain, A. K. M. F., "Turbulence suppression in free shear flows by controlled excitation," *Journal of Fluid Mechanics*, Vol. 103, 1981, pp. 133–159.
- [33] Jones, G. W., Cincotta, J. J., and Walker, R. W., "Aerodynamic Forces on a Stationary and Oscillating Circulate Cylinder at High Reynolds Numbers," *Nass Technical Report*, NASA TR R-300 1969.
- [34] Hald, O. H., "Convergence of Vortex Methods for Euler's Equations. II," *SIAM Journal of Numerical Analysis*, Vol. 16, No. 5, October 1979.
- [35] Chorin, A., "Numerical study of slightly viscous flow," *Journal of Fluid Mechanics*, Vol. 57, 1973, pp. 785–796.

- [36] Ashurst, W. and Meiburg, E., "Three-dimensional shear layer via vortex dynamics," *Journal of Fluid Mechanics*, Vol. 189, 1988, pp. 87–116.
- [37] Inoue, O. and Leonard, A., "Vortex Simulation of Forced/Unforced Mixing Layers," *AIAA Journal*, Vol. 25, No. 11, November 1987.
- [38] Basu, A., Prabhu, A., and Narasimha, R., "Vortex Sheet Simulation of a Plane 'Canonical' Mixing Layer," *Computers and Fluids*, Vol. 21, No. 1, 1992, pp. 1–30.
- [39] Ashurst, W., "Numerical Simulation of Turbulent Mixing Layers via Vortex Dynamics," *Turbulent Shear Flows (Durst, Editor)*, Springer-Verlag, 1979.
- [40] Blevins, R., "Application of the Discrete Vortex Method to Fluid-Structure Interaction," *ASME Journal of Pressure Vessel Technology*, Vol. 113, August 1991.
- [41] Inoue, O., "Vortex Simulation of Spatially Growing Three-Dimensional Mixing Layers," *AIAA Journal*, Vol. 27, No. 11, 1989.
- [42] Katz, J. and Plotkin, A., *Low-Speed Aerodynamics, from Wing Theory to Panel Methods*, McGraw Hill Inc., 1991.
- [43] Leonard, A., "Vortex methods for flow simulation," *J. Comput. Physics*, Vol. 37, 1980, pp. 289.
- [44] Kundu, P. K., *Fluid Mechanics*, Academic Press, 1990.
- [45] Srigrarom, S., *On the Formation of Vortex Breakdown over Delta Wings*, Ph.D. Dissertation, University of Washington, 2001.
- [46] Bonnet, J. P., Delville, J., Glauser, M., Antonia, R. A., and et. al., "Collaborative testing of eddy structure identification methods in free turbulent shear flows," *Experiments in Fluids*, Vol. 25, 1998.
- [47] Cohen, J., Marasli, B., and ski, V. L., "The interaction between the mean flow and coherent structures in turbulent mixing layers," *Journal of Fluid Mechanics*, Vol. 260, 1994, pp. 81–94.
- [48] Jian-Guo Liu and Zhouping Xin, "Convergence of the Point Vortex Method for 2-D Vortex Sheet," *Mathematics of Computation*, Vol. 70, No. 234, April 2000.
- [49] Kuwahara, K., "Study of Turbulent Wake behind a Bluff Body by Vortex Method," *Proceedings of IUTAM Symposium on Turbulence and Chaotic Phenomena in Fluids (T. Tatsumi editor)*, 1983.

- [50] Sementi, J. P., "Wing Flap and Engine Exhaust Interaction," *Masters Thesis*, University of Washington, 2002.

## Appendix A

The data presented in Appendix A represents the remaining experimental data, beyond that presented in Chapter 3, and is presented for completeness.

### A.1 Fixed Position, Variable Velocities

The PSD profiles presented in this section are taken at fixed downstream and vertical positions, on the dimensionless axes of normalized Lift PSD vs Strouhal number, and display the change in character of the PSD profile with increasing velocity.

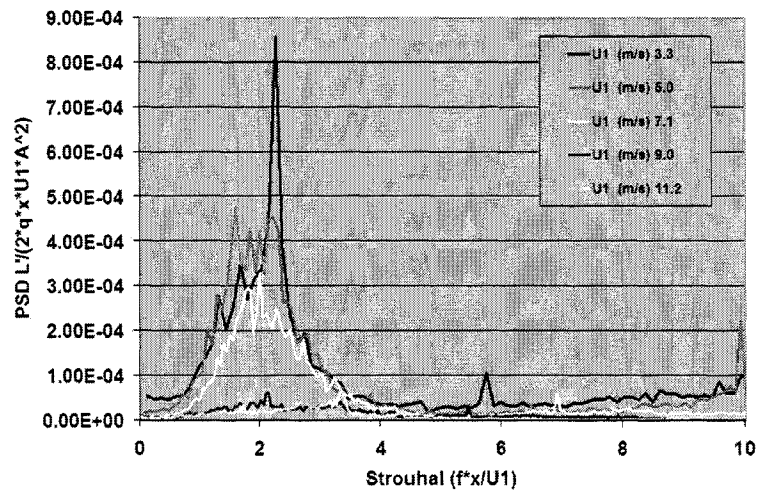


Figure A.1: Experimental Lift PSD  $\eta = 0.05$ ,  $x=1.19\text{m}$

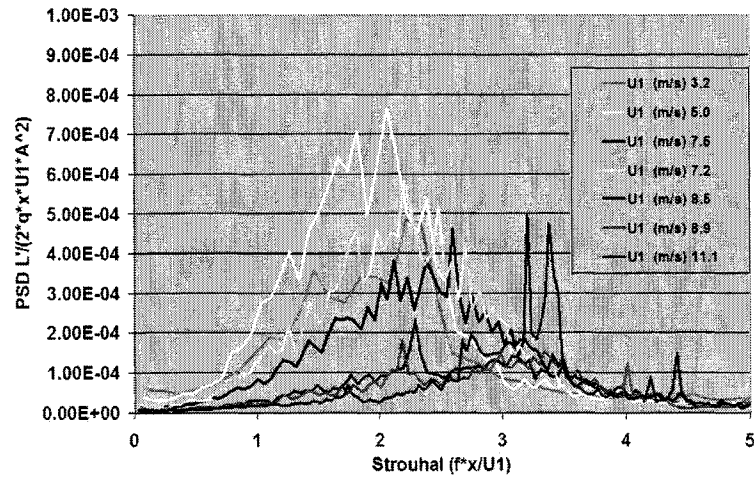


Figure A.2: Experimental Lift PSD  $\eta = -0.05$ ,  $x=1.19\text{m}$

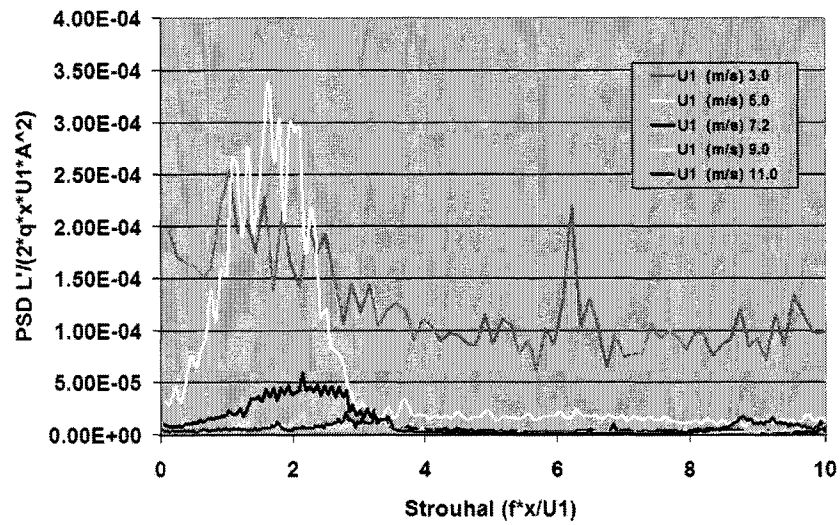


Figure A.3: Experimental Lift PSD  $\eta = -0.09$ ,  $x=1.19\text{m}$

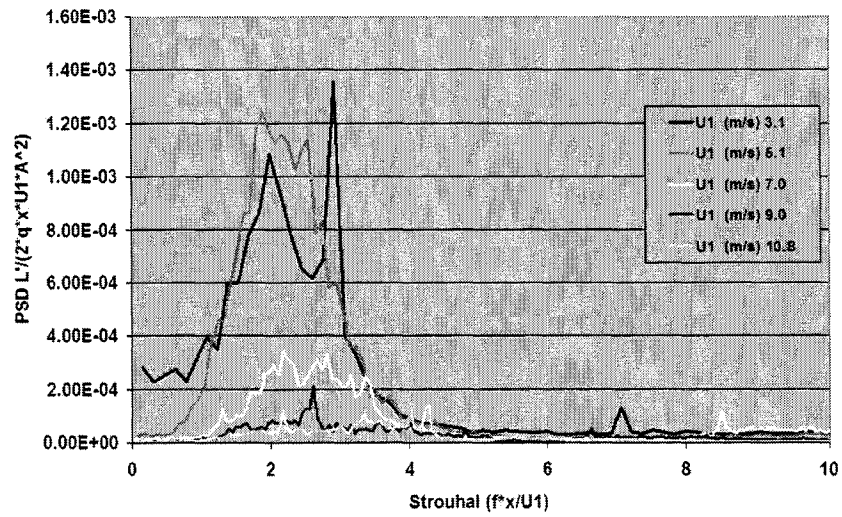


Figure A.4: Experimental  $L'_{rms}$  PSD,  $x=1.45$  m,  $\eta=0.05$

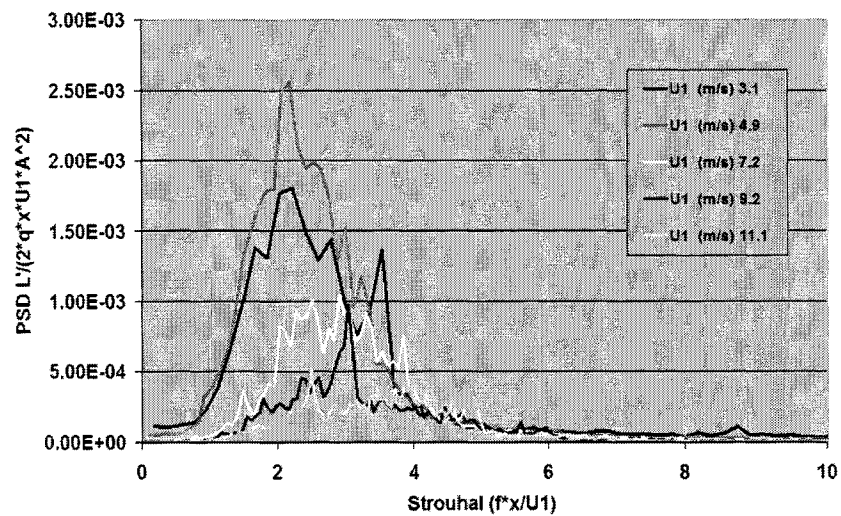


Figure A.5: Experimental  $L'_{rms}$  PSD,  $x=1.70$  m,  $\eta=0.02$

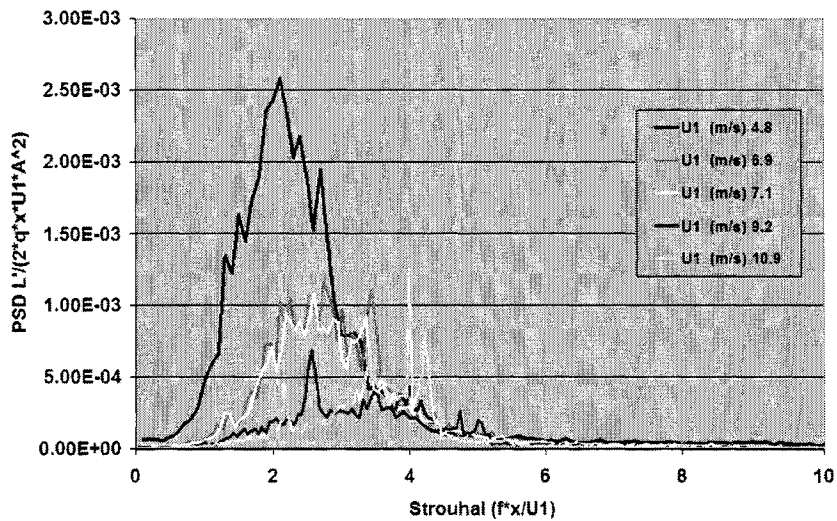


Figure A.6: Experimental Lift PSD  $\eta = -0.015$ ,  $x=1.45m$

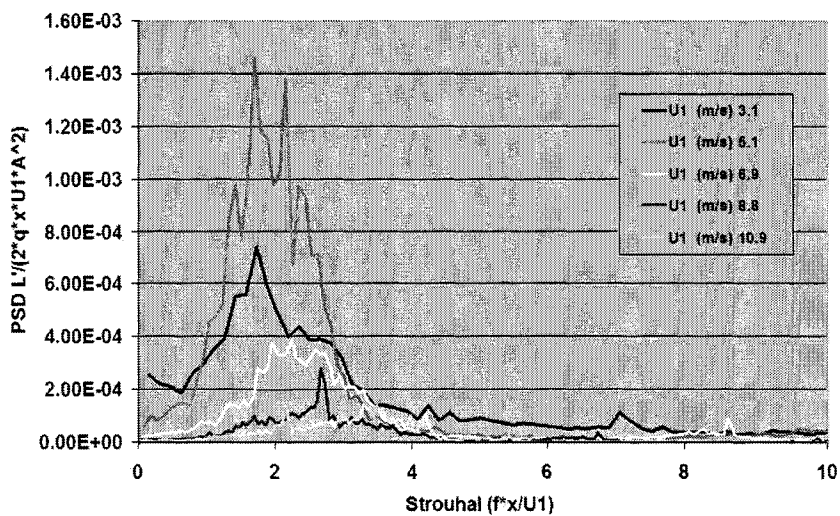


Figure A.7: Experimental Lift PSD  $\eta = -0.05$ ,  $x=1.45m$

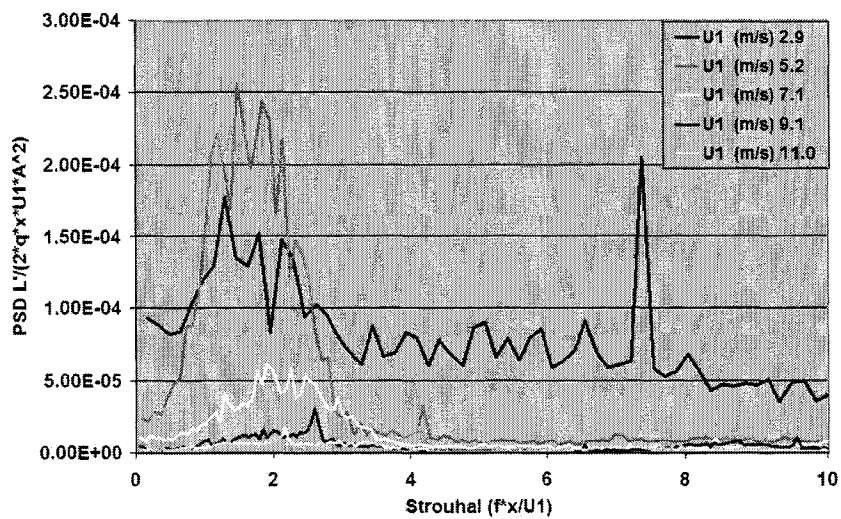


Figure A.8: Experimental Lift PSD  $\eta = -0.09$ ,  $x = 1.45\text{m}$

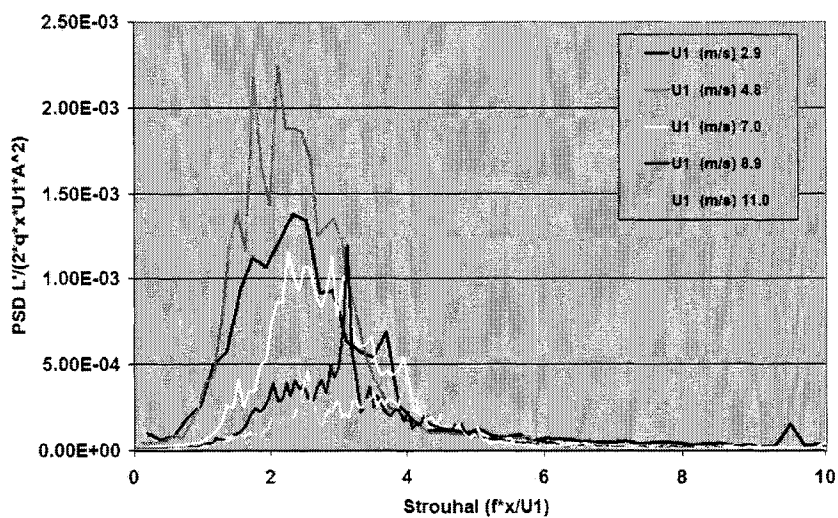


Figure A.9: Experimental Lift PSD  $\eta = -0.015$ ,  $x = 1.70\text{m}$

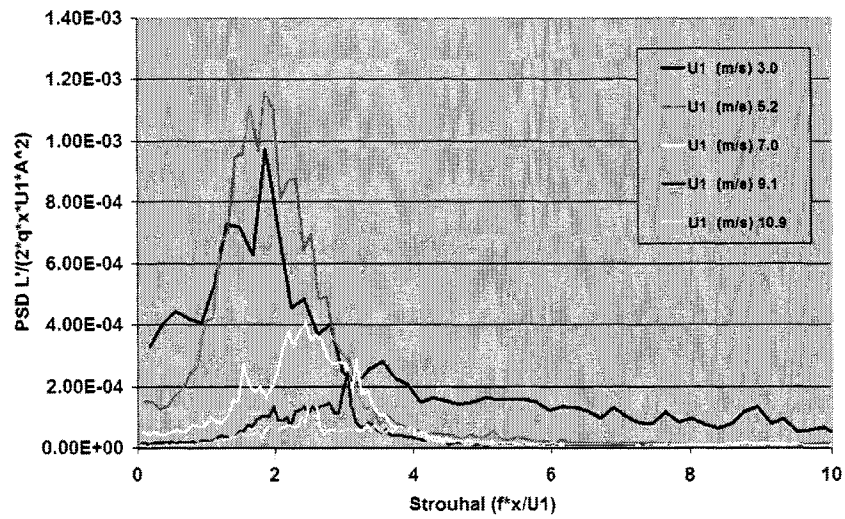


Figure A.10: Experimental Lift PSD  $\eta = -0.05$ ,  $x=1.70\text{m}$

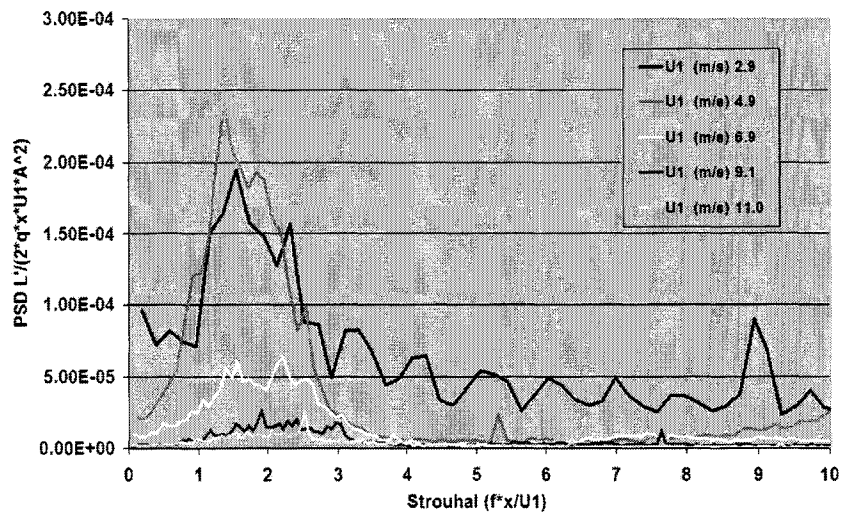
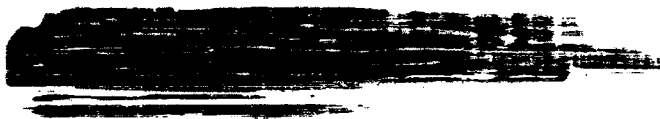


Figure A.11: Experimental Lift PSD  $\eta = -0.09$ ,  $x=1.70\text{m}$



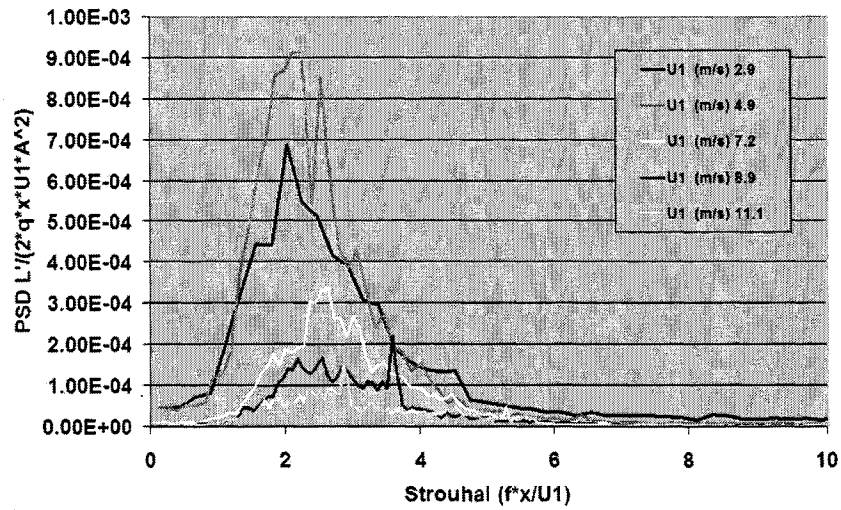


Figure A.12: Experimental Lift PSD  $\eta = 0.05$ ,  $x=1.96\text{m}$

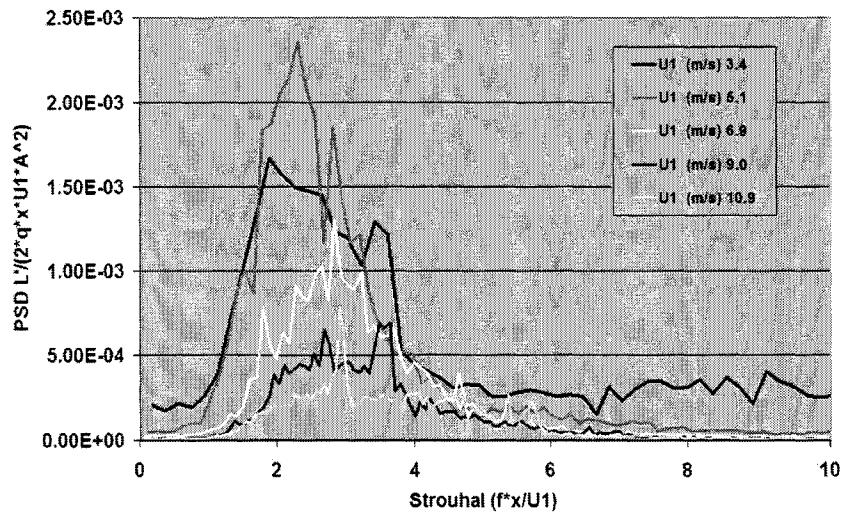


Figure A.13: Experimental  $L'_{rms}$  PSD,  $x=1.96\text{ m}$ ,  $\eta=0.02$

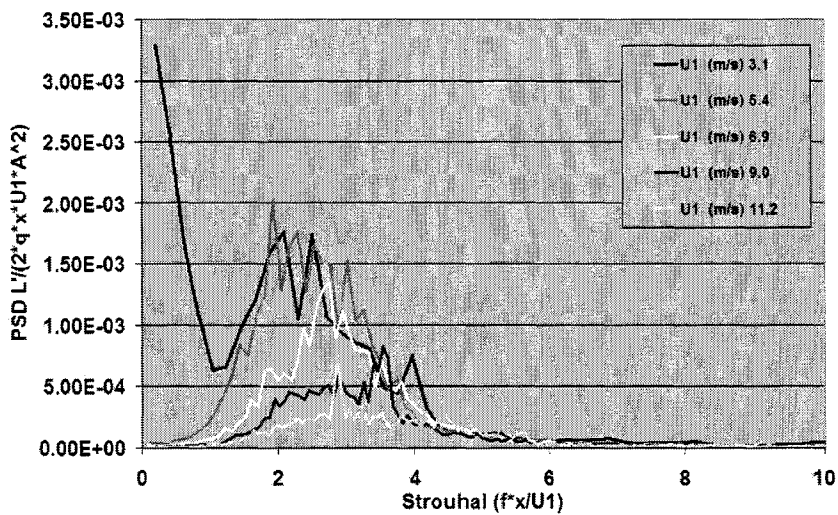


Figure A.14: Experimental Lift PSD  $\eta = -0.015$ ,  $x=1.96m$

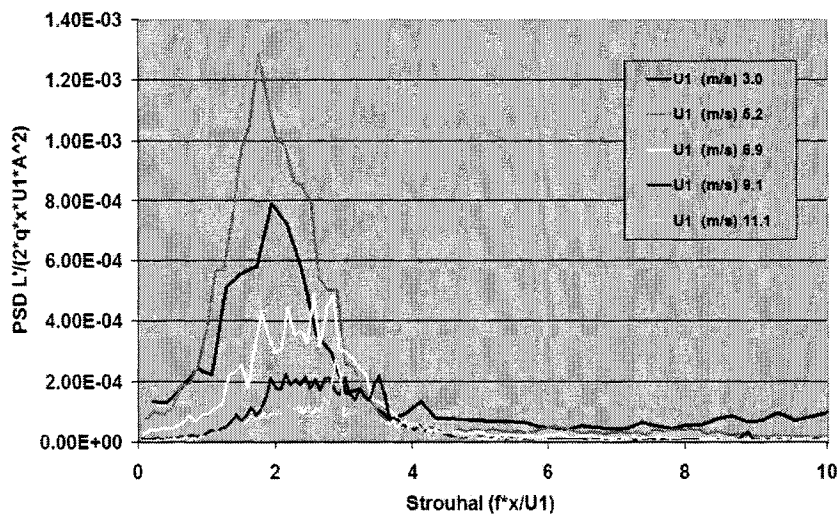


Figure A.15: Experimental Lift PSD  $\eta = -0.05$ ,  $x=1.96m$

### A.2 Fixed Height, Fixed Velocity, Variable Downstream Distance

The PSD profiles presented in this section are presented at fixed vertical positions and fixed velocities, displaying the change in character of the PSD profile with increasing velocity.

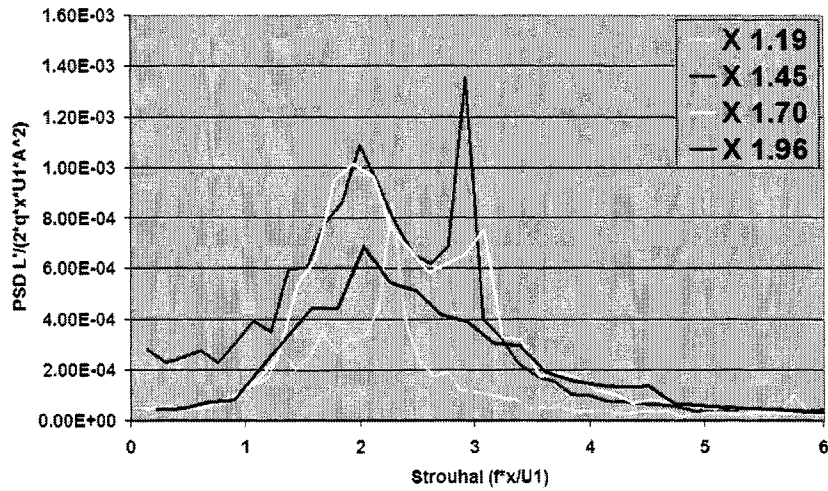


Figure A.16: Experimental Lift PSD  $\eta = 0.05$ ,  $U_1=3$

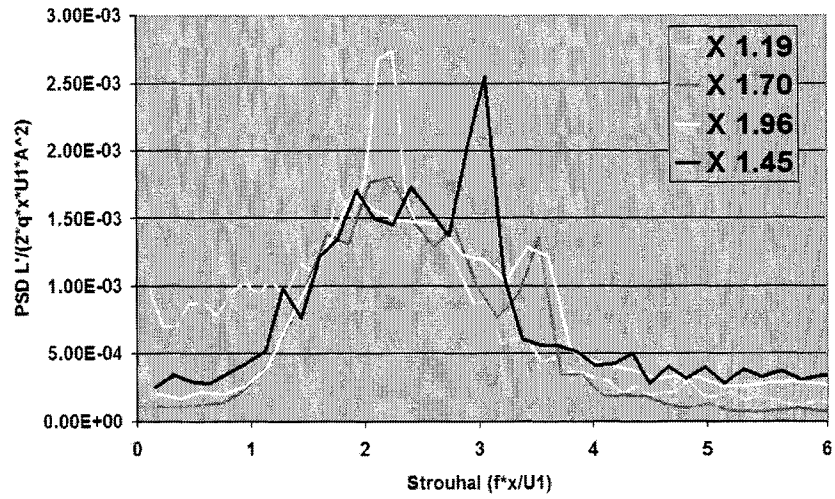


Figure A.17: Experimental  $L'_{rms}$  PSD,  $\eta=0.02$ ,  $U_1=3$  m/s

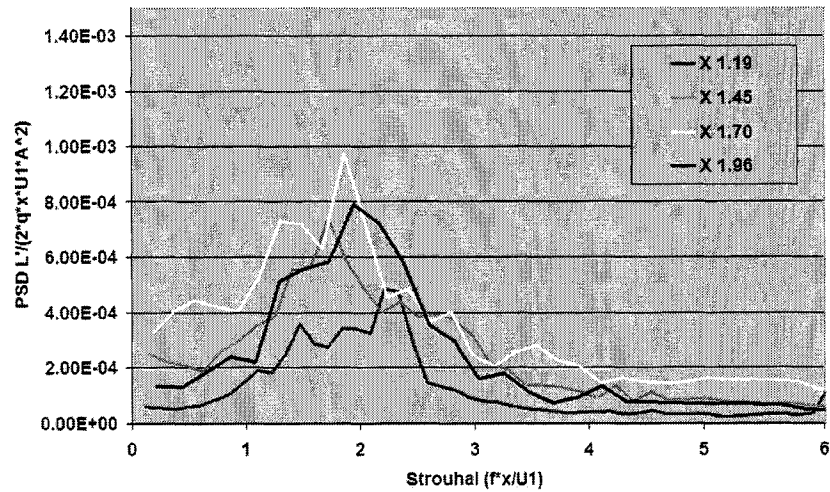


Figure A.18: Experimental Lift PSD  $\eta = -0.05$ ,  $U_1=3$

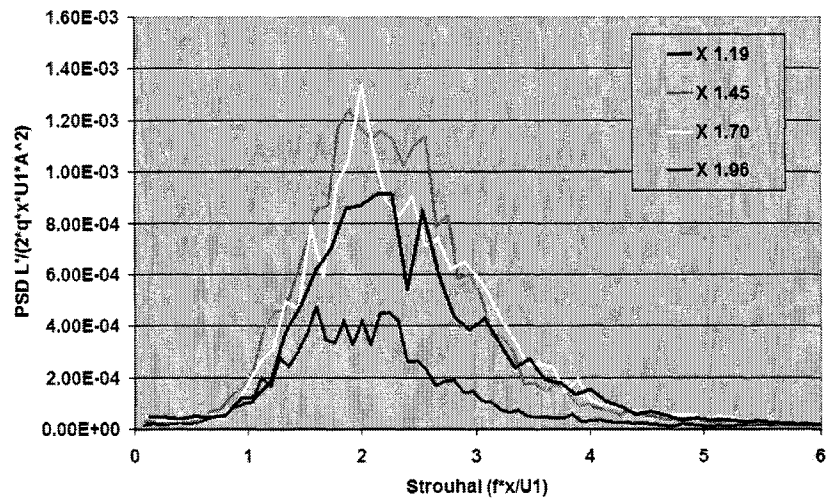


Figure A.19: Experimental Lift PSD  $\eta = 0.05$ ,  $U_1 = 5$

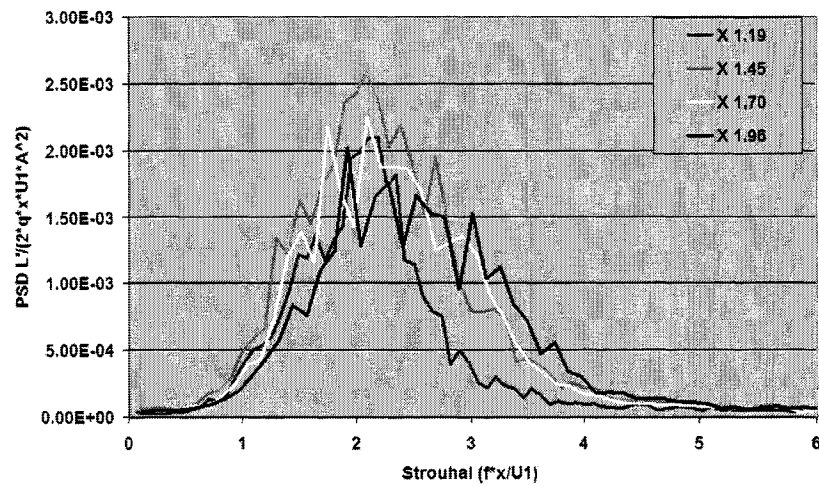


Figure A.20: Experimental  $L'_{rms}$  PSD,  $\eta = -0.015$ ,  $U_1 = 5$  m/s

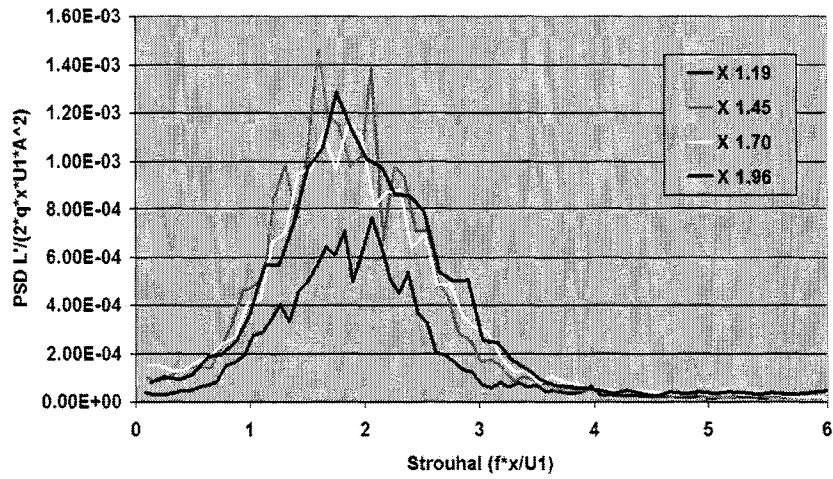


Figure A.21: Experimental Lift PSD  $\eta = -0.05$ ,  $U_1=5$

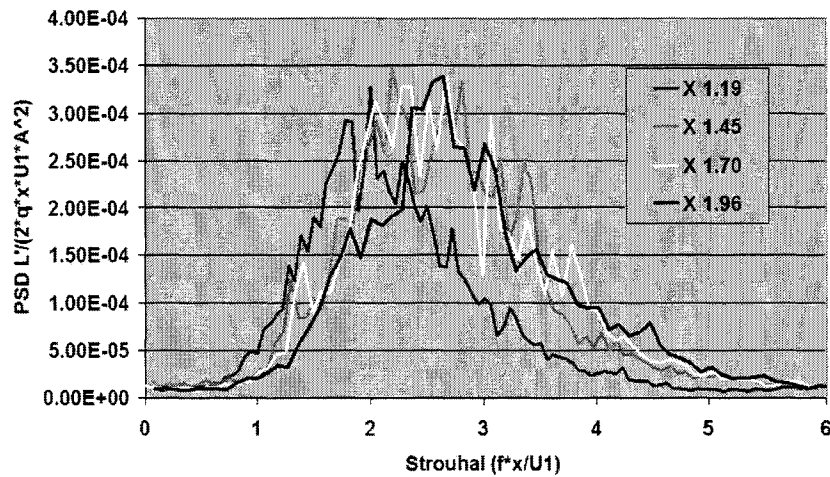


Figure A.22: Experimental Lift PSD  $\eta = 0.05$ ,  $U_1=7$

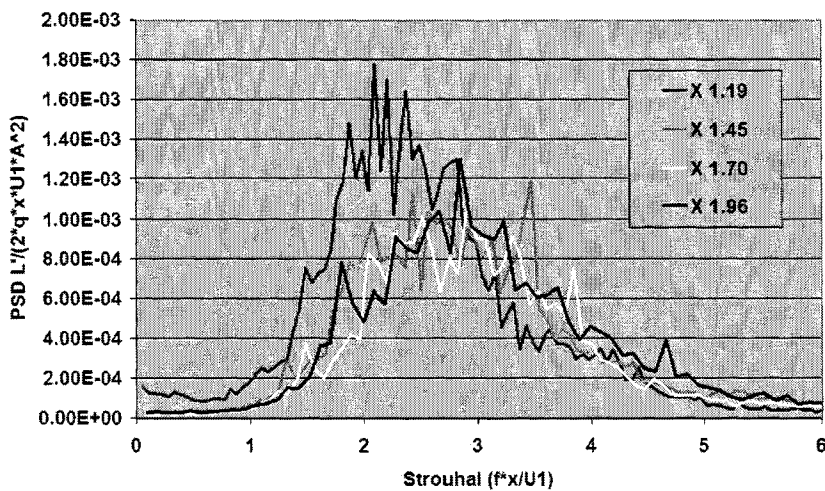


Figure A.23: Experimental Lift PSD  $\eta = 0.02$ ,  $U_1 = 7$

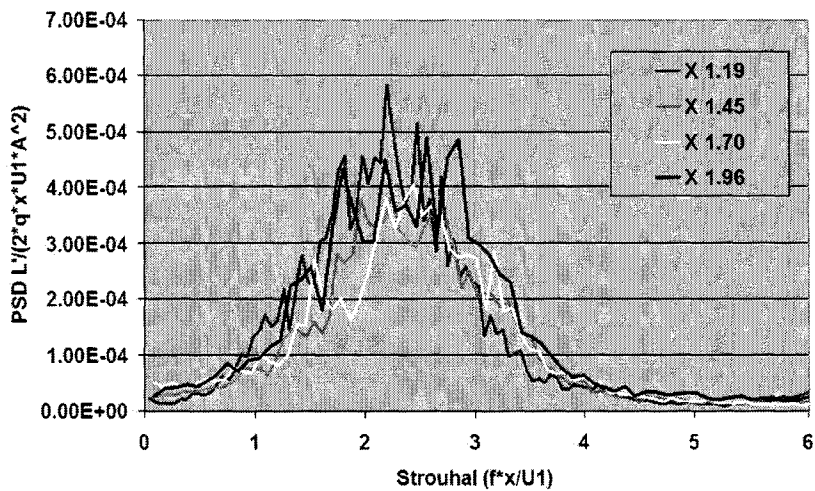


Figure A.24: Experimental  $L'_{rms}$  PSD,  $\eta = -0.05$ ,  $U_1 = 7$  m/s

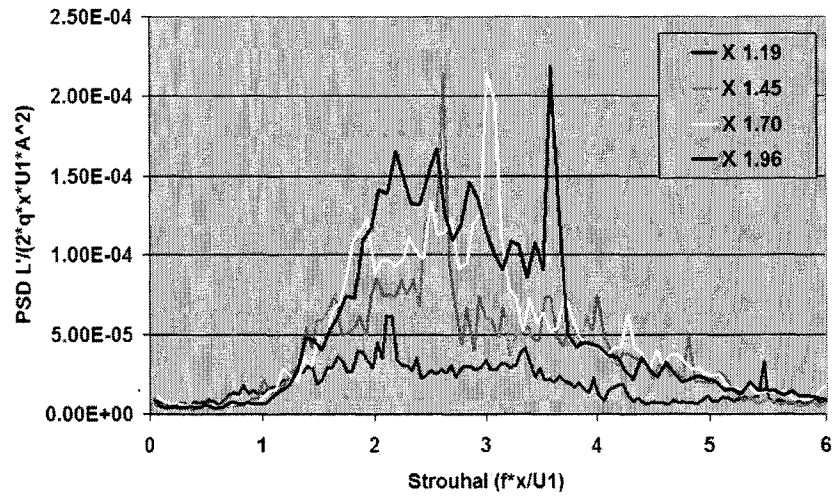


Figure A.25: Experimental Lift PSD  $\eta = 0.05$ ,  $U_1=9$

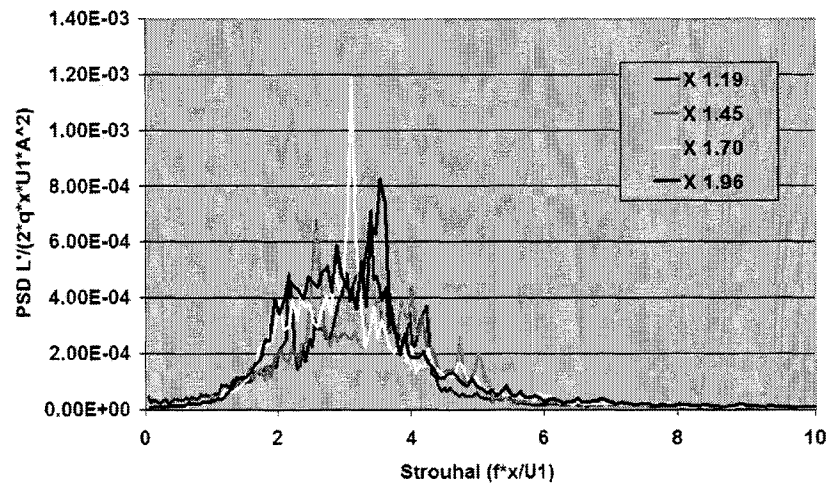


Figure A.26: Experimental Lift PSD  $\eta = -0.015$ ,  $U_1=9$

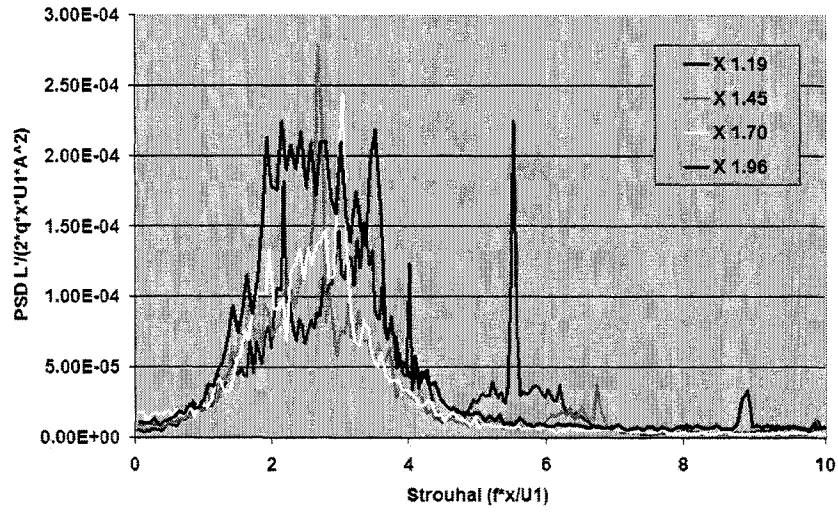


Figure A.27: Experimental  $L'_{rms}$  PSD,  $\eta = -0.05$ ,  $U_1 = 9$  m/s

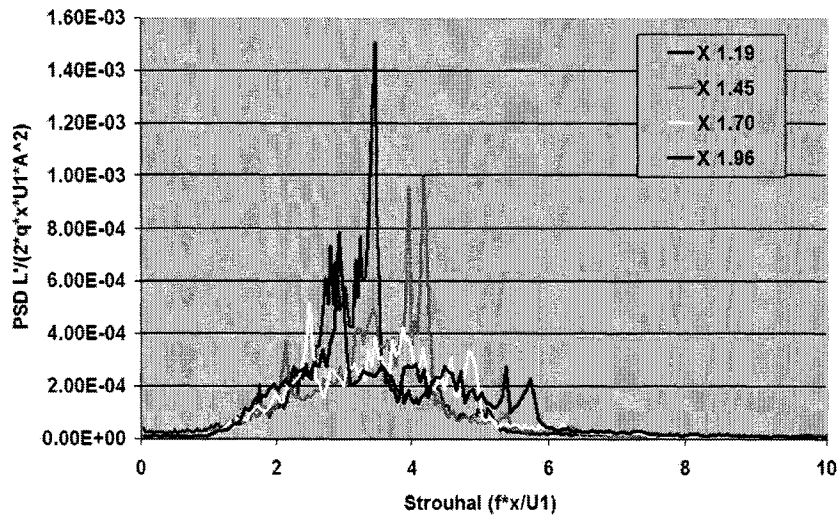


Figure A.28: Experimental Lift PSD  $\eta = 0.02$ ,  $U_1 = 11$

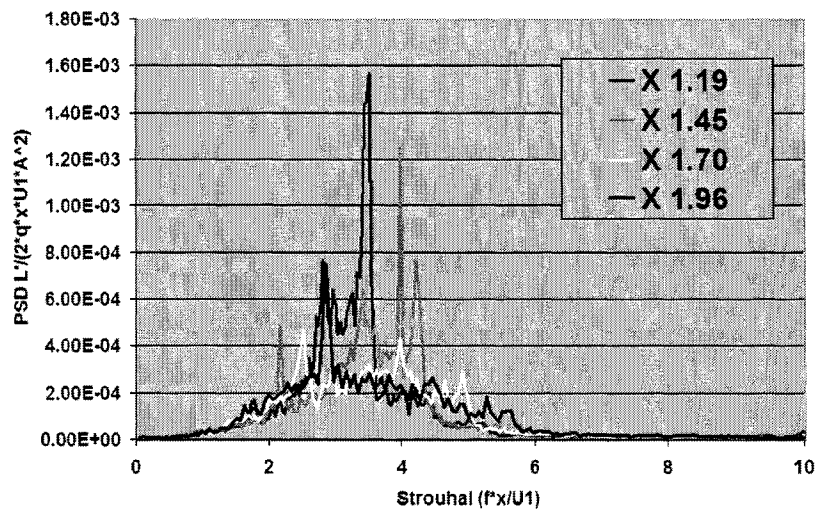


Figure A.29: Experimental  $L'_{rms}$  PSD,  $\eta=-0.015$ ,  $U1=11$  m/s

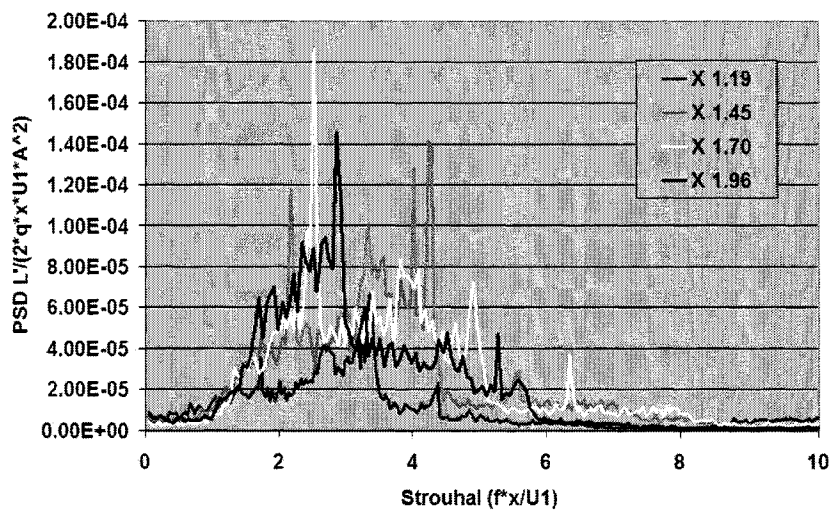


Figure A.30: Experimental Lift PSD  $\eta = -0.05$ ,  $U1=11$

### A.3 Fixed Velocity Profile

The PSD profiles presented in this section are presented at fixed vertical positions and fixed velocities, displaying the change in character of the PSD profile with increasing velocity.

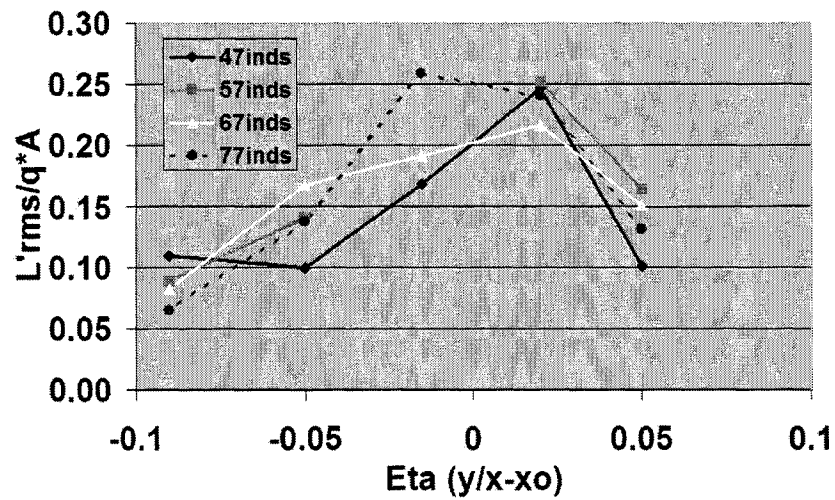


Figure A.31: Experimental  $L'_{rms}$  Profile,  $U_1=3$  m/s

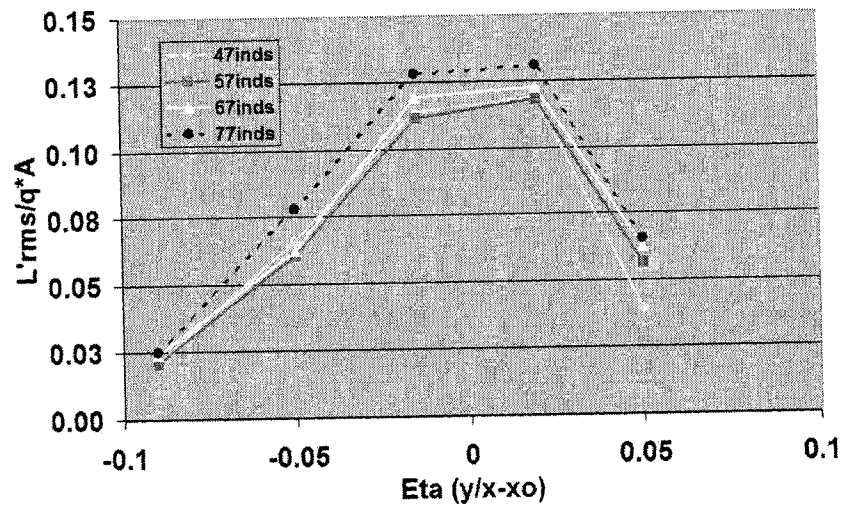


Figure A.32: Experimental  $L'_{rms}$  Profile,  $U_1=9$  m/s

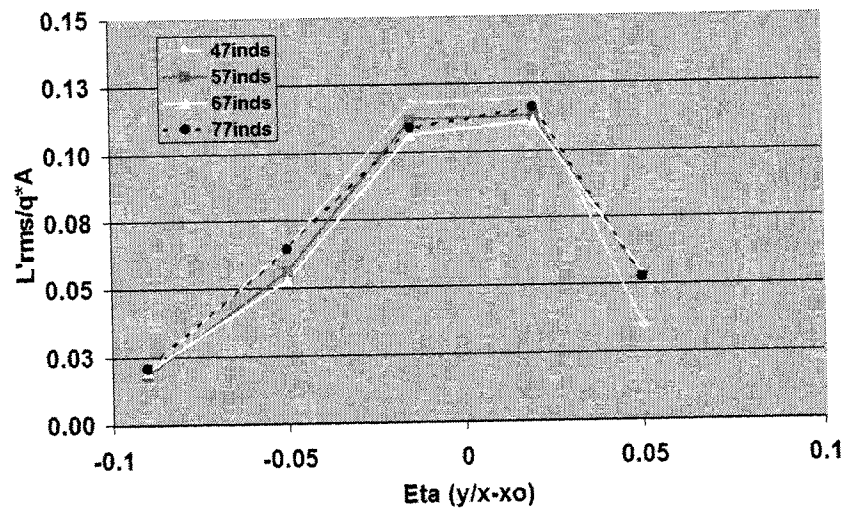


Figure A.33: Experimental  $L'_{rms}$  Profile,  $U_1=11$  m/s

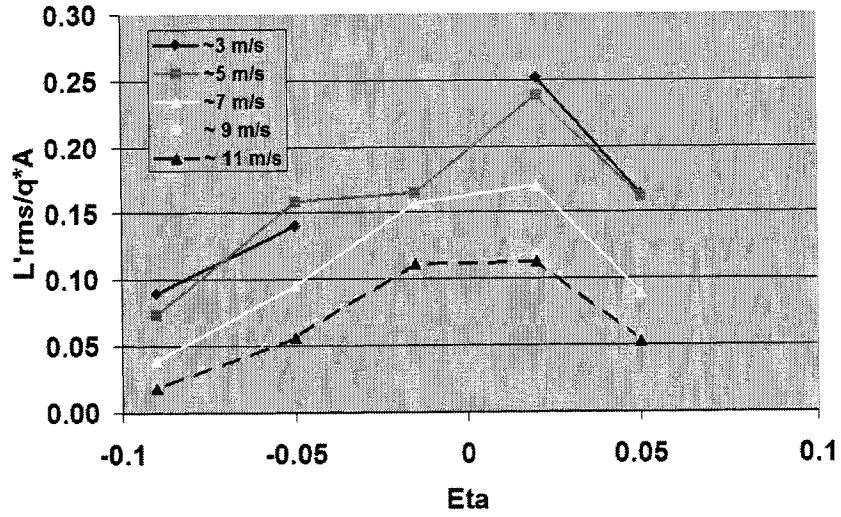


Figure A.34: Experimental  $L'_{rms}$  Profile,  $x=1.45$  m

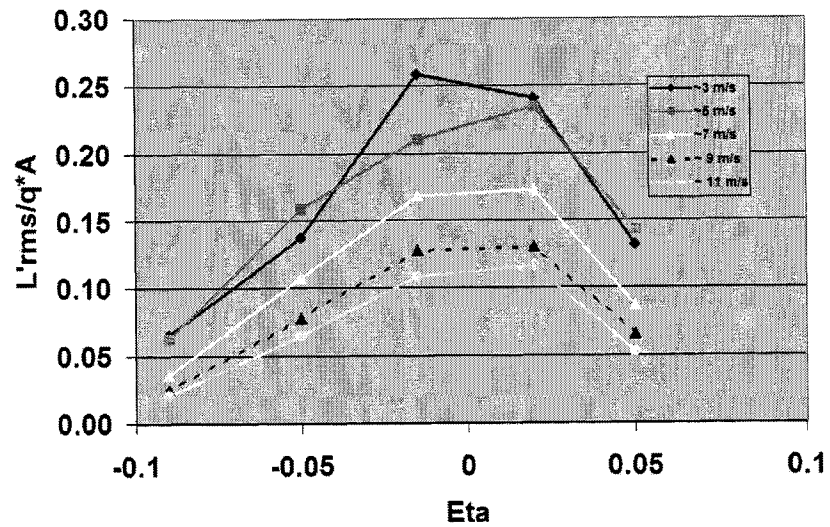


Figure A.35: Experimental  $L'_{rms}$  Profile,  $x=1.96$  m

## Appendix B

The data presented in Appendix B represents the remaining numerical data, beyond that presented in Chapter 4, and is presented for completeness.

### *B.1 Fixed Position Numerical Data*

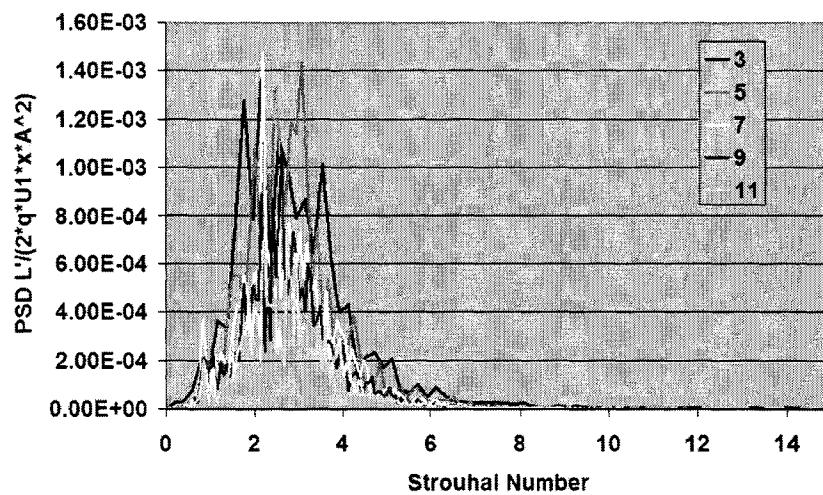


Figure B.1: Numerical  $L'_{rms}$  PSD,  $x=1.19\text{m}$ ,  $\eta=0.07$

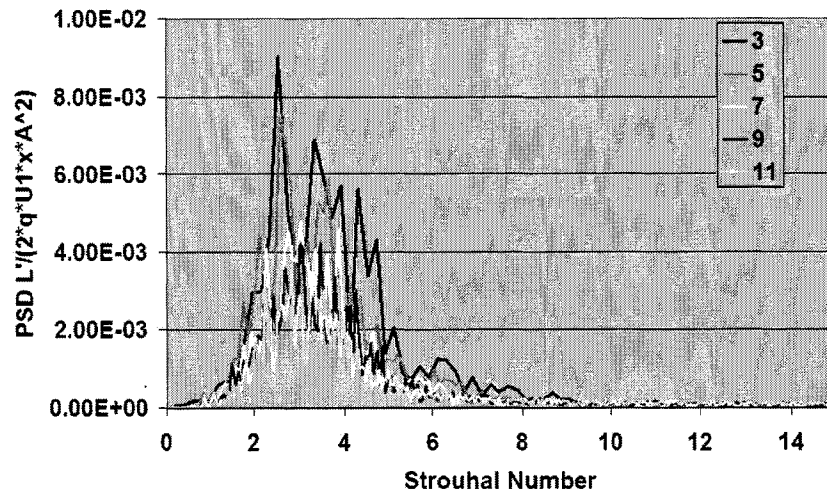


Figure B.2: Numerical  $L'_{rms}$  PSD,  $x=1.19$  m,  $\eta=0.03$

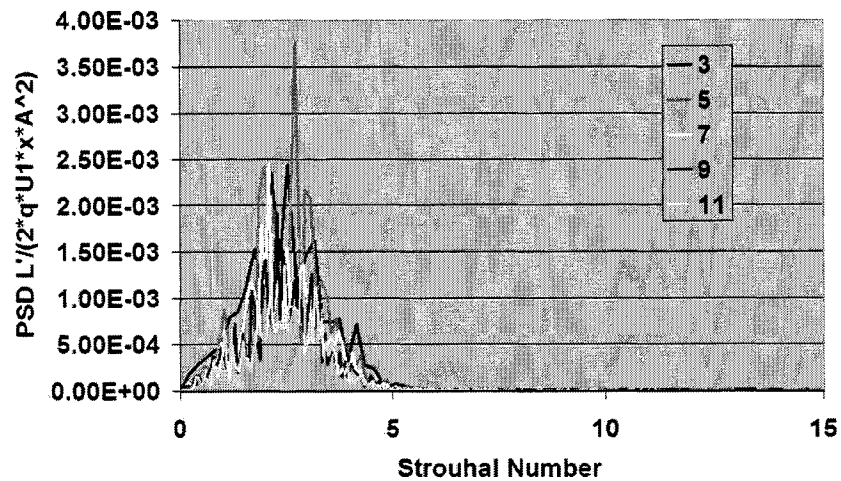


Figure B.3: Numerical  $L'_{rms}$  PSD,  $x=1.19$  m,  $\eta=-0.07$

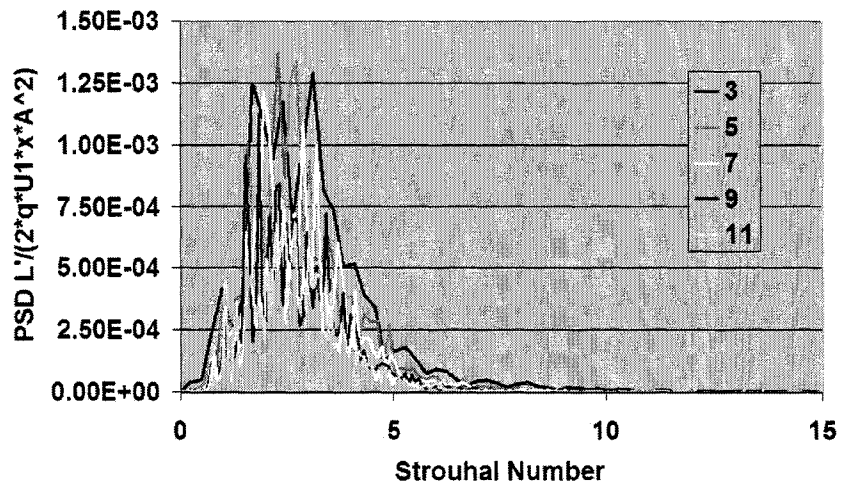


Figure B.4: Numerical  $L'_{rms}$  PSD,  $x=1.45$  m,  $\eta=0.07$

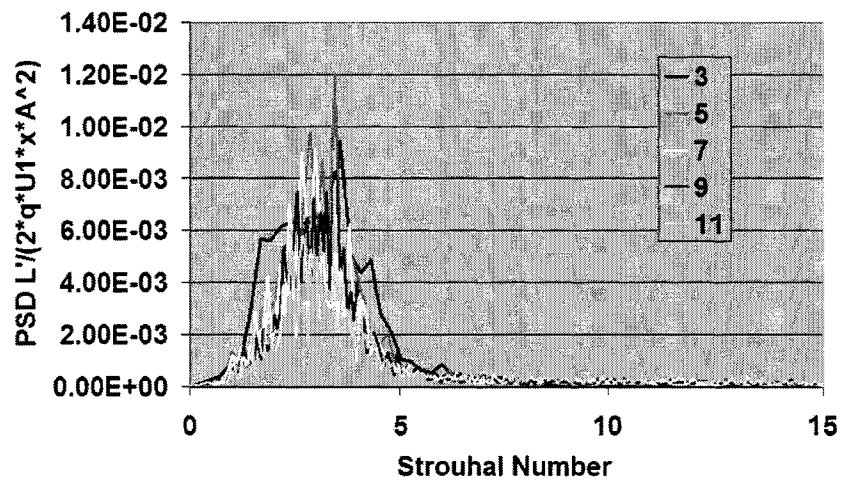


Figure B.5: Numerical  $L'_{rms}$  PSD,  $x=1.45$ m,  $\eta=-0.03$

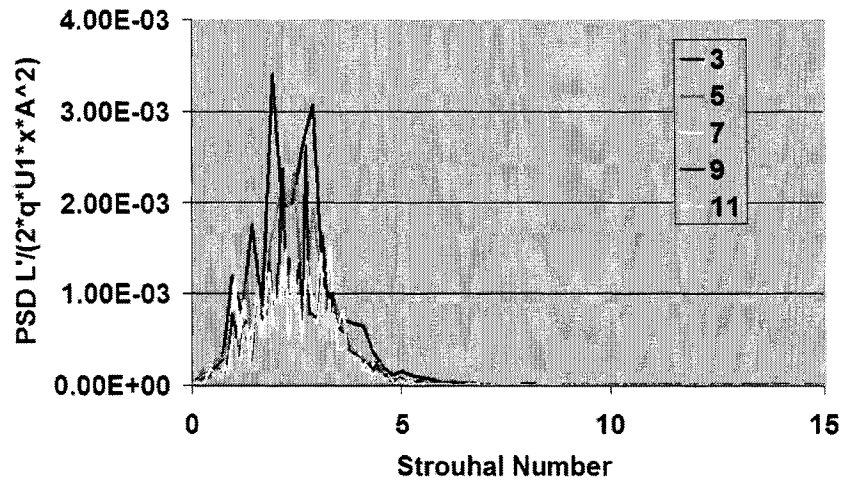


Figure B.6: Numerical  $L'_{rms}$  PSD,  $x=1.45$  m,  $\eta=-0.07$

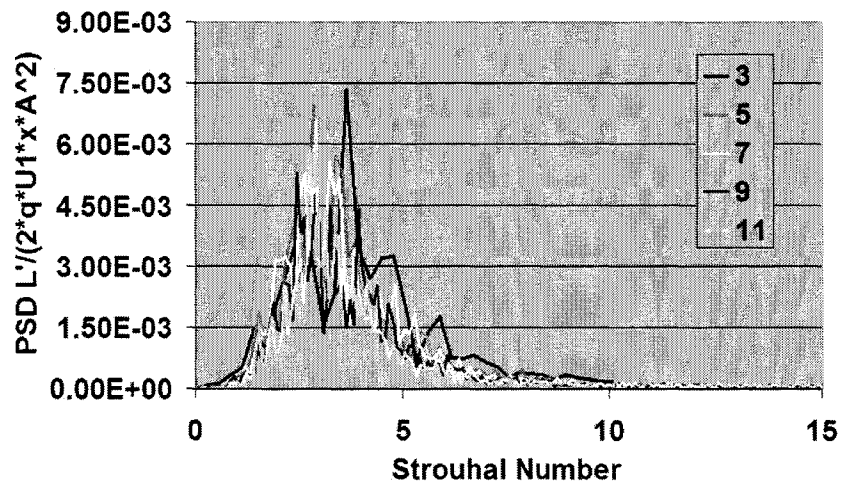


Figure B.7: Numerical  $L'_{rms}$  PSD,  $x=1.70$ m,  $\eta=0.03$

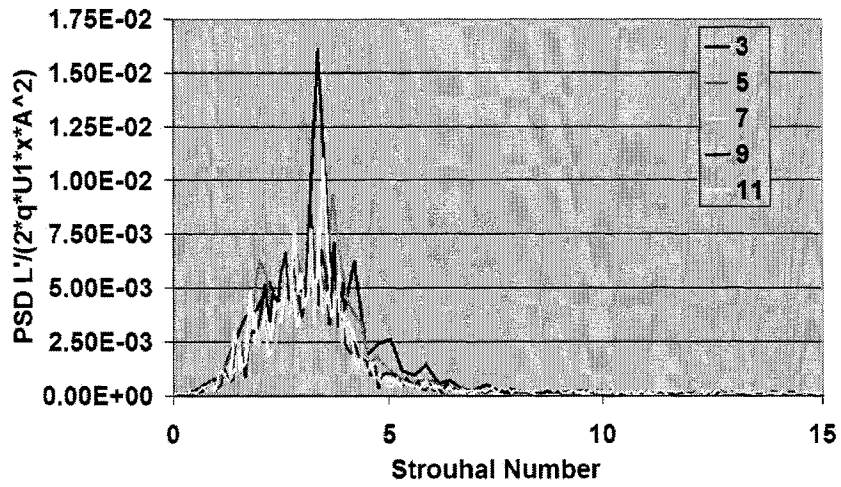


Figure B.8: Numerical  $L'_{rms}$  PSD,  $x=1.70$  m,  $\eta=-0.03$

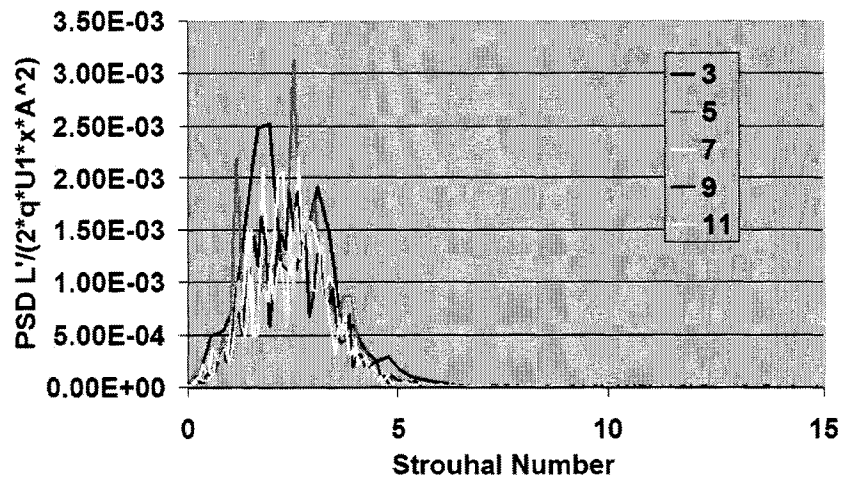


Figure B.9: Numerical  $L'_{rms}$  PSD,  $x=1.70$  m,  $\eta=-0.07$

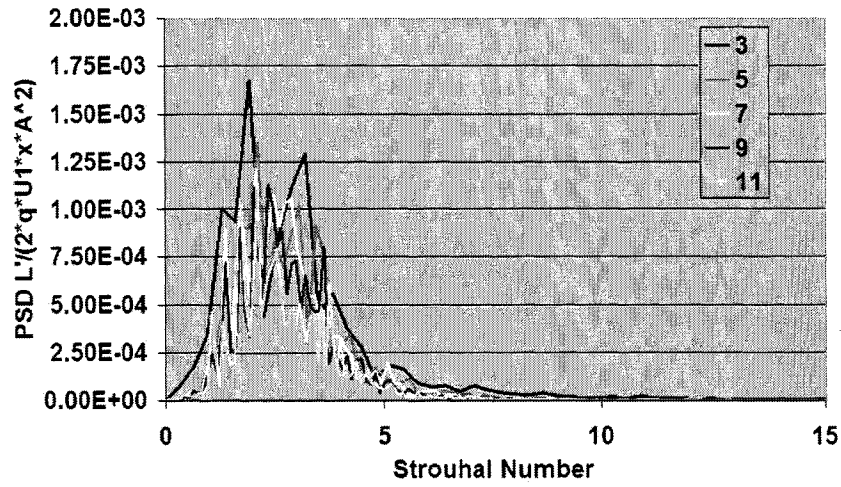


Figure B.10: Numerical  $L'_{rms}$  PSD,  $x=1.96$  m,  $\eta=0.07$

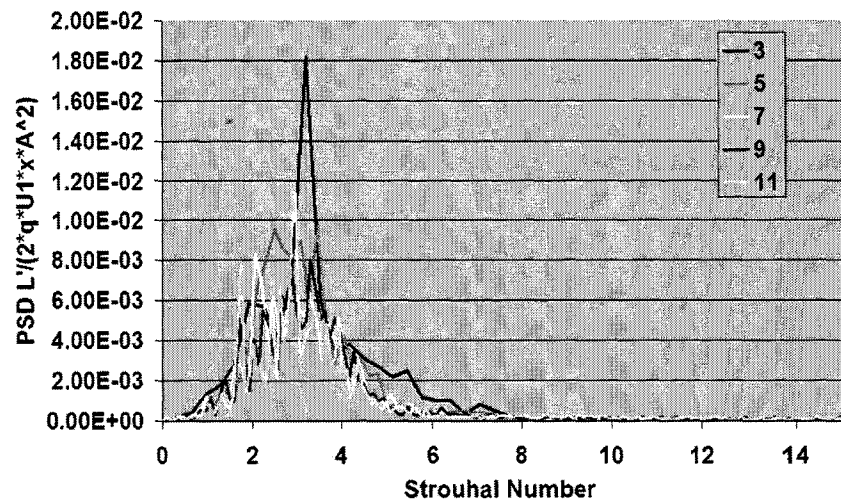


Figure B.11: Numerical  $L'_{rms}$  PSD,  $x=1.96$  m,  $\eta=-0.03$

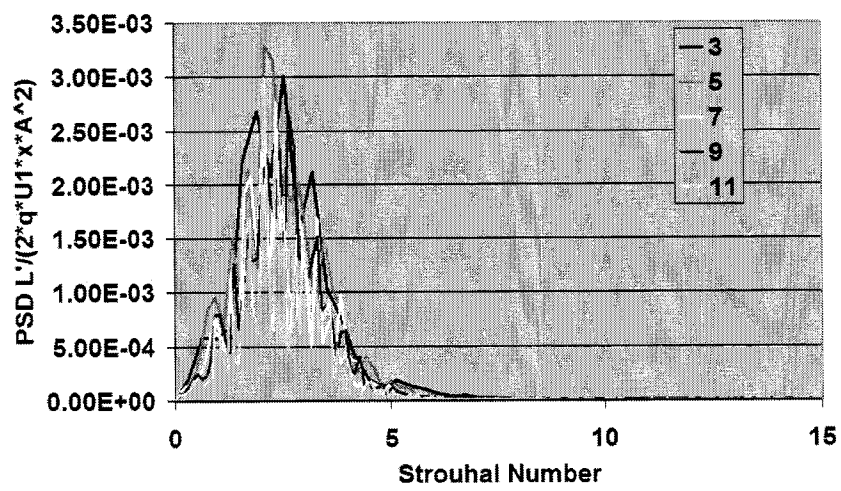


Figure B.12: Numerical  $L'_{rms}$  PSD,  $x=1.96m$ ,  $\eta=-0.07$

## B.2 Variable Downstream Position Numerical Data

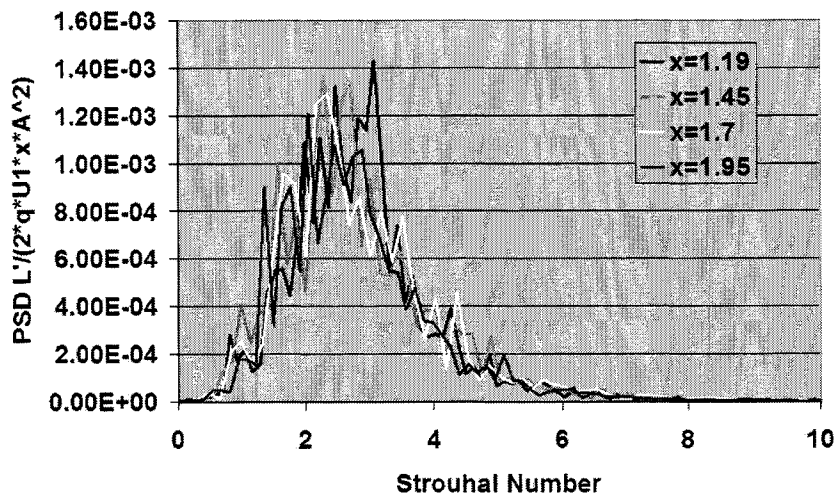


Figure B.13: Numerical  $L'_{rms}$  PSD,  $\eta=0.07$ ,  $U_1=5$  m/s

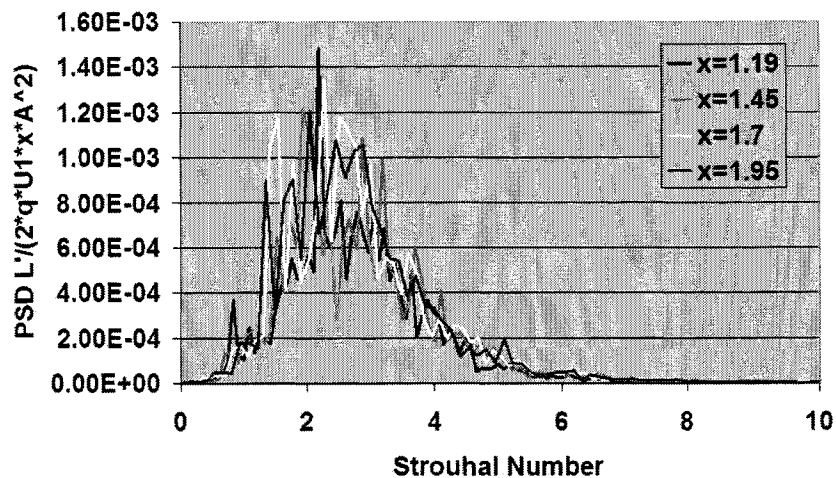


Figure B.14: Numerical  $L'_{rms}$  PSD,  $\eta=0.07$ ,  $U_1=3$

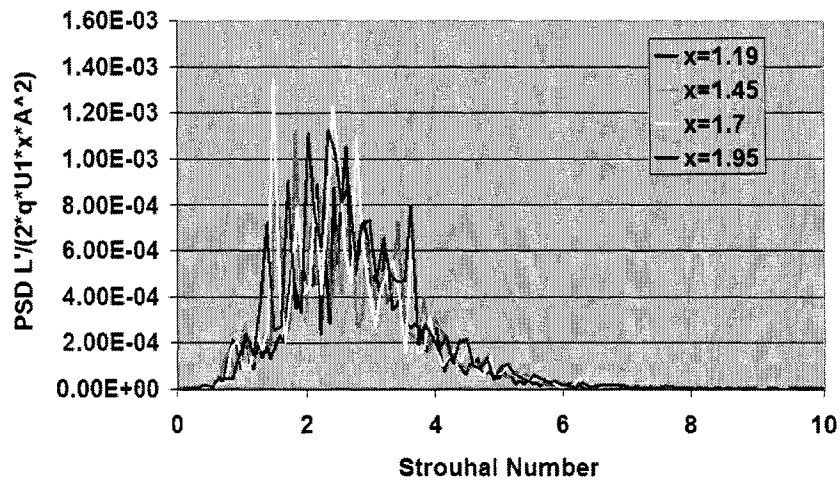


Figure B.15: Numerical  $L'_{rms}$  PSD,  $\eta=0.07$ ,  $U_1=9$  m/s

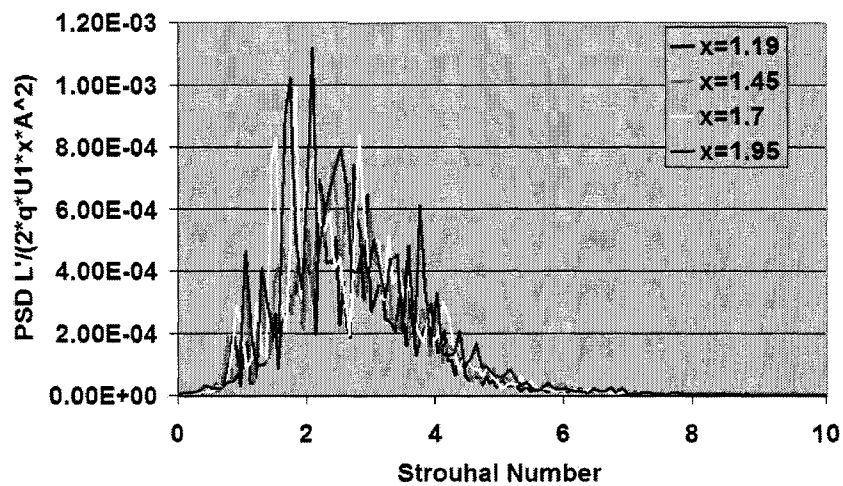


Figure B.16: Numerical  $L'_{rms}$  PSD,  $\eta=0.07$ ,  $U_1=11$  m/s

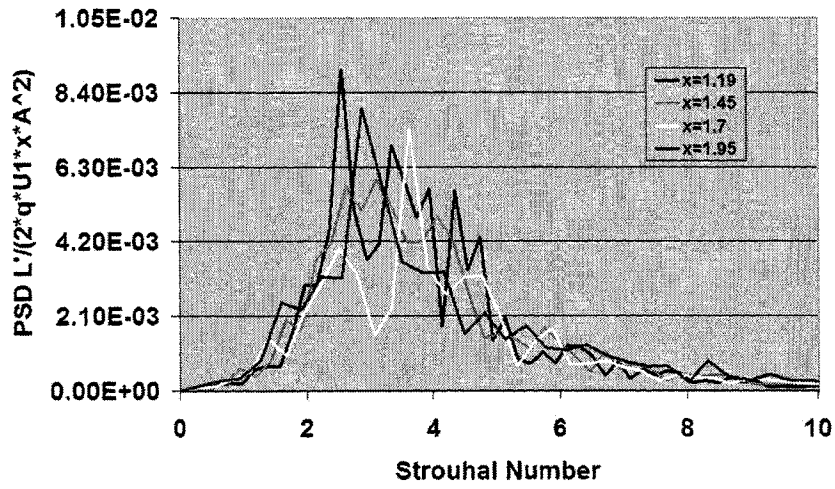


Figure B.17: Numerical  $L'_{rms}$  PSD,  $\eta=0.03$ ,  $U_1=3$  m/s

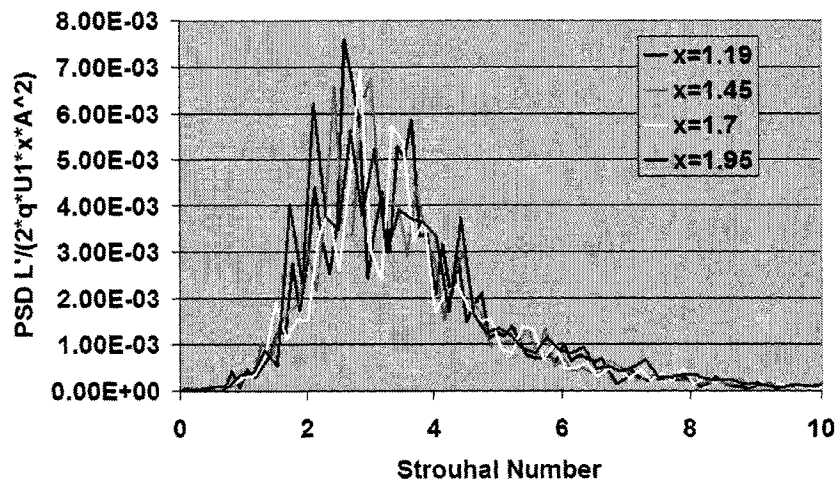


Figure B.18: Numerical  $L'_{rms}$  PSD,  $\eta=0.03$ ,  $U_1=5$  m/s

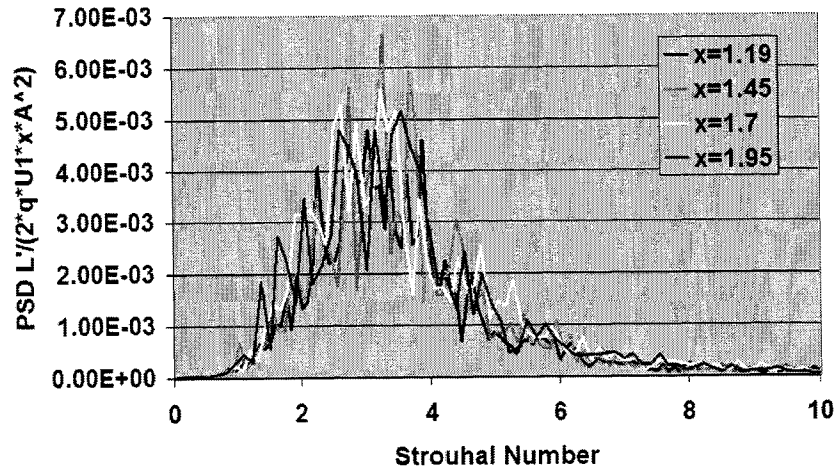


Figure B.19: Numerical  $L'_{rms}$  PSD,  $\eta=0.03$ ,  $U_1=7$  m/s

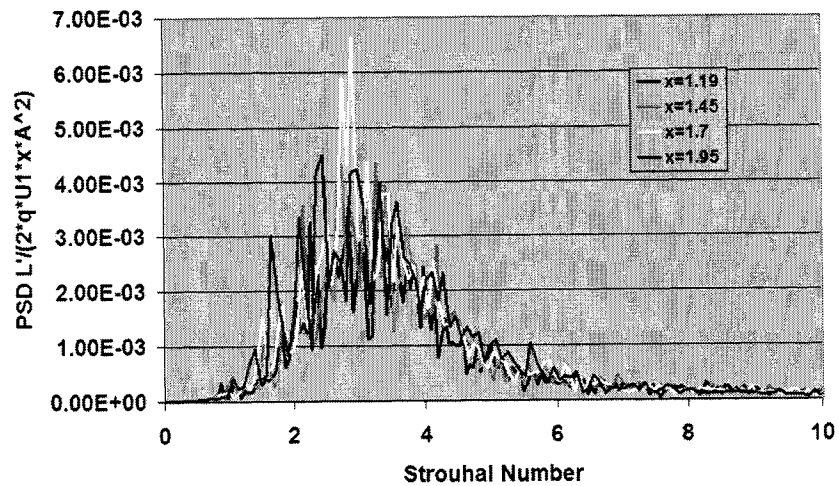


Figure B.20: Numerical  $L'_{rms}$  PSD,  $\eta=0.03$ ,  $U_1=11$  m/s

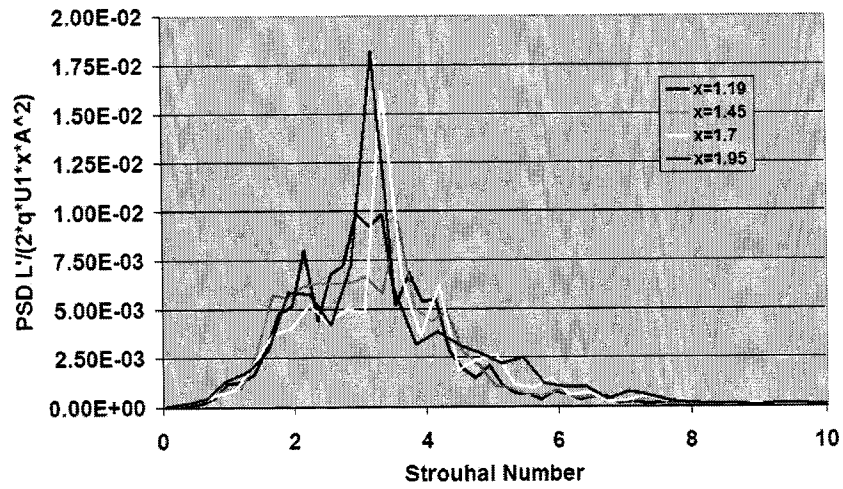


Figure B.21: Numerical  $L'_{rms}$  PSD,  $\eta=-0.03$ ,  $U_1=3$  m/s

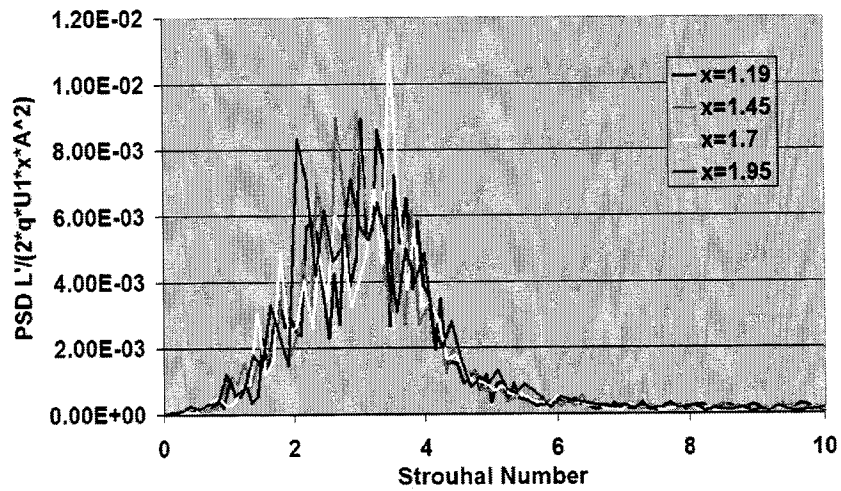


Figure B.22: Numerical  $L'_{rms}$  PSD,  $\eta=-0.03$ ,  $U_1=7$  m/s

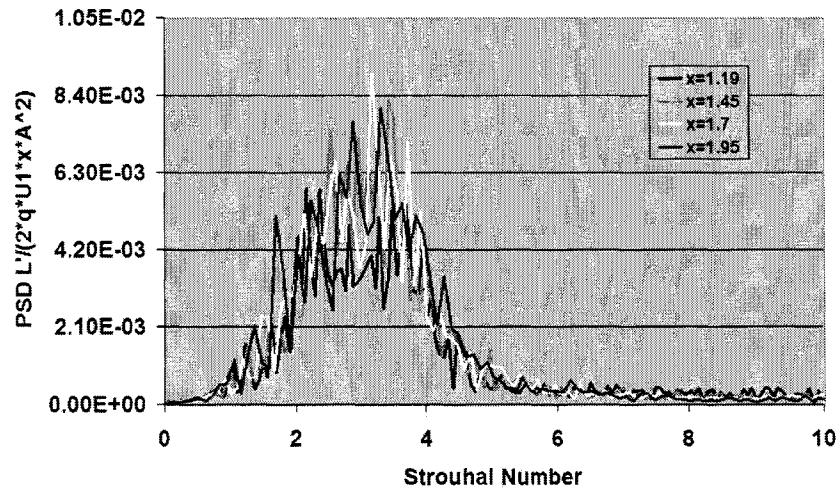


Figure B.23: Numerical  $L'_{rms}$  PSD,  $\eta=-0.03$ ,  $U_1=9$  m/s

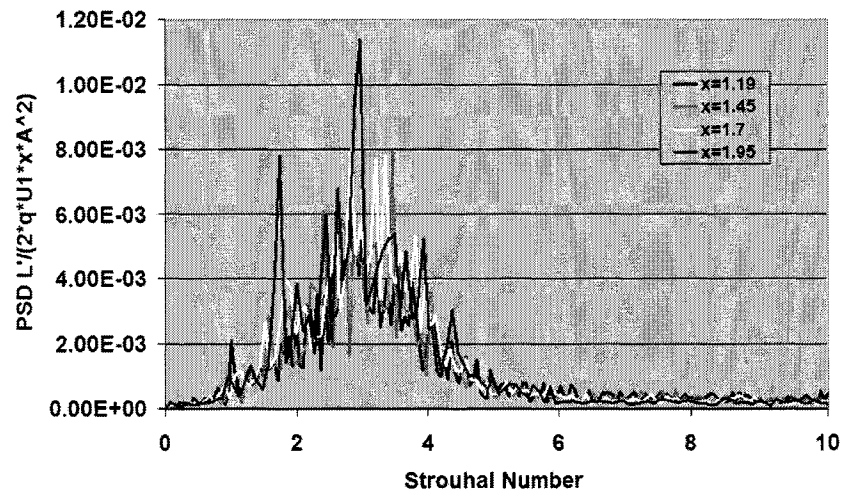


Figure B.24: Numerical  $L'_{rms}$  PSD,  $\eta=-0.03$ ,  $U_1=11$  m/s

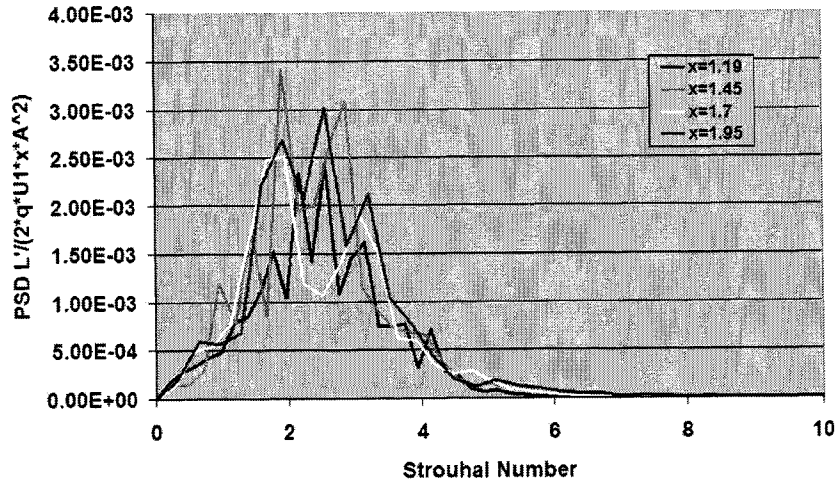


Figure B.25: Numerical  $L'_{rms}$  PSD,  $\eta=-0.07$ ,  $U_1=3$  m/s

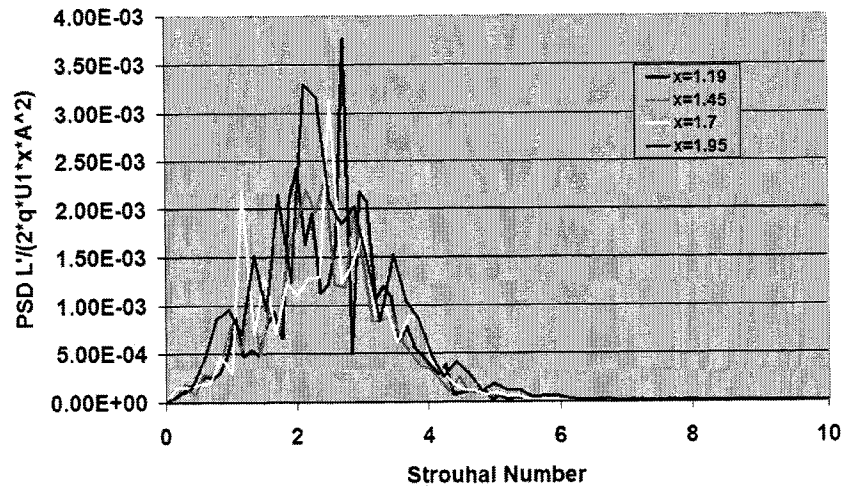


Figure B.26: Numerical  $L'_{rms}$  PSD,  $\eta=-0.07$ ,  $U_1=5$  m/s

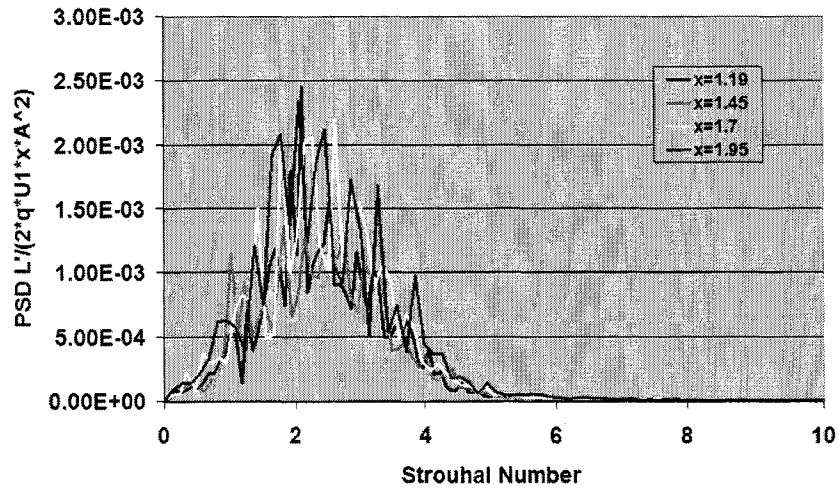


Figure B.27: Numerical  $L'_{rms}$  PSD,  $\eta=-0.07$ ,  $U_1=7$  m/s

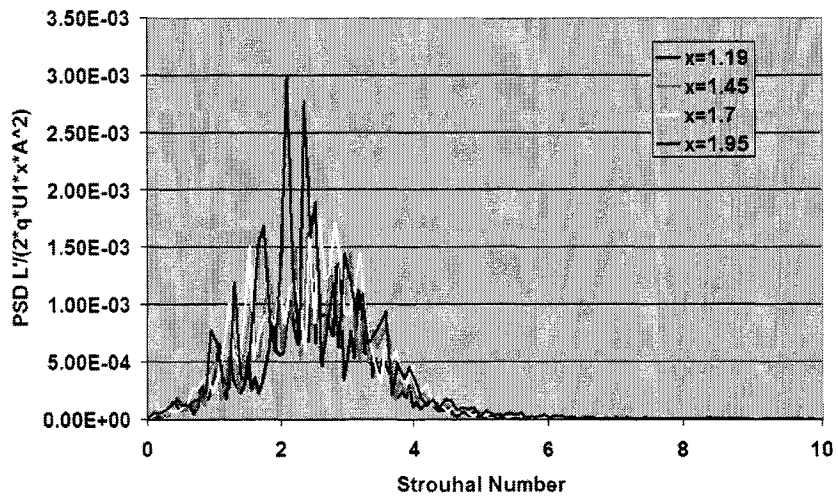


Figure B.28: Numerical  $L'_{rms}$  PSD,  $\eta=-0.07$ ,  $U_1=11$  m/s

### B.3 Numerical $L'_{rms}$ Cross Layer Profiles

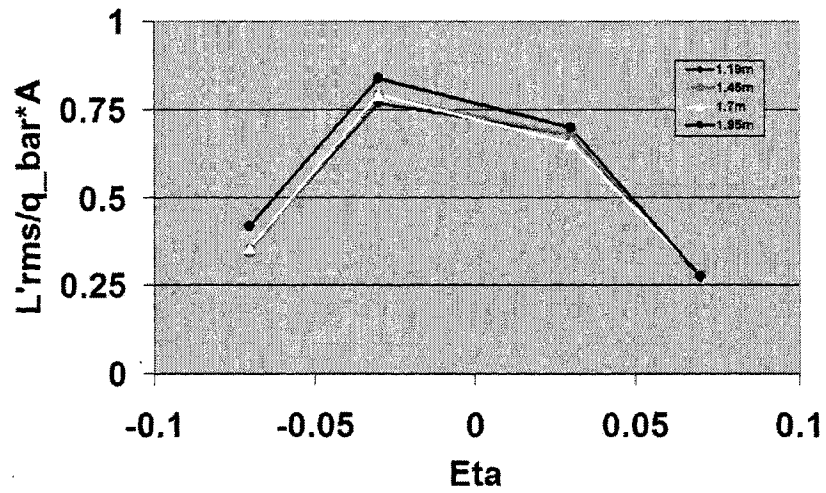


Figure B.29: Numerical  $L'_{rms}$  Profile,  $U_1=5$  m/s

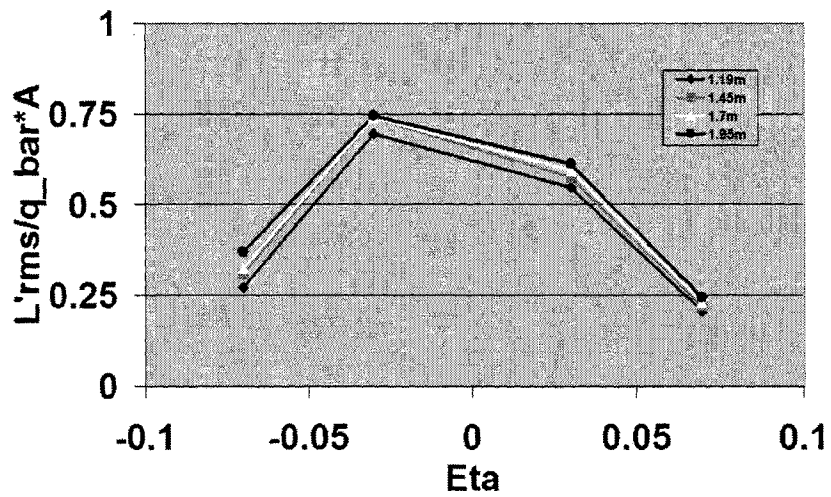


Figure B.30: Numerical  $L'_{rms}$  Profile,  $U_1=9$  m/s

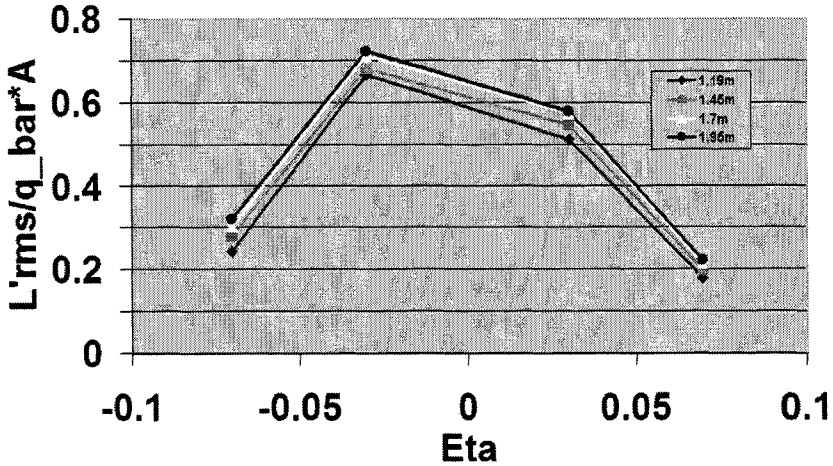


Figure B.31: Numerical  $L'_{rms}$  Profile,  $U_1=11$  m/s

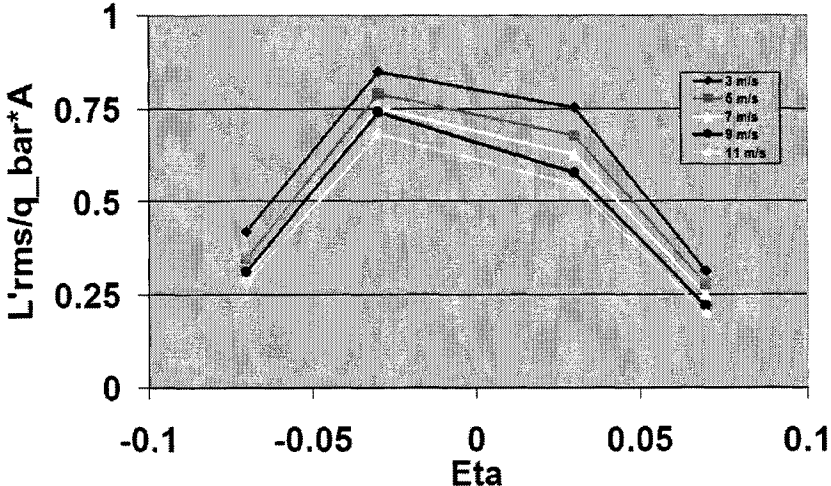


Figure B.32: Numerical  $L'_{rms}$  Profile,  $x=1.45$  m

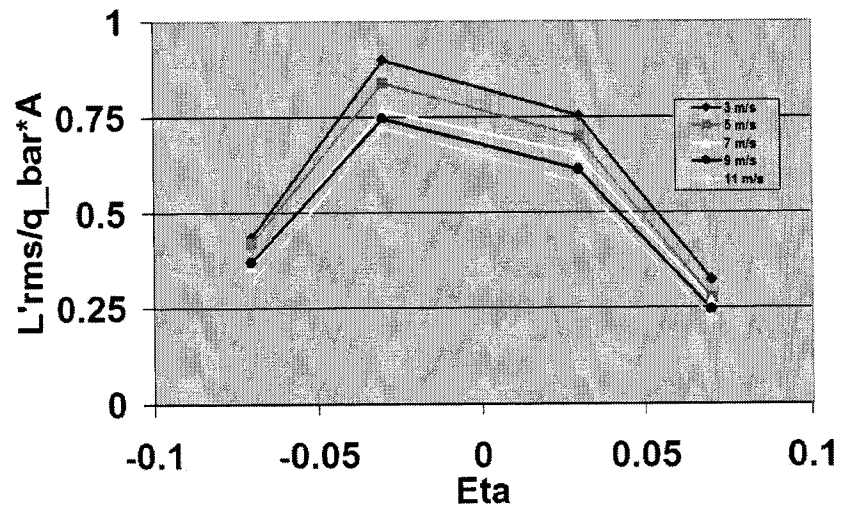


Figure B.33: Numerical  $L'_{rms}$  Profile,  $x=1.96$  m

Appendix C  
**CALIBRATION DATA**

This appendix presents the calibration data for the pressure transducer used to measure  $U_1$  and the data for calibration of the Hot-Film Anemometer.

Table C.1: Pressure Transducer Calibration Data

Inches $H_2O$	Torr
7.34	3.85
8.5	4.5
8.63	4.55
12.84	6.8
16.85	8.9
18.35	9.8
22.37	11.95
23.65	12.5
27.67	14.85
29.66	16
31.3	16.9
36.7	19.6
40.85	22
44.45	24
56.5	31

### Pressure Transducer Calibration

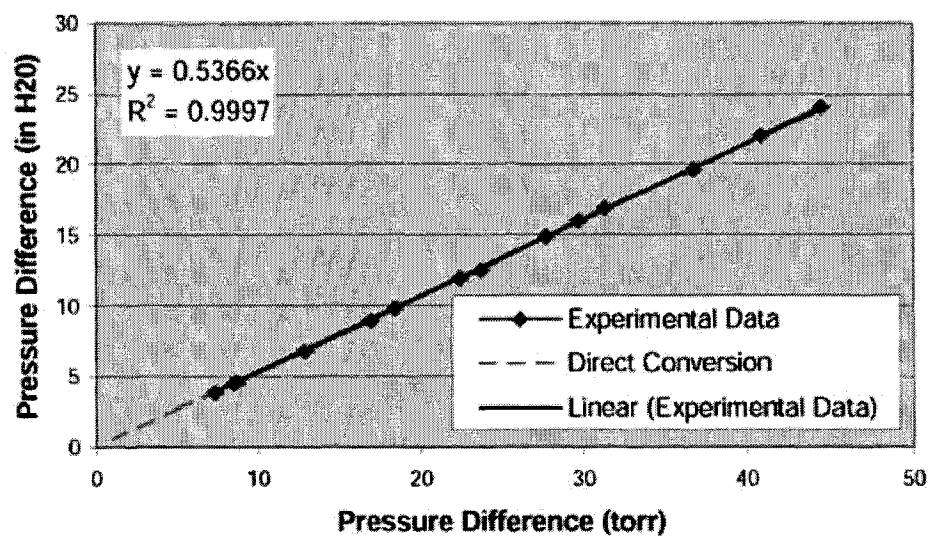


Figure C.1: Pressure Transducer Calibration Plot

Table C.2: Hot Film Anemometer Calibration Data Set: Probe 1

Velocity(m/s)	q(torr)	Temp(C)	Voltage(V)	Overheat	Calculated Velocity (m/s)	Error <sup>2</sup>
3.840	0.066	20.651	2.743	0.518	4.049	0.043
5.726	0.146	23.614	2.894	0.508	5.972	0.060
6.526	0.192	21.625	2.955	0.514	6.503	0.000
7.413	0.245	24.111	3.014	0.506	7.688	0.076
8.571	0.329	22.760	3.094	0.511	8.748	0.031
10.018	0.450	22.863	3.174	0.510	10.189	0.028
10.463	0.488	24.431	3.186	0.505	10.750	0.082
11.431	0.585	23.254	3.241	0.509	11.616	0.034
13.533	0.820	23.332	3.333	0.509	13.681	0.022
14.559	0.948	23.499	3.374	0.508	14.721	0.026
15.418	1.064	23.488	3.406	0.508	15.560	0.020
16.300	1.189	23.625	3.438	0.508	16.450	0.022
17.077	1.305	23.619	3.465	0.508	17.219	0.020
17.952	1.442	23.592	3.499	0.508	18.190	0.056
19.531	1.706	23.677	3.552	0.507	19.864	0.111
20.703	1.916	23.808	3.590	0.507	21.135	0.186

## Appendix D

### **EXPERIMENTAL DATA COLLECTION PROGRAMS**

For the current experimental process, data has been collected through the following Labview Virtual Instrument (VI). Labview Version 7.0 was used to collect the voltage output from both the Hot-Film anemometry system and directly from the Load Cell output. Labview then proceeded to analyze the data in real time producing running averages of un-normalized  $L'$  PSD profiles as well as mean values. This information was then output into a text file along with key layer information such as  $q_1$ ,  $U_1$ , and the current temperature.

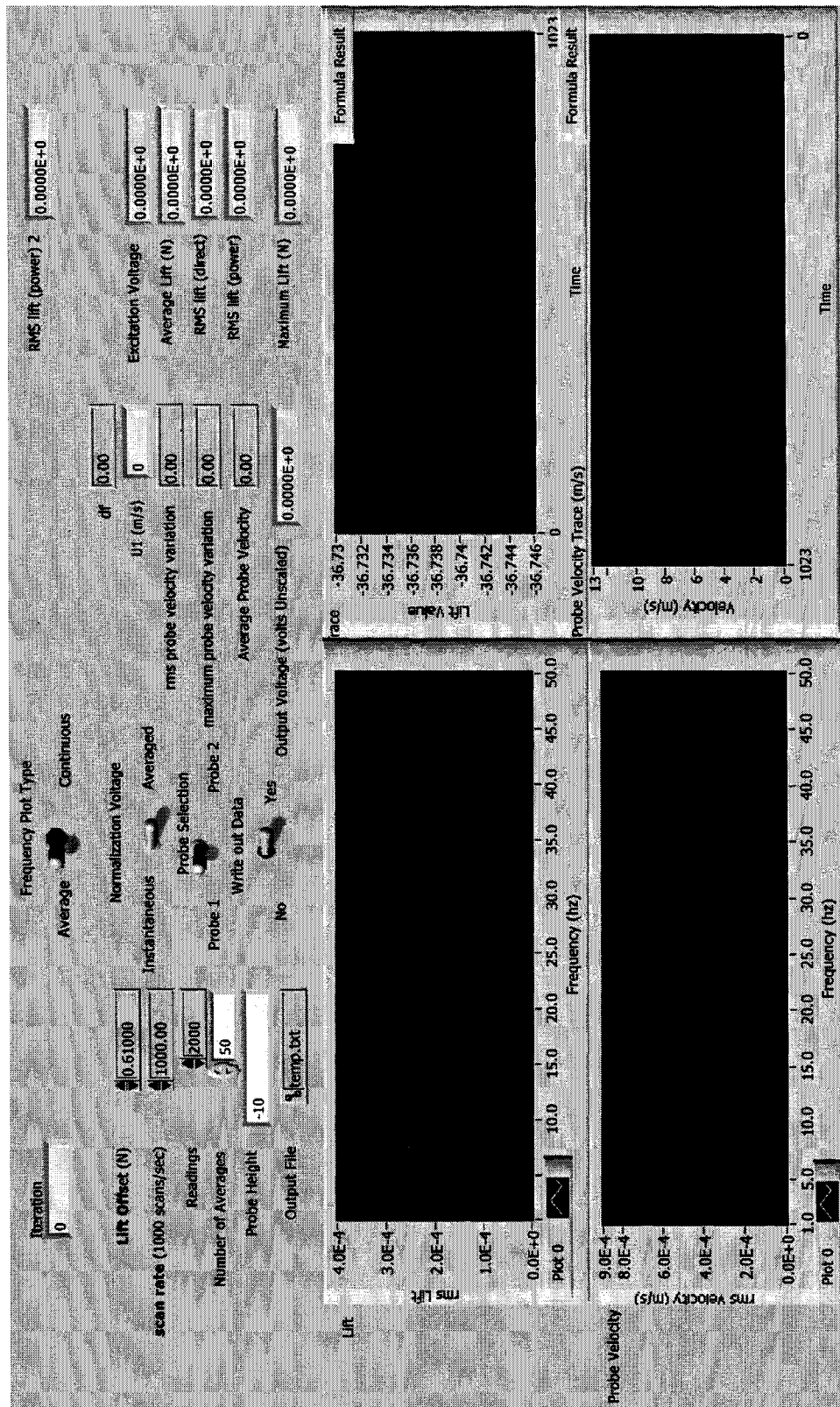


Figure D.1: Main data collection program front panel

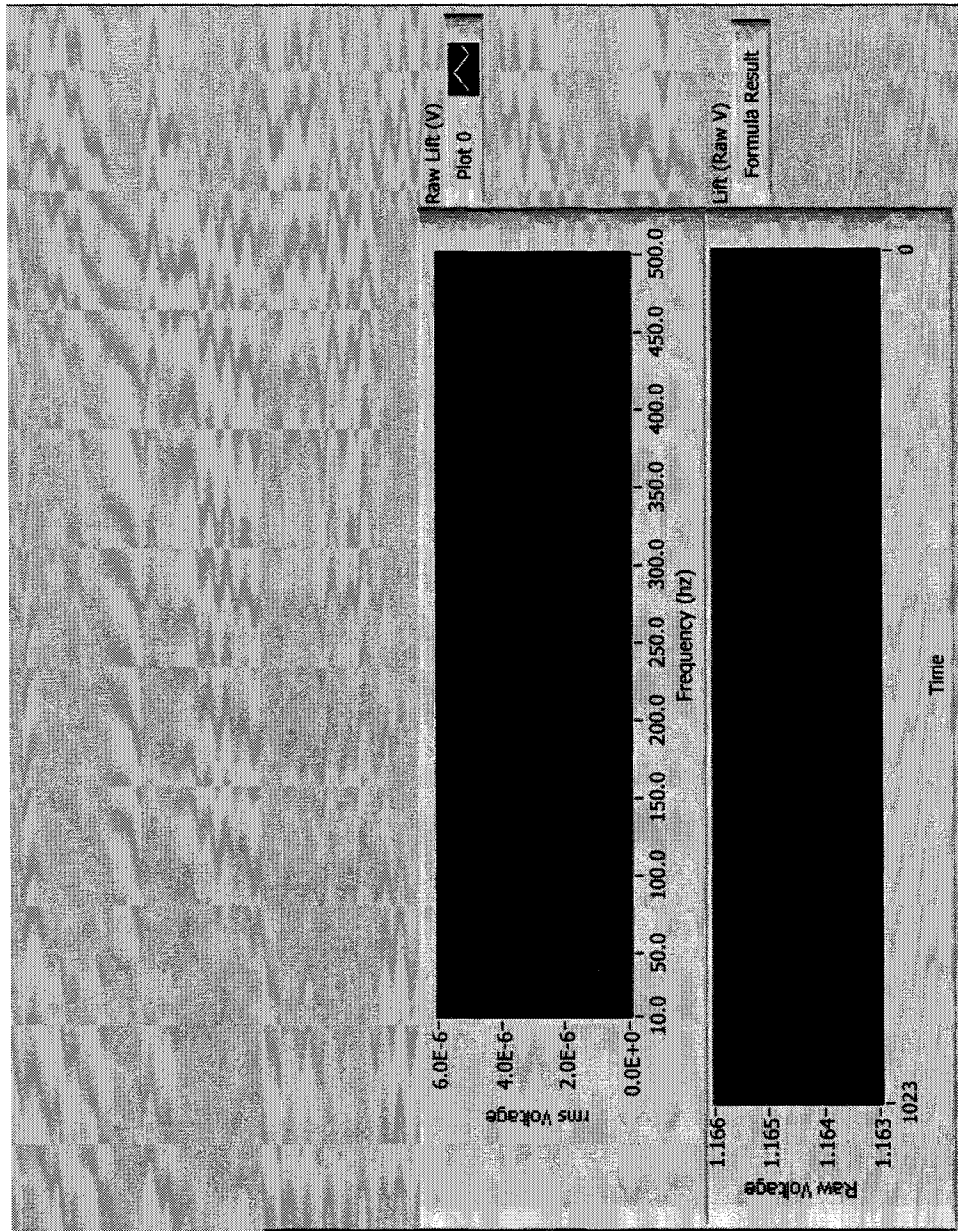


Figure D.2: Main data collection program front panel: Additional plots for trouble shooting

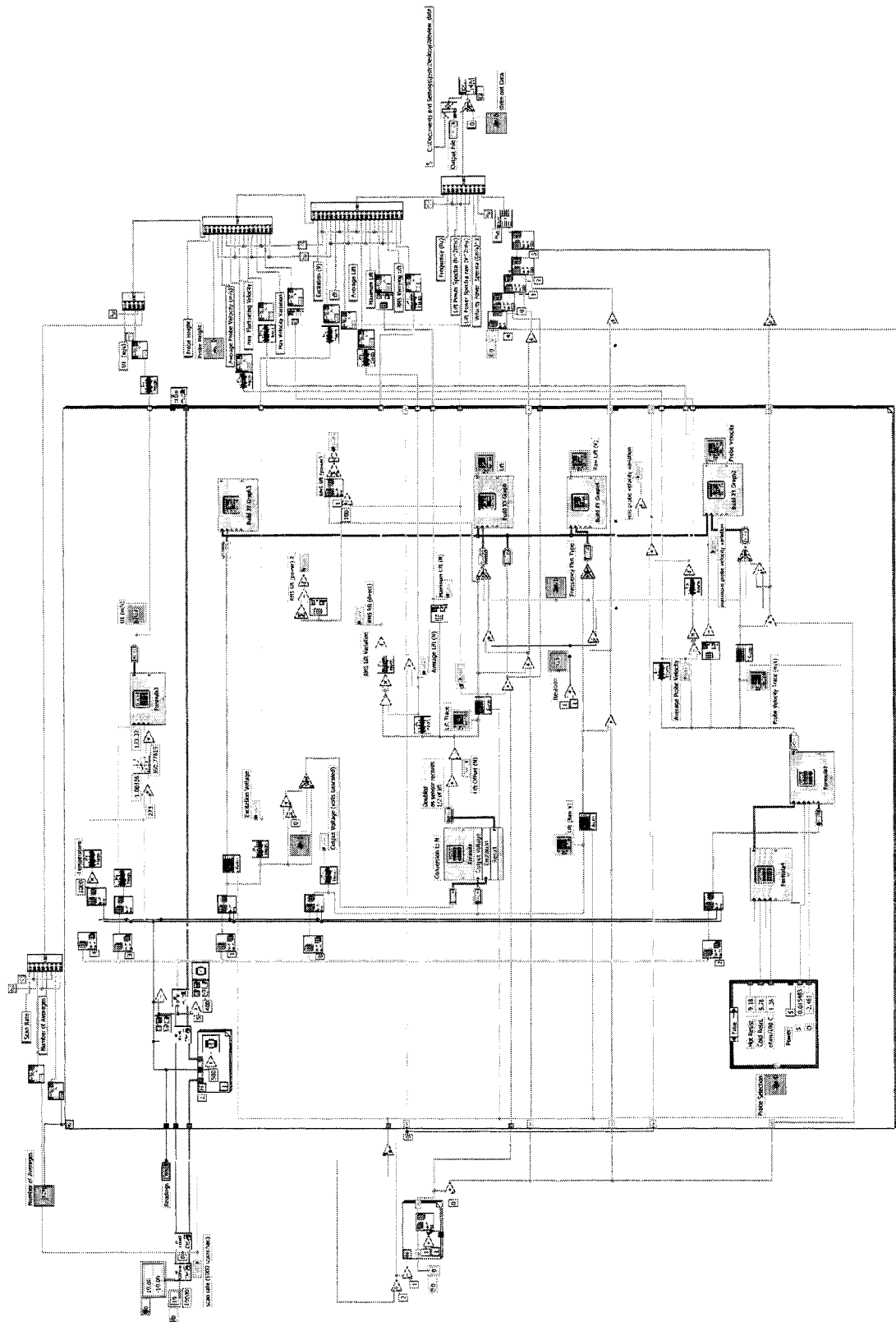


Figure D.3: Full block diagram

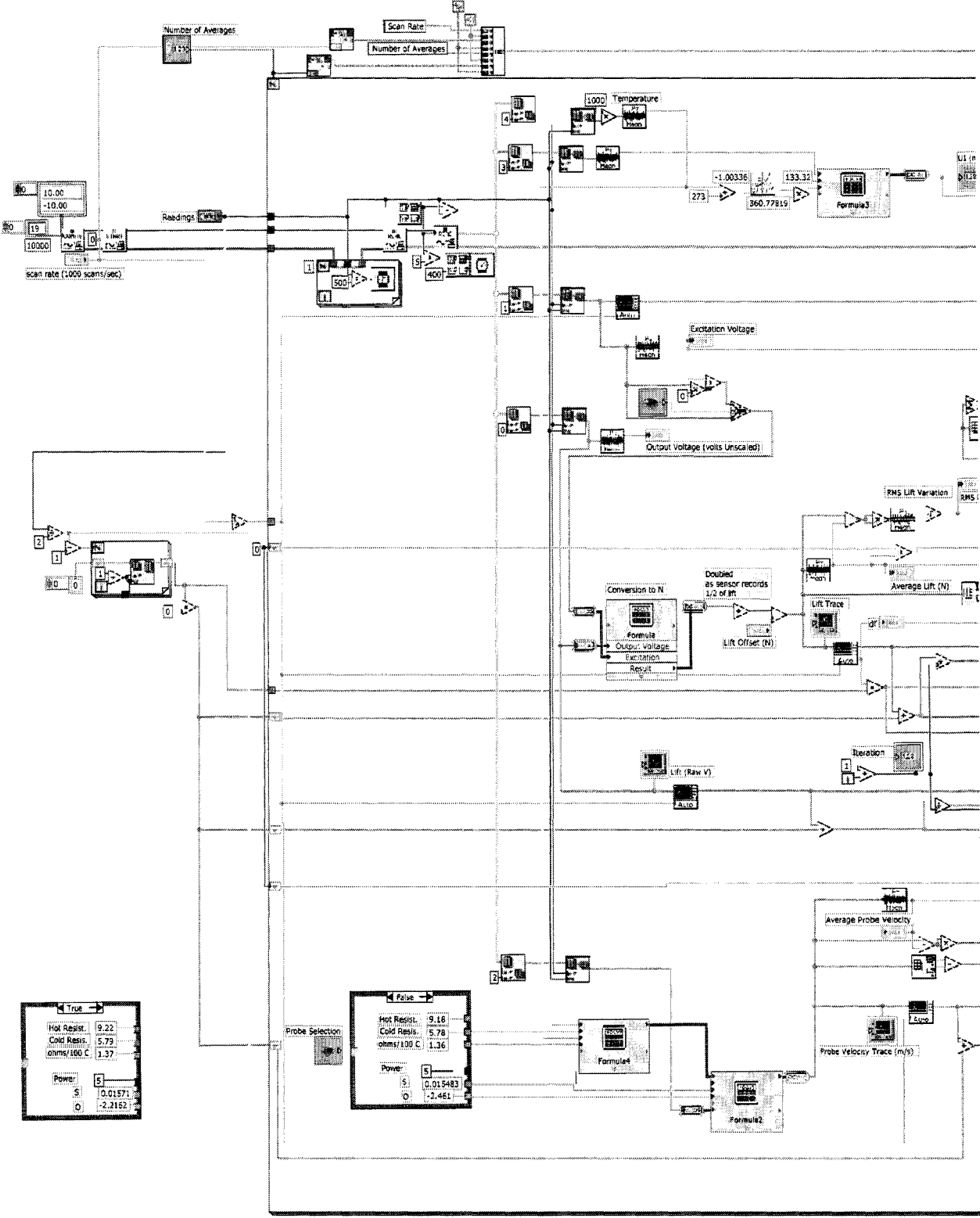


Figure D.4: Block diagram closeup: Page 1

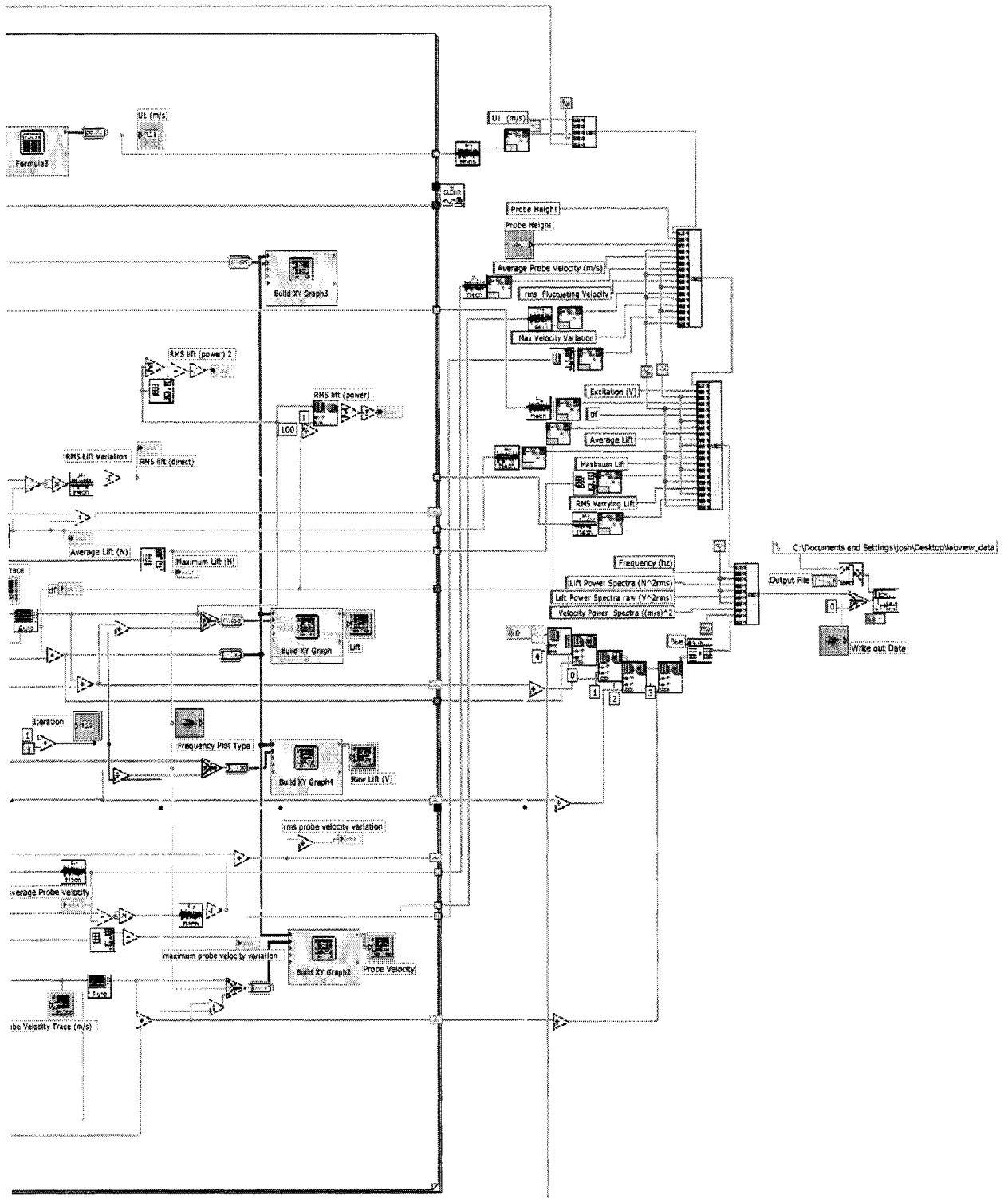


Figure D.5: Block diagram closeup: Page 2

**Convert to Dynamic Data3**

Convert to Dynamic Data

Converts numeric, Boolean, waveform and array data types to the dynamic data type for use with Express

**Convert to Dynamic Data2**

Convert to Dynamic Data

Converts numeric, Boolean, waveform and array data types to the dynamic data type for use with Express

**Build XY Graph**

Build XY Graph

formats the data displayed on an X-Y Graph.

**Formula4**

Formula

Uses a calculator interface to create mathematical formulas. You can use this Express VI to perform most math functions that a basic scientific calculator can compute.

-----  
This Express VI is configured as follows:Formula:  $(R_h - (R_c + T * \text{slope} / 100)) / (R_c + T * \text{slope} / 100)$ **Convert to Dynamic Data9**

Convert to Dynamic Data

Converts numeric, Boolean, waveform and array data types to the dynamic data type for use with Express

**Convert from Dynamic Data4**

Convert from Dynamic Data

Converts the dynamic data type to numeric, Boolean, waveform, and array data types for use with other VIs and functions.

**Formula2**

Formula

Uses a calculator interface to create mathematical formulas. You can use this Express VI to perform most math functions that a basic scientific calculator can compute.

-----  
This Express VI is configured as follows:Formula:  $((V^{**P})/a)*S+O$ **Formula**

Formula

Uses a calculator interface to create mathematical formulas. You can use this Express VI to perform most math functions that a basic scientific calculator can compute.

-----  
This Express VI is configured as follows:Formula:  $((\text{Output Voltage} / \text{Excitation}) * 28.639 - 23.523)$ **Formula4**

Formula

Uses a calculator interface to create mathematical formulas. You can use this Express VI to perform most math functions that a basic scientific calculator can compute.

-----  
This Express VI is configured as follows:Formula:  $(R_h - (R_c + T * \text{slope} / 100)) / (R_c + T * \text{slope} / 100)$

**Convert to Dynamic Data9**

Convert to Dynamic Data

Converts numeric, Boolean, waveform and array data types to the dynamic data type for use with Express

**Convert from Dynamic Data4**

Convert from Dynamic Data

Converts the dynamic data type to numeric, Boolean, waveform, and array data types for use with other VIs and functions.

**Formula2**

Formula

Uses a calculator interface to create mathematical formulas. You can use this Express VI to perform most math functions that a basic scientific calculator can compute.

-----

This Express VI is configured as follows:

Formula:  $((V * P) / a) * S + O$ **Formula**

Formula

Uses a calculator interface to create mathematical formulas. You can use this Express VI to perform most math functions that a basic scientific calculator can compute.

-----

This Express VI is configured as follows:

Formula:  $((\text{Output Voltage} / \text{Excitation}) * 28.639 - 23.523)$ 

Figure D.7: Labview block and formula descriptions: Page 2

## Appendix E

### NUMERICAL MODEL COMPUTER CODE

Appendix E contains the essential computer code which comprises the numerical model developed in Chapter 4. While the code is not extensively commented most of the critical procedures and techniques are broken into convenient functions which are called into the primary program. All computer code is presented as raw Matlab code.

#### *E.1 Cutoff Function*

This function analyzes each of the vortex particles in the flow, and determines whether or not they have convected past the downstream cutoff point. If they have convected past the boundary they are deleted from the model, and the list of vortex particles is reset.

```
function [vortex,NVpos]=cutoff(Vpos,beta)
%
%This function serves to remove all vortices from the array Vpos
% that have an x-value greater than that specified by beta
%
k=1;
[NV,dummy]=size(Vpos);
for j=1:NV;
    if Vpos(j,1)>beta;
        vortex(k,:)=Vpos(j,:);
        k=k+1;
    end
end
```

```

    end
end
[NVpos,dum]=size(vortex);

```

### ***E.2 Random Walk***

This function serves to perturb the vortex particle position to apply Chorin's Random Walk to the model.

```

function [V]=random(V,KF,NV)
for ij=1:NV
    V(ij,1)=V(ij,1)*(1+KF*rand(1)*(sign(rand(1)-rand(1))));
    V(ij,2)=V(ij,2)*(1+KF*rand(1)*(sign(rand(1)-rand(1))));
end

```

### ***E.3 Vortex Induced Velocity***

This function serves to calculate the velocity induced by the vortices in the vector  $\vec{V}_1$  on the set of points  $\vec{P}_1$ . This is the discrete application of the 2-D Bio-Savart law.  $s_1$  is the vortex core radius, used in the Rankine Core Model

```

function [U]=vortex_induced_velocity(P1,V1,s1)
%
%This Model assumes that the Vortex Circulation Strengths in V1 are
%physical values to produce a physical velocity U. Nondimensionalization
%is possible with Gamma(v1)/Gamma(ought) and Lengths Nondimensionalized
%appropriately as well.
%
%Induced Velocity of vortices V1 on the points P1
%The first column of the vectors V1 and P1 represent the 'X' position
%of the vortices, the second column the 'Y' position
%and the third column the vortex strength.

```

```

%Testing routines
%P1=[0 0 1];
%V1=[sqrt(.5) sqrt(.5) 1];
%s1=.01;
[NV,dummy]=size(V1);
[NP,dummy]=size(P1);
for j=1:NP;
    rsquared=(P1(j,1)-V1(:,1)).2+(P1(j,2)-V1(:,2)).2;
    for k=1:NV;
        if rsquared(k)>s12;
            K1(k,1)=V1(k,3)/rsquared(k);
        else
            K1(k,1)=V1(k,3)/s12;
        end
    end
end
U(j,1)=sum(K1.*(V1(:,2)-P1(j,2)));
U(j,2)=-sum(K1.*(V1(:,1)-P1(j,1)));
end
U=U./(2*pi);

```

#### ***E.4 Shear Layer Induced Velocity***

This function serves to calculate the velocity induced at the point  $V_{pos}$

```

function [SV]=shear_us_ds_angle(Vpos,beta,x1,x2,theta,gamma,Y0,X0)
[NV,dummy]=size(Vpos);
[NS,dummy]=size(theta');
y1=(x1-X0).*tan(theta)+Y0;
k1=(x2-x1)./cos(theta);
K_us=sum(gamma);

```

```

SV_us(:,2)=(1/2).*log((Vpos(:,1). $\hat{2}$ +Vpos(:,2). $\hat{2}$ )/((Vpos(:,1)-beta). $\hat{2}$ +Vpos(:,2). $\hat{2}$ ));
for i=1:NV;
%
%Upstream Layer Calculatins
%
if Vpos(i,2)==0;
    SV_us(i,1)=0;
else
    SV_us(i,1)=atan(Vpos(i,2)/Vpos(i,1))-atan(Vpos(i,2)/(Vpos(i,1)-beta));
end
%
%Downstream Layer Calculations
%
dx=Vpos(i,1)-x1;
dy=Vpos(i,2)-y1;
xpp=dx.*cos(theta)+dy.*sin(theta);
ypp=-dx.*sin(theta)+dy.*cos(theta);
vp=(gamma./2).*log(((xpp-k1). $\hat{2}$ +ypp. $\hat{2}$ )/(xpp. $\hat{2}$ +ypp. $\hat{2}$ ));
for j=1:NS;
    yp=ypp(j);
    xp=xpp(j);
    th=theta(j);
    if xpp(j) < 0
        if ypp(j)==0;
            up=0;
        elseif ypp(j) > 0
            up=gamma(j)*(atan(yp./(xp-k1(j)))-atan(yp./(xp))-pi);
        else

```

```

        up=gamma(j)*(atan(yp./(xp-k1(j)))-atan(yp./(xp))+pi);
    end
    u(j)=up*cos(th)-vp(j)*sin(th);
    v(j)=up*sin(th)+vp(j)*cos(th);
else
if ypp(j)==0;
    up=0;
else
    up=gamma(j)*(atan(ypp(j)./(xpp(j)-k1(j)))-atan(ypp(j)./xpp(j)));
end
    u(j)=up*cos(th)-vp(j)*sin(th);
    v(j)=up*sin(th)+vp(j)*cos(th);
end
end
SV_ds(i,1)=sum(u);
SV_ds(i,2)=sum(v);
clear u v up vp;
end
SV=SV_ds+SV_us*K_us;

```

### ***E.5 Main Program Sample***

This section provides a sample of the base program used to run the numerical model. The preceding functions are all called within this main program. Several variations on this basic program have been developed to investigate slightly different setups such as the wing without the presence of the layer, or the layer without the wing. It should be possible to derive these related programs from the complete base program.

```

%Shear Layer Rev 4: Left in Dimensional Units instead of
%Non-dimensionalized

```

```

clear all
close all
% Spified physical values
xo=1.70; % Position of leading edge relative to shear layer origin (x)
freq_name='x1p70_extended_chord_freq.txt';
n_freq=1028; %Frequency Data Points
freq_averages=5; % Number of frequency data sets to average
y_eta=[.03]; % Dimensionless Wing Leading Edge Heights (.05, .02, -.015, etc.)
U1=[5]; % Upper Shear Layer Velocity
chord_temp=[0.01 0.05 .1 .5 1]
[dum,nwng]=size(y_eta);
% Specified Model Values
r=0.43
delt=.002; % Dimensional Time Step (affects size of c_length)
beta2=4; % Downstream cutoff distanc
beta4=1000;
beta=-1000;
sample_delt=delt;
%For a relatively smooth curve needs more than 10, at 1028, try 15 or 20
density=1.2;
%Determining how often to sample the data flow
sample_step=floor(sample_delt/delt);
sample_delt=sample_step*delt;
freq_time_steps=sample_step*freq_averages*n_freq
S_A=10; %Spreading Angle of downstream layer portion
N_sheets=21; %Number of Vortex sheets to use in downstream Model
eta_sheet=2.4; %Range of eta for determination of  $\gamma = \Delta U_e(\hat{\eta}^2)$ 
Y0=-.05;

```

```

X0=0;
s1=.001; % Cutoff Radius to avoid singular behaviour
KF=0.001; % turbulent forcing strength
col=0;
col2=0;
for iijkl=1:nwng;
    [dum,nvel]=size(chord_temp)
    for ijk=1:nvel
        % Calculation of Wing Parameters
        %Wing Setup
        x_vo=-.02565; % Virtual Origin distance of the shear layer
        yo=y_eta(ijkl)*(xo-x_vo);
        Chord=chord_temp(ijk); % chord length (m)
        S=.4064; % Span (m)
        alpha_theory=5; %alpha degrees
        alpha=0
        np=150;
        alpha_theory=alpha_theory*pi/180;
        %Downstream Shear Layer information
        sa=(S_A*pi/180)/2;
        theta=linspace(-sa,sa,21);
        e_s=linspace(-eta_sheet,eta_sheet,N_sheets);
        g_norm=sum(exp(-e_s.^2));
        % Dimensions and control/vortex point locations
        alpha=alpha*pi/180;
        XW=linspace(1,np,np);
        for ij=1:np;
            XWing(ij)=XW(ij)-.75;

```

```

        CPwing(ij)=XW(ij)-.25;
    end
    XWing=XWing.*(Chord/np);
    CPwing=CPwing.*(Chord/np);
    Wing=zeros(np,2);
    Cwing=zeros(np,2);
    Wing(:,1)=XWing'.*cos(alpha)+xo;
    Wing(:,2)=-XWing'.*sin(alpha)+yo;
    Cwing(:,1)=CPwing'.*cos(alpha)+xo;
    Cwing(:,2)=-CPwing'.*sin(alpha)+yo;
    %
    %Setup to run for multiple velocities
    %
    U2=r*U1; % Lower Shear Layer Velocity
    % Calculated model values
    Lambda=(U1-U2)/(U1+U2); % Scaled Velocity Difference Ratio
    U0=(U1+U2)/2; % Average Velocity
    n_settle=ceil(beta2/(U0*delt));
    freq_points=n_freq*freq_averages;
    n=n_settle+freq_time_steps
    %Beta scaling for initial conditions
    N_pi=round(beta2/(U0*delt));
    beta2=N_pi*U0*delt;
    %Varying Model Information
    c=U0*delt;
    h=U0*delt/2;
    Gamma_Layer=(U1-U2)*U0*delt;
    test=U0*delt/c;

```

```

%Downstream Shear Layer info
gamma=(U1-U2)*exp(-e.s.^2)/g_norm;
gamma_input=gamma./(2*pi);
%Wing Parameters
Xwake=Chord+U0*delt/2;
xw=Xwake*cos(alpha)+xo;
yw=-Xwake*sin(alpha)+yo;
for ik=1:np; %iterates through rows of A (which control point?)
    for il=1:np; %iterates through columns of A (which vortex point?)
        A(ik,il)=(1/(2*pi*(CPwing(ik)-XWing(il))));
    end
    A(ik,np+1)=(1/(2*pi*(CPwing(ik)-Xwake))); %Inserts the wake vortex
constant
end
A(np+1,:)=1;
Con1=zeros(np,1)-U0*sin(alpha);
SV_wing=shear_us_ds_angle(Cwing,beta,beta2,beta4,theta,gamma_input,Y0,X0);
Con_1=Con1-(SV_wing(:,1).*sin(alpha)+SV_wing(:,2).*cos(alpha));
%Calculation of normalization factors
con_theory=zeros(np,1)-U0*sin(alpha_theory);
A0=A((1:np),(1:np));
G1=A0\ con_theory;
Circ_theory=sum(G1);
L_span.theory=density*U0*Circ_theory
%Initialization for the model
% Initializing the plotting dummy variable
dummy=0;
dum=0;

```

```

NW=0;
K.G=0;
ii=0;
iii=0;
i_freq=0;
V_rem=0;
L=0;
LL=0;
F_pi=10; %hz
Amp_pi=0.01;
X_pi=linspace(0,beta2, N_pi)+U0*delt;
Y_pi=Amp_pi*sin((2*pi)*F_pi*X_pi);
P(:,1)=X_pi';
P(:,2)=Y_pi';
P(:,3)=-Gamma_Layer;
NV=N_pi;
%
y_ref=linspace(-1,1);
x_ref=0;
y_ref2=y_ref;
ref_1x=linspace(0,8);
ref_1y=ref_1x*0+.01;
ref_2y=ref_1x*0-.01;
for i=1:n;
    n-i% Remaining steps
    Time=delt*i;
    %Initialization of new vortices in the system and cutoff routines
    P(NV+1,:)= [h,0,-Gamma_Layer];

```

```

[P,NV]=cutoff(P,beta2);
W(NW+1,:)=[xw,yw,0];
[W,NW]=cutoff(W,beta2);
%Velocity Caculation routines for the shear layer and wake points
% to determine convection step
%Vortex and Shear Induced velocities in the Layer
Ucp_vor=vortex_induced_velocity(Cwing,W,s1)
    +vortex_induced_velocity(Cwing,P,s1);
Ucp=-((Ucp_vor(:,1)*sin(alpha)+Ucp_vor(:,2)*cos(alpha)))+Con_1;
%Solution for the strengths of the wing and new wake vortices
Ucp(np+1)=K_G;
Gamma=A\Ucp;
W(NW,3)=Gamma(np+1);
K_G=K_G-Gamma(np+1);
for m=1:np;
    Wing(m,3)=Gamma(m);
end
Circ_wing(i)=sum(Gamma(1:np));
circ_norm(i)=Circ_wing(i)/Circ_theory;
Wake(i)=Gamma(np+1);
%
%Determination of Convection Velocities
%
%Layer Particles
SV_layer=shear_us_ds_angle(P,beta,beta2,beta4,theta,gamma_input,Y0,X0);
U_layer=vortex_induced_velocity(P,P,s1);
U_wake=vortex_induced_velocity(P,W,s1);
U_wing=vortex_induced_velocity(P,Wing,s1);

```

```

U=(SV_layer+U_layer+U_wing+U_wake)*delt;
U(:,1)=U(:,1)+U0*delt;
U(:,3)=0;
U=random(U,KF,NV);
%Wake Particles
SV_wake=shear_us_ds_angle(W,beta,beta2,beta4,theta,gamma_input,Y0,X0);
W_layer=vortex_induced_velocity(W,P,s1);
W_wake=vortex_induced_velocity(W,W,s1);
W_wing=vortex_induced_velocity(W,Wing,s1);
W_vel=(SV_wake+W_layer+W_wing+W_wake)*delt;
W_vel(:,1)=W_vel(:,1)+U0*delt;
W_vel(:,3)=0;
W_vel=random(W_vel,KF,NW);
%Vortex and Shear Induced velocities in the Wake
%Clearing unneeded velocity variables
clear U_wake U_layer U_wing SV_layer
clear W_wake W_layer W_wing SV_wake
plot_i(i)=i;
if i<2;
    ii=ii+1;
    plot_ii(ii)=ii;
    L_s=density*(U0*Circ_wing(i-1)+(Chord/(delt))*(Circ_wing(i)
        -Circ_wing(i-1)));
    L_norm(ii)=L_s./L_span_theory;
end
if i<=1;
    if dummy==10
        dummy=0;

```

```

        x_ref2=x_ref*0+U0*Time;
        subplot(2,1,1)
        plot(P(:,1),P(:,2),'b.', x_ref2, y_ref2,'r')
        hold on
        plot(ref_1x,ref_1y,'g',ref_1x,-ref_2y,'g')
        plot(Wing(:,1),Wing(:,2),'k-',W(:,1),W(:,2),'r.')
        axis([0 beta2 -.5 .5]);
        hold off
        subplot(2,1,2)
        plot(plot_ii,L_norm,'b-',plot_i,circ_norm,'m-')
        pause(.01)
    end
    dummy=dummy+1;
end
P=P+U;
W=W+W_vel;
clear U W_vel
if i_j==n_settle;
    iii=iii+1;
    dum=dum+1;
    if dum==sample_step
        dum=0;
        i_freq=i_freq+1;
        lift_freq(i_freq)=L_s;
    end
end
end
clear P W

```

```

lift_full=lift_freq*S;
for im=1:1;
    split=[1 2 4 8];
    il=split(im);
    freq_averages_temp=freq_averages*il;
    n_freq_temp=n_freq/il;
    df=(1/(sample_delt*n_freq_temp));
    f=(0:n_freq_temp/2).*df;
    clear sum_psd
    sum_psd=zeros(1,n_freq_temp);
    for ik=1:freq_averages_temp;
        fo=n_freq_temp*(ik-1)+1;
        lfreq=lift_full(1,(fo:fo+(n_freq_temp-1)));
        Varying_lift=lfreq-mean(lfreq);
        Amp=fft(Varying_lift,n_freq_temp);
        Amp=Amp.*conj(Amp)/n_freq_temp^2;
        psd_fft_lift=(Amp.^2)/df;
        sum_psd=sum_psd+psd_fft_lift;
        plot_psd=sum_psd./ik;
        hold on
        plot(f,psd_fft_lift(1:(n_freq_temp/2+1)),'b-')
        pause
    end
    sum_psd=sum_psd./freq_averages_temp;
    rms_psd=sqrt(sum(sum_psd)*df)
    fmax=8*(U1/xo);
    fmax_pos=fmax/df;
    rms_peak=sqrt(sum(sum_psd(1:ceil(fmax_pos))))*df)

```

```

close
plot(f,sum_psd(1:(n_freq_temp/2+1)),'r.-');
axis([0 50 0 2e-3])
grid on
pause
rms_lift=sqrt((sum((lift_full-mean(lift_full)).2))/i_freq)
col=col+1;
Freq_out(1,col)=U1;
Freq_out(2,col)=delt;
Freq_out(3,col)=Chord;
Freq_out(4,col)=r;
Freq_out(5,col)=xo;
Freq_out(6,col)=yo;
Freq_out(7,col)=n_freq_temp;
Freq_out(8,col)=rms_lift;
Freq_out(9,col)=rms_psd;
Freq_out(10,col)=beta2;
Freq_out((12:(n_freq_temp/2+12)),col)=f';
col=col+1;
Freq_out(4,col)=n_freq_temp;
Freq_out((12:(n_freq_temp/2+12)),col)=sum_psd(1:(n_freq_temp/2+1))';
Freq_out(11,:)=1;
end
clear Amp fo l_freq Varrying_lift df f ps psd_fft_lift n_freq_temp
end
end
%
dlmwrite(freq_name,Freq_out,'');

```

## CURRICULUM VITAE

**Josh Sementi**

### **Education**

- University of Washington (Seattle, Wa.) Ph.D. A.A. Fluid Mechanics, Dec. 2005.
- University of Washington (Seattle, Wa.) M.S.A.A., Fluid Mechanics, December 2001.
- University of Idaho (Moscow, Id) B.S.M.E. Mechanical Engineering, May 1999.

### **Academic Positions**

- ENGR 100, Course Manager, 8/04-12/05. Managed many aspects of ENGR 100 (Introduction to Engineering Design) including purchasing, budget tracking, hiring, curriculum development, training, and instructor assessment.
- ENGR 100, Instructor Sept. 9/03-12/05. Responsibilities include teaching, grading, lab prep, TA supervision and other duties as needed.

### **Research Positions**

- Shear Layer-Wing Interaction Research, (1/01-12/05) University of Washington. Experimental and Numerical investigation of the interaction between a shear layer and a wing.

- Towed Cable Drag Reduction Investigation, (6/01-9/01) Analytical Methods Inc. and University of Washington. Wind tunnel testing and computer code verification in support of an SBIR grant.
- Blue crab juvenile response to prevailing ocean currents, (06/98-08/98), University of Delaware. Operated and modified computational code modeling the scatter of blue crab larvae due to ocean currents and local wind conditions.
- Micro-gravity thermodynamic property investigation. (9/97-6/98) University of Idaho. Investigation of vapor yield due to pressure induced boiling under normal and micro-gravity conditions.

### **Presentations and Papers**

- Non-Steady Loads on Surfaces Embedded in a 2-D Shear-Layer, J.P. Sementi and D.A. Russell, 34th AIAA Fluid Dynamics Conference and Exhibit, 2004.
- Jet Exhaust and Wing Flap Interactions, J.P. Sementi, 40th AIAA Annual Aerospace Sciences Meeting and Exhibit, 2002.
- Jet Exhaust and Wing Flap Interactions, J.P. Sementi, AIAA Region VI Student Conference, 2001.
- University of Idaho Design Expo, Exhibit Presenter 1998 and 1999.
- Micro-gravity Thermodynamic Property Investigation, 1998 University of Idaho Design Expo. invited presentation.
- Micro-gravity Thermodynamic Property Investigation, 1998 American Astronautical Society National Conference, invited technical poster.